

Trailing Edge Noise Generation of Porous Airfoils

**Von der Fakultät für Maschinenbau, Elektrotechnik und
Wirtschaftsingenieurwesen der Brandenburgischen Technischen
Universität Cottbus zur Erlangung des akademischen Grades
eines Doktor-Ingenieurs genehmigte Dissertation**

vorgelegt von

Diplom-Ingenieur

Thomas F. Geyer

geboren am 07.01.1981 in Radebeul

Vorsitzender: Prof. Dr.-Ing. Christoph Egbers

Gutachter: Prof. Dr.-Ing. Ennes Sarradj

Gutachter: Prof. Dr.-Ing. Thomas Carolus

Tag der mündlichen Prüfung: 18.08.2011

Contents

Nomenclature	v
Danksagung	ix
1 Introduction	1
2 Review on literature	5
2.1 Porous airfoils	5
2.1.1 Aerodynamics of porous airfoils	5
2.1.2 Application of flow-permeable trailing edges for noise control	6
2.2 Airfoil trailing edge noise	9
2.2.1 Dependence on flow speed	9
2.2.2 Dependence on angle of attack	15
2.2.3 Trailing edge noise spectral shape	15
2.3 Effects of surface roughness	20
3 Measurement setup	21
3.1 Porous airfoils	21
3.1.1 Characterization of the porous materials	21
3.1.2 Airfoil data	26
3.2 Wind tunnel	30
3.3 Aerodynamic force measurements	34
3.4 Acoustic measurements and data processing	37
3.4.1 Beamforming theory	37
3.4.2 Microphone array characteristics	42
3.4.3 Two-dimensional beamforming	44
3.4.4 Three-dimensional beamforming	52
3.5 Constant temperature anemometry measurements	63

4	Measurement results and discussion	69
4.1	Aerodynamic measurements	69
4.2	Acoustic measurements	73
4.2.1	Two-dimensional beamforming results	74
4.2.2	Three-dimensional beamforming results	75
4.3	Constant temperature anemometry measurements	91
4.3.1	Velocity profiles	92
4.3.2	Boundary layer integral parameters	97
4.3.3	Turbulence parameters in the wake	105
4.3.4	Turbulence spectra	106
5	Development of a basic trailing edge noise prediction model	119
5.1	Development of the model	119
5.1.1	Theory	119
5.1.2	Trailing edge noise prediction based on measured turbulence spectra and measured mean velocity	122
5.1.3	Trailing edge noise prediction based on modeled turbulence spectra and mean velocity	134
5.2	Prediction of the trailing edge noise of porous airfoils	140
5.2.1	Comparison of predicted and measured trailing edge noise	141
5.2.2	Discussion of the results and possible improvements to the model	143
6	Conclusion	145
7	Zusammenfassung	149
	Literature	153
	List of Figures and Tables	161
A	Additional wind tunnel data	169
B	Microphone positions	171
C	Photographs of the experimental setup	173
D	Comparison of three-dimensional beamforming algorithms for a single point source	175

E Additional turbulence spectra 177

E.1 Influence of the spanwise position 177

E.2 Normalization approach 178

E.3 Turbulence spectra at different chord positions 178

Copyright / Rechtliche Bedingungen

This work is licensed under the Creative Commons Attribution-NonCommercial-NoDerivs 3.0 Unported License. To view a copy of this license, visit <http://creativecommons.org/licenses/by-nc-nd/3.0/> or send a letter to Creative Commons, 444 Castro Street, Suite 900, Mountain View, California, 94041, USA.

Sämtliche Rechte am Inhalt dieser Arbeit verbleiben beim Autor. Der Autor überträgt der Brandenburgischen Technischen Universität Cottbus das einfache Verbreitungsrecht, also das Recht, im Rahmen der gesetzlichen Aufgaben der Hochschulbibliotheken weitere Kopien dieser Dissertation herzustellen und zu verbreiten bzw. in Datennetzen zur Verfügung zu stellen.

Diese Arbeit darf heruntergeladen und frei verwendet werden, wenn sie entsprechend zitiert wird. Eine Bearbeitung von Inhalten dieser Arbeit (Bilder, Tabellen) bedarf der Erlaubnis des Autors. Eine kommerzielle Nutzung der Dissertation und die Vervielfältigung aus kommerziellen Zwecken sind ausgeschlossen.

Nomenclature

Functions and scalars

a		transfer function
\mathbf{A}		(acoustic) transfer matrix
A_s	[m ²]	cross-sectional area of the porous sample
A_{socket}	[m ²]	cross-sectional area of the socket outlet for the measurement of the in situ air flow resistance
b	[m]	spanwise extent / wingspan
\mathbf{B}		transfer matrix of the six-component balance
c	[m/s]	speed of sound
c_l	[m]	chord length
C_D		drag coefficient
C_L		lift coefficient
d_f	[m]	fibre diameter
d_{min}	[m]	characteristic sensor size
d_p	[m]	pore diameter
d_s	[m]	thickness of the porous sample
D	[m]	nozzle diameter
\overline{D}		directivity function
e		exponent
$E\{\}$		expectation operator
f	[s ⁻¹]	frequency
f_c	[s ⁻¹]	third-octave band center frequency
f_S	[s ⁻¹]	sample frequency
F		spectral shape function
F_D	[N]	drag force
F_L	[N]	lift force
F_S	[N]	side force
\mathbf{F}		matrix of aerodynamic forces and moment
g		proportionality factor
\mathbf{G}		cross spectral matrices of microphone signals
$\hat{\mathbf{G}}$		estimate of the cross spectral matrices of microphone signals
h	[m]	trailing edge thickness
\mathbf{h}		steering vector
H_{12}		shape factor

I	[W/m ²]	sound intensity in the far field
\mathbf{I}		identity matrix
k	[m ⁻¹]	wave number
k'	[m ²]	thermal permeability
k_v	[m ²]	viscous permeability
K		constant
L_p	[dB]	third octave band sound pressure level
$L_{p,\text{tot}}$	[dB]	overall sound pressure level
m		arbitrary integer
m_i		slope of a linear function i
M		number of sound sources
Ma		Mach number
M_P	[Nm]	pitching moment
M_R	[Nm]	rolling moment
M_Y	[Nm]	yawing moment
n	[Pa]	amplitude of noise signals; arbitrary integer
n_B		number of blocks
\mathbf{n}		matrix of noise signals
N		number of microphones
p	[Pa]	sound pressure
\mathbf{p}		matrix of sound pressures p
p_0	[Pa]	reference sound pressure, $2 \cdot 10^{-5}$ Pa
q	[m ³ /s]	sound energy flux
q_s	[m ³ /s]	volume flow velocity through a porous sample
r	[Pa s/m ²]	air flow resistivity
R	[m]	distance between source and observer
R_s	[Pa s/m]	specific air flow resistance
Re		Reynolds number based on chord length
s	[m]	distance between two adjacent pores
S	[m ²]	wing area
\mathbf{S}		cross spectral matrices of source signals
S_{XX}		auto power spectral density
Str_{c_l}		Strouhal number based on chord length
Str_{δ_1}		Strouhal number based on boundary layer displacement thickness
SR	[m ⁻¹]	spatial resolution
T	[s]	(measurement) duration
TR	[s ⁻¹]	time resolution
Tu		Turbulence intensity
u	[m/s]	turbulent velocity fluctuations
\bar{u}_b	[m/s]	mean velocity at the edge of the laminar sublayer
u_0	[m/s]	characteristic velocity scale of the turbulence
u_s	[m/s]	flow velocity through a porous sample
u_v	[m/s]	measure of the turbulent velocity fluctuations in the unsteady vortical flow over an airfoil or wing according to [Lilley, 1998]
U	[m/s]	fluid velocity
U'	[m/s]	(spline) fit of the fluid velocity
U_0	[m/s]	wind tunnel flow speed
U_c	[m/s]	turbulence convection velocity

v_i	[v]	signals from the single load cells ($i = 1, 2, \dots, 6$)
V	[m ³]	turbulent eddy volume
V_p	[m ³]	pore volume of a porous material
V_s	[m ³]	volume of the skeletal material of a porous material
V_t	[m ³]	(total) volume of a porous material
\mathbf{V}		matrix of signals from load cells
w		arbitrary scalar
W	[kg]	(aircraft) weight
x, y, z	[m]	cartesian coordinates
\mathbf{x}		position vector
Δx	[m]	streamwise extent of porous treatment

Greek symbols

α	[°]	geometric angle of attack
β	[°]	angular coordinate of a cylindrical eddy according to [Ffowcs Williams and Hall, 1970]
γ		normalized turbulence intensity
δ	[m]	boundary layer thickness
δ_b	[m]	thickness of the laminar sublayer
δ_1	[m]	boundary layer displacement thickness
δ_2	[m]	momentum thickness
δ_3	[m]	energy thickness
η	[N s/m ²]	dynamic viscosity
θ	[°]	inclination angle
Λ	[m]	characteristic viscous dimension
Λ'	[m]	thermal characteristic dimension
λ	[m]	(sound) wave length
ν	[m ² /s]	kinematic viscosity
Ξ	[°]	angle between convection velocity and trailing edge
ρ	[kg/m ³]	fluid density
ρ_s	[kg/m ³]	density of the skeletal material of a porous material
ρ_t	[kg/m ³]	(total) density of a porous material
σ_s		surface porosity
σ_v		volume porosity
τ		tortuosity
Θ	[°]	sideline angle
Φ_{uu}	[m ² /s]	power spectral density of streamwise velocity fluctuations
Ψ	[°]	elevation angle
ω	[s ⁻¹]	circular frequency
ω_0	[s ⁻¹]	characteristic source frequency of turbulent eddies
Ω	[°]	trailing edge solid angle
ℓ	[m]	turbulence correlation length

Indices, superscripts and special characters

H		conjugate transpose (Hermitian transpose)
$+$		Moore-Penrose pseudoinverse
D		drag
i, j, k		arbitrary indices
is		in situ
L		lift
n		normalized
peak		characterizing a spectral peak
por		porous
ref		reference (non-porous)
s		(porous) sample; surface
v		viscous; volume
W		wing
$\bar{\quad}$	(overline)	mean value
\sim	(tilde)	root-mean-square

Abbreviations

BPM	noise prediction model by Brooks, Pope and Marcolini [Brooks et al., 1989]
CFD	Computational Fluid Dynamics
CTA	Constant Temperature Anemometry
FFT	Fast Fourier Transformation
LDA	Laser Doppler Anemometry
PSD	power spectral density
PSF	point spread function
TNO	noise prediction model developed at the Netherlands Organisation for Applied Scientific Research [Moriarty et al., 2005]

Danksagung

In erster Linie danke ich Prof. Dr.-Ing. Ennes Sarradj für die ausgezeichnete Betreuung, die vielen hilfreichen Anregungen und Gespräche und die Möglichkeit, im Rahmen meiner Tätigkeit als wissenschaftlicher Mitarbeiter diese Arbeit anfertigen zu können.

Ich danke Herrn Prof. Dr.-Ing. Thomas Carolus dafür, dass er sich trotz vollen Terminplanes freundlicherweise dazu bereit erklärt hat, das Zweitgutachten für diese Dissertation anzufertigen.

Herrn Prof. Dr.-Ing. Christoph Egbers möchte ich vor allem dafür danken, dass er den Vorsitz der Prüfungskommission übernommen hat. Außerdem waren er und die Mitarbeiter des Instituts für Aerodynamik und Strömungslehre immer für Fragen offen.

Bei meinen Kollegen Jens Giesler, Christoph Fritzsche, Carsten Langhof, Christian Schulze und Thomas Windisch möchte ich mich für die gute Zusammenarbeit, die vielen Diskussionen, die mir geholfen haben, ein oder andere Problem zu lösen, und für die tatkräftige Unterstützung bei vielen Messungen und Messaufbauten herzlich bedanken.

Mein Dank gilt darüber hinaus den studentischen Hilfskräften Christian Voigt, Thomas Drescher, Viktor Kalimbach, Marcus Hobracht, Manuel Bartsch und Falko Krüger, die an vielen Stellen einen Beitrag zu dieser Arbeit geleistet haben.

Für die Hilfe bei der Korrektur meiner schriftlichen Arbeit danke ich Andrew Whittaker und Ute Gebel.

Schließlich danke ich meiner Freundin Carina Römer und meiner Tochter Johanna für ihre Geduld und ihr Verständnis, vor allem in den letzten Wochen.

Chapter 1

Introduction

The noise generated at the trailing edge of flat plates and airfoils is still a main field of interest for aeroacoustic research. It appears as part of the noise generated by aircraft, at the trailing edge of wings and high-lift devices, as well as at the trailing edges of fans, ventilators and wind turbines. Basic approaches for noise control include the modification of the rigid and sharp trailing edge, for example through the application of serrations, flow-permeable treatments or elastic materials.

The subject of the present work is the noise generated by a turbulent boundary layer flow over the trailing edge of an airfoil model and the potential reduction of trailing edge noise by means of airfoils made completely out of open-porous, flow-permeable materials.

In order to achieve a reduction of airfoil trailing edge noise, some basic knowledge on the underlying physical mechanisms of this noise source is essential. For common technical wings or airfoils in a quasi non-turbulent subsonic flow, there exist five theoretical noise generation mechanisms [Brooks et al., 1989]. These are the interaction of a turbulent boundary layer with the trailing edge of the wing or airfoil (turbulent boundary layer - trailing edge noise), the separation of the flow from the airfoil surface (separation-stall noise), the interaction of a laminar boundary layer with the trailing edge (laminar boundary layer vortex shedding noise), the interaction of the boundary layer with the wing tip (tip vortex formation noise) and the interaction of the boundary layer with a blunt trailing edge (trailing edge bluntness vortex shedding noise). These airfoil self noise mechanisms do not include the noise that is generated when an airfoil is subject to a turbulent inflow.

The focus of the present thesis is the generation of trailing edge noise due to the interaction of a turbulent boundary layer with the trailing edge of an airfoil, and thus consists of turbulent boundary layer - trailing edge noise and, to some extent, trailing edge bluntness vortex shedding noise.

For the intended experimental study of airfoil trailing edge noise, it has to be known that the noise generated at the trailing edge of an airfoil or flat plate may only be examined separately from the noise generated at the leading edge, when the airfoil or plate is not acoustically compact [Hayden, 1972, Blake, 1986]. This means that its characteristic dimension, usually the chord length c_l , has to be larger than the acoustic wavelength λ of interest,

$$c_l > \lambda \tag{1.1}$$

and thus

$$f > \frac{c}{c_t}, \quad (1.2)$$

where f is the frequency and c the speed of sound. This condition is commonly called the non-compactness condition.

According to theory, the basic physical mechanism causing the generation of noise at the trailing edge is a scattering of velocity fluctuations, which are convected along the airfoil surface within the boundary layer, by the airfoil rear edge [Blake, 1986]. Additional vortex shedding may occur at a blunt trailing edge for a fully turbulent boundary layer. Figure 1.1 illustrates the basic principle of the generation of turbulent boundary layer - trailing edge noise. The resulting acoustic source at the trailing edge shows the characteristics of a “half-baffled” dipole [Hayden, 1972], due to the cancellation of acoustic pressure fluctuations from suction side and pressure side downstream of the trailing edge in the streamwise direction. This directivity leads to a maximum noise emission at an angle of 90° to the airfoil chord, above and below the airfoil, in the vertical plane perpendicular to the trailing edge.

A more detailed description of the processes leading to the generation of trailing edge noise is presented in Figure 1.2, which is taken from the work of Hayden [Hayden, 1972]. In addition to the basic principle of the trailing edge noise generation illustrated in Figure 1.1, it includes the induction of pressure fluctuations on the airfoil surface as a result of the velocity fluctuations within the boundary layer, and a possible feedback of the acoustic pressure fluctuations, which are radiated into the acoustic far field, on the fluid disturbances.

As mentioned above, one feasible method to reduce trailing edge noise is the use of open porous and flow-permeable airfoils. (The term “porous airfoil” is used in the present thesis to describe a technical airfoil model manufactured completely out of an open-porous material without internal barriers.) However, besides some studies on the use of porous materials for noise control in selected applications (e.g. [Chanaud, 1972, Chanaud et al., 1976, Fink and Bailey, 1980]), there exist only few findings on the influence of the parameters of the porous materials on the noise generation and on the physical mechanisms responsible for the differences of the trailing edge noise of porous airfoils compared to common non-porous airfoils. No experimental database is available that allows for a more detailed investigation of the effect of a porous trailing edge on the generation of trailing edge noise. Such experimental data could eventually be used as a basis for numerical investigations or for the development of empirical airfoil self noise prediction models. Furthermore, the

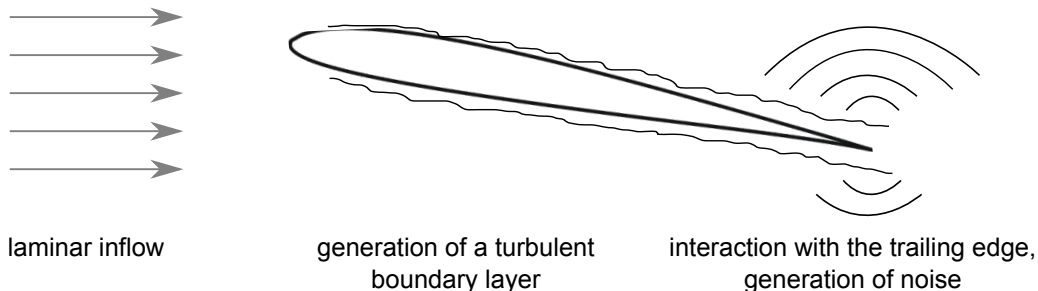


Figure 1.1: Basic principle of the noise generation due to a fluid flow interacting with the trailing edge of an airfoil

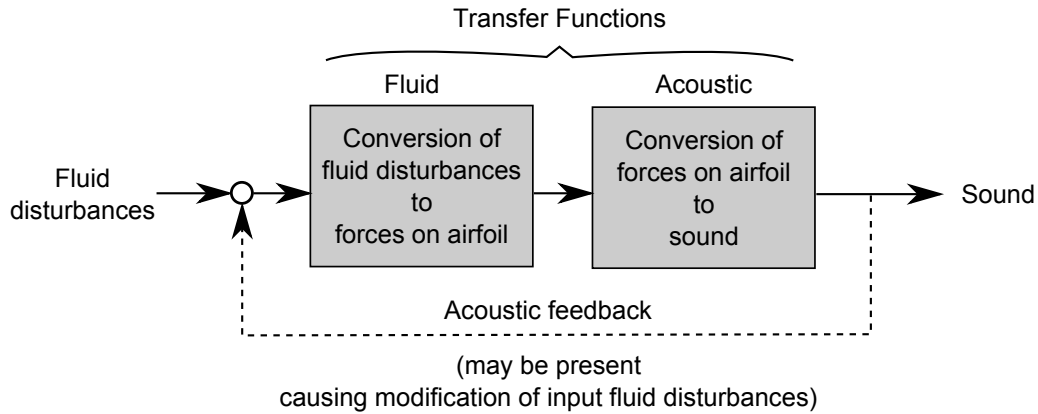


Figure 1.2: Block diagram of the noise generation due to a fluid flow interacting with rigid surfaces (figure prepared according to artwork originally given in [Hayden, 1972], Figure 1¹)

influence of porous materials on the aerodynamics of flow-permeable airfoils or wings also requires clarification.

Within the scope of the present thesis, an experimental study on the potential trailing edge noise reduction of porous airfoils and the cause of this noise reduction was performed. This study should provide a large database that will be used to develop an initial trailing edge noise model for porous airfoils, but may also serve as a validation for future numerical studies.

The main objective of this work is the identification of the influence of the material parameters of the porous airfoils on the trailing edge noise reduction. To this end, detailed aerodynamic and acoustic measurements were conducted on a large set of airfoil models in an aeroacoustic wind tunnel to examine the noise radiated from the trailing edge of porous airfoils relative to a non-porous reference airfoil in a subsonic flow. Besides the acoustic measurements, performed using microphone array measurement technique, the lift and drag forces acting on the airfoils were measured simultaneously. The present study provides the first extensive and systematic investigation of the noise generation by porous airfoil models that is based on such a large number of different open-porous materials. In order to draw conclusions on the mechanisms causing the reduction of trailing edge noise, additional hot-wire measurements were performed within the turbulent boundary layer of a subset of the airfoils.

The remaining part of the present thesis is organized as follows: First, a short review will be given on common noise reducing techniques, on the basic aerodynamics of airfoils and on the generation of noise at the trailing edge of flat plates and technical airfoils. The latter consists of an overview of selected theoretical and empirical trailing edge noise prediction models.

Second, the setup of the experimental study will be presented. This includes a detailed description of the porous airfoils, the aeroacoustic open jet wind tunnel, the setup used for the measurement of the aerodynamic forces acting on the airfoils, the microphone array measurement technique and the corresponding data processing as well as the hot-wire measurement setup.

¹The above diagram is reproduced by permission of Raytheon BBN Technologies Corp., the copyright holder. Further reproduction without permission is prohibited.

Following the presentation and discussion of the results from the aerodynamic, acoustic and constant temperature anemometry measurements, a basic trailing edge noise prediction model will be developed, based on measured velocity fluctuations inside the turbulent boundary layer of a subset of the airfoils. As a first validation of the model, results of the trailing edge noise prediction for the porous airfoils will be compared to measured trailing edge noise spectra. Finally, future work toward a potential improvement of the model will be proposed.

Chapter 2

Review on literature

This chapter will review selected literature on the possible noise control due to the application of flow-permeable trailing edges as well as literature on airfoil trailing edge noise and aerodynamics, both theoretical and experimental, and will review some of the basic airfoil trailing edge noise theories. The selection of literature is by no means complete, but focuses on studies that may be relevant to the present experimental study.

2.1 Porous airfoils

2.1.1 Aerodynamics of porous airfoils

Flow-permeable treatments as a means to reduce trailing edge noise are in the focus of aeroacoustic research for several years. In order to provide a serious alternative compared to conventional airfoils, for example in fans and wind turbines, the aerodynamic efficiency of the permeable airfoils should not be significantly lower than that of common airfoils.

The aerodynamic efficiency can be described in the most simple way by the lift force F_L and the drag force F_D . When an airfoil is immersed in a fluid flow, characterized by the flow speed or freestream velocity U_0 , the flow causes a pressure distribution as well as a shear stress distribution over the body surface. Integrating over the body forces determines the actual forces and moments acting on the surface. The lift force F_L is the (upward) component of the total force perpendicular to U_0 while the drag force F_D is the component parallel to (and pointing toward the same direction as) the flow speed U_0 . In some studies, the forces are not defined relative to the direction of the stream, but relative to the airfoil chord.

Normalizing the aerodynamic forces with the freestream dynamic pressure $0.5 \cdot \rho \cdot U_0^2$ and the wing or airfoil area S , leads to the definition of the common dimensionless aerodynamic coefficients for airfoils [Anderson, 1984]. These are the lift coefficient,

$$C_L = \frac{2 \cdot F_L}{\rho \cdot U_0^2 \cdot S}, \quad (2.1)$$

and the drag coefficient,

$$C_D = \frac{2 \cdot F_D}{\rho \cdot U_0^2 \cdot S}, \quad (2.2)$$

with ρ being the density of the fluid.

The lift force generated by an airfoil in a uniform flow does not only depend on the flow speed and the airfoil shape and geometry, but also on the angle of attack α . It is known that, for small and moderate angles of attack, the lift coefficient varies linearly with angle of attack. When α increases further, the flow starts to separate from the suction side surface of the airfoil, a process which is called stalling, resulting in a sudden decrease in lift and an increase in drag.

It is reasonable to assume that porous airfoils produce less lift than non-porous airfoils, due to a presumed fluid flow through the porous material from the pressure side to the suction side, but a higher drag force, caused by an increase in shear stress due to the increased surface roughness of porous airfoils compared to the surface of common non-porous airfoils. Since it is not likely that the use of airfoils with flow-permeable trailing edges results in aerodynamic advantages, there exist only few solely aerodynamic studies on such airfoils. After all, the main reason to consider flow-permeable trailing edges is the potential reduction of airfoil trailing edge noise.

An experimental study on the effect of a porous upper surface on the aerodynamic characteristics of a NACA 0012 airfoil was performed by Mineck and Hartwich [Mineck and Hartwich, 1996]. The experiments included the measurement of the chordwise pressure distribution and the total pressure in the wake of an airfoil model with a fully porous upper surface, spanning a number of chordwise cavities, and a solid lower surface. The results indicate possible losses in aerodynamic efficiency due to an increased skin friction, which effectively lead to an increased drag coefficient compared to the solid surface. As a result of the porous surface, the lift coefficient increased less strongly with increasing angle of attack.

Vad et al. [Vad et al., 2006] performed aerodynamic and acoustic measurements on a RAF-6E-shaped airfoil that was not flow-permeable, but coated with soft filaments (velvet). They found that the coating reduced the lift but increased the drag.

The investigation by Geyer et al. [Geyer et al., 2010a] on the trailing edge noise generation of porous airfoils, which will be subject to the present thesis, confirmed the above assumption: The porous airfoils were found to generate a smaller lift force, but a higher drag force compared to a non-porous reference airfoil of the same geometry.

2.1.2 Application of flow-permeable trailing edges for noise control

The use of porous materials is one potential approach to reduce the noise radiation from the trailing edge of an airfoil. In general, concepts for trailing edge noise reduction are mostly efforts to change the acoustic impedance of the trailing edge, and hence either its shape or its material. Possible applications of a treatment with flow-permeable materials for noise control include the use of porous blades in wind turbines, fans or blowers.

Lowson [Lowson, 1968] mentioned the use of porous leading or trailing edges to reduce the forces upon the rotor blades as one potential method for the reduction of axial flow compressor noise.

Chanaud et al. [Chanaud, 1972, Chanaud et al., 1976] examined the noise reduction of propeller fans composed of rigid porous blades. They investigated the influence of the extent of the porous material by successively closing the pores of the porous blade with increasing fan diameter by use of hard wax. A noticeable noise reduction was measured for both a free fan and a ducted fan until only the outer one inch (25.4 mm) of the blades was porous. When closing the pores beyond this point, the measured sound level gradually returned to the solid blade value.

An early study on the use of porosity to reduce trailing edge noise was conducted by Bohn [Bohn, 1976], who equipped a flat plate with porous trailing edge extensions and measured the noise generation when one side of the plate was subject to jet flow. The results showed that the maximum noise reduction was at a frequency proportional to $U_0/\Delta x_p$, with Δx_p being the streamwise extent of the porous edge.

When Fink and Schlinker examined the noise generation at different airframe components [Fink and Schlinker, 1979], they mention noise reduction concepts such as the application of porous and serrated trailing edges.

An experimental study on the noise reducing effects of modifications to trailing-edge flap and leading-edge slat of a wing model with different flow-permeable treatments was performed by Fink and Bailey [Fink and Bailey, 1980]. They found that the treatment of the flap trailing edge alone did not yield a significant noise reduction. Results obtained for a perforated leading edge of a trailing-edge flap showed that, to some extent, high frequency noise was generated by the airflow over the perforations. Using a porous leading edge, a noise reduction of 1 dB to 2 dB was measured at high frequencies. Experiments involving modifications to a leading-edge slat showed that a slat with a serrated trailing edge was louder than a conventional slat, while a slat with a perforated trailing edge lead to a noise reduction of about 2 dB over a large frequency range.

Revell et al. [Revell et al., 1997] measured the noise radiated from trailing-edge flaps with porous acoustic treatment at the flap side edge. The porous materials were characterized by their flow resistance, taking into account non-linearity effects and hence a dependence of the flow resistance on the flow speed. A noise reduction was measured over a large frequency range. The non-linear behavior of the porous materials was found to be beneficial, since low velocity oscillating flows between suction side and pressure side of the flap encounter a lower flow resistance than the high velocity tangential flows, and hence the generated lift force was found to be only minimally affected.

A recent experimental study on flow-permeable trailing edges, realized through comb-like or slit edge modifications, was done by Herr [Herr, 2007], who performed acoustic tests on a flat plate and a NACA 0012-like airfoil. The acoustic results were scaled using a U_0^5 scaling approach and plotted versus the Strouhal number based on boundary layer displacement thickness or on a constant correlation length. The study showed that there exists a significant potential for a broadband noise reduction through the use of these edge modifications.

As mentioned above, the use of airfoils made completely out of open-porous materials to reduce trailing edge noise was the subject of recent work by Geyer et al. [Geyer et al., 2010a, Geyer et al., 2010b]. Their experimental trailing edge noise study is described in more detail in the present thesis.

Another possible approach to reduce trailing edge noise is the use of trailing edge serrations, which was discussed in detail by Howe [Howe, 1991a, Howe, 1991b], who developed a theoretical model for the noise reduction of a serrated trailing edge. According to Howe, noise is generated only at those regions along the trailing edge where the wavenumber vector of the dominant turbulent eddies convecting over the airfoil is normal to the edge. The noise reduction is therefore related to the effective reduction of the spanwise length of the airfoil and the optimum noise reduction can be achieved when the edge is inclined by angles smaller than 45° to the mean flow direction. Additionally, the noise reducing effect is minimal for eddies with large length scales compared to the dimensions of the serrations, and so a noticeable noise reduction will only occur at high frequencies.

Dassen et al. [Dassen et al., 1996] measured the trailing edge noise of airfoils and flat plates with serrated trailing edges. The noise reductions obtained were significant (in the order of 5 dB), but were found to be notably smaller than the noise reduction predicted by the model developed by Howe [Howe, 1991b].

Another study on trailing edge serrations as a means to reduce trailing edge noise from a NACA 6512-10 airfoil was done by Gruber et al. [Gruber et al., 2010]. They performed acoustic measurements in an open jet wind tunnel and found considerable discrepancies compared to the model developed by Howe [Howe, 1991b]. The overall level of the noise reduction predicted by Howe's theory was considerably higher than the measured noise reduction.

The acoustic experiments performed by Vad et al. [Vad et al., 2006] on an airfoil with a soft coating showed that the A-weighted overall sound pressure level was reduced by about 1.5 dB due to the coating. Unfortunately, no source separation was performed and hence it is not completely clear where exactly the airfoil noise originated from. Since the inflow turbulence was in the order of 0.5 % only, it can be assumed that the trailing edge was the major noise source.

Regarding the possible cause of the noise reduction at flow-permeable trailing edges, there exist different theories on the mechanisms that may be responsible. Lowson [Lowson, 1968] assumes that in his case of a porous rotor blade, primarily the porous material would allow for the interaction between pressure fluctuations on suction side and pressure side. Second, Lowson states that a porous trailing edge would act as a sound absorbing material. According to Blake [Blake, 1986], the impedance of the trailing edge strongly affects the scattering of turbulence at the edge, and hence its effectiveness as a noise source. Revell et al. [Revell et al., 1997] discussed different mechanisms potentially responsible for the reduction of both surface pressure fluctuations and far field sound pressure levels measured at trailing-edge flaps with porous acoustic treatment, including dissipation, a fluid flow through the porous flap, vortex modification and a reduction of the surface impedance due to the porous treatment. Thereby, the second mechanism, the so-called "flow-trough leakage", was assumed to be the main reason for the success of the porous side edge, while at high frequencies the absorption of near field noise supposedly adds to the noise reduction. Herr [Herr, 2007] concluded that the noise reduction measured at flow-permeable trailing edges is caused by the damping of turbulent flow pressure amplitudes, an effect which she called hydrodynamic absorption.

After this brief introduction to noise reducing mechanisms and possible applications of flow-permeable and, especially, porous trailing edges and airfoils, the basic principles of the noise generation at the trailing edge of an airfoil will be further discussed. The following section

provides an overview on selected studies on the noise generation at the trailing edge of flat plates and airfoils.

2.2 Airfoil trailing edge noise

Of general interest for the present study is the influence of different flow parameters on the spectrum of trailing edge noise generated by airfoils in a subsonic flow. The following sections address the dependence of the trailing edge noise on the flow speed U_0 and the angle of attack α . However, it has to be considered that in most studies the dependence of the trailing edge noise on the flow speed refers to an overall sound pressure level only. Additional information will be provided on the characteristic spectral shape of trailing edge noise.

2.2.1 Dependence on flow speed

A large number of studies on airfoil trailing edge noise are based on the fundamental theoretical work by Ffowcs Williams and Hall [Ffowcs Williams and Hall, 1970] on the noise generated by the interaction of a turbulent flow with the edge of a flat half plane.

According to the Ffowcs Williams and Hall theory, the far field intensity I of the sound generated by a turbulent flow over the edge of the half plane at zero angle of attack is a function of a typical fluid velocity U , the radius of the turbulent eddy ℓ and the distance between the sound source at the edge and the field point R (the “distance of the observer”):

$$I = \frac{k^4 \cdot \sin\Theta \cdot \sin^2(\Psi/2) \cdot \rho \cdot U^4 \cdot \gamma^2 \cdot \sin^2\Xi \cdot \left\{ \begin{array}{c} \cos^2 \\ \sin^2 \end{array} \right\} (\beta/2) \cdot V^2}{\pi^3 \cdot c \cdot R^2 \cdot (k \cdot \bar{r}_o)^3}, \quad (2.3)$$

where $k = \omega/c$ is the wave number and γ is the normalized turbulence intensity. The cosine or sine of the term in brackets has to be chosen if the original volume integral of the turbulent eddy contains a cosine or sine (the reader is referred to the original work by Ffowcs Williams and Hall [Ffowcs Williams and Hall, 1970] for more information).

Regarding the noise generation at a trailing edge, the angles Θ and Ψ basically describe the directivity of the radiated noise, where Θ is the (lateral) angle between the trailing edge and the observer and Ψ is the angle between the virtual extension of the plate downstream of the trailing edge and the observer. Ξ is the angle between the flow and the edge of the half plane. V is the volume of the eddy, which Ffowcs Williams and Hall regard as a cylinder of diameter 2ℓ centered on the edge of the half plane. The corresponding length of the cylindrical eddy would then be equal to the spanwise extent b of the plane. \bar{r}_0 is the radius of the turbulence region “of perfect correlation” in cylinder coordinates with $\bar{r}_0 \leq \ell$. Both \bar{r}_0 and β are described as part of the cylinder coordinates relative to the center of the eddy.

For $\bar{r}_0 = \ell$ the maximum value of the sound intensity is given by

$$I_{\max} \approx \frac{\rho \cdot k \cdot U^4 \cdot V^2 \cdot \gamma^2}{\pi^3 \cdot c \cdot R^2 \cdot \ell^3}. \quad (2.4)$$

The formulations given in Equation (2.3) and (2.4) are valid only for small Mach numbers at which the Doppler effect can be omitted [Crighton, 1995].

Ffowcs Williams and Hall state that the typical frequency of the turbulent source is in the order of $U/(2\ell)$. Thus, the wave number would be equal to $\pi U/(c \cdot \ell)$, and the theory then implies that the far field acoustic intensity generated by an eddy within one acoustic wavelength of the trailing edge scales with the fifth power of the fluid velocity U .

In the theoretical trailing edge noise model developed by Amiet [Amiet, 1976] the noise radiated into the far field is calculated based on airfoil surface pressure spectra upstream of the trailing edge. It is assumed that the turbulent velocity field moving past the trailing edge of the semi-infinite plate is unaffected by the presence of the edge. The noise generation is modeled as induced surface dipoles near the trailing edge. In Amiet's model the eddies within the turbulent boundary layer are taken to travel with a turbulence convection velocity $U_c = 0.8 \cdot U_0$ along the surface of the airfoil.

A fundamental contribution to the understanding of the noise generated at the trailing edge of a flat plate or an airfoil was provided by Howe (for example [Howe, 1998]). This includes a detailed review on theories of the noise generation at the trailing edge of a semi-infinite flat plate [Howe, 1978]. In this study he gives a comparison of different approaches to calculate the sound generated at the trailing edge and concludes that they are essentially identical when a common system of flow parameters is used. The noise prediction method proposed by Ffowcs Williams and Hall, given in Equation (2.3), is expressed by Howe in the form

$$\bar{p}^2 \propto \rho^2 \cdot (\bar{u})^2 \cdot U_c^2 \cdot Ma \cdot \frac{b \cdot \ell}{R^2} \cdot \sin(\Theta) \cdot \sin^2(\Psi/2) \cdot \cos^3(\Xi), \quad (2.5)$$

with $(\bar{u})^2$ being the mean square turbulent fluctuation velocity and $Ma = U_c/c$ the Mach number. Ξ is the angle between the convection velocity of the turbulence and the trailing edge in the “flight” plane (the “sweepback angle” of the trailing edge), the third power is derived from an additional weighting of relative contributions from turbulent eddies according to their distance from the edge (see [Howe, 1978] for details). When taking into account that both the mean square turbulent fluctuation velocity as well as the turbulence convection velocity are proportional to the flow speed U_0 , it becomes obvious that Howe's formulation of the Ffowcs Williams and Hall method essentially shows the same dependence of the trailing edge noise of an airfoil on the fifth power of the flow speed.

A detailed review on the noise generation by lifting surfaces is given by Blake [Blake, 1986], who provides an extensive theoretical overview on the subject and the different existing trailing edge noise theories. Similar to the assumption made by Amiet [Amiet, 1976], the convection velocity of the turbulence is estimated by Blake as $U_c \approx 0.9 \cdot U_0$. Blake states that the ideally sharp trailing edge is the best noise radiator compared to other edge contours and that the far field intensity of the trailing edge noise scales with U_0^5 .

The chapter on airframe noise in the book “Aeroacoustics of flight vehicles” written by Crighton [Crighton, 1995] provides a detailed overview of airframe noise studies, including scaling approaches. Although it is aimed at correlations for whole aircraft, a major part covers the noise generated at the trailing edge of a flat plate or an airfoil. The theory by Ffowcs Williams and Hall [Ffowcs Williams and Hall, 1970] is cited as one of the first analyses of the theoretical half plane trailing edge problem. Based on this overview on trailing edge noise studies, Crighton concludes a dependence of the overall sound pressure level on the fifth power of the flow speed.

A fundamental overview on the theory of noise produced by a flow over rigid surfaces, including both a fluid flow over the trailing edge of a plate and an airfoil immersed in a turbulent flow, was given by Hayden [Hayden, 1972]. Hayden first considers a flow over one side of a rigid surface only and states that the resulting noise spectra obey a Strouhal number distribution based on the turbulent boundary layer thickness δ and the flow speed U_0 . According to Hayden, for the flow over one side of the edge the radiated sound power decreases with increasing edge thickness. For the far field overall sound pressure level $L_{p,\text{tot}}$ (in dB), Hayden gives the following empirical formulation:

$$L_{p,\text{tot}} = 10 \cdot \log_{10}(\delta \cdot b \cdot U_0^6) - 20 \cdot \log_{10}(R) + 10 \cdot \log_{10}[\sin^2\Theta \cdot \cos^2(\Psi/2)] + K_1, \quad (2.6)$$

where δ is a characteristic dimension of a flow disturbance (such as the boundary layer thickness), b is a measure proportional to the spanwise extent of the edge given in feet (1 ft = 0.3048 m) and U_0 is the mean flow speed in feet per second (1 fps = 0.3048 m/s). Θ and Ψ describe the source directivity and K_1 is a constant that takes values between -18.5 dB and -13.5 dB depending on the region inside the jet flow (and thus the flow regime). Equation (2.6) shows that the overall sound pressure level was found to scale with U_0^6 .

Hayden then examines a flow on both sides of a rigid edge and finds the same dependence on the mean flow parameters and the same directivity as for the one-sided flow. Additionally, Hayden observed a narrow band sound which was produced by the interaction of the wake of the plate with its trailing edge and which also scales with U_0^6 .

Besides research that focuses strongly on the noise generation of airfoils in a fluid flow, various studies give attention to the noise generated by complete aircraft. These aircraft noise studies are often based on flyover measurements on airplanes, especially in the landing configuration. Airframe noise includes the airfoil trailing edge noise mechanism, since the noise generated at the trailing edge of the wings and high-lift devices of an airplane dominates the noise generation in the “clean” airframe case, which refers to the airplane during flight, with flaps, slats and undercarriage retracted.

The dependence on the sixth power of the flow speed as given by Hayden [Hayden, 1972] is used in the simple empirical model developed by Healy [Healy, 1974]. It is intended for the prediction of the overall sound pressure level and the spectral shape of the noise generated by clean aircraft, based on the results from flyover measurements on five gliding airplanes.

Hardin et al. [Hardin et al., 1975] differentiate between two approaches of airframe noise predictions. The first method considers an aircraft as a whole, while the second considers each single component that generates aerodynamic noise, like wings, flaps and struts. Regarding the noise generated by an aircraft considered as an entity (in the “clean” configuration), Hardin gives an estimation based on measured data from 28 flights:

$$L_{p,\text{tot}} = 10 \cdot \log_{10} \left[\frac{(Ma)^{3.47} (W/\rho c^2 b^2)^{0.62}}{(R/b)^{1.59} (ar)^{2.39}} \right] + 154.9 \text{ dB}, \quad (2.7)$$

where $ar = b^2/S$ is the aspect ratio and S is the wing area. The weight of the aircraft is equal to the lift force at equilibrium flight,

$$W = \frac{\rho}{2} \cdot C_L \cdot S \cdot U_0^2, \quad (2.8)$$

leading to a dependence of $L_{p,\text{tot}}$ on $U_0^{4.71}$.

The second approach, the identification of airframe components that are acoustically independent noise sources, includes the noise produced by a turbulent flow over a trailing edge. The corresponding theory is based on the work of Hayden [Hayden, 1972].

The airframe noise prediction model by Hersh et al. [Hersh et al., 1976] was derived from the results of acoustic flyover measurements on three large commercial aircraft. The dominant noise sources were assumed to consist of trailing edge noise, and hence the model bases on the theory by Ffowcs Williams and Hall [Ffowcs Williams and Hall, 1970]. Hersh et al. found the overall sound pressure level of the wing to be proportional to the drag coefficient of the wing and to the 4.8th power of the flight speed.

A very common airframe noise component model is the model developed by Fink [Fink, 1976, Fink, 1977, Fink, 1979], who calculates the noise generated by an aircraft as the sum of the uncorrelated noise sources at the individual aircraft components. The part of Fink's model containing the noise generation at the trailing edge is based on the work by Ffowcs Williams and Hall [Ffowcs Williams and Hall, 1970], which is used to scale an overall sound pressure level. This includes the scaling with the fifth power of the flight speed. Furthermore, Fink assumes that the far field noise intensity is proportional to the product of wing area S and the boundary layer thickness δ of a flat plate having a chord length equal to the gross geometric chord length of the airframe wing. This boundary layer thickness is taken to be proportional to $Re^{-0.2}$ [Eckert and Drake jr., 1959], with Re being the Reynolds number based on wing gross geometric chord length.

The results from flyover noise measurements on four airplanes performed by Lasagna et al. [Lasagna et al., 1980] were scaled with U_0^5 , based on the airframe noise prediction model by Hersh et al. [Hersh et al., 1976]. The measured overall sound pressure levels were normalized to an aircraft weight W of 155,680 N, and the corresponding simple approach for the estimation of the overall sound pressure level $L_{p,tot}$ yields

$$L_{p,tot} = 10 \cdot \log_{10} U_0^5 + 10 \cdot \log_{10} W - 74.0 \text{ dB.} \quad (2.9)$$

The aircraft weight W is used in Equation (2.9) since it is taken to be proportional to the effective area of the lifting devices that generate the noise.

Brooks and Hodgson [Brooks and Hodgson, 1981] presented a trailing edge noise prediction model based on surface pressures measured on a NACA 0012 airfoil model. The measured acoustic far field spectra showed good agreement with the theory by Ffowcs Williams and Hall [Ffowcs Williams and Hall, 1970] regarding directivity and scaling of the overall sound pressure level with the flow speed. For a sharp trailing edge the corresponding noise was found to scale with $U_0^{5.07}$, while the noise from a blunt edge was found to scale with $U_0^{5.3}$.

Schlinder and Amiet [Schlinder and Amiet, 1981] performed an experimental study on trailing edge noise as part of a helicopter noise prediction model. Measured third-octave band sound pressure levels were found to scale with the fifth power of the Mach number. The results of additional boundary layer measurements on a helicopter rotor blade segment using hot-wire anemometry showed good agreement with results from the calculation of the boundary layer thickness based on flat plate theory. The resulting semi-empirical model includes a dependence of the noise on the fifth power of the flow speed and a linear dependence on the turbulent boundary layer thickness δ , which may be substituted by the turbulent boundary layer displacement thickness δ_1 since δ is assumed to be proportional to δ_1 . The influence of angle of attack and airfoil shape was considered indirectly, as both are assumed to have an effect on the turbulent boundary layer thickness.

The results of the studies by Brooks and Hodgson [Brooks and Hodgson, 1981], Brooks and Marcolini [Brooks and Marcolini, 1985] and Schlinker and Amiet [Schlinker and Amiet, 1981] were integrated in the fundamental semi-empirical trailing edge noise model developed by Brooks, Pope and Marcolini [Brooks et al., 1989], in the remaining part of this thesis referred to as the BPM-model. The report by Brooks et al. is an extensive study of the five airfoil self-noise mechanisms mentioned in Chapter 1. The BPM-model is based on a large experimental database and the resulting equations are often very complex as they take into account various dependencies. The model employs boundary layer parameters obtained from empirical equations as a function of chord length and chord based Reynolds number. Only a short summary for two noise source mechanisms will be given in the following paragraphs. For additional information, the reader is referred to the original report [Brooks et al., 1989].

The total turbulent boundary layer - trailing edge noise is calculated in the model as the energetic sum of the incoherent contributions from both suction side and pressure side of the airfoil, $L_{p,s}$ and $L_{p,p}$, and a contribution $L_{p,\alpha}$ for the noise due to a non-zero angle of attack:

$$L_{p,s} = 10 \cdot \log_{10} \left(\frac{\delta_s \cdot (Ma)^5 \cdot b \cdot \bar{D}}{R^2} \right) + G_1 \left(\frac{Sr_s}{Sr_1} \right) + K_2 - 3 \text{ dB}, \quad (2.10)$$

$$L_{p,p} = 10 \cdot \log_{10} \left(\frac{\delta_p \cdot (Ma)^5 \cdot b \cdot \bar{D}}{R^2} \right) + G_1 \left(\frac{Sr_p}{Sr_1} \right) + K_2 + \Delta K_2 - 3 \text{ dB} \quad (2.11)$$

and

$$L_{p,\alpha} = 10 \cdot \log_{10} \left(\frac{\delta_s \cdot (Ma)^5 \cdot b \cdot \bar{D}}{R^2} \right) + G_2 \left(\frac{Sr_s}{Sr_2} \right) + K_3, \quad (2.12)$$

where the index “s” denotes the suction side parameters and “p” the pressure side parameters. Each equation contains a scaling based on the fifth power of the Mach number. The parameter K_2 in Equation (2.10) and (2.11) depends on the chord based Reynolds number, K_3 in Equation (2.12) depends on the angle of attack α and \bar{D} is a directivity function. The parameter ΔK_2 in Equation (2.11) is a function of the Reynolds number based on the pressure side displacement thickness $\delta_{1,p}$ for the level adjustment at non-zero angle of attack.

Another noise source mechanism, which may be important regarding the measurement of the trailing edge noise subject to the present thesis, is the trailing edge bluntness noise, since it is practically impossible to manufacture airfoils with an ideally sharp trailing edge (especially out of porous material). The noise generated at the airfoil trailing edge due to its finite thickness h is given by Brooks et al. as

$$L_{p,\text{blunt}} = 10 \cdot \log_{10} \left(\frac{h \cdot (Ma)^{5.5} \cdot b \cdot \bar{D}}{R^2} \right) + G_3 \left(\frac{h}{\bar{\delta}_1}, \Omega \right) + G_4 \left(\frac{h}{\bar{\delta}_1}, \Omega, \frac{Sr_h}{Sr_{h,\text{peak}}} \right). \quad (2.13)$$

The boundary layer displacement thickness $\bar{\delta}_1$ is the arithmetic mean of the displacement thicknesses of suction side and pressure side, Ω is the trailing edge solid angle, $Sr_h = f_c \cdot h/U_0$ is the Strouhal number based on trailing edge thickness and $Sr_{h,\text{peak}}$ the corresponding peak Strouhal number. The bluntness noise contribution was found by Brooks, Pope and Marcolini to scale best with $U_0^{5.5}$ instead of a fifth or sixth power.

The BPM-model, although relatively complex and time-consuming in its implementation, is widely used for the prediction of airframe noise, since it is the most detailed and comprehensive prediction method. One disadvantage of the model is that it is based solely

on measurements using a flat plate or a NACA 0012 airfoil, and no asymmetric or semi-symmetric airfoils were used.

The more simplified model provided by Grosveld [Grosveld, 1985] is intended for the noise prediction of horizontal axis wind turbines. It includes the noise generation caused by the interaction of the turbulent boundary layer with the trailing edge of the blades and the noise generation caused by vortex shedding at the blunt trailing edge. Grosveld employs the semi-empirical trailing edge noise prediction model developed by Schlinker and Amiet [Schlinker and Amiet, 1981] and hence a U_0^5 dependency of the trailing edge noise.

Another simplified model for the prediction of wind turbine noise, that uses simplified calculation procedures based on both the BPM-model [Brooks et al., 1989] and the work of Grosveld [Grosveld, 1985], was developed by Lowson [Lowson, 1992, Lowson, 1993]. For the noise generation caused by a turbulent boundary layer flow over an airfoil trailing edge, his model contains the normalization

$$L_p = 10 \cdot \log_{10} \left[\frac{(Ma)^5 \cdot \delta_1 \cdot b}{R^2} \right] + 128.5 \text{ dB}, \quad (2.14)$$

as given by Brooks, Pope and Marcolini for chord based Reynolds numbers greater $8 \cdot 10^5$. Equation (2.14) includes a scaling approach based on the fifth power of the flow speed U_0 . A method is derived for the estimation of the boundary layer thickness of a technical airfoil. This boundary layer thickness is assumed to be equal to the theoretical flat plate value given by Eckert and Drake [Eckert and Drake jr., 1959] multiplied with an empirical factor, which, according to Lowson, ranges between 2 and 4.

A model, intended for the prediction of the overall noise radiated by flying birds and gliders, was derived by Lilley [Lilley, 1998]. It is inspired by flyover noise measurements on owls performed by Kroeger et al. [Kroeger et al., 1971] for a study on the silent flight of owls. Lilley states that the far field noise of birds and gliders is dominated by sound scattered at the trailing edge of the wings and proposed a simple noise prediction model. The far field sound intensity is estimated based on the Ffowcs Williams and Hall formula [Ffowcs Williams and Hall, 1970] in the notation of Howe [Howe, 1978], resulting in an equation for the calculation of the far field noise intensity given by

$$I = \frac{K_4}{2\pi^3} \left(\frac{u_v}{U_0} \right)^4 \cdot \frac{F_L \cdot U_0^3}{c^2 R^2}, \quad (2.15)$$

where u_v is a measure of the turbulent velocity fluctuations in the vortex, assuming an unsteady vortical flow over the wing, and K_4 is a parameter describing the relation between the vorticity fluctuations near the trailing edge and the mean circulation around the wing. Additionally, the assumption that $u_v/U_0 = \text{const}$ [Brooks and Marcolini, 1985] and some additional simplifications regarding the flow field in the vicinity of the trailing edge are taken into account. In Equation (2.15), K_4 is a constant factor given by Lilley as 0.1.

Lilley's model contains the direct dependence of the trailing edge noise on the third power of the flight speed and it incorporates the dependence on the lift force with $F_L \propto U_0^2$, and hence an overall dependence on the fifth power of the flow speed. According to the resulting model, the trailing edge noise is a function of the flight speed and the mass of the bird or glider only.

A semi-empirical prediction model for the noise from wind turbines was developed by Moriarty and Migliore [Moriarty and Migliore, 2003], based on the model by Brooks et al.

[Brooks et al., 1989] and the model by Lawson [Lawson, 1992]. The turbulent boundary layer - trailing edge noise is scaled with the fifth power of the flow speed.

An experimental study of airfoil self noise using microphone array technique was performed by Oerlemans and Migliore [Oerlemans, 2004, Oerlemans and Migliore, 2004]. The measured trailing edge noise spectra of seven airfoils of different shape, with tripping tape applied, were found to scale with $U^{4.5}$ when plotted versus the chord based Strouhal number.

This brief overview shows that airfoil trailing edge noise can be expected to scale with U_0^n , where n may take values approximately between 4.5 and 6.

2.2.2 Dependence on angle of attack

The trailing edge noise model by Brooks, Pope and Marcolini [Brooks et al., 1989] takes into account a wind tunnel correction for non-zero angles of attack, which was developed based on experiments on flat plates and NACA 0012 airfoils [Brooks et al., 1984, Brooks et al., 1986]. For increasing absolute value of the corrected angle of attack up to a limiting value, roughly corresponding to stall, it was found that the peak of the trailing edge noise shifts toward higher Strouhal numbers based on the suction side displacement thickness, the level increases and the spectra become sharper at the edges. Beyond this limiting value, the trailing edge noise spectra were found to change significantly.

A detailed study on the effect of the angle of attack on the trailing edge noise radiation was performed by Hutcheson and Brooks [Hutcheson and Brooks, 2004], who state that with increasing angle the spectral peak of the trailing edge noise shifts to lower frequencies and the level of the peak increases, while the higher frequency range of the spectrum is seemingly not affected.

Recent research on the influence of the angle of attack on the trailing edge noise generated by an SD7003 airfoil model [Fritzsche et al., 2010] showed that the dependence of the trailing edge noise on the angle of attack is rather complex. For mean values of the chord based Strouhal number of 8 to 16, derived by averaging over the corresponding Strouhal number octave band, the trailing edge noise level increases with increasing positive angle of attack, while it decreases for mean octave band Strouhal numbers greater 16.

2.2.3 Trailing edge noise spectral shape

As is commonly known (for example [Fink, 1977, Brooks et al., 1989]), the characteristic spectral shape of trailing edge noise consists of a spectral peak at a relatively low frequency, and a smooth decrease of the level toward higher and lower frequencies. The peak frequency depends on the flow speed and the airfoil geometry. If trailing edge bluntness noise occurs, a second spectral peak may be present at higher frequencies depending on the thickness of the edge. In the following section, different approaches to determine the spectral shape or the peak Strouhal number of trailing edge noise will be summarized, which are taken from various airfoil trailing edge noise or airframe noise studies.

Healy [Healy, 1974] graphically determined a “smoothed” or idealized frequency spectrum, based on measured third-octave band sound pressure level spectra from flyover measure-

ments on gliding airplanes, by removing tonal components generated by protrusions such as antennas and pitot tubes. From the peak frequencies f_{peak} of these idealized spectra and the wing thicknesses h of the airplanes, Healy determined the corresponding peak Strouhal number based on flight speed U_0 and wing thickness as characteristic dimension, $f_{\text{peak}} \cdot h/U_0$, to be equal to 1.3.

The peak third–octave band of the noise from three aircraft that were subject to flyover measurements by Hersh et al. [Hersh et al., 1976] were found to have the same center frequency of 1.25 kHz, independent of flight speed and aircraft geometry. As a possible reason for this independence it was argued that the local structure of the turbulent flow close to the surface and near the trailing edge of the wing may more likely be governed by local trailing edge shear forces than by global parameters such as the chord based Reynolds number, and hence may be relatively insensitive to chord length and flight speed.

In the fundamental airframe noise model by Fink [Fink, 1977, Fink, 1979] a semi–empirical equation for the normalized spectral density is given as the third–octave band sound pressure level L_p based on the overall sound pressure level $L_{p,\text{tot}}$:

$$L_p - L_{p,\text{tot}} = 10 \cdot \log_{10} \left(0.631 \left(\frac{f_c}{f_{\text{peak}}} \right)^4 \cdot \left[\left(\frac{f_c}{f_{\text{peak}}} \right)^{3/2} + 0.5 \right]^{-4} \right) - 0.03 \cdot \left(\frac{R}{500 \text{ ft}} \right) \cdot \left| \frac{f_c}{f_{\text{peak}}} - 1 \right|^{3/2}. \quad (2.16)$$

Therein, f_c/f_{peak} is the third–octave band center frequency relative to the center frequency of the maximum third–octave band sound pressure level. Hence the method developed by Fink gives the slope of the trailing edge noise spectrum relative to the peak frequency, which has to be known a priori, for example from measurements. According to Fink, the subtrahend in Equation (2.16) is a correction term to include the strong decay of trailing edge noise at large frequency ratios due to atmospheric attenuation.

The spectral shape according to Equation (2.16) is shown in Figure 2.1 (but instead of a normalized frequency it is plotted versus an arbitrary normalized Strouhal number). To show the influence of the atmospheric attenuation at high frequencies, an altitude of $R = 500$ ft is assumed in Figure 2.1. Note that the second term of Equation (2.16) is included only in [Fink, 1979], while in the original report [Fink, 1977] Fink suggests the use of tabulated atmospheric attenuation constants for distances much different from 500 ft.

Fink found the peak frequency in Equation (2.16) to be related to a peak Strouhal number of approximately 0.1, with $f_{\text{peak}} = 0.1 \cdot U_0/\delta$, wherein the flight speed U_0 is given in fps.

Regarding the spectral shape of aircraft flyover noise, Lasagna et al. [Lasagna et al., 1980] state that the peak is independent of flight speed and weight of the aircraft, but add that the width of the spectra seemingly increases with increasing aircraft size.

Brooks and Hodgson [Brooks and Hodgson, 1981] found the peak Strouhal number based on boundary layer displacement thickness $f_c \cdot \delta_1/U_0$ to be within the range of 0.07 to 0.1 for a sharp trailing edge at zero angle of attack. Regarding the contribution of trailing edge bluntness noise, they found a dependence on the trailing edge thickness h according to a Strouhal number $f_c \cdot h/U_0 \approx 0.1$.

Similar to the work of Fink [Fink, 1977], the noise prediction model by Schlinker and Amiet [Schlinker and Amiet, 1981] is based on the assumption that the overall sound pressure

level $L_{p,\text{tot}}$ and the third-octave band sound pressure level are related by a spectrum function $F(Sr)$ according to

$$L_p = L_{p,\text{tot}} + F(Sr). \quad (2.17)$$

Schlinker and Amiet apply the spectrum shape function used in the noise prediction model by Fink [Fink, 1977] given in Equation (2.16), but without the second term that takes into account the strong decay of the trailing edge noise at large frequency ratios.

The corresponding spectral shape is included in Figure 2.1 (showing clearly that it is essentially identical to the spectral shape given by Fink except for the decay at high Strouhal numbers). Based on measured data, Schlinker and Amiet derive the peak Strouhal number based on boundary layer thickness, $f_{\text{peak}} \cdot \delta / U_0$, for airfoil trailing edge noise to be approximately 0.1, which is consistent with the result of Fink.

The equations for the prediction of both overall sound pressure level and third-octave band sound pressure level using the approach by Schlinker and Amiet then are

$$L_{p,\text{tot}} = 10 \cdot \log_{10}(U_0/(100 \text{ kn}))^5 + 10 \cdot \log_{10} \frac{\delta \cdot b}{R^2} + 10 \cdot \log_{10} \bar{D} + 93.2 \text{ dB}, \quad (2.18)$$

with the flow speed U_0 in knots and the directivity function \bar{D} ($\bar{D} = 1$ when the angle between direction of flight and observer is 90°), and

$$L_p = L_{p,\text{tot}} + 10 \cdot \log_{10} \left(0.631 \left(\frac{Sr}{Sr_{\text{peak}}} \right)^4 \cdot \left[\left(\frac{Sr}{Sr_{\text{peak}}} \right)^{3/2} + 0.5 \right]^{-4} \right), \quad (2.19)$$

respectively.

The scaling approach developed by Fink [Fink, 1977], with a universal spectrum shape depending on the Strouhal number based on boundary layer thickness, was also employed by Brooks and Marcolini [Brooks and Marcolini, 1985]. They performed acoustic measurements on a set of flat plates and NACA 0012 airfoils with sharp trailing edges. Supplementary to the acoustic measurements, hot-wire measurements were performed in the turbulent boundary-layer and near-wake region of the trailing edge. The acoustic data were normalized using the measured boundary layer thicknesses. Brooks and Marcolini found that a better fit to their data could be achieved using a peak Strouhal number based on boundary layer thickness of 0.25 or 0.3 instead of 0.1 as proposed by Fink.

In the noise prediction model by Brooks, Pope and Marcolini [Brooks et al., 1989] an approach for the description of the spectral shape is used that depends on the ratio of the chord based Strouhal number to the corresponding peak Strouhal number, as was introduced by Fink [Fink, 1977]. Accordingly, the function $G_1(x)$ in Equation (2.10) through (2.12) determines the spectrum shape, taking into account the Strouhal numbers for the suction and pressure side of the airfoil based on the corresponding boundary layer displacement thickness, $Sr_s = f_c \delta_{1,s} / U_0$ and $Sr_p = f_c \delta_{1,p} / U_0$, respectively. Both Strouhal numbers are normalized using the Strouhal numbers

$$Sr_1 = 0.02 \cdot (Ma)^{-0.6} \quad (2.20)$$

and

$$Sr_2 = K_5 \cdot Sr_1, \quad (2.21)$$

where K_5 is a parameter depending on angle of attack. According to Brooks et al., the function $G_1(x)$ is an even function, wherein $x = |\log_{10}(Sr/Sr_{\text{peak}})|$ is the absolute value of the logarithmic ratio of the corresponding Strouhal number Sr_1, Sr_2 or the average value of Sr_1 and Sr_2 , to the peak Strouhal number. Depending on the chord based Reynolds number, the function $G_1(x)$ is an interpolation of two curves $G_{1,\text{min}}(x)$ for small Reynolds numbers and $G_{1,\text{max}}(x)$ for larger Reynolds numbers. Both functions $G_{1,\text{min}}(x)$ and $G_{1,\text{max}}(x)$ are divided into three segments. The peaks of the curves are approximated by a function of the form

$$\sqrt{(K_6 - K_7 \cdot x)} - K_8, \quad (2.22)$$

with K_6, K_7 and K_8 being constants. The strong decay of the spectrum at moderate values of x is approximated by a linear function, while the decay at high values of x is approximated by a third order polynomial function. Due to the use of the absolute value of $\log_{10}(Sr/Sr_{\text{peak}})$, the functions $G_{1,\text{min}}(x)$ and $G_{1,\text{max}}(x)$ are symmetric about the peak Strouhal number. Both functions are presented in Figure 2.1.

Similar to the function $G_1(x)$, $G_2(x)$ in Equation (2.12) describes the spectral shape of the noise contribution for non-zero angle of attack.

Regarding the bluntness noise contribution, which is included in the BPM-model, the function $G_3(x)$ in Equation (2.13) determines the peak level of the spectrum depending on the ratio of the trailing edge thickness to the average of the displacement thicknesses of suction side and pressure side, $h/\bar{\delta}_1$, and the trailing edge solid angle Ω , while $G_4(x)$ defines the shape of the spectrum, again as a function of $h/\bar{\delta}_1$ and Ω .

When comparing the measured trailing edge noise spectrum of a tripped NACA 0012 airfoil with the corresponding measurements from Brooks et al. [Brooks et al., 1989], Oerlemans and Migliore [Oerlemans, 2004, Oerlemans and Migliore, 2004] noted that the measured third-octave band spectra from Brooks et al. contain a dominant hump around 1 kHz, which did not appear in the measured spectra presented by Oerlemans and Migliore. One possible reason provided by Oerlemans is that the data from Brooks et al. contains extraneous noise originating from the junctions between the sideplates and the trailing edge of the airfoil. Other assumptions include differences in the tripping method and differences in the measurement and data processing techniques. Besides the spectral peak, the data generally showed good agreement.

As opposed to the rather complex calculation of the spectral shape of trailing edge noise in the BPM-model, Lawson [Lowson, 1992, Lowson, 1993] uses a more simplified formula for the prediction of the spectral shape,

$$F(f_c) = \frac{4 \cdot (f_c/f_{\text{peak}})^m}{(1 + (f_c/f_{\text{peak}})^m)^2}. \quad (2.23)$$

According to Lawson, a good fit of the spectrum shape can be achieved when the power law m in Equation (2.23) is chosen to be equal to 2.5. The frequency term f_c/f_{peak} is the ratio of third-octave band center frequency to the peak center frequency f_{peak} , which is estimated based on the peak Strouhal number equation used in the BPM-model and given in Equation (2.20),

$$f_{\text{peak}} = 0.02 \cdot (Ma)^{-0.6} \cdot \frac{U_0}{\delta_1}. \quad (2.24)$$

The spectral shape function given by Lawson is included in Figure 2.1, but plotted as a function of an arbitrary normalized Strouhal number instead of a normalized frequency. It

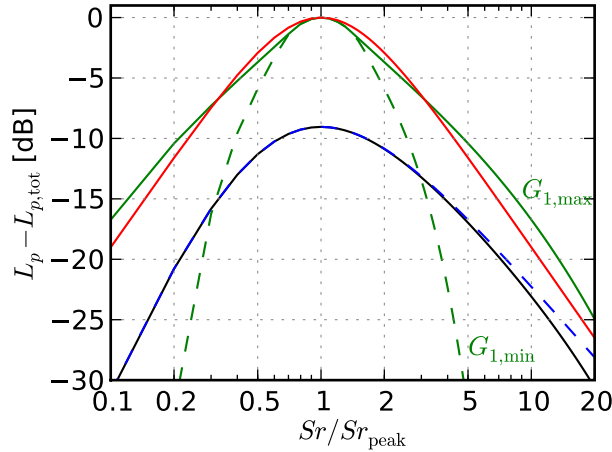


Figure 2.1: Comparison of the spectral shape of turbulent boundary layer - trailing edge noise according to different prediction models: **—** Fink [Fink, 1977], **- -** Schlinker and Amiet [Schlinker and Amiet, 1981], **- -** Brooks et al., small chord based Reynolds numbers Re [Brooks et al., 1989], **—** Brooks et al., high Re [Brooks et al., 1989], **—** Lowson [Lowson, 1992]

is visible that Lowsons spectrum function is derived from the function $G_{1,\max}(x)$ given by Brooks et al. [Brooks et al., 1989].

The resulting prediction model by Lowson incorporates both the turbulent boundary layer - trailing edge noise as well as the trailing edge bluntness noise:

$$L_p = 10 \cdot \log_{10} \left(\frac{(Ma)^5 \cdot \delta_1 \cdot b}{R^2} \right) + 10 \cdot \log_{10} \left(\frac{4(f_c/f_{peak})^{2.5}}{(1 + (f_c/f_{peak})^{2.5})^2} \right) + 128.5 \text{ dB}. \quad (2.25)$$

In a study on airframe noise from both “clean” and “dirty” aircraft (referring to flaps, slats and undercarriage stowed/deployed), Lilley gives information on the noise generated by aircraft flying straight and level, gliders and birds [Lilley, 2001]. Regarding the typical spectrum of the noise, he states that it has a broad peak before the frequency spectrum falls with f^n with $n = 1.5$ to 2. The decay depends on aircraft geometry.

A software tool that enables the calculation of spectra for both airfoil trailing edge noise and leading edge noise is the NAFNoise prediction code (NREL AirFoil Noise, NREL being the National Renewable Energy Laboratory) [Moriarty, 2005]. It provides the easiest opportunity to compare measured trailing edge noise spectra with theory. Regarding the prediction of trailing edge noise it employs the BPM-model for the calculation of turbulent boundary layer - trailing edge noise and trailing edge bluntness vortex shedding noise. The required boundary layer parameters can be either calculated according to the BPM-model or by using the software XFOIL [Drela, 1989]. For the prediction of turbulent boundary layer - trailing edge noise, the TNO-model (developed at TNO, the Netherlands Organisation for Applied Scientific Research) by Moriarty et al. [Moriarty et al., 2005] is also implemented in NAFNoise. The TNO-model uses turbulent boundary layer parameters calculated by XFOIL. And while the BPM-model is originally developed for the symmetric NACA 0012 airfoil only, the calculation of the boundary layer parameters using XFOIL expands the usability for every possible airfoil shape.

2.3 Effects of surface roughness

Since it can be assumed that the surface roughness of the porous airfoils leads to the generation of surface roughness noise, some basic information on the generation of surface roughness noise will be given in this section.

One early experimental study on the aeroacoustic noise generated from surface roughness was performed by Hersh [Hersh, 1983]. His measurement setup consisted of sand of different grain sizes distributed over one half of the wetted internal area of a pipe exhausting into a semi-anechoic room. Surface roughness noise was found to correlate with the theoretical U_0^6 dipole source behaviour. The results showed that for increasing roughness size the intensity of the radiated high frequency noise increased and that the frequency of the maximum noise generation of large roughness sizes was lower than that from smaller roughness treatments. Hersh states that for a given surface roughness the noise increases with decreasing thickness of the turbulent boundary layer.

A detailed theoretical study on surface roughness noise generated by a distribution of rigid, hemispherical bosses on a rigid plane in a low Mach number flow was conducted by Howe [Howe, 1984]. He describes the roughness by the radius of the bosses and a roughness density as the fractional area of the plane covered by bosses. Howe confirms the conclusion by Hersh [Hersh, 1983], that for a given surface roughness the efficiency of the noise generation increases with decreasing thickness of the turbulent boundary layer. The spectral peak of the predicted surface roughness noise spectra was found to be shifted towards higher frequencies for increasing roughness density. Howe did not take into account the influence of the surface roughness on the evolution of the turbulent boundary layer, but assumes that such effects are existent. The dependence of the roughness noise on the sixth power of the flow speed is reproduced by the model.

The investigation of the effect of surface roughness noise on total airframe noise by Liu et al. [Liu and Dowling, 2007, Liu et al., 2008] aimed at the prediction of both the spectral shape and the absolute level of the far field radiated surface roughness noise. Liu et al. developed a numerical method for the calculation of surface roughness noise and performed additional measurements to validate the numerical method. The setup consisted of a flat plate, containing a square region with rigid, hemispherical plastic beads, in an open jet. Regarding the influence of surface roughness on the total airframe noise radiated from a wing model, it was found that the roughness noise was significant at very high frequencies. In this range it may become comparable to trailing edge noise or even exceed the trailing edge noise, provided that the size of the roughness elements is not too small. Due to the surface roughness, both friction velocity and boundary layer thickness increase compared to a smooth surface, leading to an additional enhancement of the trailing edge noise. The results of a parametric study showed that roughness height has a stronger effect on the roughness noise than roughness density. Microphone array sound maps showed that downstream roughness elements are more dominant as sound scatterers than upstream elements due to the increasing boundary layer thickness.

A fundamental study on surface roughness noise was provided by Grissom [Grissom, 2007], who examined the influence of parameters like flow speed, boundary layer thickness and roughness size on both spectral shape and level of the roughness noise. Grissom states that the surface roughness noise acoustic levels increase with “at least” the fifth power of the flow speed.

Chapter 3

Measurement setup

The measurements of the trailing edge noise generated by porous airfoils took place in the aeroacoustic wind tunnel at Brandenburg University of Technology in Cottbus. The acoustic measurements were performed using a planar 56 channel microphone array, while simultaneously the lift and drag forces acting on the porous airfoils were measured using a six-component balance. Additionally, hot-wire measurements were performed in the boundary layer of a subset of the porous airfoils. The following section describes in detail the experimental setup used for the measurements.

3.1 Porous airfoils

In this section, the airfoils that were used for the experiments in the wind tunnel are described regarding their shape and material.

3.1.1 Characterization of the porous materials

The porous airfoils were manufactured completely from porous material. The term “porous material” is used in the present thesis to characterize solid materials that contain open pores which are interconnected (open-porous materials). Materials with pores that are not connected to each other and the ambient fluid are not subject to the present study since no interaction between the fluid and the porous material can take place and hence no trailing edge noise reduction due to the porous structure is expected.

In order to understand the influence of the porous materials on the sound generated at the trailing edge of porous airfoils, it is important to properly characterize the properties of the porous media. Examples for porous materials are polyurethane (PUR) foams, metal foams or felts. In the present study, the materials can be described as homogeneous if their structural dimensions, as the size and distance of the pores, capillaries or fibres, are small compared to the wavelength of the acoustic sound waves. The materials can be completely characterized and modeled using six macroscopic parameters defined according to the acoustic theory for porous absorbers with a rigid frame (for example [Zwikker and Kosten, 1949, Lafarge et al., 1997, Sarradj et al., 2006]):

- the air flow resistivity r , which describes the resistivity of a porous material against a fluid flow through the material (r is related to the viscous permeability k_v by $k_v = \eta/r$, with η being the dynamic viscosity of the fluid),
- the volume porosity σ_v , which is the ratio of the volume of the pores to the overall volume, including the rigid frame and the pores,
- the tortuosity τ as a measure for the ratio of the effective length of the flow path through the pores of the porous material to the minimum length between flow inlet and outlet,
- the thermal permeability k' , which is a thermal analogue to the dynamic viscous permeability k_v ,
- the characteristic viscous dimension Λ that indirectly describes the irregularity of the pore cross section and
- the thermal characteristic dimension Λ' , which characterizes the high-frequency behavior of the compressibility in the pores.

Since it is believed that the air flow resistivity r has the most significant influence on a possible noise reduction at the trailing edge of the porous airfoils, it is the main parameter used to describe the porous materials in the present thesis. Additionally, the volume porosity σ_v of the open-porous materials, as another parameter to possibly affect the flow around the porous airfoils and the resulting trailing edge noise, will be considered.

In the present study, the tortuosity τ of the porous materials has not been used to characterize the porous materials due to the difficulty to measure the tortuosity of the various porous materials, especially if the materials are electrically conductive.

The same can be said about the use of the thermal permeability k' and the characteristic dimensions Λ and Λ' to characterize the porous materials used for the present study: The measurement of these parameters is very difficult and their influence on the trailing edge noise generation, especially compared to the influence of the air flow resistivity r , is believed to be of minor importance only.

Air flow resistivity

The air flow resistivity r is defined as the ratio of a static pressure difference Δp across a sample of porous material (in flow direction) to the product of the flow velocity u_s of a static fluid flow through the sample and the sample thickness d_s [ISO 9053, 1993]:

$$r = -\frac{\Delta p}{u_s \cdot d_s}, \quad (3.1)$$

or, using the volume flow velocity $q_s = u_s \cdot A_s$, with the cross sectional area A_s of the porous sample:

$$r = -\frac{\Delta p \cdot A_s}{q_s \cdot d_s}. \quad (3.2)$$

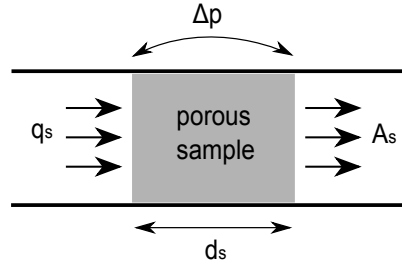


Figure 3.1: Definition of the air flow resistivity, Equation (3.2)

Table 3.1: Materials used for the manufacturing of the airfoils (given are the air flow resistivity r and the open volume porosity σ_v)

No	Name	Material	r [Pa s/m ²]	σ_v
1	Reference	non-porous	∞	0
2	M&K felt, 0.36 g/cm ³	woolen felt	506,400	0.73
3	Porex	polyethylene granulate	316,500	0.40 - 0.46
4	M&K felt, 0.22 g/cm ³	woolen felt	164,800	0.82
5	Needlona felt, SO 2002	synthetic felt	130,200	≈ 0.86
6	ArmaFoam Sound	elastomer foam	112,100	0.85 - 0.9
7	Needlona felt, WO-PE 1958	woolen / synthetic felt	40,100	≈ 0.89
8	Arpro Porous 4025	expanded polypropylene foam	23,100	>0.36
9	Reapor	porous glass granulate	16,500	>0.96
10	Basotect	melamine resin-foam	9,800	>0.99
11	Recemat	metal foam	8,200	>0.95
12	Balzer RG 3550	polyurethane foam	4,400	>0.99
13	Panacell 90 ppi	polyurethane foam	4,000	>0.99
14	Panacell 60 ppi	polyurethane foam	3,600	>0.99
15	M-Pore PU 45 ppi	polyurethane foam	1,500	0.86
16	M-Pore Al 45 ppi	metal foam	1,000	0.90
17	Panacell 45 ppi	polyurethane foam	700	>0.99

The air flow resistivity of the porous materials was measured according to ISO 9053 [ISO 9053, 1993], method A. This method implies the measurement of the differential pressure over a cylindrical sample with a cross sectional area A_s of 0.1 m. To this end, the porous sample has to be fitted exactly into the cylindrically shaped sample container. It is important that no unwanted air flow occurs through slits between the sample and the container. Especially for rigid porous materials, care must be taken to completely seal such slits. The air flow resistance $\Delta p/q_s$ is defined as the resistance at a flow velocity u_s of $0.5 \cdot 10^{-3}$ m/s. In practice, it is difficult to generate a static air flow this low, so that measurements are conducted at a number of higher air flow velocities and the correct value for the air flow resistance is obtained through extrapolation onto $u_s = 0.5 \cdot 10^{-3}$ m/s.

The parameter r is a measure for the resistance of the porous material against the permeation of a fluid flow, which is specific for each material and not dependent on its dimensions. Theoretically, it may take values between 0 (permeable without resistance) and ∞ (impermeable). The same physical mechanism, which is described by Equation (3.1), is also described by Darcy's law, as for example given in [Scheidegger, 1974]. Table 3.1 gives an overview of the airfoils used in the experiments and their air flow resistivity r .

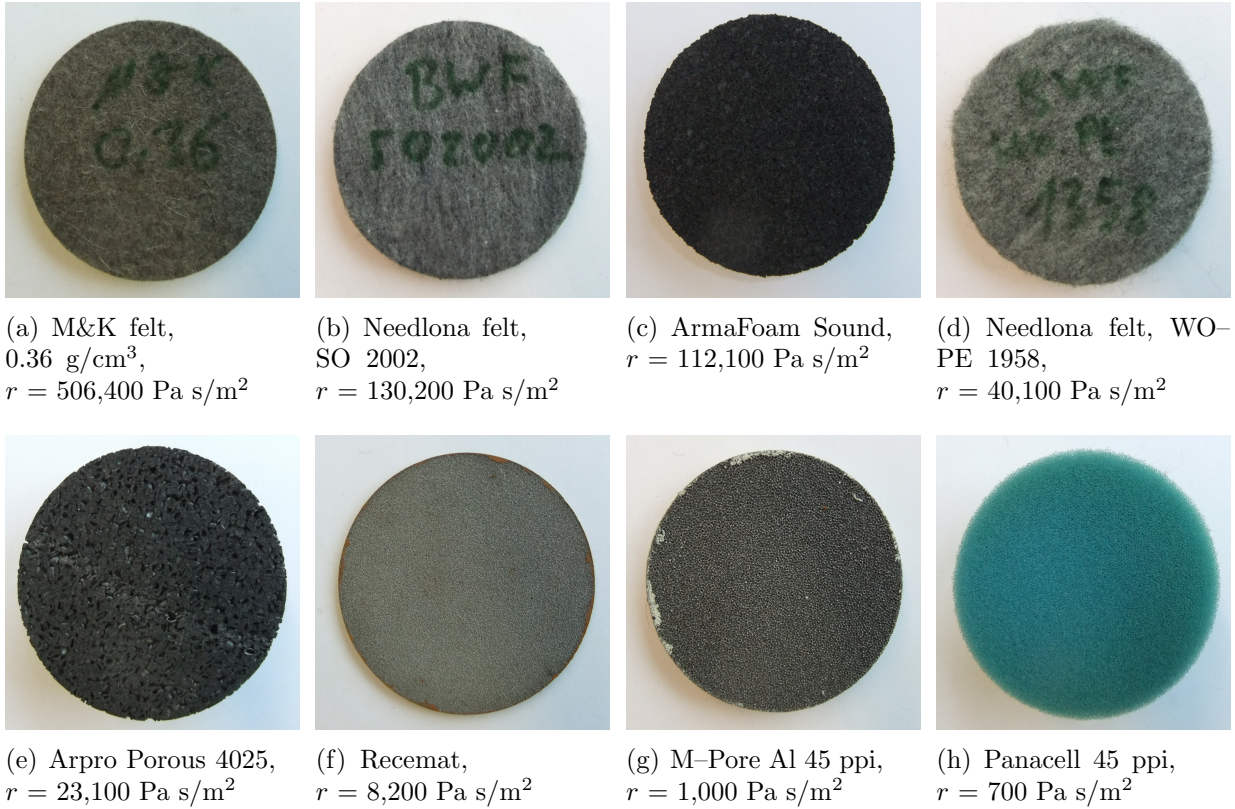


Figure 3.2: Photographs of some of the porous materials from Table 3.1 (the materials are cut into circular cylinders with a diameter of 0.1 m)

Photographs of some of the porous materials are given in Figure 3.2.

Volume porosity

The volume porosity σ_v of the porous materials can be calculated as the ratio of the pore volume V_p to the total volume V_t of the porous material,

$$\sigma_v = \frac{V_p}{V_t}. \quad (3.3)$$

In theory, it may take values between zero (no pores) and one (only pores, no skeletal material). As mentioned above, in order to be acoustically effective, the pores have to be both interconnected and connected to the surrounding fluid (open pores). The pore volume therefore refers to the volume of the accessible pores only. Using the total density ρ_t of the porous material and the density ρ_s of the skeletal material of volume V_s , Equation (3.3) can be rewritten as

$$\sigma_v = \frac{V_t - V_s}{V_t} = 1 - \frac{\rho_t}{\rho_s}. \quad (3.4)$$

Thus, the volume porosity of the materials given in Table 3.1 was determined by using Equation (3.4). The density of most of the porous materials was either measured or taken from the corresponding data sheets provided by the manufacturer, while the density of the skeletal material was taken from the data sheets.

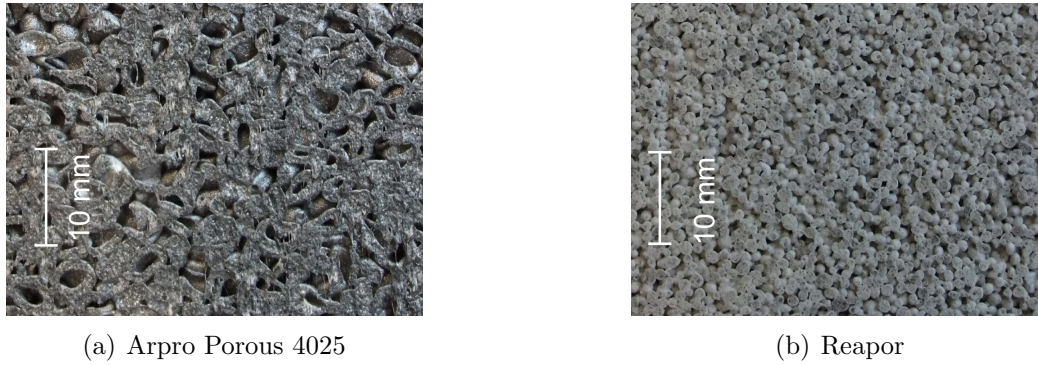


Figure 3.3: Detailed photographs of the surface of two of the porous materials

The determination of the porosity of the material Arpro was more difficult since it is a material that consists of densely packed, hollow cylindric plastic beads that are molded into a lightweight synthetic material by different molding processes. The beads themselves are made of a closed-cell polypropylene (ethylene propylene copolymer) with a bulk density of 22 g/l to 28 g/l, while the resulting molded material has a higher density between 30 g/l and 45 g/l. Arpro is characterized by a macro porosity, relating to the larger pores defined by the voids between the beads (When the material is cut, the hollow elliptic beads on the surface may be cut open and an additional micro porosity on the surface of the material is generated, which is related to the small inner pores of the bulk material). Figure 3.3(a) shows a detailed photograph of the surface of the material. The macro porosity of Arpro was estimated based on the theory for densely packed spheres (see for example [Sarradj et al., 2006]). If the most simple model of a random packing of identical spheres is assumed, the porosity is known to be greater than 0.36 [Torquato et al., 2000], which can be taken as a first estimation and is given in Table 3.1. Taking in consideration that the beads are not spheres but hollow cylinders, the porosity may take a higher value than 0.36. If, on the other hand, the higher packing density is taken into account, caused by a compression of the material and the subsequent decrease of the size of the pores between the beads, it is reasonable to assume a lower porosity. However, since most materials used in the present study, especially the polyurethane foams, have porosities well above 0.9, the porosity of Arpro is still considerably below that of the other materials, even if a value greater than 0.36 is assumed.

The open volume porosity of the woolen felts (M&K felt, 0.36 g/cm³, and M&K felt, 0.22 g/cm³) was derived based on an approximate value for the bulk density of wool (mainly consisting of the protein Kerotin) of $\rho_s = 1.31$ [Möhlmann, 2011]. No such bulk density was available for the synthetic Needlona felt SO 2002 and for the Needlona felt WO-PE 1958, which is a mixture of natural and synthetic fibres. To still obtain an estimate for the open volume porosity of these felts regardless of the missing data, the porosity was calculated based on the bulk density $\rho_s = 1.31$ used for the woolen felts.

Another material which has to be mentioned, because its structure is completely different from that of the other porous materials, is Reapor, a porous glass granulate. It is composed of single pellets of recycled glass, which are sintered to form a rigid porous material with a (nominal) density of 270 kg/m³. Figure 3.3(b) provides a detailed photograph of the material.

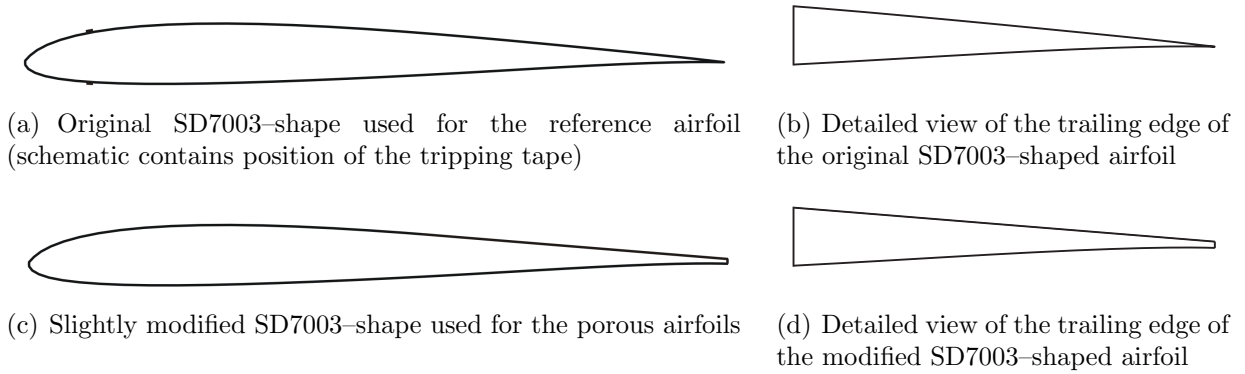


Figure 3.4: Comparison of the two airfoil designs, both having the same chord length $c_l = 0.235$ mm

In the present study, the volume porosity of the materials is used as an additional parameter to help describing the porous materials, while the air flow resistivity is the main parameter chosen for the characterization of the porous materials in order to develop a trailing edge noise model for porous airfoils.

3.1.2 Airfoil data

Airfoil shape and dimensions

The trailing edge noise measurements were performed on a set of 16 porous airfoils and one non-porous reference airfoil (Table 3.1). All airfoils had a chord length c_l of 0.235 m and a wingspan b of approximately 0.4 m, resulting in an aspect ratio of 1.7. The non-porous reference airfoil had an SD7003 shape [Selig et al., 1989] with a trailing edge thickness h of 0.5 mm and a trailing edge solid angle Ω of 8.6° . To ensure the existence of a turbulent boundary layer at the trailing edge of the non-porous airfoil, it was provided with a tripping tape on both the pressure side and the suction side at 10.6 % of the chord with a thickness of 1.6 mm and a height of 0.15 mm (The effectiveness of the tripping was confirmed in preliminary acoustic experiments, when for the lowest flow speed used for the present study, $U_0 \approx 25$ m/s, the tonal noise components, due to laminar boundary layer vortex shedding, disappeared and only broadband noise was audible.). The SD7003 airfoil is a semi-symmetrical, cambered airfoil with a maximum camber of 1.46 % (approximately 3.4 mm for the chosen chord length), the maximum thickness is 8.51 % (approximately 20 mm).

The porous airfoils had a slightly modified SD7003 shape, which had an increased trailing edge thickness compared to the original shape. The thickness of the modified edge has been increased to 1.59 mm compared to the original shape (theoretically 0.00235 mm) due to manufacturing reasons, since some of the porous materials are very fragile. Both the original and the modified SD7003 airfoil shapes can be seen in Fig. 3.4. The surface roughness provided by the porous materials ensured the existence of a turbulent boundary layer, and hence no extra tripping devices had to be applied.

Assembling of the porous airfoils

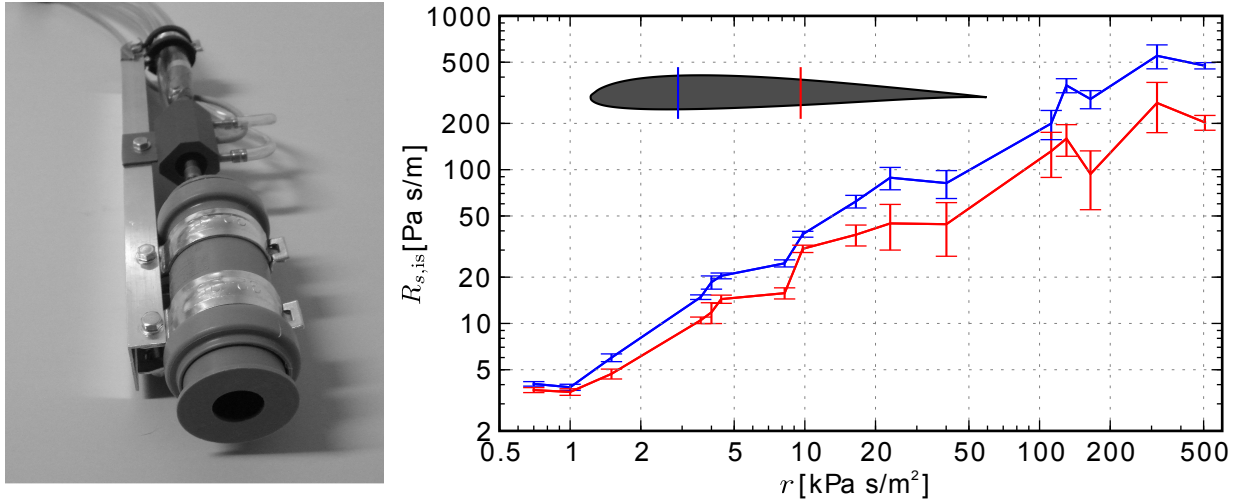
The porous airfoils were cut from boards or sheets of the basic porous materials using the water jet cutting technology. The resulting slices with thicknesses between 5 mm and 50 mm, depending on the dimensions of the porous materials, were then assembled manually to obtain airfoils with a span width of approximately 0.4 m. A photograph of four of the porous airfoils is provided in Figure C.1 in Appendix C. Although due care has been exercised in the assembling of the porous airfoils, the flow resistivity of the resulting airfoils can be slightly smaller than the flow resistivity of the basic porous materials given in Tab. 3.1. This is caused by possible, very thin slits between single slices of the porous material. At present, the flow resistivity of the assembled airfoil in streamwise direction can not be measured directly.

However, to provide additional information on the air flow resistance of the porous airfoils, in situ measurements were conducted to obtain the in situ specific air flow resistance $R_{s, \text{is}}$ of the porous airfoils at different chord positions (the index “is” stands for “in situ”). To this end, measurements of the air flow resistance $\Delta p/q_s$ were performed using a special handheld measurement socket, which has to be pressed on the upper surface of the porous airfoil under a constant force and allows for an air flow u_s from the suction side of the airfoil to the pressure side. The socket was originally designed to enable measurements of the specific air flow resistance of prepared specimen of bird wings [Windisch, 2007] and is shown in Figure 3.5(a). The contact area of the socket is equipped with a soft foam enclosed by a thin impermeable foil (not shown in Figure 3.5(a)). This foam should seal the contact area between the porous materials and the air outlet during the measurement and prevent an unwanted air flow between the socket and the porous material that does not permeate the material.

The air outlet of the socket has a diameter of 12 mm. The in situ specific air flow resistance can be calculated from the measured pressure difference between the point where the socket contacts the airfoil surface and the ambient pressure and the volume flow q_s (see Equation (3.2)) according to

$$R_{s, \text{is}} = \frac{\Delta p \cdot A_{\text{socket}}}{q_s}, \quad (3.5)$$

where A_{socket} is the cross sectional area of the socket outlet. The in situ specific air flow resistance is not independent from the thickness of the porous material (or in this case, from the airfoil thickness at the corresponding chord position) but increases with increasing thickness. It has to be noted that the in situ measurements using this handheld socket are fundamentally different from the measurement according to ISO 9053, since the air does not flow through a porous material sample of constant cross sectional area, where the streamlines are straight and parallel, but the air enters the porous material and is able to propagate in all directions inside the material. This means that when the flow enters the porous airfoils on the suction side, part of it flows straight through the airfoils, leaving the material on the pressure side, and part of the flow may also leave the porous airfoil on the suction side near the adapter. This is especially important when considering porous materials with very high air flow resistivities r , where it is supposed that a large portion of the air does not flow through the airfoil but flows laterally and leaves the airfoil at its suction side, or, even worse, leaks through small slits between airfoil and socket despite the sealing described above.



(a) Socket used for the in situ measurements (b) Specific in situ air flow resistance $R_{s, is}$ of the porous airfoils, characterized by their air flow resistivity r (see Table 3.1)

Figure 3.5: In situ measurement of the specific air flow resistance, measured at two chord positions, $x/c_l = 0.22$, 0.53

The in situ specific air flow resistance $R_{s, is}$, measured at two chord positions, $x/c_l = 0.22$ and $x/c_l = 0.53$, is shown in Figure 3.5(b) as a function of the air flow resistivity r for the 16 porous airfoils from Table 3.1. To obtain a better statistical reliability of the measurements, single measurements were conducted at eight different span positions for each of the two chord positions. Accordingly, Figure 3.5(b) gives the mean value of the eight measurements as well as the standard deviation. The resulting mean in situ specific air flow resistances $R_{s, is}$ measured at the first chord position, $x/c_l = 0.22$, which is near the position of maximum thickness of the airfoil, are approximately between 3 Pa s/m and 550 Pa s/m. In general, airfoils from materials with larger air flow resistivities r also have a larger in situ specific air flow resistance $R_{s, is}$. As would be expected, a monotonous dependence between the in situ specific air flow resistance of the porous airfoils and the air flow resistivity of the porous materials can be observed from Figure 3.5(b).

The results from the second chord position, $x/c_l = 0.53$, basically show the same relation between r and $R_{s, is}$: With increasing air flow resistivity of the materials, the in situ specific air flow resistance measured at $x/c_l = 0.53$ increases. As would be expected, $R_{s, is}$ is larger at $x/c_l = 0.22$ due to the greater thickness of the airfoil at this position. Since the measured in situ specific air flow resistance of the porous airfoils leads to roughly the same order of the airfoils as the air flow resistivity of the porous materials and does not provide any additional information regarding the characterization of the airfoils, the porous airfoils will be characterized by their air flow resistivity r for the remaining part of this thesis.

Airfoil surface roughness

Another effect of the different air flow resistivities is the resulting surface roughness of the porous airfoils. Examining the pores of the airfoils, it becomes evident that porous airfoils with lower air flow resistivities r are mostly characterized by larger pores. For some airfoils, this can even be recognized from the information on the pore density given by the manufacturer, which means the number of pores per inch (ppi), for example for the

Panacell airfoils or the airfoils made of M-Pore Al and M-Pore PU. Larger pores most often result in an increased surface roughness compared to smaller pores. As described in Section 2.3, in existing surface roughness noise studies [Howe, 1984, Liu and Dowling, 2007, Liu et al., 2008], the surface roughness is characterized by a roughness density and the radius of roughness particles. Regarding such models, the skeletal material between the pores or cells of the porous materials may be taken as equivalent to the roughness particles, while the pore size would have a strong effect on the roughness density. Larger pores would therefore lead to larger distances between the cell walls of the skeletal material and hence to a decrease of the roughness density. Thus, porous airfoils with lower air flow resistivities and larger pores are basically characterized by a higher surface roughness than airfoils with a higher air flow resistivity and smaller pores.

When, as a first approximation, the majority of the porous materials of the present study is described using the simple model of a rigid structure with regular round pores (longitudinal or inclined), the ‘‘Rayleigh model with round capillaries’’, the volume porosity σ_v can be calculated based on the pore diameter d_p and the distance s between two pores [Mechel, 2008] using

$$\sigma_v = \frac{\pi}{4} \left(\frac{d_p}{s} \right)^2. \quad (3.6)$$

The surface porosity σ_s of such a porous material, defined as the ratio of the pore area (circular holes) to the total area, can also be calculated using the Equation (3.6). Based on the volume porosity and the dynamic viscosity η of the fluid, the air flow resistivity r is given by

$$r = \frac{1}{\sigma_v} \cdot \frac{8\eta}{d_p^2} = \frac{32\eta}{\pi} \cdot \frac{s^2}{d_p^4}. \quad (3.7)$$

When the surface of the porous materials is seen as a rough surface generated by the skeletal material, it is reasonable to assume that the roughness density increases with decreasing surface porosity. This can be shown analytically. Using the terminology given above, the roughness density σ_{rough} is determined by the ratio of the total area minus pore area to the total area,

$$\sigma_{\text{rough}} = 1 - \frac{\pi}{4} \left(\frac{d_p}{s} \right)^2 = 1 - \sigma_s. \quad (3.8)$$

Using the first notation of Equation (3.7) and the fact that $\sigma_v = \sigma_s$ for the Rayleigh model of a porous material yields

$$\sigma_{\text{rough}} = 1 - \frac{1}{r} \cdot \frac{8\eta}{d_p^2}. \quad (3.9)$$

When the pore diameter d_p decreases, but the air flow resistivity r in Equation (3.9) is virtually kept constant, the roughness density also decreases. If it is assumed that a decreasing pore size of the porous foams used in the present study is a result of an increasing air flow resistivity, then Equation (3.9) confirms that the roughness density of the porous airfoils decreases when the air flow resistivity increases.

The Rayleigh model with round capillaries may be used to describe the structure of the open-porous foams that are used in the present study. The felts from Table 3.1 would rather be described as fibrous materials with round fibres transversal to the flow, where

according to [Mechel, 2008] the volume porosity and surface porosity are given by

$$\sigma_v = 1 - \frac{\pi}{4} \left(\frac{d_f}{s} \right)^2 \quad (3.10)$$

and

$$\sigma_s = 1 - \frac{d_f}{s}, \quad (3.11)$$

where d_f is the diameter of the fibres and s is the distance of the fibres. Again, the roughness density σ_{rough} , defined as the ratio of (transversal) fibre area to the total area (and hence fibre diameter to fibre distance) can be calculated as

$$\sigma_{\text{rough}} = 1 - \sigma_s. \quad (3.12)$$

The air flow resistivity of a fibrous material with random fibre radius distribution and random fibre orientation can be estimated by the empirical relation [Mechel, 2008]

$$r = K \frac{\eta}{(\overline{d_f/2})^2} \cdot (1 - \sigma_v)^e, \quad (3.13)$$

where the overline denotes the average value, K is a constant and the exponent e is greater one (for glass fibre materials it takes a value of 1.42 and for mineral fibre materials a value of 1.59). Substituting d_f/s in Equation (3.10) with the roughness density and inserting the resulting term in Equation (3.13) leads to the expression

$$r = K \frac{\eta}{(\overline{d_f/2})^2} \cdot \left(\frac{\pi}{4} \cdot \sigma_{\text{rough}}^2 \right)^e. \quad (3.14)$$

Equation (3.14) shows that for the felts the air flow resistivity increases for an increasing surface roughness and vice versa, which means that the airfoils made of felts with a high air flow resistivity are assumed to have a high roughness density. This is consistent with what would be expected, since for an increasing number of fibres with constant fibre diameter both the air flow resistivity and the roughness density increase.

The more appropriate parameter to describe the surface roughness of the felts seems to be the fibre radius $d_f/2$, which can be taken to be equivalent to the roughness height. According to Equation (3.14), the square of the fibre radius is inversely proportional to the air flow resistivity for a given roughness density. A decreasing air flow resistivity would therefore be related to an increasing roughness height for a constant roughness density.

3.2 Wind tunnel

The aeroacoustic wind tunnel at Brandenburg University of Technology Cottbus is an open jet wind tunnel. The test facility is divided into a room for the wind tunnel driving machinery and a quiet room that contains the test section. Additional information on the aeroacoustic wind tunnel facility, including a detailed description of the aerodynamic and acoustic wind tunnel design, can be found in reference [Sarradj et al., 2009].

For the trailing edge noise experiments, a circular nozzle of Witoszynski type with an exit diameter of 0.2 m and a contraction ratio of 16 was used. The maximum flow speed that can

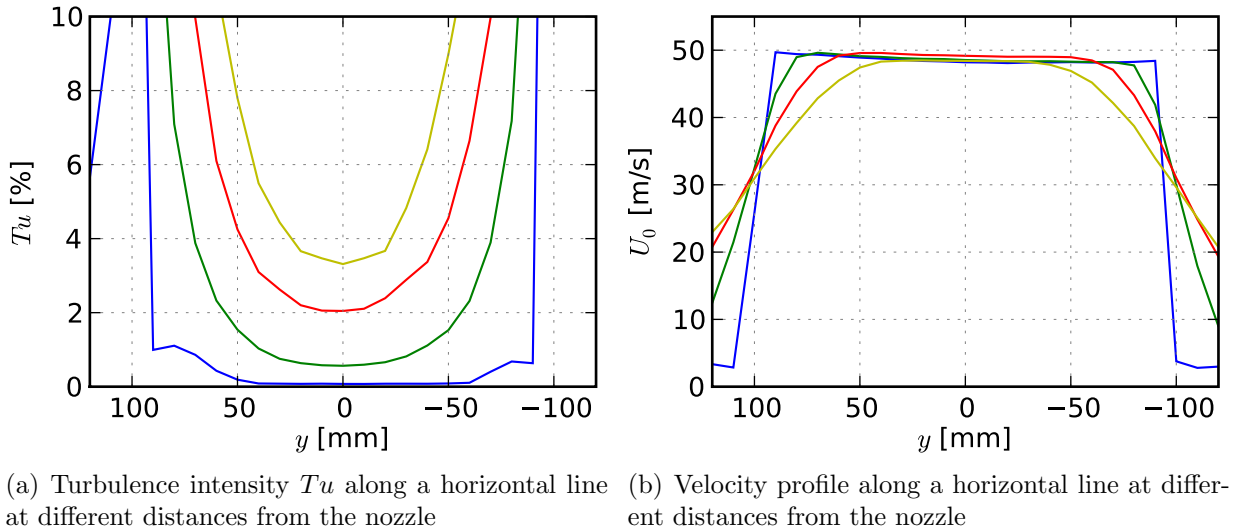


Figure 3.6: Wind tunnel nozzle characteristics: Turbulence intensity Tu according to Equation (3.15) and velocity profile for a flow speed of $U_0 \approx 50$ m/s at four different distances from the nozzle (diameter $D = 200$ mm): $x/D =$ ■ 0.07, ■ 1, ■ 2, ■ 3

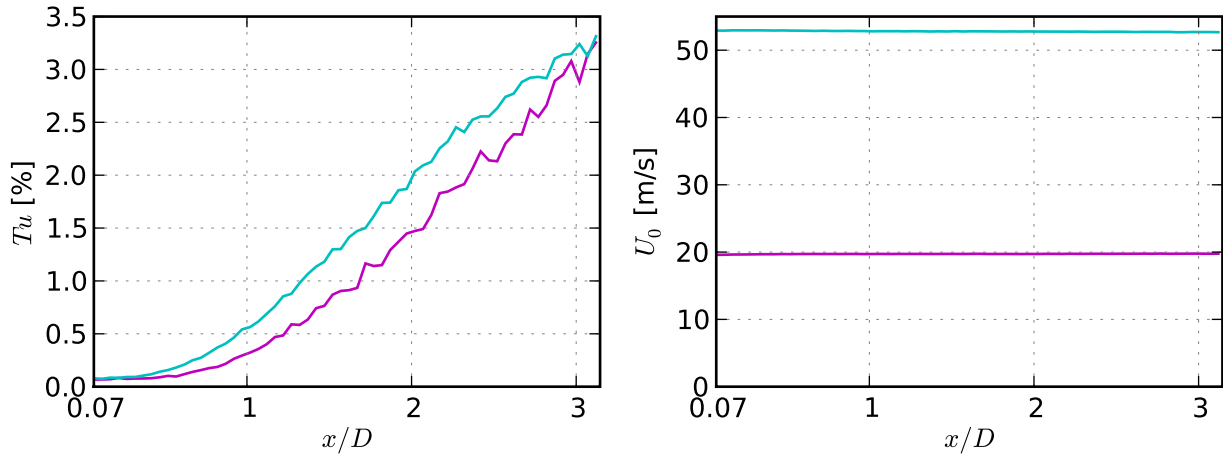
be achieved using this nozzle is about 60 m/s. The resulting wind tunnel core jet has a very low turbulence, which was confirmed by measuring the local turbulence intensity Tu for different flow speeds U_0 at various distances from the nozzle exit. The turbulence intensity is defined as the ratio of the root-mean-square of the turbulent velocity fluctuations, which are assumed to be equal in all dimensions x , y and z for local isotropic turbulence, to the mean flow speed of the open jet:

$$Tu = \frac{\tilde{u}_x}{U_0} = \frac{\tilde{u}_y}{U_0} = \frac{\tilde{u}_z}{U_0} = \frac{\sqrt{\tilde{u}^2}}{U_0}. \quad (3.15)$$

The measurements of the wind tunnel turbulence were performed using constant temperature anemometry with a standard single-wire DANTEC type P11 probe. Figure 3.6 shows the turbulence intensities and the resulting velocity profiles measured in front of the nozzle for a flow speed of 50 m/s along the horizontal diameter at different distances from the nozzle exit. The turbulence intensity at a distance of 14 mm to the nozzle exit area is below 0.1 % at a flow speed of 50 m/s, characterizing the flow as virtually not turbulent.

Figure 3.7 shows the turbulence intensity and the velocity profiles measured along the nozzle axis for two flow speeds, 20 m/s and 50 m/s. Since extensive hot-wire-measurements have been conducted within the scope of this research in order to characterize the flow field of the nozzle used for the experiments, additional turbulence data of the wind tunnel are given in Appendix A. This includes the turbulence intensity and the velocity profile measured over a complete plane parallel to the nozzle exit area as well as additional data at a flow speed of 20 m/s.

To enable acoustic measurements of airfoil trailing edge noise, the wind tunnel background noise has to be significantly lower than the noise emitted from the test items. Figure 3.8 shows the A-weighted overall sound pressure level of the aeroacoustic wind tunnel, including third-octave bands with center frequencies from 100 Hz to 20 kHz. It can be observed that the wind tunnel background noise is well below 60 dB at a flow speed of 50 m/s.



(a) Turbulence intensity Tu along the wind tunnel axis (b) Velocity profile along the wind tunnel axis

Figure 3.7: Wind tunnel characteristics: Turbulence intensity Tu according to Equation (3.15) and velocity profile for two different flow speeds ($U_0 \approx$ ■ 20, ■ 50 m/s) along the wind tunnel axis

During the acoustic measurements, the test section in front of the wind tunnel nozzle was surrounded by a mobile cabin that is equipped with three absorbing side walls for frequencies above 500 Hz to provide a semi-anechoic acoustic environment. The microphone array, consisting of a fully reflecting aluminum plate holding the microphones, forms the ceiling of the cabin (see Figure 3.9(a)). The dimensions of the cabin are 2.0 m length (in direction of the flow) \times 1.5 m height \times 1.55 m width (in spanwise direction).

The airfoils subject to the flow were positioned in front of the nozzle at a distance of 0.05 m to the nozzle exit area at the height of the horizontal nozzle center plane, as shown in Figure 3.9(a). The airfoil tips were attached to a six-component-balance to simultaneously measure the aerodynamic performance. The spanwise extent of the airfoils is greater than the nozzle exit diameter to avoid aerodynamic and acoustic effects caused at the tips or the mountings. Figure 3.9(b) shows a schematic top view of the experimental setup, including

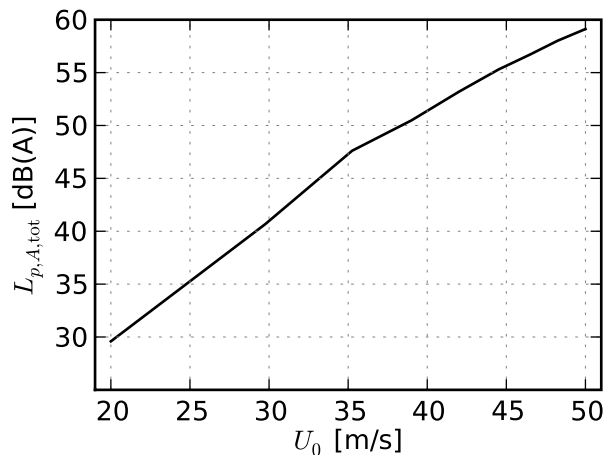


Figure 3.8: A-weighted overall sound pressure level of the aeroacoustic wind tunnel at a distance of 1 m at 90° to the nozzle axis

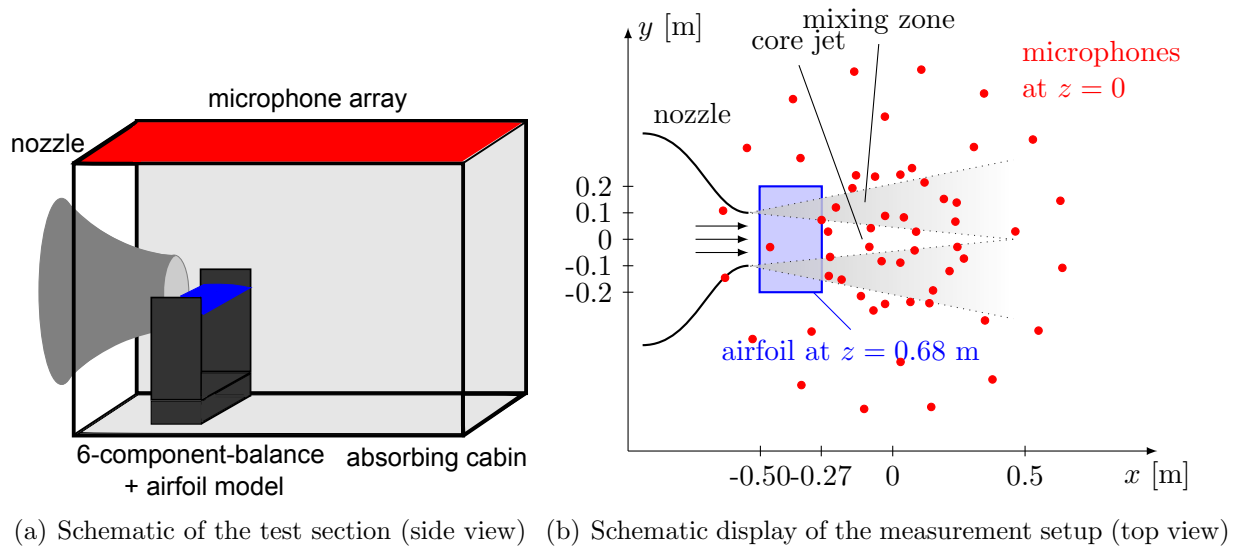


Figure 3.9: Measurement setup in the aeroacoustic wind tunnel

the wind tunnel nozzle, the core jet and the shear layers as well as the position of the airfoil. The red dots represent the positions of the 56 microphones in the microphone array.

In the present study, the lower limit of the flow speed was approximately 25 m/s. Below this flow speed, laminar boundary layer trailing edge noise was occasionally detected for the non-porous airfoil, recognizable due to the resulting tonal noise. No such tonal noise components were noticed for flow speeds above 25 m/s.

As discussed in [Geyer et al., 2010a], the large dimensions of the airfoil compared to the nozzle diameter induce a deflection of the core jet and, subsequently, a curvature of the shear layer. The blockage of the nozzle is not negligible, especially at higher angles of attack. Additionally, the width of the core jet is not constant at different spanwise locations of the airfoil. The consequence is that the loading of the airfoil may vary in the spanwise and the chordwise direction along the airfoil. These limitations imply that the experimental setup used for the present study cannot be compared to a common benchmark trailing edge noise measurement setup, as for example the setup used by Brooks et al. [Brooks et al., 1989] or the one used by Oerlemans [Oerlemans, 2004, Oerlemans and Migliore, 2004].

Moreau et al. [Moreau et al., 2001] performed numerical simulations in order to compare the flow around an airfoil in an open jet with the same airfoil under free flow conditions, as well as experiments on a cambered airfoil. They discuss in detail the restrictions of different experimental setups that are affected by a finite jet width and interference from the nozzle exit. A simple correction of the angle of attack was found to not be successful in open jet wind tunnels where the shear layers have a strong effect on the flow around the airfoil. According to Moreau et al. [Moreau et al., 2001], in cases where the jet width is not sufficiently large compared to the frontal area of the airfoil, the resulting flow field rather resembles the flow field obtained when the same airfoil is placed in a cascade setup than that around an isolated airfoil.

For configurations including airfoils that are small compared to the nozzle exit area and a rectangular wind tunnel nozzle with side plates, thus providing a nearly two-dimensional flow regime, the geometric angle of attack α is usually converted into an effective angle of

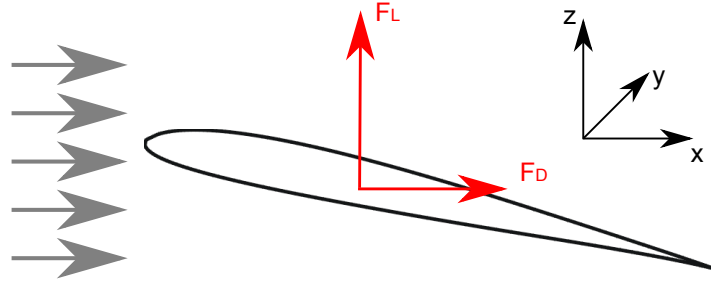


Figure 3.10: Definition of the measured lift and drag forces F_L and F_D

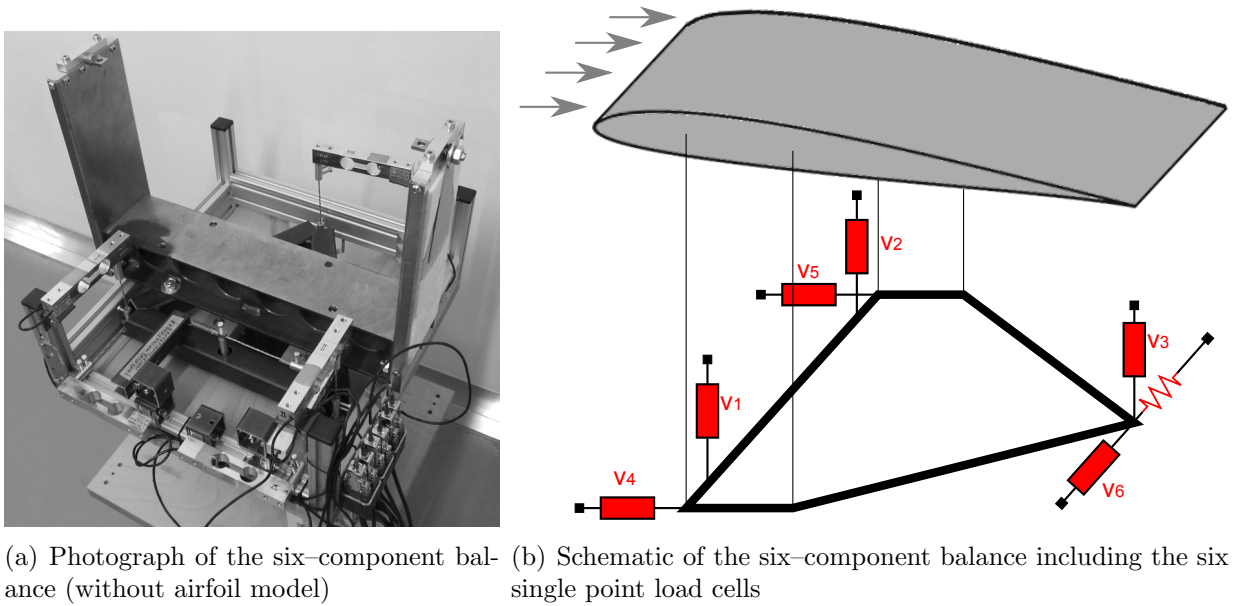
attack. Such correction should account for the free flow conditions as opposed to the flow conditions and pressure distributions in an open jet wind tunnel. A common correction procedure is the method proposed by Brooks et al. [Brooks et al., 1984, Brooks et al., 1986], according to which the effective angle of attack of a symmetrical airfoil is estimated based on the chord length c_l of the airfoil and the nozzle dimension D . It was developed using several flat plates and NACA 0012 airfoils with different chord lengths in an open jet wind tunnel with a rectangular nozzle and side plates. This correction is widely used in aeroacoustic studies. Hutcheson and Brooks [Hutcheson and Brooks, 2004] even use this method for a slightly cambered airfoil, where the camber leads to a simple modification of the correction equation.

Knight and Harris [Knight and Harris, 1930] developed a correction method based on the fundamental wing theory by Prandtl (as for example given by Glauert [Glauert, 1983]). It takes into account the effect of the free jet boundaries based on an assumed elliptical lift distribution over the airfoil span, using the airfoil dimensions and the jet dimensions as well as the lift coefficient of the airfoil. This method is employed in older aerodynamic studies like the ones by Theodorsen and Silverstein [Theodorsen and Silverstein, 1934] and Silverstein and Katzoff [Silverstein and Katzoff, 1937].

Due to the fact that the airfoil dimensions are large compared to the dimensions of the nozzle, especially at high angles of attack, and due to the slightly asymmetric SD7003 airfoil shape, common procedures to correct the angle of attack cannot be successful in the present study. Additionally, the porous consistency of the airfoils most probably leads to different flow effects for each individual airfoil. Hence, the angle of attack was not corrected. Instead, the geometrical angle of attack α is given only as a means of comparison between different working points of the airfoils based on the measurement setup used, with its restrictions described above.

3.3 Aerodynamic force measurements

To determine the aerodynamic performance of the porous airfoils in comparison to the reference airfoil, the lift and drag forces acting on the airfoils were captured simultaneously to the acoustic measurements. In the present thesis, the lift force F_L is defined as the vertical force in direction of the (positive) z -axis, perpendicular to the direction of the flow. Accordingly, the drag force F_D is the horizontal force in direction of the flow (see Figure 3.10).



(a) Photograph of the six-component balance (without airfoil model) (b) Schematic of the six-component balance including the six single point load cells

Figure 3.11: Setup used for the aerodynamic measurements

The forces were measured using a six-component balance, a photograph of which can be seen in Figure 3.11(a). It consists of six single point load cells of parallelogram-type made of an aluminum alloy. Each load cell has a nominal load of 10 kg, a limit load of 20 kg and a combined error of 0.017 %. The high nominal load was chosen because the cells have to support not only the airfoil, but also a triangular steel frame with a mass of more than 5 kg that holds lateral mounting plates. These side plates were used to position the airfoil in front of the nozzle, additionally allowing for the adjustment of the angle of attack. Both the lateral mountings and the steel frame are out of the flow.

The balance was designed to be capable of measuring the forces acting on various airfoils of different weight at both positive and negative angles of attack, and therefore the load cells have to bear the weight of the steel frame, the mountings and the airfoil as well as the negative lift force acting on the airfoil at negative angles of attack. The angle of attack α can be measured using an electronic balance with an accuracy of 0.1° . The transmission of the forces from the steel frame to each load cell is realized through thin steel cables. The forces acting on the load cells cause a variation of the internal electrical resistance of the load cells, which is measured by a Wheatstone bridge electrical circuit contained in a National Instruments 24 Bit full bridge analog input module.

Three of the six load cells (load cell 1 to 3) are used to determine the vertical component of the forces acting on the airfoil, two cells (load cell 4 and 5) are used to determine the streamwise component and one load cell (load cell 6) measures a potential lateral force component. From the signals v_1 through v_6 , which are voltages proportional to the forces measured by the six load cells as shown in Figure 3.11(b), the aerodynamic forces and

moments acting on the airfoil can be calculated using the relation

$$\begin{pmatrix} F_L \\ F_D \\ F_S \\ M_P \\ M_R \\ M_Y \end{pmatrix} = \mathbf{B} \cdot \begin{pmatrix} v_1 \\ v_2 \\ v_3 \\ v_4 \\ v_5 \\ v_6 \end{pmatrix}, \quad (3.16)$$

or, in a notation using the matrix of the physical forces and moments, \mathbf{F} , and the matrix of the signals from the load cells, \mathbf{V} ,

$$\mathbf{F} = \mathbf{B}\mathbf{V}. \quad (3.17)$$

In Equation (3.16), F_L , F_D and F_S are the lift force, drag force and side force, respectively. M_P , M_R and M_Y are the pitching moment, the rolling moment and the yawing moment. The moments are defined with respect to the center of mass of the airfoil.

The 6×6 transfer matrix \mathbf{B} is inherent to the mechanical system. In an ideal, frictionless mechanical system, in which each loading cell would bear only the component of the force that it is designed to measure, the first three rows of the transfer matrix would contain only ones and zeros, while the last three rows would contain only the appropriate factors according to the particular length of the lever arms that add to the respective moment. In this theoretic case, the vertical load cells would bear only the z -component of the force, the streamwise load cells would bear the x -component and the lateral cell would bear only the y -component. For example, the lift force could then be calculated as the (negative) sum of the output of the first three load cells,

$$F_L = -1 \cdot v_1 \frac{\text{N}}{\text{V}} - 1 \cdot v_2 \frac{\text{N}}{\text{V}} - 1 \cdot v_3 \frac{\text{N}}{\text{V}} + 0 \cdot v_4 + 0 \cdot v_5 + 0 \cdot v_6, \quad (3.18)$$

and the drag force would be equal to the sum of the output of the fourth and fifth load cell,

$$F_D = 0 \cdot v_1 + 0 \cdot v_2 + 0 \cdot v_3 + 1 \cdot v_4 \frac{\text{N}}{\text{V}} + 1 \cdot v_5 \frac{\text{N}}{\text{V}} + 0 \cdot v_6. \quad (3.19)$$

The first three factors in Equation (3.18) are negative because load cell 1 to 3 produce a positive output voltage when the vertical force component is directed in opposite direction to that defined for a positive lift force (see Figure 3.10 and 3.11(b)).

In a real mechanical system, however, the matrix B also contains some parasitic effects. This is due to the fact that the load cells, to some extent, receive other components of the force besides the component that they are designed to measure. This ‘‘crosstalk’’ effect results in a matrix that contains non-zero elements and slightly differs from the idealized matrix described above. Prior to the aerodynamic measurements of the present study, the matrix \mathbf{B} was determined by calibrating the six-component balance through the application of a set of defined forces and moments.

During the aerodynamic measurements, the voltage from the National Instruments input module was recorded with a sample frequency of 1 kHz and time-averaged. The DC component of the signals from the load cells, obtained as the moving average of the resulting data, was used to calculate the corresponding lift and drag forces according to Equation (3.16), using the transfer matrix \mathbf{B} that was determined for the six-component balance.

3.4 Acoustic measurements and data processing

The acoustic measurements were performed using a planar microphone array, which consists of a $1.5 \text{ m} \times 1.5 \text{ m}$ aluminum plate that holds 56 flush-mounted 1/4th inch microphone capsules. The microphones are Panasonic WM-61A omnidirectional back electret condenser microphone cartridges. The exact position of the 56 microphones is given in Appendix B. The setup of the microphone array relative to the wind tunnel nozzle and the airfoil can be seen in Figure 3.9(b), where each red dot represents one single microphone. Each microphone was calibrated using a hand-held microphone calibrator. The array was positioned out of the flow at a distance of 0.68 m above the airfoil model. The data were recorded using a National Instruments 24 Bit multichannel measurement system with a sample frequency of 51.2 kHz and a measurement duration of 40 s, leading to 2,048,000 samples per measurement and channel. This resulted in a data amount of approximately 453 MByte per measurement. The raw data were stored on a RAID storage system.

The effects of the sound refraction at the shear layer of the free jet on the source localization and the magnitude of the sound sources have been estimated in prior tests. The effect on the source localization was found to be negligible due to the relatively low flow Mach numbers $Ma < 0.15$ (subsonic flow). The effect on the magnitude of the localized sound sources was also found to be negligible. One reason for the small differences is the distance of the microphone array in relation to the distance between the airfoil and the shear layer. The latter distance, between airfoil and shear layer, is at most equal to the radius of the nozzle (0.1 m), but most likely it is smaller since the airfoil is not positioned directly in front of the nozzle. On the other hand, the (vertical) distance between the airfoil and the microphone array is 0.68 m, and hence almost seven times the distance between airfoil and shear layer.

Additionally, the present study focuses on the noise generation at the trailing edge of porous airfoils relative to the noise generation at the trailing edge of the non-porous reference airfoil only. Thus, correct absolute values of the generated trailing edge noise are actually not very important, as long as the small errors are constant for all examined airfoils.

Another important fact is that the exact geometry of the shear layer of the setup used is not known. The supposedly conical shape of the shear layer does not agree very well with the available correction models. At most, a very abstract and reduced model of the shear layer could have been used, thus creating more problems than it might actually help to solve. Accordingly, no shear-layer-correction, like that proposed by Amiet [Amiet, 1978] and Schlinker and Amiet [Schlinker and Amiet, 1980], has been used for the acoustic measurements of the present study.

3.4.1 Beamforming theory

In this section, a basic introduction to the theory of beamforming will be given. The focus will be on the conventional delay-and-sum beamforming only. If necessary, additional information on advanced beamforming algorithms are given in later sections.

When acoustic measurements are performed with a phased array of microphones, as opposed to measurements using only a single microphone, beamforming is the basic step of the post-processing that focuses (or “steers”) the array to different locations. The micro-

phone array is a directional microphone system that can basically be regarded similar to an acoustic concave mirror. The general working principle is the steering of the array focus point (corresponding to the focus point of the acoustic concave mirror) to each point in a given grid of potential source locations, and the measurement of the noise contribution from this grid point. Two main objectives are pursued when this measurement technique is used: first, the identification of the noise source locations and, second, the identification of the associated source strengths. The results of such microphone array measurements are usually displayed as two-dimensional or three-dimensional maps of the spatial sound pressure contributions, so-called sound maps, similar to an “acoustic photograph”.

Both the design of the array as well as the beamforming algorithm determine the array directivity pattern. This pattern basically consists of a so-called main lobe at the location of maximum sensitivity (the main beam of the array directivity pattern), determining the direction along which the array is steered, and several secondary lobes. These side lobes are false source indications, lower in level than the main lobe, and they do not point toward the direction to which the array is steered. The effective dynamic range of the microphone array depends on the ratio of the strength of these side lobes to the strength of the main lobe [Mueller, 2002]. The beamwidth, defined as the 3 dB width of the main lobe, determines the resolution of the microphone array. It is advantageous when the beamwidth is as small as possible.

The following basic theory of the sound field model and the delay-and-sum beamforming is taken from the work of Sarradj [Sarradj, 2010] and Stoica and Moses [Stoica and Moses, 1997].

Description of the sound field model

The microphone array consists of N microphones located at \mathbf{x}_n ($n = 1, 2, \dots, N$). First, the presence of only one single monopole source will be assumed, located at \mathbf{x}_s in the acoustic far field of the array, without flow or any reflecting boundaries present. The complex-valued sound pressure p at the i -th microphone (located at \mathbf{x}_i) due to the sound pressure p' at an arbitrary reference position \mathbf{x}_0 (for example the array center) is then given by

$$p(\mathbf{x}_i) = a(\mathbf{x}_i, \mathbf{x}_0, \mathbf{x}_s) \cdot p'(\mathbf{x}_s). \quad (3.20)$$

The transfer function a depends on the source location, source type and environmental parameters. For a monopole source in the far field of the microphones and the reference point \mathbf{x}_0 , Equation (3.20) simplifies to

$$a(\mathbf{x}_i, \mathbf{x}_0, \mathbf{x}_s) = \frac{R_0}{R_i} \cdot e^{-jk(R_i - R_0)}, \quad (3.21)$$

where $R_0 = |\mathbf{x}_s - \mathbf{x}_0|$ and $R_i = |\mathbf{x}_s - \mathbf{x}_i|$ are the distance between array reference position and monopole source and the distance between source and microphone position, respectively. This form of the transfer function a is based on the solution of the wave equation for spherical waves,

$$p(R) = \frac{jk}{4\pi R} \rho c q \cdot e^{-jkR}, \quad (3.22)$$

where k is the acoustic wave number and R is the distance from the field point to the monopole source with the sound energy flux q . For N microphones, the sound pressure due

to a single source at \mathbf{x}_s is given by

$$\mathbf{p} = \mathbf{a}(\mathbf{x}_0, \mathbf{x}_s) \cdot p'(\mathbf{x}_s), \quad (3.23)$$

with the transfer vector $\mathbf{a}(\mathbf{x}_0, \mathbf{x}_s)$ containing N transfer functions $a(\mathbf{x}_i, \mathbf{x}_0, \mathbf{x}_s)$. Since realistic sound fields are conveniently modeled as a superposition of the sound fields from several sound sources, the sound pressure at each microphone can be described as a superposition of the sound pressure contributions from each source. For M sources, the sound pressures at the N microphones are given by

$$\mathbf{p} = \mathbf{A}\mathbf{p}' + \mathbf{n}. \quad (3.24)$$

Each column of the $N \times M$ matrix \mathbf{A} contains the transfer vector \mathbf{a}_m ($m = 1, 2, \dots, M$) corresponding to the m -th source. The $N \times N$ matrix \mathbf{n} contains additional noise sources. Regarding measurements in a wind tunnel environment, this noise is most often generated by non-acoustic pressure fluctuations, the microphone electronics and data acquisition hardware. The elements n_i of \mathbf{n} are not correlated to any of the noise sources p'_j . Hence, the cross spectrum between the source signals and the noise, $E\{p'_j n_i^*\}$, is zero. $E\{\}$ denotes the expectation operator, which has to be used for the calculation of the cross spectrum because both signals are the Fourier transformation of time data recorded during a finite measurement duration T . The matrix of the cross spectrum elements of the microphone signals can be written as

$$E\{\mathbf{p}\mathbf{p}^H\} = \mathbf{A}E\{\mathbf{p}'\mathbf{p}'^H\}\mathbf{A}^H + E\{\mathbf{n}\mathbf{n}^H\}, \quad (3.25)$$

with $()^H$ denoting the conjugate transpose. If it is assumed that the noise signals n_i are mutually uncorrelated and of the same amplitude n , so that $E\{n_i n_j^H\}$ equals zero for $i \neq j$ and n for $i = j$, Equation (3.25) can be rewritten as

$$\mathbf{G} = \mathbf{A}\mathbf{S}\mathbf{A}^H + n^2\mathbf{I}. \quad (3.26)$$

\mathbf{G} and \mathbf{S} are the cross spectral matrices of the microphone signals and the source signals, respectively, and \mathbf{I} is the identity matrix. This equation describes the sound field generated by M monopole sound sources, as measured by N microphones.

From Equation (3.26), the cross spectral matrix of the source signals \mathbf{S} can theoretically be calculated as a function of the microphone signals \mathbf{G} using

$$\mathbf{S} = \mathbf{A}^+(\mathbf{G} - n^2\mathbf{I})\mathbf{A}^{H+}, \quad (3.27)$$

where the $+$ superscript denotes the Moore-Penrose pseudoinverse [Gentle, 2007]. If only one single source is present, the transfer matrix \mathbf{A} contains only one column (the transfer vector $\mathbf{a}(\mathbf{x}_s)$) and Equation (3.27) becomes

$$S = \frac{\mathbf{a}(\mathbf{x}_s)^H}{\mathbf{a}(\mathbf{x}_s)^H \mathbf{a}(\mathbf{x}_s)} (\mathbf{G} - n^2\mathbf{I}) \frac{\mathbf{a}(\mathbf{x}_s)}{\mathbf{a}(\mathbf{x}_s)^H \mathbf{a}(\mathbf{x}_s)}. \quad (3.28)$$

Delay-and-sum beamforming

The conventional delay-and-sum beamforming technique can best be described as a spatial filter, which is realized through the implementation of a steering vector. This steering

vector \mathbf{h} consists of a set of phase delays for each microphone, depending on the differences of the travel time from the source at \mathbf{x}_s to each microphone at \mathbf{x}_i . This means that time delays are added to the signals of each microphone in a way that the time-domain signals, received from the direction that the array is steered to, are in phase for each channel.

The steering vector \mathbf{h} should meet two conditions: When the array is steered to a certain grid point \mathbf{x} , signals from a source located at this grid point should be passed undistorted, while signals originating from other grid points should be attenuated as much as possible. The first condition can be formulated as

$$\mathbf{h}^H(\mathbf{x} = \mathbf{x}_s)\mathbf{a}(\mathbf{x} = \mathbf{x}_s) = 1. \quad (3.29)$$

Using the steering vector \mathbf{h} , the output signal of the delay-and-sum beamformer, when steered to an arbitrary position \mathbf{x}_k , is given by

$$p_F(\mathbf{x}_k) = \mathbf{h}^H(\mathbf{x}_k)\mathbf{p}, \quad (3.30)$$

with the corresponding auto power spectral density (or auto power spectrum)

$$S_{XX}(p_F(\mathbf{x}_k)) = E\{p_F(\mathbf{x}_k)p_F^*(\mathbf{x}_k)\} = \mathbf{h}^H(\mathbf{x}_k)\mathbf{G}\mathbf{h}(\mathbf{x}_k). \quad (3.31)$$

The signals from any other location than the source location \mathbf{x}_s are considered to be spatially white noise, which means that these signals impinge on the microphone array with equal power at the same time. Per definition, the autocorrelation of spatially white noise is a multiple of the identity matrix, $E\{pp^*\} = w \cdot \mathbf{I}$, where w is a scalar. Thus, for signals coming from other grid points than the one that the array is steered to (\mathbf{x}_k), the delay-and-sum beamformer output according to Equation (3.31) yields (for $w = 1$)

$$S_{XX}(p_F(\mathbf{x} \neq \mathbf{x}_k)) = \mathbf{h}^H(\mathbf{x} \neq \mathbf{x}_k)\mathbf{h}(\mathbf{x} \neq \mathbf{x}_k). \quad (3.32)$$

The second requirement for the steering vector, a maximum attenuation for signals arriving from other grid points than \mathbf{x}_k , is equivalent to the minimization of the auto power spectrum given in Equation (3.32). As proven in reference [Stoica and Moses, 1997], both conditions are met when

$$\mathbf{h} = \frac{\mathbf{a}(\mathbf{x}_k)^H}{\mathbf{a}(\mathbf{x}_k)^H\mathbf{a}(\mathbf{x}_k)}, \quad (3.33)$$

which is consistent with the formulation used in Equation (3.28). Again, when one single monopole source is considered to be located at \mathbf{x}_s , the transfer vectors $\mathbf{a}(\mathbf{x}_s)$ can be determined using the solution to the wave equation for spherical waves, Equation (3.22), and the elements of \mathbf{h} become

$$h_i = \frac{1}{R_0 R_i \sum_{m=1}^N \frac{1}{R_m^2}} e^{-jk(R_i - R_0)}. \quad (3.34)$$

In practice, the theoretical cross spectral matrix of the microphone signals \mathbf{G} is not known so that it has to be replaced by an estimate for the cross spectral matrix based on the digital signals recorded by the data acquisition hardware. This estimate $\hat{\mathbf{G}}$ is obtained blockwise after dividing the sampled signal in n_B blocks:

$$\hat{\mathbf{G}} = \frac{1}{n_B} \sum_{i=0}^{n_B} E\{\mathbf{p}(i)\mathbf{p}^H(i)\}. \quad (3.35)$$

This leads to the estimation of the location and strength of the sound sources, as they are determined by the peaks of the function

$$S_{XX}(p_F(\mathbf{x}_k)) = \mathbf{h}^H(\mathbf{x}_k) \hat{\mathbf{G}} \mathbf{h}(\mathbf{x}_k). \quad (3.36)$$

To eliminate the influence of channel noise in $\hat{\mathbf{G}}$, the main diagonal of that matrix can be removed. Since this noise is not correlated between different microphones, it is not contained in the off-diagonal elements of $\hat{\mathbf{G}}$. The diagonal removal, however, has some effect on the absolute value of $S_{XX}(p_F)$.

Equation (3.36) yields a maximum for $\mathbf{x}_k = \mathbf{x}_s$, when only one source is present at \mathbf{x}_s . In that case, $S_{XX}(p_F(\mathbf{x}_s))$ gives a good estimation for the strength of the source. In the general case of more than one source, the performance of the delay-and-sum beamformer depends on the transfer matrix \mathbf{A} of the beamformer, and hence on the source locations, the frequency and the number of the microphones used as well as the layout of the microphones in the array. Certain circumstances may degrade the performance of the delay-and-sum beamformer: If sources are closely spaced, the limited resolution of the beamformer may lead to an erroneous result. Additional sources with low source strengths compared to the highest source strength may not be located at all if the signal-to-noise ratio is too low. The estimation of strength and location of sources with wavelengths not small compared to the array aperture may also yield wrong results. Additional problems may arise when sources are correlated to each other.

One possibility to deal with some of these problems is to think of the beamformer as a system that assigns an initially unknown source distribution $Q(\mathbf{x}_s)$ to an image $S_{XX}(\mathbf{x}_k)$ by using a characteristic array-specific point spread function $PSF(\mathbf{x}_s, \mathbf{x}_k)$:

$$S_{XX}(\mathbf{x}_k) = \sum_{\mathbf{x}_s} PSF(\mathbf{x}_s, \mathbf{x}_k) Q(\mathbf{x}_s), \quad (3.37)$$

for each grid point \mathbf{x}_k . This process can be imagined as adding several layers of sub-images, one layer for each noise source M , to obtain the image $S_{XX}(\mathbf{x}_k)$, which is done for every point in the grid to receive the final image S_{XX} . Each sub-image is determined by the multiplication of the source positioned at \mathbf{x}_s (the source distribution) with a transfer function that describes the influence of a monopole sound source, located at \mathbf{x}_s , on the grid point \mathbf{x}_k . Thus, the point spread function can be described as the response of the microphone array to a point source.

In an ideal case, the point spread function would return one when the array is steered directly to the grid point containing the source ($\mathbf{x}_k = \mathbf{x}_s$) and zero everywhere else ($\mathbf{x}_k \neq \mathbf{x}_s$). In practice, however, the point spread function contains values > 0 for $\mathbf{x}_k \neq \mathbf{x}_s$ due to the side lobes. Microphone array layouts are purposely designed in a way that the point spread function yields a minimum for $\mathbf{x}_k \neq \mathbf{x}_s$. The basic principle of deconvolution algorithms like the DAMAS (deconvolution algorithm for the mapping of acoustic sources) [Brooks and Humphreys, 2004] or the CLEAN-SC [Sijtsma, 2007] is the removal of the influence of the point spread function from the result of the beamformer.

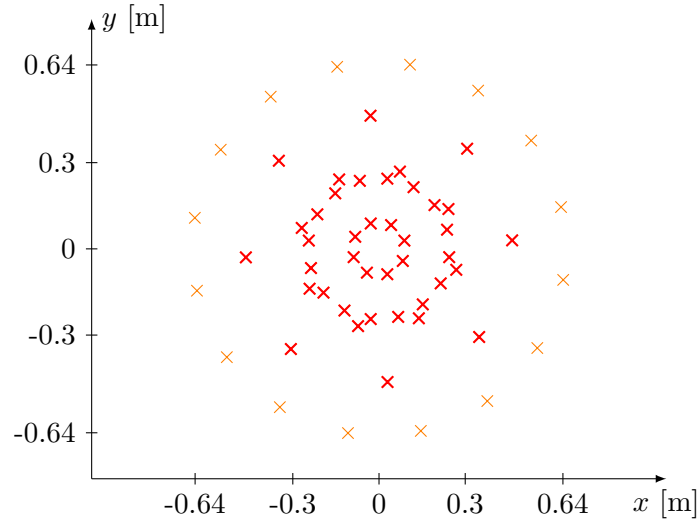


Figure 3.12: Microphone array design (red crosses indicate the position of the microphones)

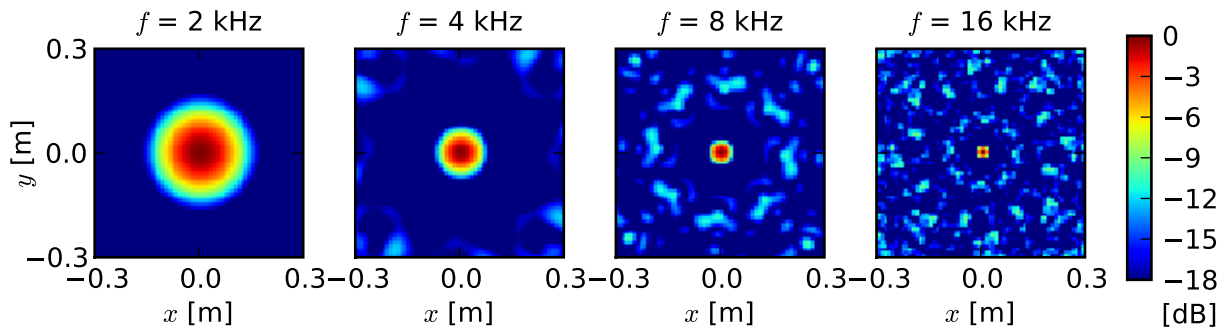


Figure 3.13: Beam pattern (directivity pattern) of the 56-microphone array at different frequencies, showing the main lobe at $x = 0$, $y = 0$ and side lobes (Note that the dynamic range of the plot is very high, 18 dB, to demonstrate the increasing number of side lobes for increasing frequency.)

3.4.2 Microphone array characteristics

This section provides a short description of the design of the microphone array used for the present study. The 56 microphones, flush-mounted into the aluminum plate, are arranged within two overlapping subgroups of 32 microphones each [Schulze et al., 2004], as can be seen in Figure 3.12. This design lead to the following approximative values for the frequency-dependent width of the main lobe at a distance of 0.68 m from the array: 0.62 m at 500 Hz, 0.29 m at 1 kHz, 0.18 m at 1.6 kHz (as the lowest third-octave band used in following analyses), 0.14 m at 2 kHz, 0.07 m at 4 kHz, 0.034 m at 8 kHz, 0.016 m at 16 kHz and 0.014 m at 20 kHz. The corresponding qualitative directivity pattern or beam pattern, including the main lobe and several side lobes, can be seen for selected frequencies in Figure 3.13.

A more recent investigation on the usability of microphone array measurement techniques for wind tunnel measurements performed by Oerlemans et al. [Oerlemans et al., 2007] paid attention particularly to the investigation of coherence loss effects. Coherence loss may occur when sound is scattered by turbulence, for example at the shear layer in an open jet wind tunnel. According to [Oerlemans et al., 2007], coherence loss effects increase with

increasing distance of the array microphones, with increasing frequency and with increasing flow speed. As a means to reduce coherence loss for the open jet wind tunnel measurements, Oerlemans et al. reduced the effective array size with increasing frequency.

To determine the influence of coherence loss in the present measurement setup, a practical approach proposed by Sijtsma and Stoker [Sijtsma and Stoker, 2004] was used. According to their report, the outer microphones of an array design are affected by coherence loss if the reduction of array size does result in increasing peak levels and decreasing noise levels, thus giving a better performance than the original, larger array. If coherence loss is not present, the reduction of array size will result in a lower resolution of the sound map. Figure 3.14 shows the comparison of two-dimensional third-octave band sound maps, derived from two different array designs:

- the original 56 microphone array, with the microphone positions as shown by both the thick red crosses and the orange crosses from Figure 3.12, and
- a reduced 40 microphone array, using only the 40 inner microphones of the original array (the respective microphone positions are indicated by the thick red crosses from Figure 3.12).

The corresponding measurement included the non-porous airfoil at zero angle of attack and maximum flow speed, $U_0 \approx 50$ m/s. The sound maps from Figure 3.14 were calculated using conventional delay-and-sum beamforming with the main diagonal of the microphone signal cross spectral matrix removed in order to reduce uncorrelated background noise (Additionally, delay-and-sum beamforming sound maps without diagonal removal have been examined, but they did not provide any extra information.). The flow direction in the maps is from left to right, the shape of the airfoil is indicated by the dotted black line.

The comparison shows that the reduction of array size did not lead to a higher resolution of the sound maps. The peak values obtained by the 40 microphone array design are only slightly higher (below 2 dB for all examined third-octave bands) than those obtained by the original array design. At very high frequencies, as for example the 20 kHz third-octave band, where coherence loss effects would be expected to have the greatest impact on the results, the differences regarding source strength, source localization and background noise are negligible. Therefore, all analyses described in the present thesis were performed using the original array design with 56 microphones.

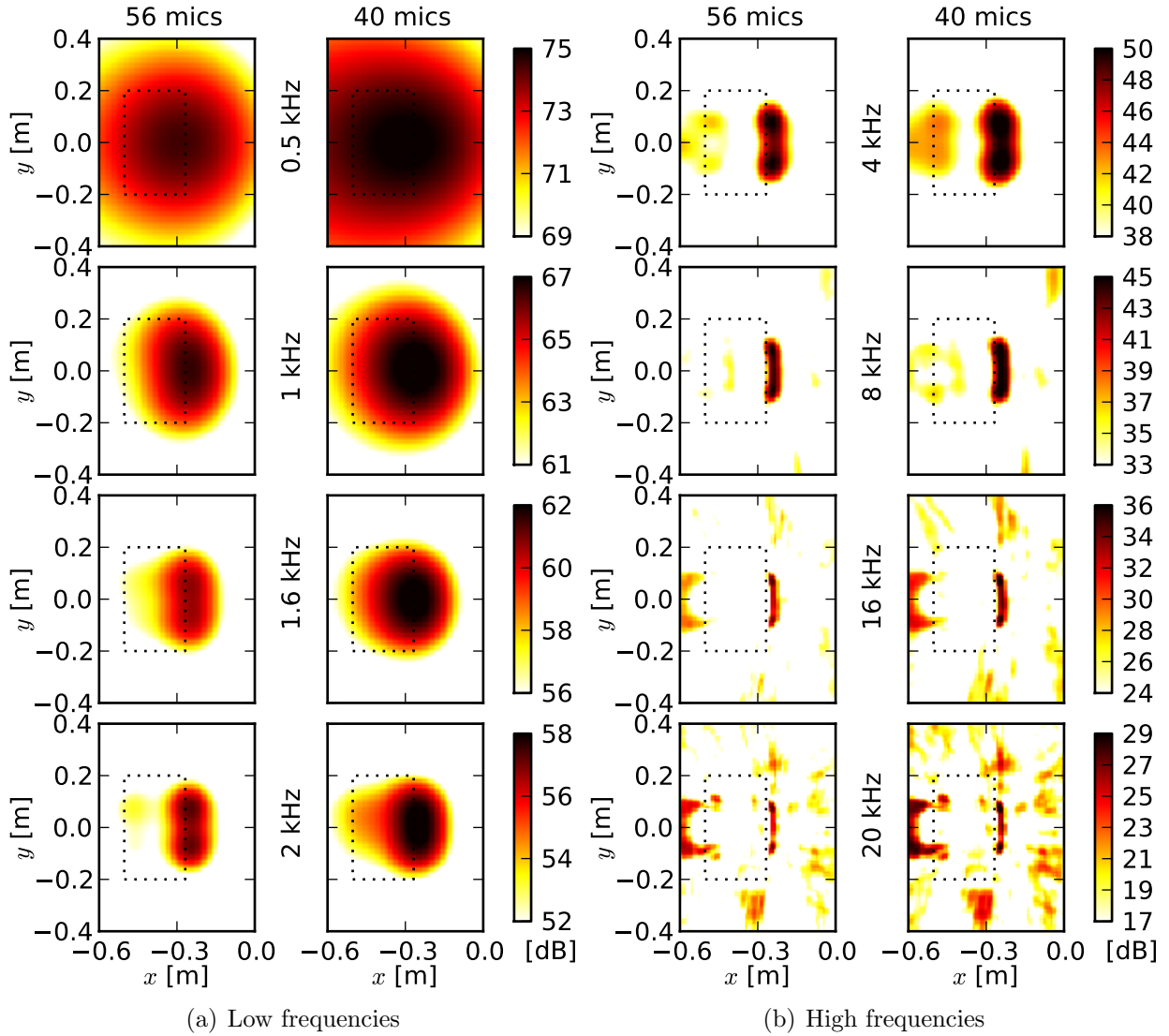


Figure 3.14: Comparison of the third-octave band sound maps calculated from all 56 microphones and from the inner 40 microphones to determine the influence of coherence loss, delay-and-sum sound maps show the noise generation at the reference airfoil at zero angle of attack and maximum flow speed, flow from left to right. (Note that the dynamic range is different between the sound maps for low and high frequencies.)

3.4.3 Two-dimensional beamforming

In a first step, the acoustic data were analyzed using two-dimensional beamforming algorithms, where sound sources are mapped onto a planar grid, which in the present case is parallel to the microphone array at a distance of $z = 0.68$ m. Many of the information given in this section were already presented in [Geyer et al., 2010a, Geyer et al., 2010b].

The raw acoustic data were transformed using a Fast Fourier Transformation (FFT) with a Hanning window and 4,096 samples per block, resulting in a frequency line spacing of 12.5 Hz. With 50 % overlap the $56^2 = 3,136$ cross spectra of all 999 blocks were calculated and averaged to obtain the cross spectral matrix. Then, a classic delay-and-sum beamforming technique [Mueller, 2002] was applied. The result of the beamforming are

two-dimensional sound maps. The maps have a total size of 0.6 m in streamwise direction and 0.8 m in spanwise direction. They include the complete airfoil and the wind tunnel nozzle as possible sound sources.

Beamforming algorithms

The data were further processed by the use of different beamforming algorithms, including advanced deconvolution algorithms. Besides the conventional delay-and-sum beamforming, the algorithms that were tested are:

1. DAMAS [Brooks and Humphreys, 2004]: This deconvolution method is based on the calculation of a theoretical point spread function for each point in the beamforming map and the subsequent solving of a set of equations for the strengths of any assumed point source in the map. It uses a special iterative Gauss-Seidel-Technique to remove the convolution of the image of the sound sources with the point spread function. The system of equations that has to be solved, given by Equation (3.37), contains as many equations as there are grid points in the scanning plane, and hence the computational effort strongly increases with increasing number of grid points or increasing grid resolution and the number of iterations. As stated in reference [Brooks and Humphreys, 2004], the performance of the DAMAS depends not only on array resolution and beamwidth (and thus frequency), but also on the resolution of source region detail.
2. CLEAN-SC [Sijtsma, 2007]: This deconvolution algorithm is based on the CLEAN algorithm as used in radioastronomy. It does not use a theoretical point spread function like the DAMAS, but the spatial coherence between sources in the sound map and their side lobes. The algorithm includes the following steps: An unprocessed sound map is obtained by applying conventional beamforming as given by Equation (3.36) (the “dirty” map) and the peak location is searched in this map. Then, coherent sources are subtracted from the map and replaced by a “clean” beam (without side lobes) at the peak location (often weighted by a factor between 0 and 1, the so-called loop gain). These steps are iteratively repeated until a stop criterion is reached. The resulting map is then given by the sum of all maps consisting of the weighted source components.
3. OB (orthogonal beamforming) [Sarradj, 2010]: This method is based on an eigenvalue-decomposition of the cross spectral matrix of the microphone signals \mathbf{G} into a matrix containing the positive real-valued eigenvalues and a matrix containing the corresponding eigenvectors. Each eigenvalue represents one noise source within the sound map. The OB uses the eigenvalues to estimate the absolute source levels, from the strongest noise source within the map to the weakest, while the source location is derived by assigning the eigenvalues to the location of the highest peak in the beamforming sound map constructed for the corresponding eigenvector. As is often done for conventional delay-and-sum beamforming, the main diagonal of the reduced cross spectral matrices for each eigenvalue may be removed to reduce uncorrelated noise.

Each of the beamforming algorithms tested has its own advantages and disadvantages. On the one hand, the DAMAS is known to produce good results especially at low fre-

quencies, where it correctly localizes noise sources. As described by Shannon and Morris [Shannon and Morris, 2008], one advantage of the DAMAS is that the size of the source contribution areas is reduced and side lobe effects are eliminated. This is due to the assumption underlying the DAMAS algorithm, that sources are taken as being point sources located at the corresponding grid points. On the other hand, the assumption that the actual directivity pattern of a point source is adequately described by the theoretical point spread function is also a limitation of the algorithm. Additionally, DAMAS is computationally very expensive, resulting in high demands regarding the computer hardware and long calculation durations. In this context, depending on the concrete measurement task, the dependence of the DAMAS performance on the resolution of source region detail may also be disadvantageous, since more complicated noise source distributions require more iterations than a simpler source distribution.

The CLEAN-SC algorithm provides the advantage that the use of a theoretical point spread function is avoided, and hence the underlying assumption that the sound field is composed of a number of distinct point sources (and the corresponding uniform source directivity). It is computationally faster than the DAMAS algorithm, partly due to the noticeably smaller number of iterations necessary. Sijtsma [Sijtsma, 2007] states that the total processing time is only about twice as long as for the conventional (delay-and-sum) beamforming in practice.

The OB has the advantage that the sum of all source strengths within the map is never greater than the sum of the microphone autospectra as the effectively measured sound pressure level. Hence, the acoustic source strengths are not overestimated and the results of the OB algorithm remain physically correct. This is due to the working principle of the algorithm as briefly described above, which consists of an eigenvalue-decomposition of the cross spectral matrix of the N microphone signals that results in a reduced number of point sources in the map less than or equal to the number of microphones. The respective source strengths are directly derived from the corresponding eigenvalues. Another advantage of the OB algorithm is that it is relatively fast compared to other deconvolution algorithms. This is especially the case since very often the most important noise sources are correctly estimated by using a number of eigenvalues that is smaller than the number of microphones, due to the fact that the first eigenvalues represent the strongest sources and the last eigenvalues represent sources that only marginally contribute to the overall noise level.

Determination of the integration sector

To obtain acoustic spectra from the sound maps, the sound pressure contributions within chosen regions of interest are integrated. This integration over a selected sector yields the sound pressure level generated by the sound sources that are positioned within this sector as measured at the array center.

In order to examine the noise generated at the trailing edge of the airfoils only, a sector was chosen that contains the part of the airfoil trailing edge located within the core of the open jet. The leading edge of the airfoil and the impingement region of the shear layers were excluded from the sector, which has a chordwise extent of 0.15 m and a spanwise extent of 0.12 m (see Figure 3.15). According to theory [Schulz-Hausmann, 1985], the length of the core jet of an open jet wind tunnel is approximately five times the nozzle diameter D , resulting in a length of 1 m in the present case. Thus, at the position of the trailing edge,

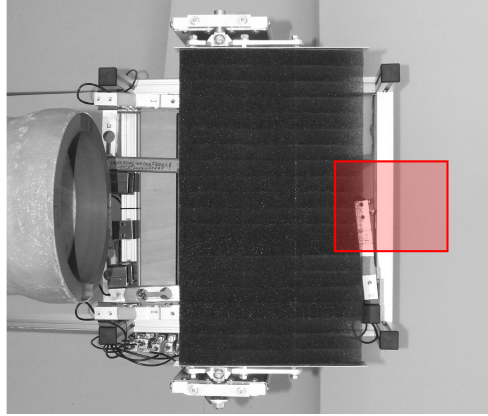


Figure 3.15: Schematic representation of the two-dimensional sector used for the integration of the trailing edge noise sources

approximately 0.285 m from the nozzle exit, the core jet has an estimated width of 0.14 m. According to Goldstein [Goldstein, 1976], the length of the core jet at subsonic flow speeds is about four nozzle diameters, which would lead to a width of the jet of approximately 0.13 m at the position of the airfoil trailing edge. These values are supported by the measured velocity profiles and turbulence intensities in front of the nozzle, as shown in Figures 3.6(a) and 3.6(b). They confirm that the chosen trailing edge sector is located completely within the core jet.

Comparison of different beamforming algorithms

Figure 3.16 and 3.17 show the comparison of octave band sound maps obtained from different two-dimensional beamforming algorithms, exemplarily for the non-porous airfoil and one porous airfoil, respectively. The grid resolution is 0.01 m for the delay-and-sum beamforming, the orthogonal beamforming and the CLEAN-SC, while for the DAMAS (with 100 iterations) a grid resolution of 0.02 m was used to save computation time.

It can be seen that the three advanced beamforming algorithms (DAMAS, CLEAN-SC and OB) deliver comparable results regarding the source localization, but some differences regarding the source strength. For the non-porous airfoil in Figure 3.16, the differences between the results from the three advanced algorithms are relatively small and negligible. For the porous airfoil in Figure 3.17, the differences are more noticeable, especially at high frequencies. In the 16 kHz octave band, for example, the DAMAS locates sound sources with source strengths above those of the sources determined using the OB algorithm. The corresponding CLEAN-SC result is lower than that of the OB and, given the chosen dynamic range of the plot, not even visible in the sound map.

This trend has been detected for most of the porous airfoils: The DAMAS produces good results at low frequencies, while at high frequencies it tends to overestimate the emitted noise for some of the porous airfoils, the reason for which is not completely clear. However, the iterative procedure using the Gauss-Seidel technique is not limited to a maximum result and convergence is not implicit. The results obtained by the CLEAN-SC algorithm at low frequencies are slightly above those of the other algorithms for some airfoils, while at high frequencies the CLEAN-SC occasionally fails to locate noise sources at the trailing edge

at all. Apart from very low frequencies, the orthogonal beamforming gives an overall good performance.

The spectra given in Figure 3.18(a) through 3.18(d) support these observations. The results represent the sound pressure levels as would be measured in the microphone array center. Figure 3.18(a) shows the comparison of the spectra obtained for different airfoils by integration over the trailing edge sector shown in Figure 3.15. Figure 3.18(b) through 3.18(d) present the comparisons between the spectra obtained by the three advanced beamforming algorithms, when integrated over the complete source region defined by the grid, with the averaged sum of the autospectra of all 56 microphones divided by the number of microphones. The calculation of the averaged sum of the microphone autospectra includes the weighting of the signals from each microphone with the distance between the trailing edge at midspan and the individual microphone location, normalized to the distance between trailing edge and array center. The resulting arithmetic mean of the microphone autospectra is consistent with the maximum noise physically measured by the microphones. Hence, the beamforming algorithms should not produce spectral results that exceed this averaged microphone autospectrum.

The DAMAS may produce noise levels above the averaged sum of the microphone autospectra, especially at high frequencies, while the CLEAN-SC results may be noticeably lower than the autospectra in this range of frequencies. The OB algorithm delivers results close to the microphone autospectra. As would be expected, the OB results improve with an increasing number of eigenvalues used.

The good performance of the DAMAS at low frequencies and the advantages of the OB at medium and high frequencies lead to the decision to use the DAMAS at frequencies below the 4 kHz third-octave band, corresponding to a frequency limit of 3,549 Hz, and the OB (using 24 eigenvalues) for frequencies above this limit for the two-dimensional beamforming.

As mentioned above, the spatial resolution of the DAMAS was set to 0.02 m, resulting in 1,271 grid points for the chosen map, while the resolution of the OB was set to 0.01 m and thus 4,941 grid points. This is due to the otherwise exceeding computational cost for the DAMAS. The diagonal of the cross-spectral-matrix was removed for the OB. The distance of the array focus plane was adjusted to the trailing edge of the airfoils. At 0° angle of attack it was 0.68 m, as indicated in Figure 3.9, while for angles of attack not equal to 0° the distance was corrected accordingly.

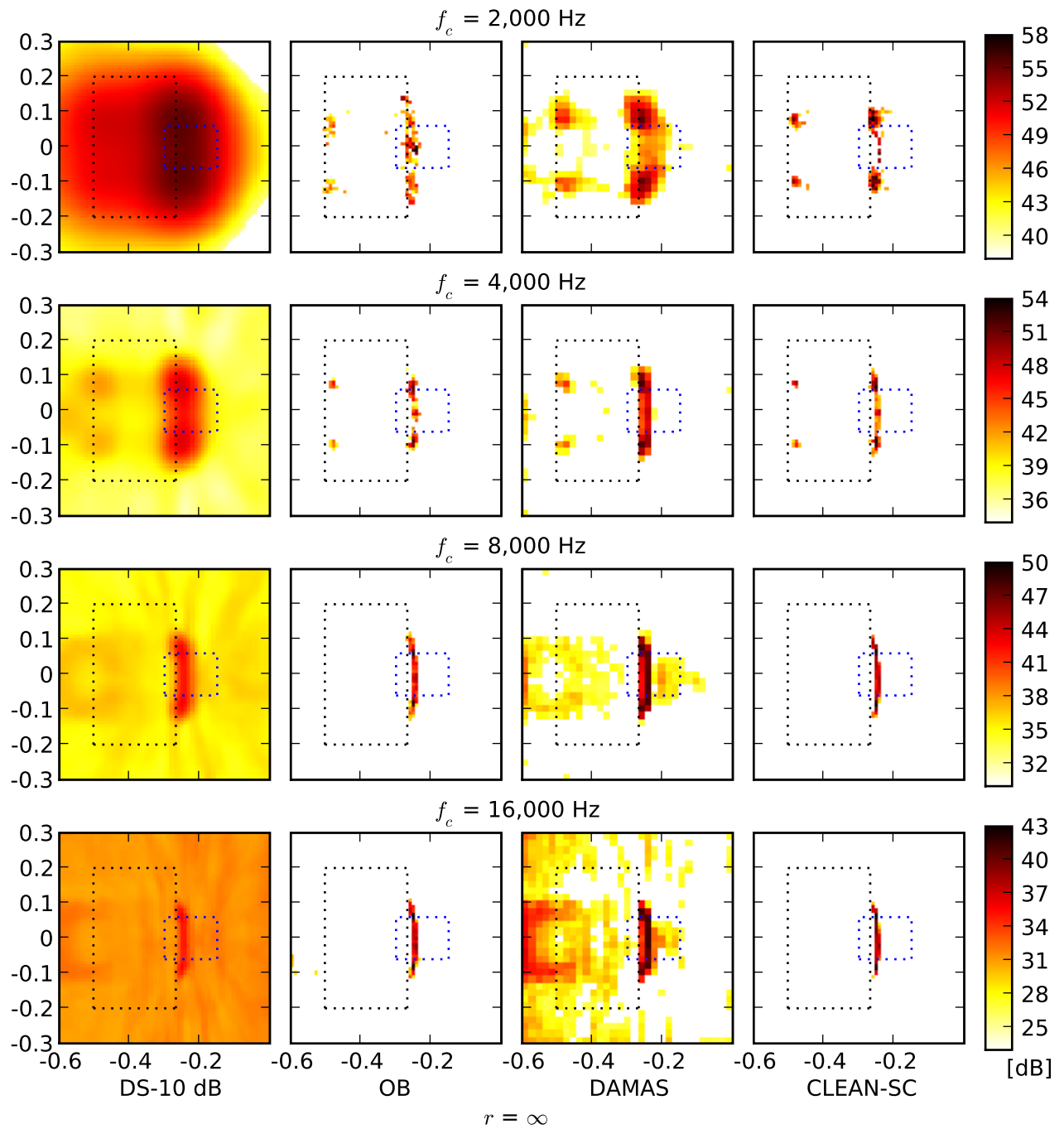


Figure 3.16: Comparison of sound maps obtained by using different two-dimensional beamforming algorithms (from left to right: delay-and-sum, orthogonal beamforming, DAMAS, CLEAN-SC) for the non-porous reference airfoil, flow speed $U_0 = 50$ m/s, angle of attack $\alpha = 0^\circ$, octave band sound maps, center frequencies indicated (dotted black line: airfoil, dotted blue line: integration sector).

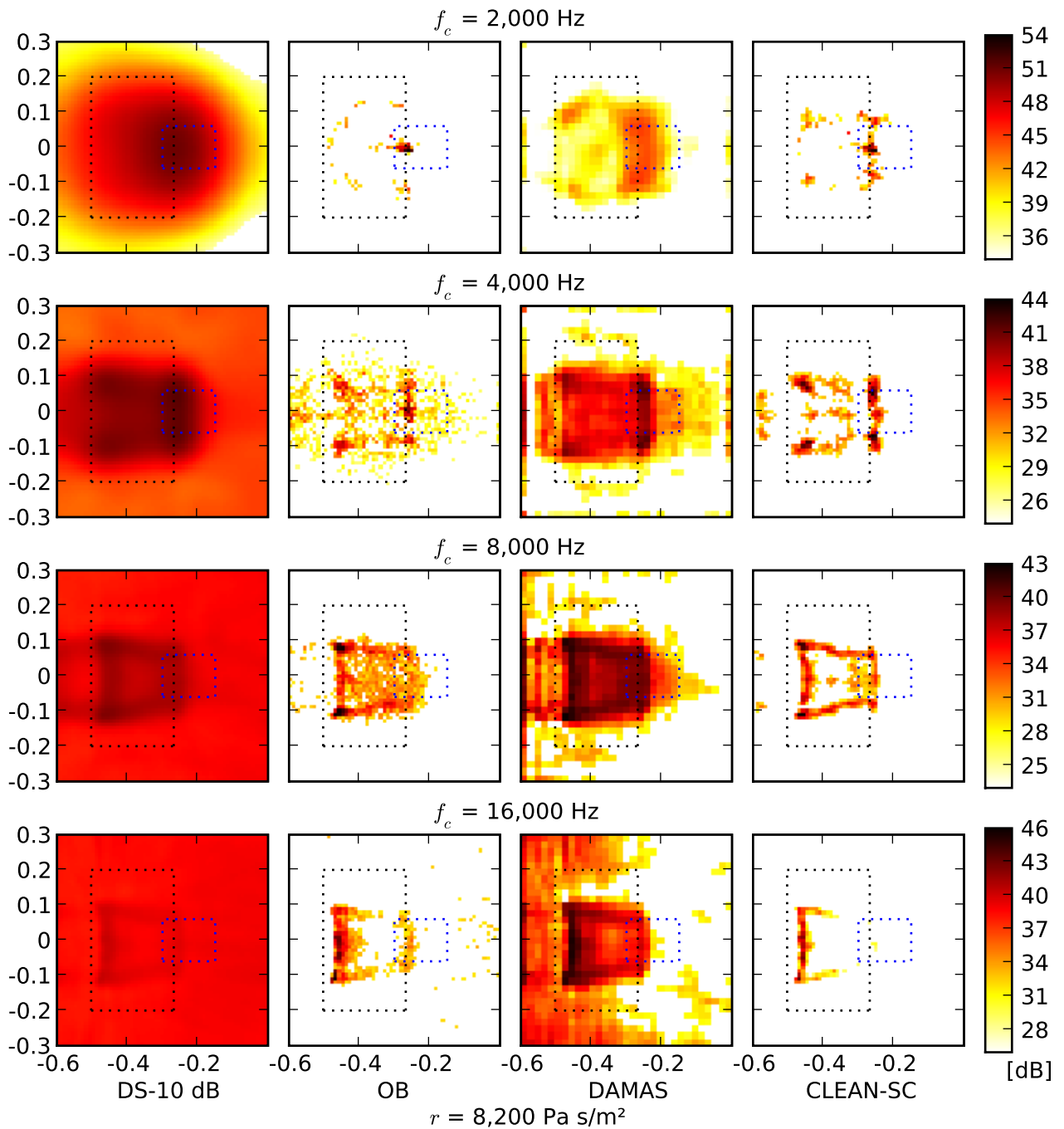
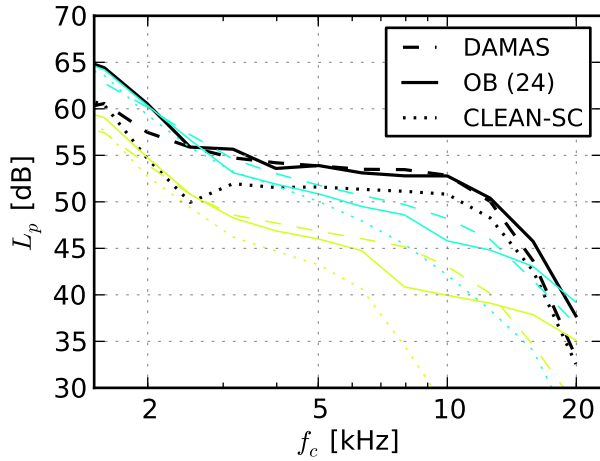
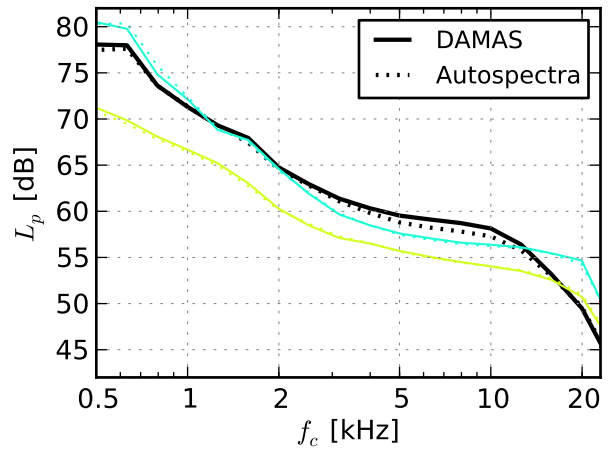


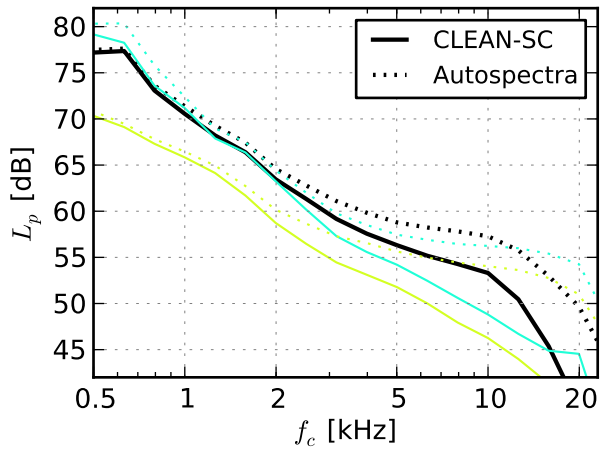
Figure 3.17: Comparison of sound maps obtained by using different two-dimensional beamforming algorithms (from left to right: delay-and-sum, orthogonal beamforming, DAMAS, CLEAN-SC) for one porous airfoil (Recemat, $r = 8,200 \text{ Pa s/m}^2$), flow speed $U_0 = 50 \text{ m/s}$, angle of attack $\alpha = 0^\circ$, octave band sound maps, center frequencies indicated (dotted black line: airfoil, dotted blue line: integration sector).



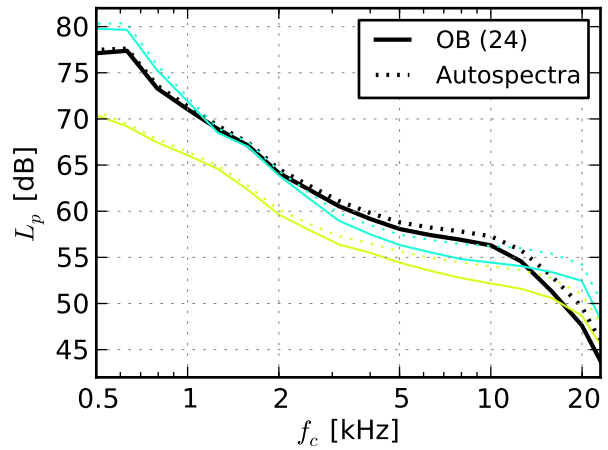
(a) Comparison of Orthogonal beamforming (OB), DAMAS and CLEAN-SC, integrated over the trailing edge sector shown in Figure 3.15



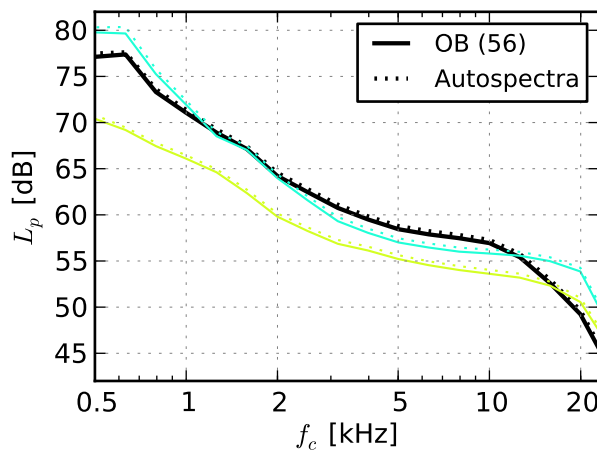
(b) Comparison of DAMAS, integrated over the complete beamforming map, and microphone autospectra



(c) Comparison of CLEAN-SC, integrated over the complete beamforming map, and microphone autospectra



(d) Comparison of two-dimensional OB (based on 24 eigenvalues), integrated over the complete beamforming map, and microphone autospectra



(e) Comparison of OB (based on all 56 eigenvalues), integrated over the complete beamforming map, and microphone autospectra

Figure 3.18: Comparison of different two-dimensional beamforming algorithms for three airfoils ($r = \infty$, 40,100, 9,800 Pa s/m²), flow speed $U_0 = 50$ m/s, angle of attack $\alpha = 0^\circ$

3.4.4 Three-dimensional beamforming

When two-dimensional beamforming is applied, the noise sources are mapped onto a two-dimensional plane only, providing a poor depth resolution and possibly leading to erroneous results when deconvolution algorithms are used. The availability of advanced high performance computer clusters makes the application of three-dimensional beamforming feasible. Whereas for the two-dimensional beamforming a two-dimensional grid, in the present case positioned in the array focus plane (x - y -plane), is virtually scanned with the microphone array, for the three-dimensional beamforming a three-dimensional grid is used instead. Thus, the result is not mapped onto a plane, but onto a three-dimensional source region. This provides the advantage that sources, which are positioned in front of or behind the two-dimensional mapping plane, are located more accurately. If deconvolution algorithms are performed on a three-dimensional grid, then the underlying assumption is that possible monopole noise sources may be situated at any point of that grid.

For the application of three-dimensional beamforming, the steering vector \mathbf{h} is especially important. In general, different steering vectors are available in the literature, leading to differences in source location and source strength. A recent study focuses on the comparison of these steering vectors and their usability for aeroacoustic investigations [Sarradj, 2011]. In the present work, the formulation of the steering vector was chosen that was found to deliver the best results regarding source location, as for example used in [Dougherty, 2002, Suzuki, 2010].

As an example for three-dimensional beamforming, Figure 3.19 presents the three-dimensional sound map obtained for the non-porous reference airfoil at a flow speed of 50 m/s and zero angle of attack. The main noise sources at the non-porous airfoil are clearly visible: Two major noise sources are located at the position where the shear layers interact with the trailing edge. The noise source of interest in the present study is located in between these two sources, at the position where the turbulent boundary layer inside the core jet interacts with the trailing edge of the airfoil.

Selection of the beamforming algorithm

Three-dimensional beamforming implies the calculation of a multitude of complex mathematical systems of equations. Therefore, large quantities of disk space and fast connections between single processors of the cluster and disk space are required. As one consequence of this high computational cost, the calculation of the three-dimensional DAMAS beamforming algorithm is not effective any more for the present experimental study.

To give an example, a test of the three-dimensional calculation with the same resolution and accuracy as for the two-dimensional calculation described above was performed (DAMAS for frequencies below the 4 kHz third-octave band, grid increment 0.02 m, 100 iterations and orthogonal beamforming for the higher frequency range starting with the 4 kHz third-octave band, grid increment 0.01 m). In the third dimension, along the z -axis, the grid had an extent of only 0.12 m. In the case of the DAMAS beamforming algorithm, with a grid increment of 0.02 m, this lead to a total of 8,897 grid points, seven times the number used for the two-dimensional beamforming. This calculation generated a point spread function with a size of approximately 127.4 GByte, while the cache files for each measurement had a size of several GByte. However, the storage of these data is not a problem, as is the fact

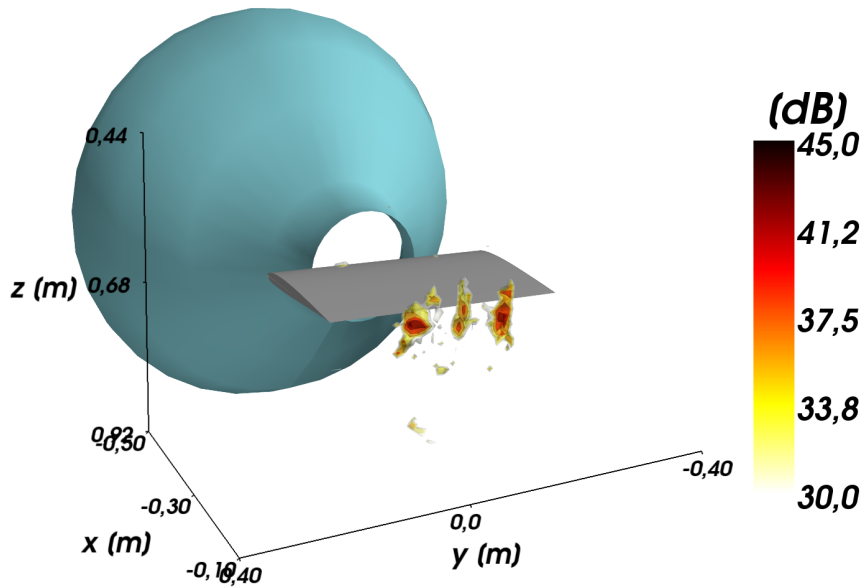


Figure 3.19: Example of a three-dimensional beamforming result: 4 kHz octave band sound map of the non-porous airfoil at zero angle of attack and maximum flow speed (orthogonal beamforming)

that for each iteration the corresponding data have to be loaded to the main memory and the complex system of equations has to be solved. Additionally, it has to be considered that a vertical dimension of 0.12 m of the three-dimensional grid is relatively small, a more realistic grid would most probably have an extent of more than 0.06 m above and below the trailing edge.

However, to at least include an approximative analysis of the performance of the three-dimensional DAMAS algorithm, despite the large computational cost necessary, the results of the DAMAS for a reduced grid with a more coarse resolution are given in form of the power spectral density PSD re $4 \cdot 10^{-10}$ Pa²/Hz for only a small range of frequencies. The three-dimensional grid used for these comparisons has a reduced size of $-0.55 \text{ m} < x < -0.1 \text{ m}$, $-0.25 \text{ m} < y < 0.25 \text{ m}$ and $0.44 \text{ m} < z < 0.80 \text{ m}$ with an increment of 0.02 m for the DAMAS and 0.01 m for the orthogonal beamforming and the CLEAN-SC, but it still contains all potential noise sources. This includes sources located at the airfoil or the wind tunnel nozzle. Figure 3.20(a) shows the resulting power spectral densities of all three beamforming algorithms for a range of low frequencies, Figure 3.20(b) shows the results for medium frequencies and Figure 3.20(c) for high frequencies. The results were obtained through an integration over the complete three-dimensional source region, and hence should contain all noise sources detected. The results represent the sound pressure levels as would be measured at the microphone array center.

Basically, the same conclusions as for the comparison of the different beamforming algorithms in the two-dimensional case, shown in Figure (3.18), can be drawn: At low frequencies the differences between the results from the three algorithms are relatively small (in the order of 3 dB), especially for the OB and the DAMAS. All three curves show a similar spectral shape. Both OB and CLEAN-SC deliver results below the averaged sum of the weighted microphone autospectra, but while the OB results are only slightly below the autospectra, with differences below 1 dB, the CLEAN-SC results are about 2 to 3 dB lower. The power spectral densities calculated using the DAMAS algorithm are slightly

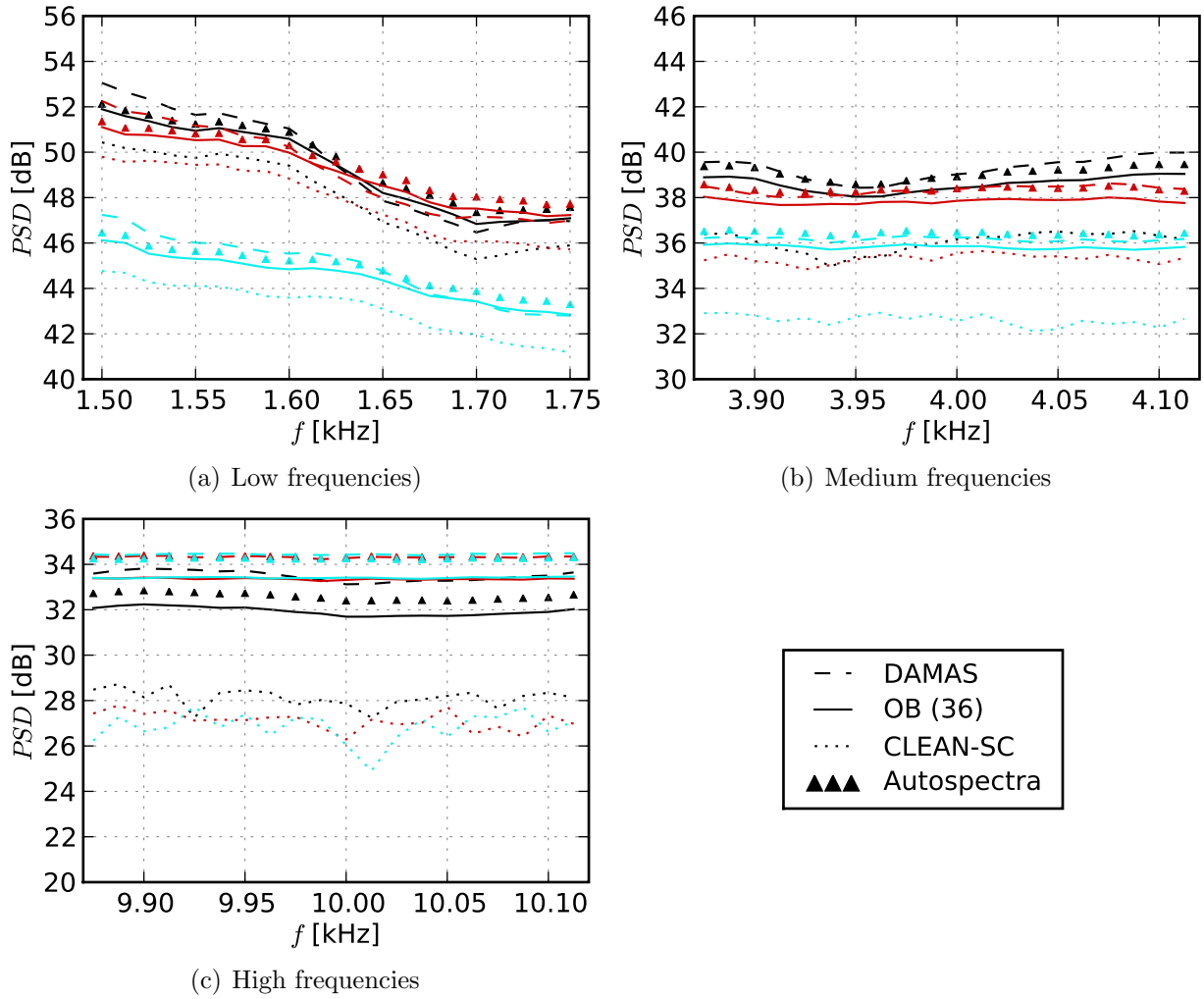


Figure 3.20: Comparison of the power spectral density re $4 \cdot 10^{-10} \text{ Pa}^2/\text{Hz}$ for all three beamforming algorithms and the weighted sum of the microphone autospectra, integrated over the complete three-dimensional grid, for three airfoils ($r = \infty$, \blacksquare 316,500, \blacksquare 8,200 Pa s/m^2), flow speed $U_0 = 50 \text{ m/s}$, angle of attack $\alpha = 0^\circ$

higher than the microphone autospectra at low frequencies, which is not physically correct. At medium frequencies, the results of the DAMAS and the OB are nearly equal, both giving an amplitude comparable to the microphone autospectra. The results obtained by the CLEAN-SC are noticeably below the autospectra, with a difference in the order of 4 dB. This trend continues for high frequencies, at which the CLEAN-SC results are up to 5 dB below the microphone autospectra. The power spectral density calculated by the orthogonal beamforming algorithm is only slightly below the microphone autospectra (less than 1 dB for the non-porous airfoil and less than 2 dB for the two porous airfoils). The DAMAS delivers results that exceed the microphone autospectra in case of the non-porous airfoil, but which are approximately equal to the microphone autospectra for the porous airfoils.

In general, the DAMAS produces good results but tends to deliver power spectral density levels that exceed the microphone autospectra, and hence the physically measured noise, by up to about 2 dB depending on the frequency. However, the computational cost required to apply the DAMAS on a three-dimensional source region with a resolution similar to that

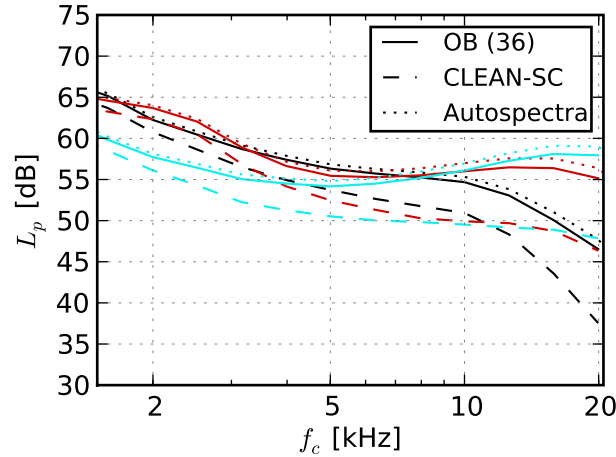


Figure 3.21: Comparison of three-dimensional beamforming algorithms: orthogonal beamforming (OB), CLEAN-SC and the weighted sum of the microphone autospectra, integrated over the complete three-dimensional grid, for three different airfoils ($r = \infty$, 316,500, 8,200 Pa s/m²), flow speed $U_0 = 50$ m/s, angle of attack $\alpha = 0^\circ$

which is possible for the OB and CLEAN-SC is too high to be feasible in the present study. Therefore, only the CLEAN-SC beamforming algorithm and the orthogonal beamforming were finally considered to be used for the three-dimensional beamforming of the measured data.

To evaluate the performance of both algorithms, Figure 3.21 shows the comparison between the orthogonal beamforming and the CLEAN-SC algorithm. The dimension of the three-dimensional grid in the $x - y$ -plane is the same as for the two-dimensional beamforming ($-0.6 \text{ m} < x < 0 \text{ m}$, $-0.4 \text{ m} < y < 0.4 \text{ m}$) and the dimension in the vertical (z -) direction is from 0.44 m to 0.92 m (0.24 m above and below the airfoil trailing edge). The grid increment in each direction is 0.01 m, leading to a total of 242,109 grid points.

The third-octave band sound pressure levels shown in Figure 3.21 are the result of the integration over the complete three-dimensional source region, and should therefore contain all the noise sources (airfoil, nozzle). The results again represent the sound pressure levels as measured at the microphone array center. Similar to the procedure used for the evaluation of the two-dimensional beamforming algorithms shown in Figure 3.18(b) through 3.18(e), the results are compared to the averaged sum of the weighted microphone autospectra. The three-dimensional orthogonal beamforming delivers results that are only slightly below the microphone autospectra, while the sound pressure levels obtained using CLEAN-SC are clearly below the microphone autospectra. At low frequencies, the difference between CLEAN-SC and the microphone autospectra is only small, in the order of 2 dB, but with increasing frequency the difference increases. At a third-octave band center frequency of 10 kHz the difference is about 4 dB for the non-porous airfoil and 7 to 8 dB for the porous airfoils, at 20 kHz the difference is nearly 10 dB for all airfoils. This indicates that the CLEAN-SC either fails to deliver correct amplitudes of the located noise sources or fails to locate noise sources at all at high frequencies.

To further analyze the performance of the CLEAN-SC beamforming algorithm and the orthogonal beamforming algorithm, three-dimensional beamforming results (three-dimensional sound maps) are compared for different airfoils at maximum flow speed. The chosen grid is consistent to that used for the comparison shown in Figure 3.21.

CLEAN-SC sound maps for three airfoils (the non-porous airfoil, $r = \infty$, the Porex airfoil, $r = 316,500 \text{ Pa s/m}^2$ and the Recemat airfoil, $r = 8,200 \text{ Pa s/m}^2$) are presented in Figure 3.22 for the 4 kHz and the 8 kHz octave band, while Figure 3.23 shows the orthogonal beamforming sound maps for the same airfoils and the same octave bands. The maximum value in each sound map corresponds to the maximum noise source in the corresponding map, while the dynamic range of the plots is constant (15 dB) in each map.

It can be seen from Figure 3.22 that the CLEAN-SC algorithm delivers physically meaningful noise source locations for all three airfoils. Two major noise sources are located at the positions where the shear layer of the core jet interferes with the airfoil trailing edge. A third main noise source, the noise source of interest in the present study, is located laterally between these two sources, where the turbulent boundary layer (inside the core jet and hence between the two shear layer noise sources) interacts with the airfoil trailing edge. For some of the porous airfoils, additional weaker sources are located above the airfoil leading edge. The sound maps give evidence that the trailing edge noise of the porous airfoils is clearly below that of the reference airfoil. Especially at higher frequencies, the noise source due to the interaction of the turbulent boundary layer with the trailing edge is much weaker than the sources caused by the shear layer - trailing edge interaction. For the porous airfoil made of Recemat, the 8 kHz octave band sound map from Figure 3.22(f) shows that the examined noise source is at least 15 dB below the maximum noise level in the map.

Since the maximum noise level of the porous airfoil made of Recemat is noticeably lower than that of the reference airfoil, the constant dynamic range of the maps leads to the fact that for this porous airfoil additional, weaker noise sources are visible above the airfoil (see Figure 3.22(e)). These sources are not visible for the non-porous airfoil, due to the high noise level of the dominating sources at the trailing edge. The sources above the Recemat airfoil are either existing sources that are falsely located by the beamforming algorithm, or noise sources that are caused by other source mechanisms. It is not likely that these sources are caused by background noise since no such background noise sources were noticed during the measurements. Since the sources are located outside of the wind tunnel jet, it also cannot be assumed that they are artefacts of jet noise.

Comparing the three-dimensional CLEAN-SC beamforming results from Figure 3.22 to the orthogonal beamforming results from Figure 3.23, it becomes evident that the maximum amplitudes are about 1 dB higher for the orthogonal beamforming in several cases. The orthogonal beamforming algorithm correctly locates the main noise sources at the trailing edge of the airfoils, where they would be assumed to be located for the non-porous airfoil as well as for the porous airfoils. For the porous airfoil made of Recemat (Figure 3.23(e) and 3.23(f)) and, to a lesser extent, also for the airfoil made of Porex at the 8 kHz octave band (Figure 3.23(d)), the orthogonal beamforming additionally locates weaker noise sources above the airfoil trailing edge. Under the assumption that these sources are existent, but are not caused by the jet and are no plain background noise sources, as discussed in the previous paragraph, the sources indicate that another, less powerful noise source mechanism than the turbulent boundary layer - trailing edge mechanism may be present for the porous airfoils. No such mechanism seems to exist for the non-porous airfoil.

Regarding the three-dimensional sound maps obtained for the airfoil made of Porex and at the non-porous airfoil for the 4 kHz octave band, it is visible that in the orthogonal beamforming sound maps the three noise sources at the trailing edge, two from the shear

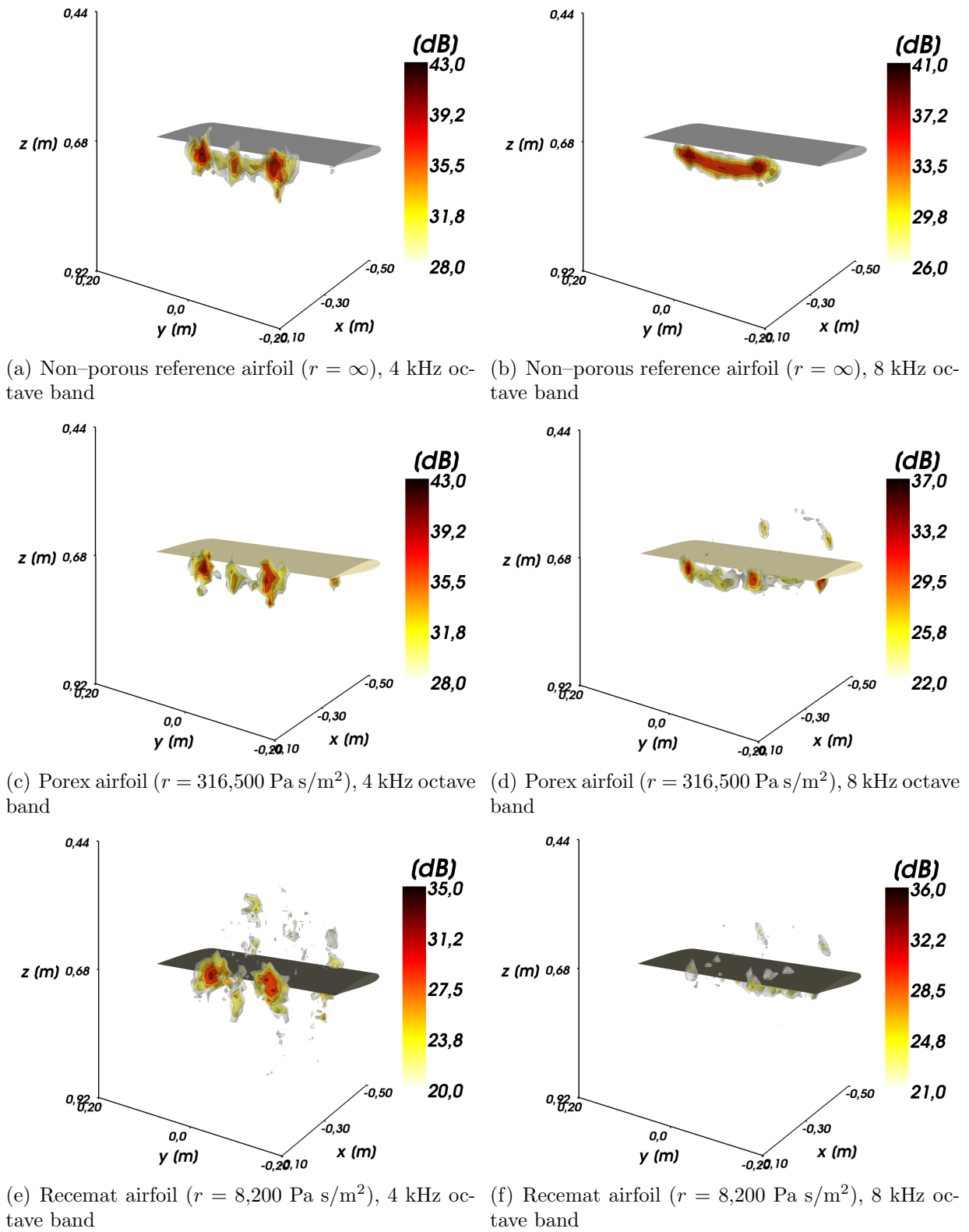


Figure 3.22: Sample three-dimensional beamforming results for three airfoils at maximum flow speed, CLEAN-SC

layer and the center source from the interaction of the turbulent boundary layer with the trailing edge, are separated more clearly than in the corresponding CLEAN–SC sound maps.

The results of the comparison of the three–dimensional sound maps from Figure 3.22 and 3.23 show that the CLEAN–SC delivers convincing sound maps with physically meaningful source locations. Both the CLEAN–SC and the orthogonal beamforming sound maps in some cases contain noise sources that are positioned above the trailing edge. These sources, which are assumed to be caused by another noise source mechanism than the turbulent boundary layer - trailing edge interaction, are more noticeable in the orthogonal beamforming sound maps.

Presently, it is not clear which mechanism causes these additional, weaker noise sources. The location of the sources above the airfoil, and even outside of the core jet, make it difficult to interpret this effect. Since no such noise sources are visible in the sound maps of the non–porous airfoil, it is unlikely that the effect is related to the three–dimensional beamforming algorithms, but it cannot be completely excluded. However, further investigations are necessary to analyze these noise sources and to draw conclusions on the underlying physical noise source mechanism and a potential involvement of the three–dimensional beamforming algorithms.

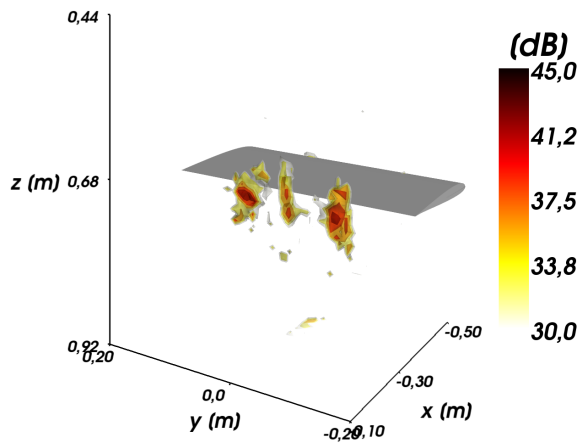
To decide which algorithm to use for the three–dimensional beamforming, it has to be considered that the results of the different beamforming algorithms, integrated over the complete source region, in comparison to the weighted sum of the microphone autospectra, as presented in Figure 3.21, showed that the CLEAN–SC fails to locate noise sources. This effect, which increases with increasing frequency, is much stronger for the porous airfoils than for the non–porous reference airfoil. Thus, it can be assumed that the use of the CLEAN–SC algorithm would yield lower sound pressure levels for the porous airfoils in relation to the reference airfoil, and hence would give a trailing edge noise reduction that could not be achieved in practice.

Finally, the facts that the three–dimensional DAMAS calculation is computationally too expensive and that the CLEAN–SC either fails to locate noise sources or delivers source strengths which are too low, especially at high frequencies, lead to the decision to use the orthogonal beamforming algorithm, based on 36 eigenvalues, for the three–dimensional beamforming of the measured data.

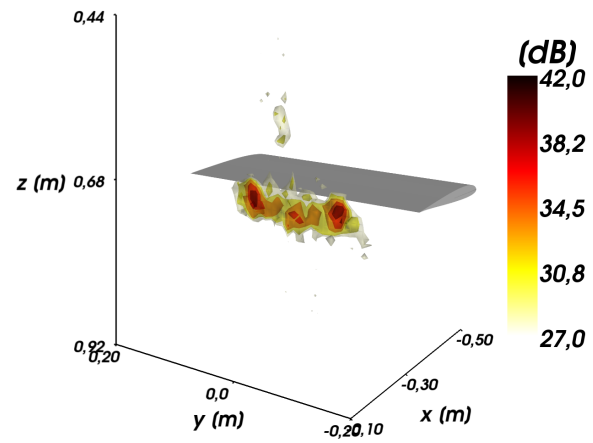
An additional comparison of the performance of the three beamforming algorithms, DAMAS, OB, and CLEAN–SC, for both a simulated point source and a single loudspeaker setup is given in Appendix D. This comparison further encourages the decision to use the orthogonal beamforming algorithm, although the differences between the results obtained by the different algorithms are smaller for the single point sources than for some of the porous airfoils.

Determination of the integration sector

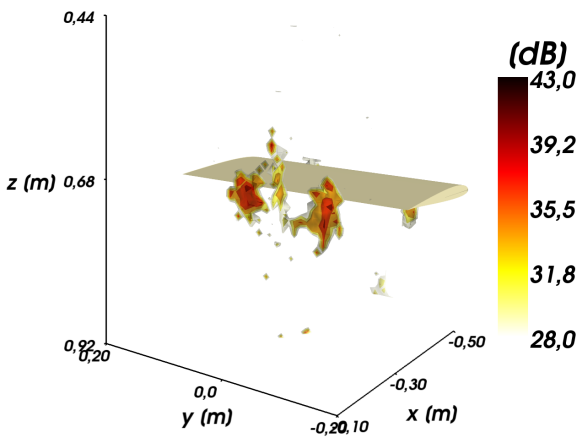
Similar to the procedure for two–dimensional beamforming, in order to obtain trailing edge noise spectra, the corresponding sound pressure contributions have to be integrated over a chosen region in the beamforming sound maps. For three–dimensional beamforming, this involves the integration over a three–dimensional volume rather than the integration over



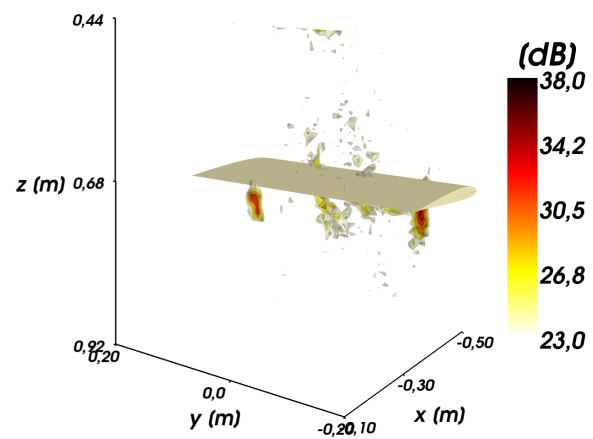
(a) Non-porous reference airfoil ($r = \infty$), 4 kHz octave band



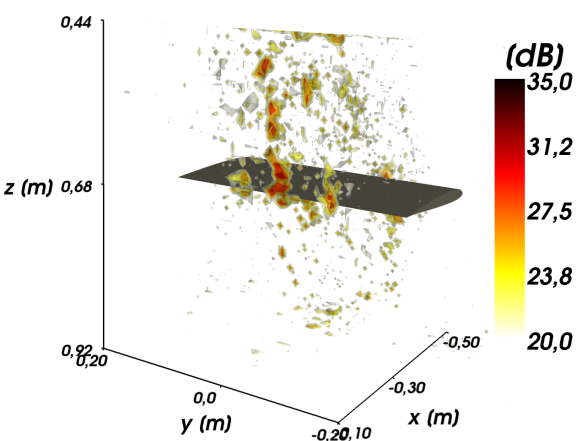
(b) Non-porous reference airfoil ($r = \infty$), 8 kHz octave band



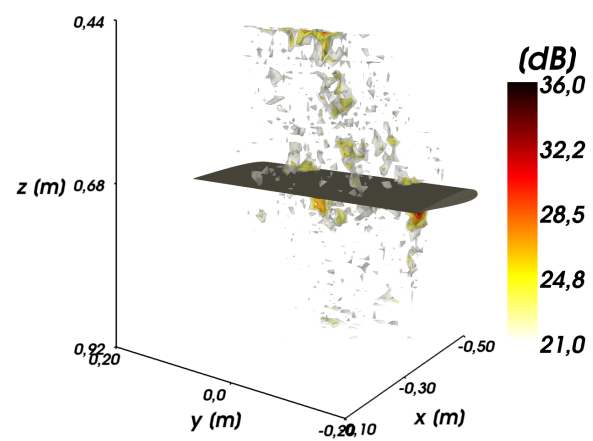
(c) Porex airfoil ($r = 316,500 \text{ Pa s/m}^2$), 4 kHz octave band



(d) Porex airfoil ($r = 316,500 \text{ Pa s/m}^2$), 8 kHz octave band



(e) Recemat airfoil ($r = 8,200 \text{ Pa s/m}^2$), 4 kHz octave band



(f) Recemat airfoil ($r = 8,200 \text{ Pa s/m}^2$), 8 kHz octave band

Figure 3.23: Sample three-dimensional beamforming results for three airfoils at maximum flow speed, orthogonal beamforming (utilizing 36 eigenvalues)

a two-dimensional area in the map. The corresponding sector has to contain the noise sources due to the interaction of the turbulent boundary layer with the trailing edge, but no other sources as for example the wind tunnel nozzle, the airfoil leading edge or the regions where the shear layers interact with the trailing edge. To this end, a sector was chosen that has the same extent in the streamwise direction and the lateral direction as for the two-dimensional beamforming: $-0.30 \text{ m} < x < -0.15 \text{ m}$ and $-0.06 \text{ m} < y < 0.06 \text{ m}$ (see Figure 3.15).

To determine the appropriate vertical extent of the trailing edge sector, Figure 3.24 shows the comparison of sound pressure level spectra obtained by integration over sectors with the same base area, but different heights Δz . For the purpose of comparison, the figures additionally contain the sound pressure level spectra calculated using two-dimensional beamforming algorithms as presented in [Geyer et al., 2010a].

Figure 3.24(a) shows that the effect of the sector height on the third-octave band sound pressure level of the non-porous airfoil is relatively small. The difference between the results from the sector with the smallest vertical extent included in the figure ($\Delta z = 0.12 \text{ m}$) and the sector whose vertical extent is equal to the vertical extent of the grid ($\Delta z = 0.48 \text{ m}$) is in the order of 1 dB at medium and high frequencies. The difference is larger at low frequencies, up to approximately 5 dB for the 1.6 kHz third-octave band. For the porous airfoils, the height of the sector has a noticeable influence on the result of the integration. As explained above, this is due to the sources that are located above the airfoil trailing edge. For example, for the airfoil made of Recemat the spectra given in Figure 3.24(c) show differences in the order of 7 dB for frequencies above 3 kHz. Sectors with a large vertical extent lead to higher amplitudes than sectors with a small vertical extent.

To better visualize the trailing edge noise sources, a three-dimensional octave band sound map, obtained for the Recemat airfoil, is given in Figure 3.24(d). It illustrates that the noise source region, which is located in the lateral direction between two major noise sources caused by the interaction of the wind tunnel shear layer with the trailing edge, has a noticeable vertical extent. It can be assumed that the part of the noise source region located directly at or near the trailing edge is the noise source of interest, caused by the interaction of the turbulent boundary layer within the core jet with the airfoil trailing edge. But it cannot be assumed that the part of the noise source region that is located outside of the jet is generated by the same noise source mechanism.

To include in the calculation of the trailing edge noise only the contributions of noise that are generated by the turbulent boundary layer within the core jet, a sector with a vertical extent of 0.12 m is chosen for the integration. The vertical extent hence is the same as the lateral extent, and the resulting three-dimensional sector has the following dimensions: In the streamwise direction it extends from $x = -0.30 \text{ m}$ to $x = -0.15 \text{ m}$, in the lateral direction from $y = -0.06 \text{ m}$ to $y = 0.06 \text{ m}$ and in the vertical direction from $z = 0.62 \text{ m}$ to $z = 0.74 \text{ m}$. The chosen sector is located completely within the wind tunnel core jet, and hence no noise contributions from the shear layers are included in the integration.

It can be seen from Figure 3.24 that the two-dimensional beamforming results are higher than the three-dimensional beamforming results for all airfoils. This is assumed to be caused by the fact that in the case of two-dimensional beamforming, more than just the noise sources located at the trailing edge are mapped onto the array focus plane and into the two-dimensional trailing edge sector. This includes possible noise sources caused by other noise source mechanisms as such that were detected in the three-dimensional sound

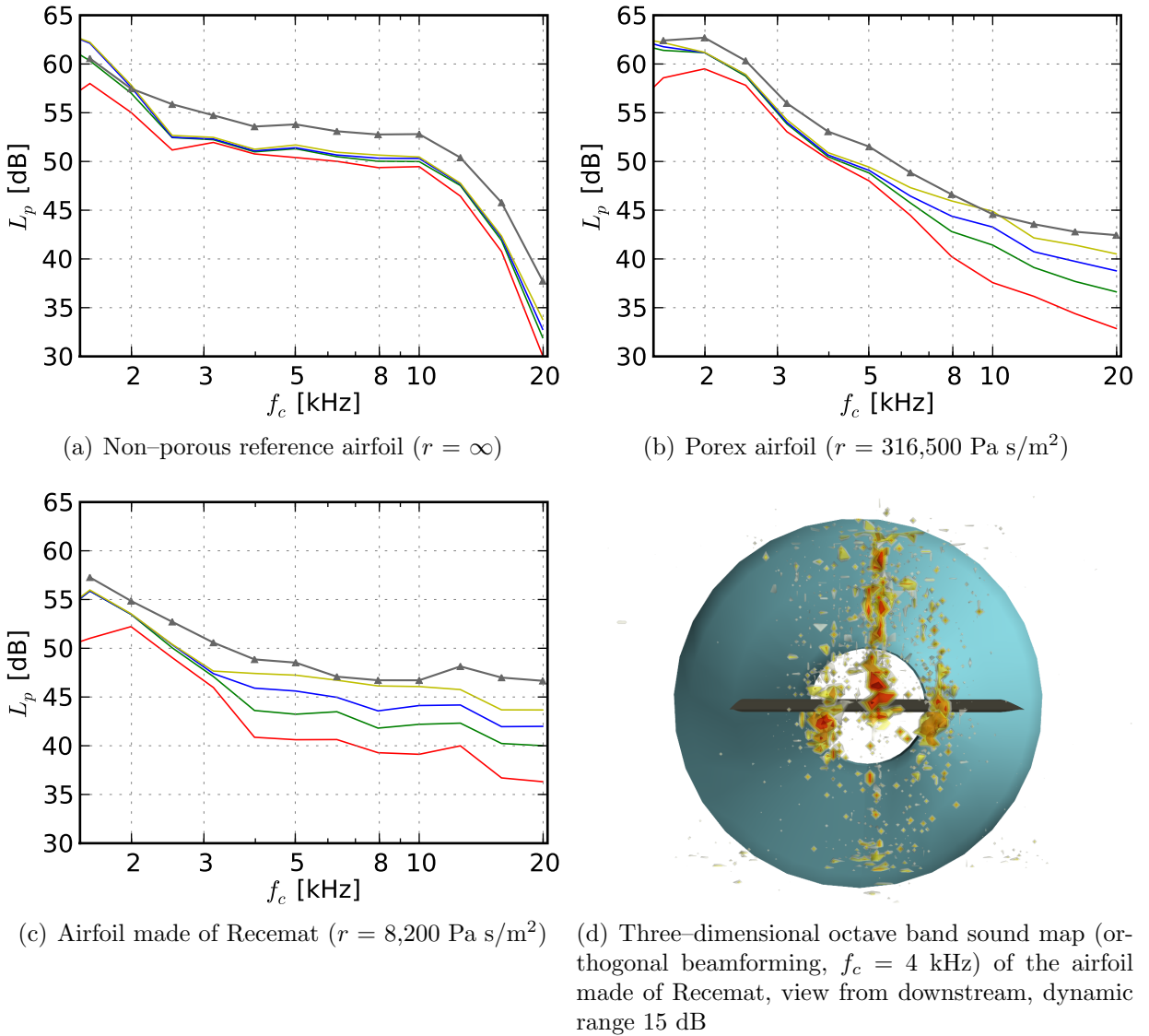
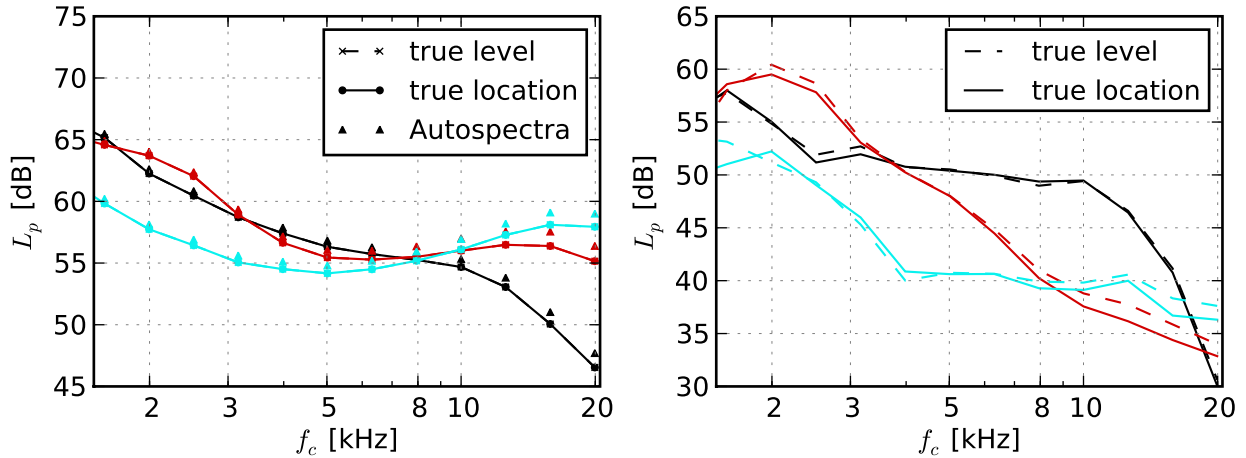


Figure 3.24: Influence of the vertical extent Δz of the trailing edge sector on third-octave band sound pressure level spectra: $\Delta z =$ ■ 0.12, ■ 0.24, ■ 0.36 and ■ 0.48 m, ▲ results of the two-dimensional beamforming as used in [Geyer et al., 2010a], all measurements performed at a flow speed of $U_0 = 50 \text{ m/s}$, angle of attack $\alpha = 0^\circ$ (The vertical extent of the sector is always symmetrical to the z -position of the trailing edge, $z = 0.68 \text{ m}$, which means that a sector with a height of 0.12 m extends from $z = 0.62 \text{ m}$ to $z = 0.74 \text{ m}$.)

maps in Figure 3.22, 3.23 and 3.24(d). The three-dimensional beamforming, on the other hand, enables a better depth resolution, a better source separation and therefore a more exact selection of noise sources that should be included in the integration.

The influence of the steering vector

In acoustic beamforming, different formulations of the steering vector \mathbf{h} are commonly used. In the present work, two formulations of the steering vector are examined that were found to give the best results [Sarradj, 2011]: This is the formulation of the steering vector as used in [Mosher, 1996, Brooks and Humphreys, 1999] (“true level”), which was found to lead to



(a) Noise generated in the complete source region, (b) Noise generated within the trailing edge noise compared with the weighted sum of the microphone sector autospectra

Figure 3.25: Comparison of the influence of different steering vectors for three airfoils ($r = \blacksquare \infty$, \blacksquare 316,500, \blacksquare 8,200 Pa s/m²), orthogonal beamforming (36 eigenvalues), flow speed $U_0 = 50$ m/s, angle of attack $\alpha = 0^\circ$

the correct source strength, and the formulation as for example used in [Dougherty, 2002, Suzuki, 2010], that leads to the correct location at the cost of a small underestimation of the source strength (“true location”). The influence of the different steering vectors on the resulting third–octave band sound pressure levels for both the complete three–dimensional source region and the chosen three–dimensional trailing edge sector is given in Figure 3.25. The first comparison contains the weighted sum of the microphone autospectra as a reference for the physically measured sound.

It can be seen from Figure 3.25(a) that the results from the integration over the complete source region are identical for both steering vector formulations. At low and medium frequencies the beamforming results are also identical to the weighted sum of the microphone autospectra. At high frequencies, approximately above 5 kHz, the beamforming results are slightly below the microphone autospectra, with differences in the order of only 1 dB.

When the trailing edge noise source contributions are integrated over the chosen trailing edge noise sector, the influence of the steering vector on the resulting spectra is also very small only, as is shown in Figure 3.25(b). For the non–porous reference airfoil no noticeable differences are visible over the complete range of frequencies examined. For the porous airfoils the main difference is that the steering vector according to the “true level” formulation results in a slightly increased amplitude at high frequencies, which are approximately 1 dB to 2 dB above the results obtained by the steering vector according to the “true location” formulation for frequencies approximately above 8 kHz. For the porous airfoil made of Recemat, the use of the steering vector according to the “true location” formulation also results in a lower sound pressure level than the use of the steering vector according to the “true level” formulation at the 1.6 kHz third–octave band, with a difference of 3 dB.

It was finally decided to use the steering vector according to the formulation that delivers the correct source location but may lead to a minor error regarding the source strength, in the present thesis.

For both the two- and three-dimensional beamforming, the resulting data are transferred to third-octave band sound pressure levels (L_p), relative to $p_0 = 2 \cdot 10^{-5} \text{Pa}$, with center frequencies between 1.6 kHz and 20 kHz. The lower frequency limit was chosen in accordance to Equation (1.2) to ensure the non-compactness condition. The third-octave band sound pressure levels were then reduced by 6 dB to account for the reflection at the microphone array plate. Note that the results presented in [Geyer et al., 2010a, Geyer et al., 2010b] are not corrected, but are explicitly given as measured at the center of the microphone array.

3.5 Constant temperature anemometry measurements

To determine the effect of the porous consistency of the materials on the turbulent boundary layer and the wake of the airfoils, constant temperature anemometry (CTA) measurements were performed on a subset of the porous airfoils and the non-porous reference airfoil.

Table 3.2 lists the airfoils used for the constant temperature anemometry measurements, with the number corresponding to the number in Table 3.1. The airfoils were chosen due to their applicability for the hot-wire measurements: A great number of the 16 porous airfoils is made out of a soft elastic material, which in some cases leads to unwanted motion of the thin trailing edge in the flow. This motion prevents the use of the hot-wire measurement technique near the surface of those airfoils since that would destroy the hot-wire probe. The porous materials of the airfoils that were found to be suitable for the CTA measurements are rigid. However, the decision to use only a subset of the porous airfoils is assumed to be no severe limitation to this investigation, since the selected porous materials cover a large range of the air flow resistivity r , and hence general statements on the influence of the air flow resistivity on the parameters of the turbulent boundary layer of the porous airfoils are still possible.

Measurement system and data processing

The CTA measurements were performed using a P15 type boundary layer probe built by DANTEC DYNAMICS, which consists of a platinum-plated tungsten wire sensor with a diameter of $5 \mu\text{m}$ and a length of 1.25 mm. The spatial resolution of the measurement system, defined as the inverse of the minimum detectable length in the flow field

Table 3.2: Porous airfoils used for the CTA measurements (the number of each airfoil corresponds to the number used in Table 3.1)

No	Name	Material	r [Pa s/m ²]	σ_v
1	Reference	non-porous	∞	0
3	Porex	polyethylene granulate	316,500	0.40 - 0.46
9	Reapor	porous glass granulate	16,500	>0.96
11	Recemat	metal-foam	8,200	>0.95
16	M-Pore Al 45 ppi	metal-foam	1,000	0.90

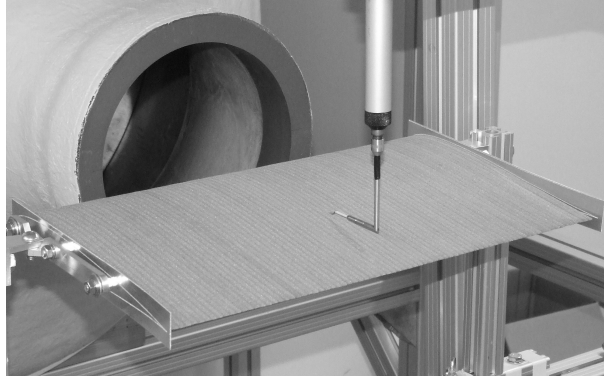


Figure 3.26: Photograph of the boundary layer probe used for the CTA measurements (also shown are the wind tunnel nozzle as well as the porous airfoil made of Recemat)

[Romano et al., 2007],

$$SR = \frac{1}{d_{min}}, \quad (3.38)$$

with the diameter of the hot-wire as the characteristic size of the sensor d_{min} , gives a value of $200,000 \text{ m}^{-1}$. According to [Romano et al., 2007], due to this high spatial resolution hot-wire anemometry is better suited to detect small, moving spatial structures inside a flow field than for example laser Doppler anemometry (LDA) or a common Pitot tube.

In the experiments the wire was aligned perpendicular to the streamwise velocity component (or longitudinal velocity component) in the spanwise (y -) direction. A lightweight traversing system, engineered by the ISEL company, with a minimum step size of 0.1 mm was used for the positioning of the boundary layer probe. According to [Klewicky et al., 2007], about 100 measurement points are recommended for hot-wire measurements in a turbulent boundary layer at a flat plate, resulting in step sizes of order 0.025 mm , which was not possible using the available traversing system.

The boundary layer probe was connected via a 90° -angled probe support to a DANTEC multichannel CTA system. The electrical circuit within this system basically contains a Wheatstone bridge to measure the change of the electrical resistance of the tungsten wire due to the cooling of the wire caused by changes of the flow velocity. The circuit further contains a low-pass filter with a cutoff frequency of 10 kHz . The DC-offset and the gain of the CTA system were adjusted to allow a maximum dynamic range of the output voltage in the required range of flow speeds. Figure 3.26 shows a photograph of the boundary layer probe and the probe support, taken during a measurement in the boundary layer of the airfoil made of Recemat ($r = 8,200 \text{ Pa s/m}^2$).

The hot-wire measurement system was calibrated with a Pitot tube using the velocity calibration method, based on 20 logarithmically spaced velocities between 2 m/s and 55 m/s . The measured data were recorded using a 24 Bit National Instruments measurement system with a sample frequency of 25.6 kHz and a measurement duration of 10 s , resulting in a total number of $256,000$ samples per measurement (the sample frequency of 25.6 kHz is equivalent to the time resolution TR used in [Romano et al., 2007]). Despite a very low traverse speed of 10 mm/s , the possibility of slight vibrations of the traversing system after each movement and before each measurement existed. To avoid the influence of vibrations of the hot-wire probe on the results, the first two seconds ($51,200$ samples) of each measured data set were omitted.

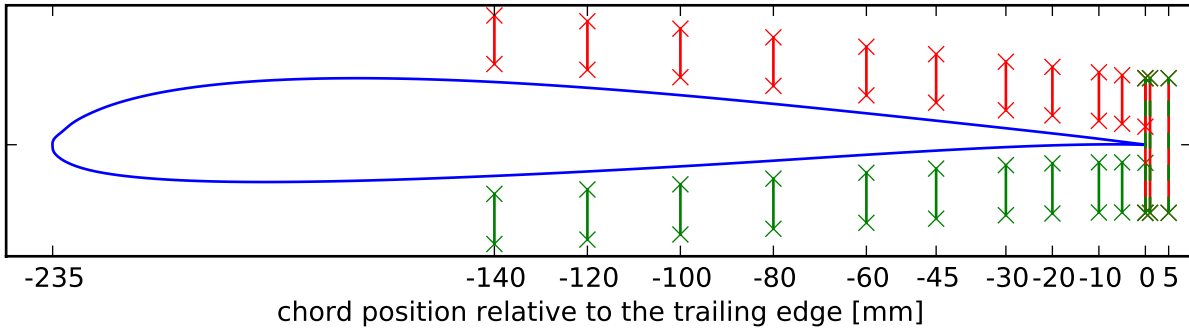


Figure 3.27: Positions for the CTA boundary layer measurements (eleven chordwise positions and two positions in the wake-region), given is the path in the x - z -plane along which the 52 measurements for each velocity profile were made

The remaining 8 s of the recorded velocity-time-data (corresponding to 204,800 samples) were then processed on a personal computer using in-house software. The time domain data were transformed into the frequency domain by an FFT with a Hanning Window and 4,096 samples per block. An additional software high-pass filter was implemented with a cutoff-frequency of 10 Hz to eliminate the offset velocity and the low-frequency-turbulence contributions from the wind tunnel that are not generated by the airfoils.

Measurement positions

The velocity profiles were measured at eleven positions along the chord on the surface of the airfoil, and at two positions in the wake of the airfoil behind the trailing edge. Figure 3.27 shows the measurement positions along the chord, relative to the airfoil trailing edge. Thereby, the distance of the x -coordinates of the measurement positions from the airfoil trailing edge is 0, 5, 10, 20, 30, 45, 60, 80, 100, 120 and 140 mm toward the leading edge (corresponding to approximately 0, 2.1, 4.3, 12.7, 19.1, 25.5, 34.0, 42.6, 51.1 and 59.6 % of the chord), while the distance of the measurement positions in the wake is 1 and 5 mm (0.4, 2.1 % of the chord).

At least 52 single measurement positions are located in the vertical (z -) direction for the determination of the turbulent boundary layer velocity profiles, and twice this number for the measurements in the wake of the airfoil. The distance between single measurement points in the vertical direction was varied: Directly above the surface, the step size was chosen to be the minimum step size of 0.1 mm, while with increasing distance from the surface the step size changed to 0.2 mm and finally to 1 mm. This led to a total number of nearly 800 measurements for one side of the airfoil at one flow speed U_0 and one angle of attack. For some of the test series, this number was exceeded. The results of these measurements are the velocity profiles $\bar{u}(z)$ at eleven positions along the chord and at two positions in the wake of the airfoil.

The spanwise position of the measurements (in y -direction) was approximately at midspan. The influence of the spanwise position on the measured boundary layer properties was tested in preliminary experiments and found to be negligible when inside the core jet of the wind tunnel. Additional information are given in Section E.1 of Appendix E.

Determination of the probe position

A special problem that had to be dealt with was the determination of the distance between the hot-wire probe and the surface of the airfoils, which is necessary to calculate the parameters of the turbulent boundary layer.

Common procedures for non-porous airfoils are based on the assumption that the velocity at the surface of the airfoil is zero, which cannot be assumed for porous airfoils that are permeable to air. Quite contrary, a fluid flow from the pressure side of the porous airfoil upstream of the trailing edge through the porous material to the suction side and the subsequent reduction of the pressure drop at the trailing edge may be a major mechanism contributing to the trailing edge noise reduction.

The procedures mentioned above for non-porous airfoils are often based on the assumed theoretical shape of the velocity profile near a non-permeable surface. One example is the Clauser plot method used to determine the wall shear stress. It is a well established graphical method which relies on the relation between the wall shear stress and the properties of the time-averaged velocity profile in the logarithmic part of the boundary layer governed by the “log law of the wall” [Klewicky et al., 2007]. But although it can be assumed that the mean velocity profiles of the porous airfoils may be similar to a logarithmic curve, no theory for the boundary condition at the surface of the porous airfoils is available.

One well-documented problem of hot-wire measurements near a wall is the conduction of heat from the hot-wire probe to the wall, which can usually be reduced by choosing a non-conductive surface and reducing the heating of the wire [Klewicky et al., 2007]. The effect of the heat conduction can be taken into account for non-porous airfoils at most, although the issue of differences between the heat transfer to the solid wall and the heat transfer to the adjacent fluid remains complicated (see [Alfredsson et al., 1988] for detailed information). However, this cooling effect may be completely different for porous materials, since it can be assumed that the porous consistency (fluid-filled interconnected pores within a solid material) has an influence on the heat transfer. Additionally, two of the porous materials are metallic (and thus electrically conductive), which further enforces the heat transfer. Furthermore, the surface roughness of the porous airfoils may have an effect on the cooling that cannot be neglected. Hence, common correction methods for the heat transfer and temperature fluctuations in the flow, like those examined by Bremhorst [Bremhorst, 1985] or Abdel-Rahman et al. [Abdel-Rahman et al., 1987], cannot be applied.

In the present case of porous airfoils, a more time consuming and approximative method had to be used for the measurement of the distance between the airfoil surface and the hot-wire: A dummy sensor with the same geometry as the boundary layer probe, simply another Dantec P15 probe without the Tungsten wire, was used to optically determine the vertical (z -) position when the prongs just touched the surface of the airfoil. Thus, the absolute accuracy of the vertical distance between airfoil surface and hot-wire probe is at the maximum equivalent to that of the traversing system (0.1 mm). The described method was used for all airfoils, including the non-porous reference airfoil. And although it may be not as accurate as common procedures, it does allow comparisons between the turbulent boundary layer properties of the porous airfoils with reference to the non-porous airfoil.

As mentioned above, one additional problem for the determination of the distance between the hot-wire probe and the airfoil surface is the roughness of the porous airfoils, since it is difficult to define $z = 0$ for a rough surface. This is especially true for airfoils with low air

flow resistivities and large pores that subsequently feature very coarse surfaces compared to the non-porous airfoil. Due to the present method used to determine the distance of the hot-wire probe, it can be assumed that $z = 0$ refers to the crest of the porous material (the cell walls). However, the resulting inaccuracy regarding the determination of the probe position relative to the airfoil surface may be in the order of 0.5 mm to 1 mm for the porous airfoils with the largest pores and hence the highest surface roughness, based on a visual estimation of the corresponding pore sizes.

Calculation of the boundary layer parameters

The measured distributions of the turbulent velocity along vertical paths perpendicular to the airfoil surface, $\bar{u}(z)$, were used to calculate different statistical boundary layer parameters for incompressible flow [Schlichting and Gersten, 2000]:

- the boundary layer thickness δ , as the vertical distance from the airfoil surface, where the mean velocity $\bar{u}(z)$ reaches 99 % of the outer velocity U_0 ,
- the boundary layer displacement thickness

$$\delta_1 = \int_{z=0}^{\infty} \left(1 - \frac{\bar{u}(z)}{U_0} \right) dz, \quad (3.39)$$

as the theoretical distance that a surface in an ideal inviscid fluid would have to be moved into the flow to give the same mass flow rate as the same surface in the real fluid,

- the momentum thickness

$$\delta_2 = \int_{z=0}^{\infty} \left(1 - \frac{\bar{u}(z)}{U_0} \right) \cdot \left(\frac{\bar{u}(z)}{U_0} \right) dz, \quad (3.40)$$

as the theoretical distance that the surface in an inviscid fluid would have to be moved to give the same momentum deficit and

- the energy thickness

$$\delta_3 = \int_{z=0}^{\infty} \left[1 - \left(\frac{\bar{u}(z)}{U_0} \right)^2 \right] \cdot \left(\frac{\bar{u}(z)}{U_0} \right) dz. \quad (3.41)$$

The integration in Equation (3.39) through (3.41) was implemented using the trapezoidal rule. The ratio of the boundary layer displacement thickness to boundary layer momentum thickness is known as the shape factor

$$H_{12} = \frac{\delta_1}{\delta_2}. \quad (3.42)$$

The shape factor is a measure of the adverse pressure gradient within the boundary layer. According to aerodynamic theory for the flow along a flat plate (see for example

[Eckert and Drake jr., 1959]), the relations between boundary layer displacement thickness and boundary layer thickness and between boundary layer momentum thickness and boundary layer thickness can be approximated by $\delta_1 \approx \delta/3$ and $\delta_2 \approx \delta/7$, respectively, for a laminar boundary layer. This leads to a theoretical shape factor of about 2.3. On the other hand, for turbulent boundary layers $\delta_1 \approx \delta/8$ and $\delta_2 \approx 7/72 \cdot \delta$, leading to a shape factor of approximately 1.3. At the point of transition from a laminar boundary layer flow to a turbulent boundary layer flow, the boundary layer displacement thickness δ_1 abruptly decreases, leading to a sharp decrease of H_{12} . Hence, through measuring the shape factor it can be determined whether a boundary layer is laminar or turbulent. According to the study of Nash [Nash, 1966], flow separation usually occurs for shape factors between 2 and 3.

According to the work of Schlinker and Amiet [Schlinker and Amiet, 1981], the boundary layer displacement thickness δ_1 is often chosen for the scaling of turbulent boundary layer trailing edge noise, although the boundary layer thickness δ would be more suitable, since the scale of the coherent structures generating the noise is assumed to be in the order of δ . However, the identification of the edge of the boundary layer based on the velocity profiles is often very difficult, and hence the displacement thickness is usually chosen and almost generally accepted [Eckert and Drake jr., 1959].

Turbulence spectra

Using the autocorrelation function of the turbulent velocity fluctuations measured above the surface and in the wake of the airfoils, the power spectral density Φ_{uu} can be obtained as the result of a Fourier transformation. As described in Section 3.5, the Fourier transformation was performed blockwise with a block size of 4,096 samples and an overlap of 50 %. The turbulence power spectral density is a physical quantity consistent with a squared velocity divided by frequency, and therefore has the unit $[(\text{m/s})^2\text{s}] = [\text{m}^2/\text{s}]$.

The examination of the power spectral density of the velocity fluctuations allows for statements regarding the distribution of kinetic energy within the turbulence. This energy distribution can be seen as consistent with the size of turbulent structures (eddies) within the turbulent boundary layer. The low frequency range of the turbulence power spectral density can be attributed to larger turbulence scales, while the high frequency range is associated with small scale turbulent structures within the boundary layer.

Furthermore, it can be assumed that the spectral shape of the turbulence is related to the spectral shape of the trailing edge noise that is generated as a result of the scattering of turbulence within the boundary layer at the trailing edge of the airfoils.

In the present study, the power spectral density of the velocity fluctuations Φ_{uu} will be converted to third-octave bands, denoted as Φ . In the remaining part of this thesis, the third-octave band turbulence power spectral density will be referred to as turbulence spectrum.

Chapter 4

Measurement results and discussion

This section presents the results of the aerodynamic measurements, the acoustic measurements and the constant temperature anemometry measurements. The correlation between the results of the different measurements is discussed. Acoustic and aerodynamic measurements were performed on all 17 airfoils given in Table 3.1 for 15 flow speeds approximately between 25 m/s and 50 m/s, leading to a chord based Reynolds number ranging from 4×10^5 to 8×10^5 and a Mach number range of about 0.07 to 0.14. The geometric angle of attack was varied from -16° to 20° in 4° steps. Constant temperature measurements were only performed on a subset of the airfoils at maximum flow speed.

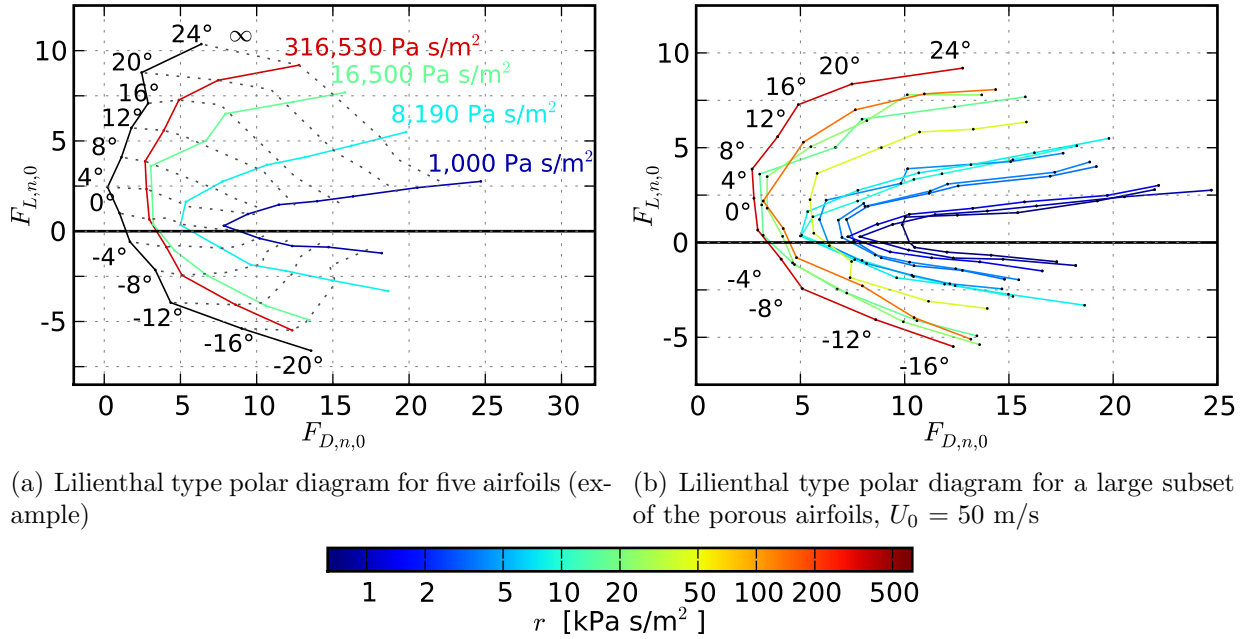
4.1 Aerodynamic measurements

In order to take advantage of the possible reduction of the trailing edge noise generation of the porous airfoils compared to the reference airfoil, the aerodynamic performance of the airfoils is of great interest. A porous or partly porous airfoil can only be a possible alternative to a non-porous airfoil, for example in a fan or blower, if the mechanical power or the efficiency is not an order of magnitude smaller than that of the reference airfoil. In this section, the results of the aerodynamic measurements on the airfoils from Table 3.1 are given, part of which were already presented in reference [Geyer et al., 2010a].

As mentioned in Section 2.1, it is assumed that the porous airfoils produce a smaller lift force but a higher drag force than the non-porous airfoil. This means that the use of porous or partly porous airfoils may be feasible for some applications if the lift force generated by the porous airfoils is not much smaller than that of the non-porous airfoil and if the drag force is not much higher. Or, in other words, the aeroacoustic advantages of the porous airfoils should outweigh the aerodynamic disadvantages.

Figure 4.1 shows the Lilienthal type polar diagrams of a subset of the porous airfoils. Presented are the measured lift and drag forces F_L and F_D of the porous airfoils for each angle of attack at the maximum flow speed, $U_0 = 50$ m/s, normalized with the lift and drag force of the non-porous reference airfoil for zero angle of attack:

$$F_{L,n,0} = \frac{F_{L,\text{por},\alpha}}{F_{L,\text{ref},0^\circ}} \quad (4.1)$$



(a) Lilienthal type polar diagram for five airfoils (example) (b) Lilienthal type polar diagram for a large subset of the porous airfoils, $U_0 = 50$ m/s

Figure 4.1: Normalized lift and drag forces $F_{L,n,0}$ and $F_{D,n,0}$ according to Equation (4.1) and (4.2), $U_0 = 50$ m/s (Assigned to the abscissa are the normalized drag forces $F_{D,n,0}$, while the normalized lift forces $F_{L,n,0}$ are assigned to the ordinate, with the geometric angle of attack α being the parameter along the curves.)

and

$$F_{D,n,0} = \frac{F_{D,\text{por},\alpha}}{F_{D,\text{ref},0^\circ}}, \quad (4.2)$$

where $F_{L,\text{por},\alpha}$ and $F_{D,\text{por},\alpha}$ are the measured lift and drag forces of the porous airfoils at the respective geometric angle of attack α , while $F_{D,\text{ref},0^\circ}$ and $F_{D,\text{ref},0^\circ}$ are the forces of the non-porous reference airfoil at $\alpha = 0^\circ$.

Figure 4.1(a) gives the Lilienthal type polar diagrams for only a small subset of four porous airfoils and the non-porous airfoil. The assumed correlation between the lift and drag forces of the porous airfoils and their air flow resistivity is confirmed: Porous airfoils with lower flow resistivities r develop a lower lift force F_L , but a higher drag force F_D than airfoils with a higher air flow resistivity. Another conclusion can be drawn from the polar diagrams shown in Figure 4.1(a): Since the SD7003 airfoil is a semi-symmetric airfoil with a positive camber, the angle of zero lift is not $\alpha = 0^\circ$ but a negative angle of attack between 0° and -4° . At an angle of attack of 0° , the SD7003 airfoil generates a noticeable lift force as opposed to a symmetric airfoil, as for example the NACA 0012 airfoil that is often used in aeroacoustic and aerodynamic studies.

It has to be mentioned again that, due to the reasons given in Section 3.2, the given angle of attack α represents different working points of the airfoils only. The reasons are the dimensions of the airfoil, which are large compared to the dimensions of the wind tunnel nozzle, the semi-symmetric shape of the SD7003 airfoil and the porous consistency of the airfoils. Therefore, the aerodynamic results, especially for large absolute values of the angle of attack, cannot be compared to results from wind tunnel studies including side plates or studies with other ratios of airfoil dimension to the dimension of the nozzle.

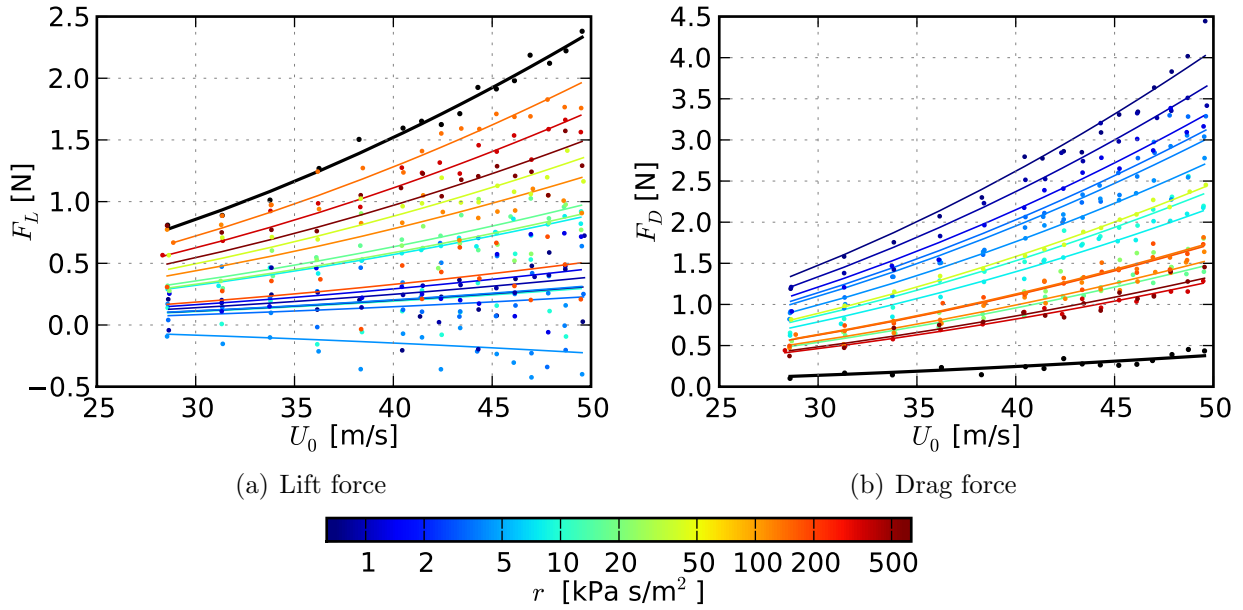


Figure 4.2: Measured lift and drag forces F_L and F_D as a function of the flow speed U_0 at an geometric angle of attack $\alpha = 0^\circ$ (dots: measured forces, solid lines: fit according to $F \propto U_0^2$)

The Lilienthal type polar diagrams for a larger set of the porous airfoils is shown in Figure 4.1(b), where similar observations can be made as for Figure 4.1(a). The lift forces of the porous airfoils increase with increasing airflow resistivity, while the drag forces decrease. The angle of attack at which the porous airfoils produce no lift, the zero lift angle, is negative, approximately between 0° and -4° . For some of the porous airfoils, the zero lift angle even seems to be below -4° .

Figure 4.2 shows the dependence of the measured lift and drag forces on the flow speed U_0 for zero angle of attack. In addition to the measured forces the figures contain a fit according to $F = \text{const} \cdot U_0^2$ which was implemented since a dependence of the aerodynamic forces on the square of the flow speed can be expected according to basic aerodynamic theory. In general, the measured forces and the fitted curves agree well. It can be seen in Figure 4.2 that the non-porous airfoil generates the highest lift and the lowest drag force. The lift of the porous airfoils increases with increasing airflow resistivity r , while the drag decreases.

The deviation of the actual measured forces from the fit is very small for the drag forces F_D , while for airfoils with low air flow resistivities the deviation of the measured lift forces F_L is considerably larger. In general, such deviations are assumed to be more visible for lower lift forces, when the load cells that measure the vertical force components (signals v_1 , v_2 and v_3) are near their position of rest. One possible source of error for the airfoils made of a soft foam or felt may be a deformation of the airfoil shape due to the aerodynamic forces acting on the airfoils in the flow.

It is visible that both lift and drag force increase with increasing flow speed U_0 except in one case. For one porous airfoil with a very low air flow resistivity the measured lift forces are mostly negative, leading to a negative slope of the fit. It can be assumed that this results either from an inaccurately adjusted angle of attack or from imprecision during the water-cutting of some of the slices of this porous material leading to a somewhat changed three-dimensional shape of the airfoil that resulted in a negative lift.

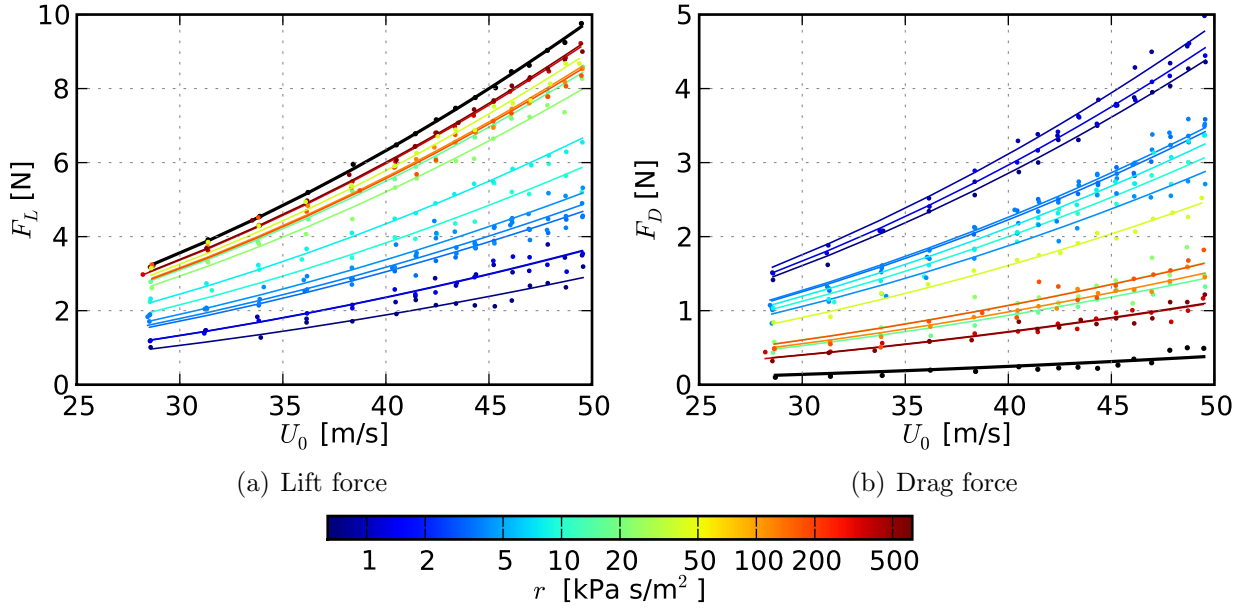


Figure 4.3: Measured lift and drag forces F_L and F_D as a function of the flow speed U_0 at an geometric angle of attack $\alpha = 8^\circ$ (dots: measured forces, solid lines: fit according to $F \propto U_0^2$)

As an example for non-zero angle of attack Figure 4.3 shows the forces measured at an angle of attack of 8° . The results confirm the basic statements discussed above: The lift force increases with increasing r and the drag force decreases. Again, the dependence of both lift and drag force on the flow speed can be approximated by using a second order polynomial fit. As opposed to zero angle of attack, Figure 4.3 does not show negative lift forces, even for porous airfoils with very low air flow resistivities.

To better illustrate the dependence of the aerodynamic performance on the air flow resistivity of the porous airfoils, Figure 4.4 shows the normalized lift and drag forces of the porous airfoils as a function of the air flow resistivity for zero angle of attack. But as opposed to the normalization used for Figure 4.1(a) and 4.1(b) according to Equation (4.1) and (4.2), the measured lift and drag forces F_L and F_D of the porous airfoils at m different flow speeds and different angles of attack are now normalized to the corresponding values of the non-porous airfoil at the same angle of attack and flow speed:

$$\bar{F}_{L,n}(\alpha) = \frac{1}{m} \sum_{i=1}^m \frac{F_L(U_{0,i}, \alpha)}{F_{L,\text{ref}}(U_{0,i}, \alpha)} \quad (4.3)$$

and

$$\bar{F}_{D,n}(\alpha) = \frac{1}{m} \sum_i^m \frac{F_D(U_{0,i}, \alpha)}{F_{D,\text{ref}}(U_{0,i}, \alpha)}. \quad (4.4)$$

F_L and F_D are the measured lift and drag forces while $F_{L,\text{ref}}$ and $F_{D,\text{ref}}$ are the forces of the non-porous reference airfoil at the same angle of attack α and the same flow speed U_0 . The normalized forces are then averaged over the complete range of flow speeds. For a better illustration of the convergence of the normalized forces with increasing air flow resistivity, the dashed black line in Figure 4.4 represents the normalized forces of the non-porous reference airfoil (which are of course equal to one).

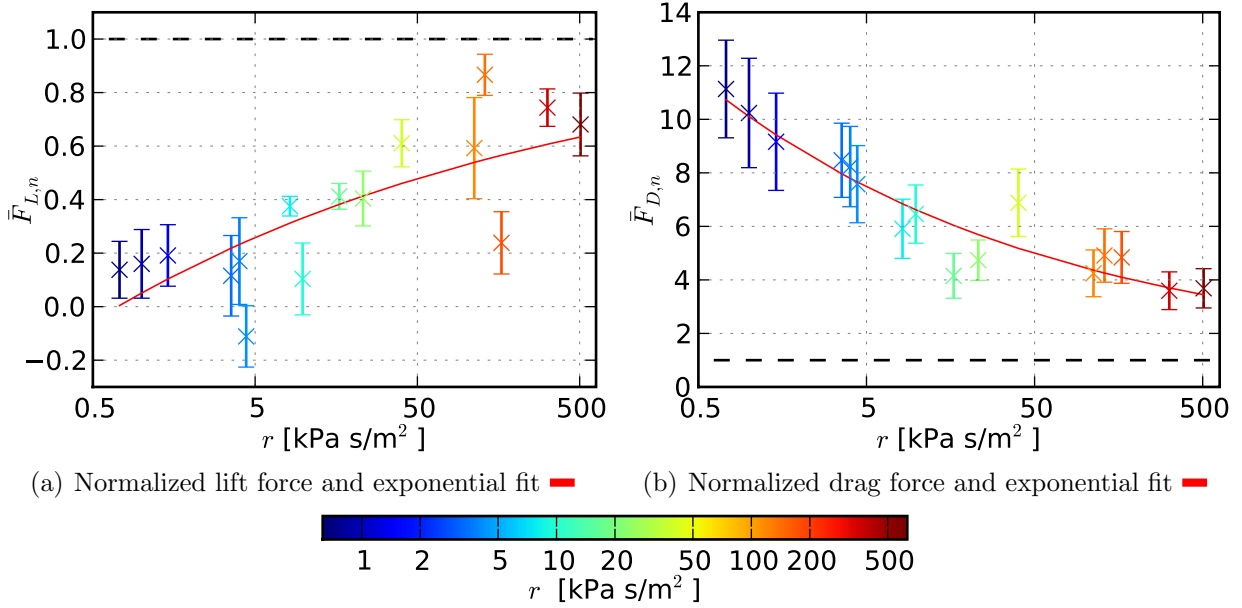


Figure 4.4: Normalized lift and drag forces $\bar{F}_{L,n}$ and $\bar{F}_{D,n}$ according to Equation (4.3) and (4.4) as a function of air flow resistivity r of the porous materials at an geometric angle of attack $\alpha = 0^\circ$ (The dashed black line represents the results of the non-porous reference airfoil. The red line shows an exponential least squares fit.)

Figure 4.4 clearly shows the dependence of the normalized lift and drag forces on the air flow resistivity. With increasing air flow resistivity r of the porous materials, the normalized lift force $\bar{F}_{L,n}$ increases, too, while the normalized drag force $\bar{F}_{D,n}$ decreases.

To obtain an estimate of the lift and drag forces $\bar{F}_{L,n}$ and $\bar{F}_{D,n}$, Figure 4.4 additionally shows an exponential least squares fit that was performed on the data. According to this fit, the normalized lift and drag forces of the porous airfoils can be estimated as

$$\bar{F}_{L,n}(r) = -2.732 \cdot \exp(-0.352 \cdot \log_{10} r) + 1 = -2.732 \cdot r^{\frac{-0.352}{\ln 10}} + 1 \quad (4.5)$$

and

$$\bar{F}_{D,n}(r) = 39.140 \cdot \exp(-0.486 \cdot \log_{10} r) + 1 = 39.140 \cdot r^{\frac{-0.486}{\ln 10}} + 1. \quad (4.6)$$

Since Equation (4.5) and Equation (4.6) were developed based on measurements using porous airfoils with air flow resistivities r between 700 Pa s/m² and 506,400 Pa s/m² at zero angle of attack, an extended validity of the equations for other air flow resistivities or angles of attack cannot be expected a priori.

The results of the aerodynamic measurements clearly give evidence that the lift force of the porous materials increases with increasing flow resistivity r , while the drag force decreases. As anticipated, the non-porous airfoil generates the highest lift and the lowest drag. Both lift and drag force increase with increasing flow speed. The dependence of the measured forces on the flow speed can be approximated by an exponential fit.

4.2 Acoustic measurements

In this section, the results of the acoustic measurements on the 16 porous airfoils and the non-porous reference airfoil given in Table 3.1 are presented. In a first step, the raw

acoustic data were analyzed using the two-dimensional beamforming algorithms, as described in section 3.4.3. The results of these analyses were already presented in reference [Geyer et al., 2010a] and, partly, in reference [Geyer et al., 2010b], and hence only a short overview and discussion will be given in the following section. The present thesis is mainly focused on the results of the three-dimensional beamforming, which will be shown and discussed after Section 4.2.1.

4.2.1 Two-dimensional beamforming results

It was found that in general a noticeable trailing edge noise reduction is possible through the use of porous airfoils [Geyer et al., 2010a]. The noise emission slightly decreases with increasing flow resistivity of the porous airfoils over a large range of low and medium frequencies. At high frequencies (starting at approximately 10 kHz for some airfoils), the noise generated at the trailing edge of the porous airfoils exceeds that of the reference airfoil. This effect is believed to be a contribution of surface roughness noise, since the porous airfoils have a rough surface compared to the non-porous reference airfoil. This assumption is further supported by the fact that porous airfoils made of materials with low flow resistivities, and hence larger pores, emitted more high frequency noise than porous airfoils made of materials with higher flow resistivities, and hence smaller pores.

To give an example for the results of the two-dimensional beamforming, the third-octave band sound pressure levels of the porous airfoils and the non-porous reference airfoil are presented in Figure 4.5 as a function of the chord based Strouhal number. The sound pressure levels are scaled with the 4.6th power of the flow speed U_0 , which was found appropriate for the scaling of the trailing edge noise of the reference airfoil obtained by the two-dimensional beamforming. No explicit scaling approach could be identified for the trailing edge noise of the porous airfoils, although the exponent of 4.6 seems to be a good first guess for most airfoils.

An overall sound pressure level $L_{p,\text{tot}}$, calculated from the third-octave bands with center frequencies between 1.6 kHz and 20 kHz, was calculated for all airfoils according to

$$L_{p,\text{tot}} = 10 \cdot \log_{10} \left(\sum_i 10^{[L_{p,i}/(10 \text{ dB})]} \right) \text{ dB}, \quad (4.7)$$

where $L_{p,i}$ is the third-octave band sound pressure level at the third-octave band i . This overall sound pressure level (obtained using the two-dimensional beamforming) is shown in Figure 4.6.

Since the spectral peak of the trailing edge noise for both the non-porous airfoil and the porous airfoils is assumed to be below 1.5 kHz (the lower frequency limit of the acoustic measurements according to Equation (1.2)), the peak third-octave band is not included in the overall sound pressure level $L_{p,\text{tot}}$. This omission of low frequency contributions to the calculation of the overall sound pressure level is a clear limitation, which is discussed in reference [Geyer et al., 2010b].

Nevertheless, $L_{p,\text{tot}}$ is given in reference [Geyer et al., 2010a] (and reprinted in Figure 4.6) for the 16 porous airfoils and the non-porous airfoil as a function of the flow speed U_0 for zero angle of attack. The trailing edge noise overall sound pressure level increases with flow speed for all airfoils, although not necessarily with the same slope.

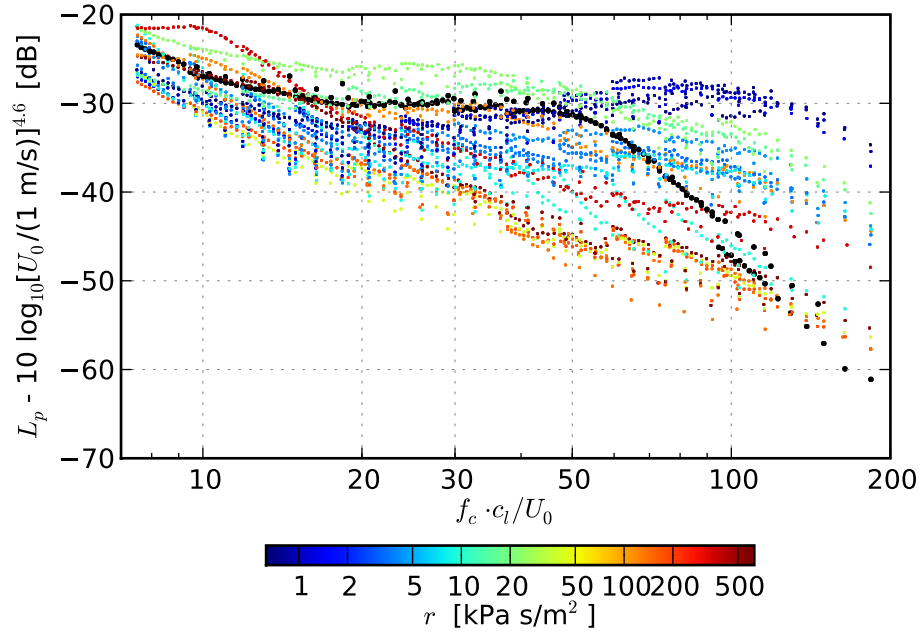


Figure 4.5: Trailing edge noise third–octave band sound pressure levels, obtained by two–dimensional beamforming [Geyer et al., 2010a], as a function of chord based Strouhal number, scaled based on $U_0^{4.6}$, angle of attack $\alpha = 0^\circ$

Additionally, the dependence of the trailing edge third–octave band sound pressure level spectra of the individual airfoils on the geometric angle of attack was examined. The spectra showed that the dependence of the trailing edge noise emission of the porous airfoils on angle of attack is rather difficult, and both spectral shape and magnitude are affected. It is assumed that an increasing absolute value of the angle of attack (positive or negative) leads to a complex flow field around the porous airfoils, since an assumed fluid flow through the porous airfoils depends not only on angle of attack, but also on the air flow resistivity r of the materials. The limitations of the measurement setup regarding measurements at angles of attack significantly smaller or greater than zero, like the curvature of the free jet (as discussed in Section 3.2), add to the difficulty to fully explain the complex relation of the trailing edge noise on angle of attack.

4.2.2 Three–dimensional beamforming results

In a second step, the measured acoustic data were analyzed using three–dimensional beamforming as described in Section 3.4. The results will be presented in this section. Due to the large amount of measurement data and the rather complex relation between the trailing edge noise of porous airfoils on the geometric angle of attack, only the results for zero angle of attack will be given. Effects like the induced curvature of the shear layer and the deflection of the jet as well as the variation of the trailing edge noise directivity can therefore be neglected. As explained at the end of Section 3.4, 6 dB were subtracted from all measured sound pressure levels to account for the reflection at the planar microphone array.

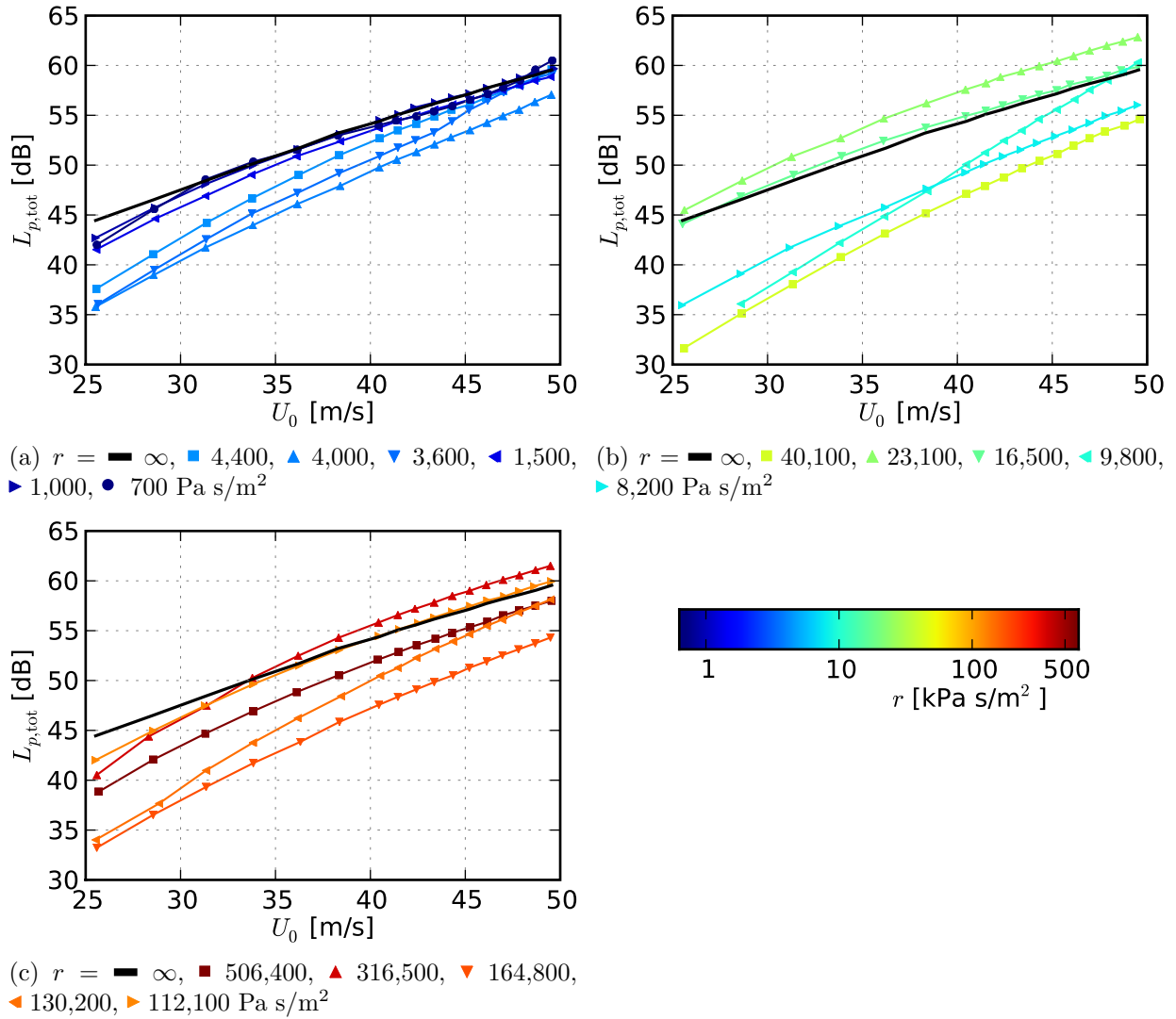
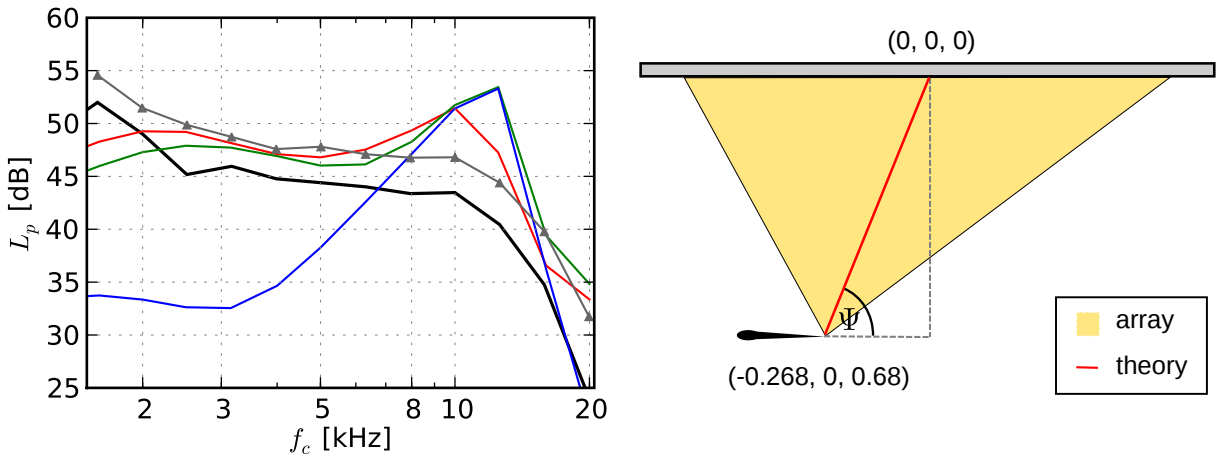


Figure 4.6: Overall sound pressure levels ($L_{p,\text{tot}}$) of the noise measured at the trailing edge, obtained by two-dimensional beamforming [Geyer et al., 2010a], as a function of the flow speed U_0 , angle of attack $\alpha = 0^\circ$

Comparison of the trailing edge noise of the reference airfoil with theory

First, a comparison between the measured trailing edge noise spectra and the spectra calculated by the NAFNoise prediction code [Moriarty, 2005] will be given to validate the measurements. Of course, this comparison can only include the non-porous reference airfoil since no trailing edge noise prediction models exist for porous airfoils. The comparison includes the results from the three-dimensional orthogonal beamforming algorithm, the results from the two-dimensional beamforming as presented in [Geyer et al., 2010a] (which were also reduced by 6 dB to enable comparison with the three-dimensional beamforming results) and three different prediction methods implemented in the NAFNoise prediction code:

- the BPM-model [Brooks et al., 1989], with the boundary layer parameters being calculated based on the estimations used in the BPM-model itself,



(a) Trailing edge noise spectra, \blacksquare measurement + 3D beamforming, \blacktriangle measurement + 2D beamforming, \color{red} NAFNoise prediction (BPM/BPM), \color{green} NAFNoise prediction (BPM/XFOIL), \color{blue} NAFNoise prediction (TNO) (b) Different viewing angles for measurement and theory (as used for the NAFNoise prediction given in Figure 4.7(a))

Figure 4.7: Comparison of measured third-octave band sound pressure level spectra for the reference airfoil ($r = \infty$) with NAFNoise prediction [Moriarty, 2005], measurement performed at a flow speed of $U_0 = 50$ m/s, angle of attack $\alpha = 0^\circ$

- the BPM-model with the boundary layer parameters calculated using XFOIL [Drela, 1989] and
- the TNO-model developed by Moriarty et al. [Moriarty et al., 2005] which uses XFOIL to predict the boundary layer parameters.

All prediction methods include the calculation of both turbulent boundary layer trailing edge noise and boundary layer bluntness noise. Besides information on airfoil geometry, flow speed, angle of attack and speed of sound, the required input data for NAFNoise include information on the position and type of the tripping tape applied to the non-porous airfoil (specified as “light tripping”), the span width (equal to the spanwise extent of the trailing edge noise sector, $\Delta y = 0.12$ m), the observer distance (equal to the distance between the trailing edge at mid-span and the microphone array center, $R = 0.73$ m) and the corresponding angle Ψ between the extension of the chordline toward $x/c_l > 1$ and the observer position (equal to 68.5°).

Figure 4.7(a) shows that basically the spectral shape of the trailing edge noise is similar for measurement and prediction. Taking into account the underlying simplifications that are integral part of the different trailing edge noise models, the agreement between measurement and prediction is quite satisfactory. The three-dimensional beamforming results are lower than the results of the two-dimensional beamforming (as discussed in Section 3.4.4) and, with the exception of the NAFNoise-TNO-model, smaller than the predicted results at medium frequencies. The TNO-model is found to predict sound pressure levels clearly below those of the other models and the measurement with the exception of a spectral peak at high frequencies.

At center frequencies of approximately 2 kHz to 2.5 kHz, the BPM-model predicts a flat spectral peak, leading to a slight decrease of the sound pressure level toward lower

frequencies. No such peak (and accordingly no drop toward lower frequencies) is visible in the measured trailing edge noise spectra and in the spectrum predicted by the TNO-model. The results given by Moriarty and Migliore [Moriarty and Migliore, 2003], although obtained at a NACA 0012 airfoil at a positive angle of attack, support the results of the present measurements, since they also lack the spectral peak when compared to the prediction of the BPM-model.

At high frequencies, all trailing edge noise models predict a very strong spectral peak (at approximately 12 kHz) due to the contribution of trailing edge bluntness noise. The measured third-octave band sound pressure levels also feature this peak, although less distinct, at around 10 kHz. The noticeable differences in peak amplitude and peak frequency may be caused by differences between predicted and existing boundary layer thickness (or displacement thickness). According to Brooks et al. [Brooks et al., 1989], an increase of the ratio of trailing edge thickness to boundary layer displacement thickness would result in an increase of the amplitude of the spectral peak and to a decrease of peak frequency. On the one hand, the large amplitude predicted by the different models indicates that the actual ratio of trailing edge thickness to boundary layer displacement thickness is smaller than the theoretical value. On the other hand, the higher peak frequency of the predicted spectra would lead to the opposite conclusion, specifically that the actual ratio of trailing edge thickness to boundary layer displacement thickness is greater than the ratio used in the NAFNoise models. Since the trailing edge thickness h used for the prediction corresponds to the value that was measured for the reference airfoil, it remains to be verified if the boundary layer displacement thickness used in the predictions is smaller or greater than the actual displacement thickness in the experiments.

The general agreement between predicted and measured spectra is a first validation for the measurement setup and data processing. However, besides the influence of differences between the present open jet setup and a free flow field (as discussed in Section 3.4), discrepancies between the amplitudes of measured and predicted third-octave band spectra may be caused by different facts: First, the spanwise extent of the trailing edge that is analyzed regarding the generation of trailing edge noise is small (0.12 m) compared to the acoustic wavelength at lower frequencies. The influence of this effect on the measured trailing edge noise spectra cannot be exactly determined yet, although the three-dimensional orthogonal beamforming sound maps indicate that the spatial extent of the trailing edge noise sources is indeed small enough for the sources to be located within the chosen sector.

Other possible sources of error are the different definitions regarding the noise source directivity and the observer location. Basis for many common beamforming algorithms, including the ones used in the present study, is the assumption of a superposition of uncorrelated monopole sources, whereas the trailing edge noise prediction models are semi-empiric models based on measurements using single microphones or on coherence based measurement techniques using more than one microphone. However, due to the fact that the angle Ψ is relatively close to 90° , the differences in the resulting directivity factor of monopole and dipole sound sources located mid-span at the airfoil trailing edge lead to a variation of the directional gain of less than 1 dB.

Another difference between microphone array measurements and trailing edge noise models is the viewing angle (see Figure 4.7(b)): While the microphone array in the present setup has a very broad viewing angle when “looking” at the airfoil trailing edge, the NAFNoise model requires the exact observer location as the distance between the trailing edge position

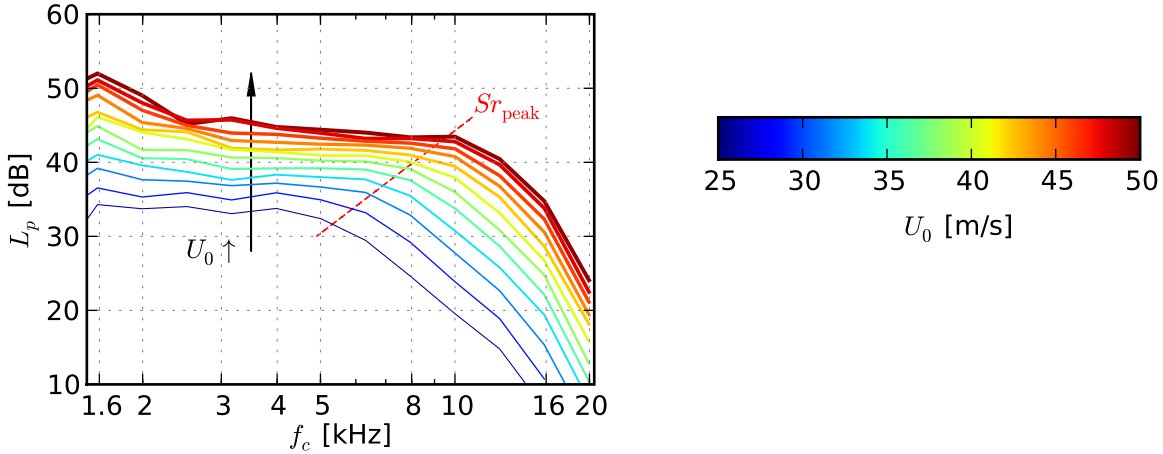


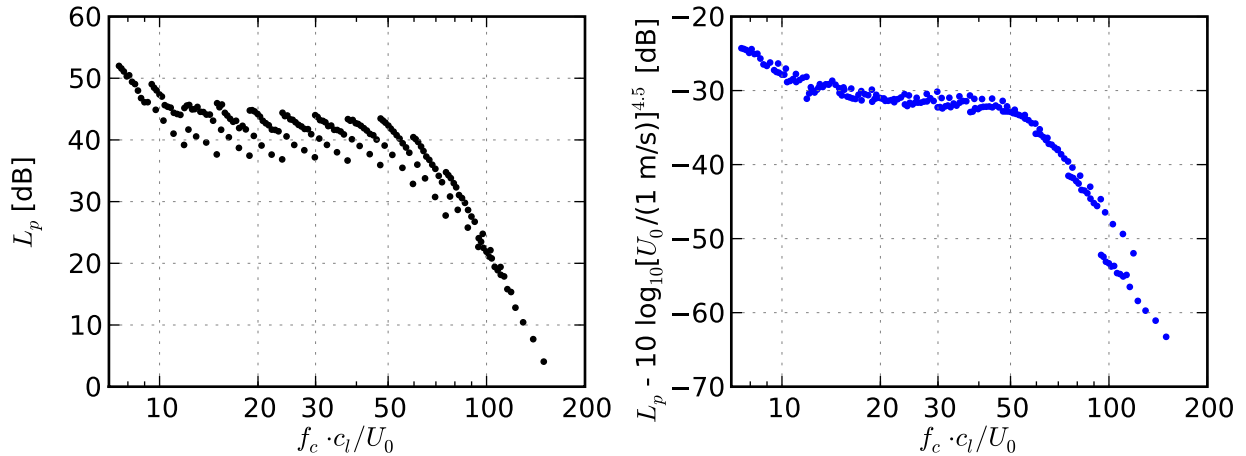
Figure 4.8: Dependence of the third–octave band sound pressure level spectra of the reference airfoil ($r = \infty$) on the flow speed U_0 , measurements performed at zero angle of attack $\alpha = 0^\circ$ (the dotted red line indicates the approximate peak Strouhal number related to trailing edge bluntness noise)

at midspan and a single observer (a single microphone) under a distinct angle Ψ . Due to the broad viewing angle of the array and the directivity of the noise source at the trailing edge, the amplitude measured by each single array microphone depends on the exact microphone position. Each microphone may therefore measure a slightly different amplitude. But again, since the differences between the source - microphone distances as well as the discrepancies due to the source directivity relative to each microphone are very small, they are of minor importance for the total differences of measured and predicted trailing edge noise spectra shown in Figure 4.7(a). For example, the maximum distance between trailing edge and one single microphone is approximately 1.14 m, the minimum distance is 0.68 m, leading to a maximum sound pressure level difference of about 4.5 dB when assuming a monopole source. Of course, regarding all 56 microphones, the average level difference due to the differences in distance is much smaller.

The measured spectra are found to agree sufficiently well with spectra predicted by NAFNoise, which can be interpreted as a basic validation of the measurement setup and data processing used in the present study.

The dependence of the noise generated at the trailing edge of the non–porous reference airfoil on the flow speed U_0 is presented in Figure 4.8. It is visible that for increasing flow speed the amplitude of the third–octave band sound pressure levels increases. Additionally, the center frequency of the trailing edge bluntness noise peak slightly shifts toward higher frequencies. This spectral peak is clearly related to a Strouhal number, since the peak frequency approximately doubles when the flow speed is increased from 26 m/s to 50 m/s.

The dependence of the trailing edge noise generated at the reference airfoil on the flow speed will be further examined. As discussed in Section 2.2.1, trailing edge noise scales with U_0^n , where the exponent n equals 5 according to basic flat plate theory [Ffowcs Williams and Hall, 1970]. According to different airfoil trailing edge noise studies, n may take values from approximately 4.5 [Oerlemans, 2004, Oerlemans and Migliore, 2004] to 5.07 for a sharp edge or 5.3 for a blunt edge [Brooks and Hodgson, 1981]. The appropriate scaling was examined by visually determining the exponent n when the plot of the scaled third–octave band sound pressure levels of



(a) Measured third-octave band sound pressure level (b) Scaled third-octave band sound pressure level

Figure 4.9: Scaling of the trailing edge noise of the non-porous reference airfoil ($r = \infty$) with the 4.5th power of the flow speed U_0 , angle of attack $\alpha = 0^\circ$

the trailing edge noise of the non-porous airfoil,

$$L_{p,\text{scaled}} = L_p - 10 \cdot \log_{10} \left(\frac{U_0}{1 \text{ m/s}} \right)^n \text{ [dB]}, \quad (4.8)$$

versus the chord based Strouhal number $f_c \cdot c_l / U_0$ resulted in the least scatter. Good results and hence smooth plots were generally obtained for exponents between 4 and 5. Due to the fact that the range of flow speeds used in the experiments is relatively small (from approximately 25 m/s to 50 m/s) and due to the lack of low frequency noise below 1.5 kHz it is difficult to determine the dependence on the flow speed more exactly.

Finally, in accordance to the studies of Oerlemans and Migliore [Oerlemans, 2004, Oerlemans and Migliore, 2004], an exponent of $n = 4.5$ was chosen. Figure 4.9(a) shows the third-octave band sound pressure levels of the trailing edge noise of the non-porous airfoil as measured and Figure 4.9(b) shows the trailing edge noise scaled according to Equation (4.8) with an exponent of 4.5, both plotted as a function of the chord based Strouhal number. The Strouhal number related to the trailing edge bluntness noise peak, as already indicated in Figure 4.8, can be determined from Figure 4.9(b) to be in the order of 50 to 60.

Trailing edge noise of the porous airfoils

The third-octave band sound pressure levels of the trailing edge noise from all airfoils examined in the present study, measured at zero angle of attack and maximum flow speed, are given in Figure 4.10. Figure 4.10(a) shows the trailing edge noise spectra of the porous airfoils with low air flow resistivities $r < 5,000 \text{ Pa s/m}^2$, Figure 4.10(b) shows the spectra for airfoils with medium air flow resistivities between 5,000 and 50,000 Pa s/m^2 and the spectra for porous airfoils with high air flow resistivities $r > 100,000 \text{ Pa s/m}^2$ are presented in Figure 4.10(c). During the analysis of the measured trailing edge noise, narrowband spectra have also been examined (as was done in [Geyer et al., 2010a]). It was found that these narrowband spectra do not contain any additional spectral information that is not visible from the corresponding third-octave band spectra.

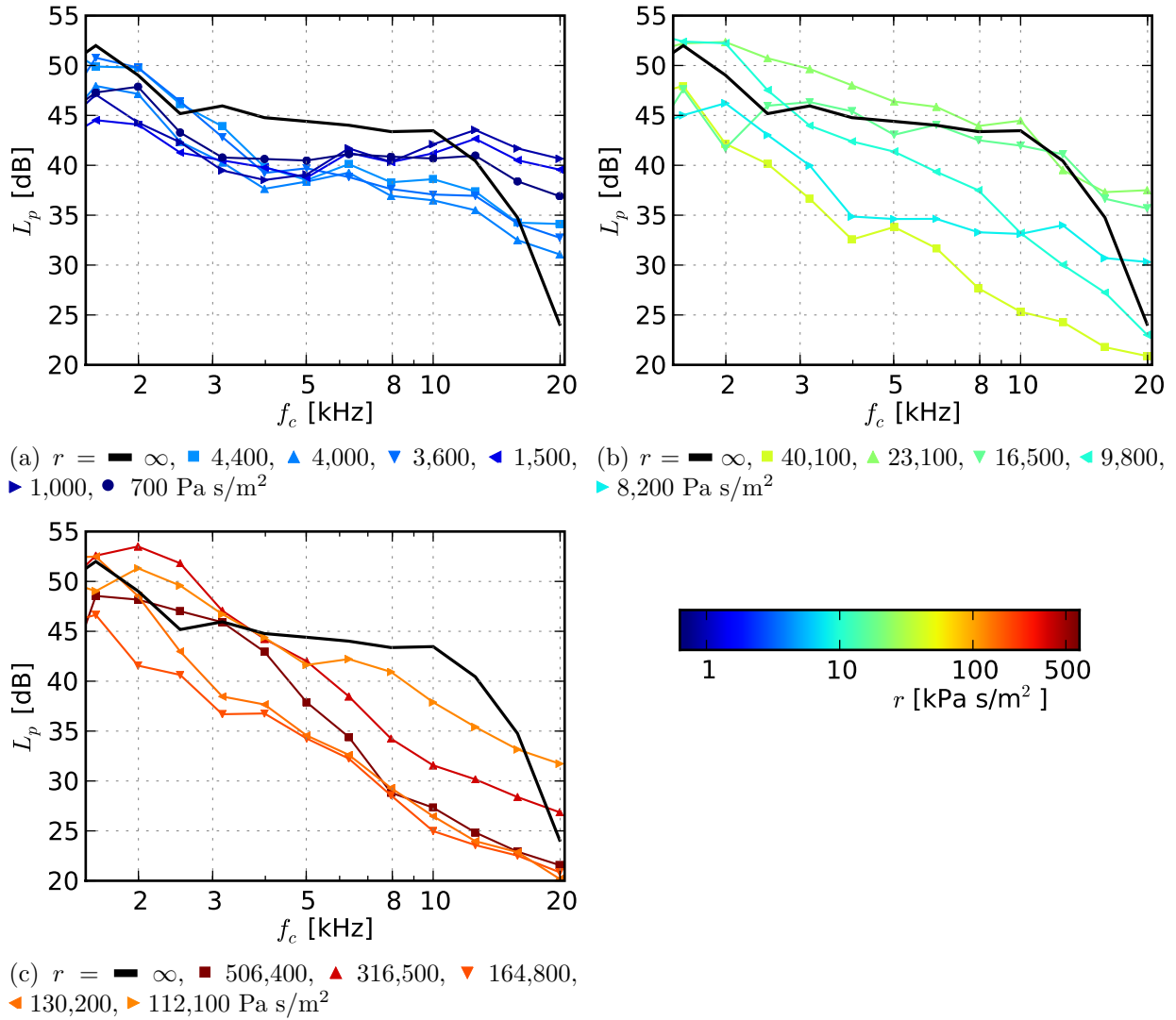


Figure 4.10: Third-octave band sound pressure levels (L_p) of the noise measured at the trailing edge of the airfoils as a function of frequency, angle of attack $\alpha = 0^\circ$ and flow speed $U_0 = 50 \text{ m/s}$ (The noise level of the non-porous reference airfoil is given as the black curve in each diagram.)

From Figure 4.10(a) it can be seen that basically the porous airfoils with low air flow resistivities lead to a maximum noise reduction in the order of 4 to 8 dB at low and medium frequencies. At high frequencies, approximately above 10 kHz, the sound pressure levels of the porous airfoils exceed the sound pressure level of the reference airfoil. This is assumed to be a contribution of surface roughness noise. This hypothesis is supported by the fact that the high frequency noise radiation seems to be stronger for airfoils with lower air flow resistivities, for example both M-Pore airfoils (M-Pore Al 45 ppi, $r = 1,000 \text{ Pa s/m}^2$ and M-Pore PU 45 ppi, $r = 1,500 \text{ Pa s/m}^2$) and the airfoil made of Panacell 45 ppi ($r = 700 \text{ Pa s/m}^2$), since these airfoils have larger pores and hence an increased surface roughness compared to the porous airfoils with higher air flow resistivities and smaller pores. This is in accordance to different roughness noise studies (see Section 2.3) in which it is reported that surface roughness noise becomes significant at high frequencies at which it may exceed the trailing edge noise.

The possible noise reduction that can be achieved by porous airfoils with medium air flow resistivities, presented in Figure 4.10(b), is higher than that for porous airfoils with low air flow resistivities. The maximum noise reduction exceeds 15 dB and was measured for the airfoil made of Needlona felt with an air flow resistivity of 40,100 Pa s/m². But it is also visible that the trailing edge noise of two of the porous airfoils exceed the trailing edge noise of the non-porous airfoil almost over the complete range of frequencies examined. These are the airfoil made of Arpro ($r = 23,100$ Pa s/m²) and the airfoil made of Reapor ($r = 16,500$ Pa s/m²).

The first material, as described in detail in Section 3.1.1, is an expanded polypropylene, the permeability of which is created only through gaps between the densely packed plastic beads. The open porosity of this material is noticeably below that of the other porous materials, which is assumed to be the reason for the increased trailing edge noise generation.

The second material, Reapor, is a porous glass granulate made of pellets of recycled glass, as mentioned in Section 3.1.1. The trailing edge of this airfoil is very fragile, and in some places it nearly consists of only one single layer of pellets. Hence, although due care has been taken in assembling the porous airfoils, it could not be avoided that some of the pellets broke out during the water cutting of the airfoil shape or the assembling of the complete airfoil out of single slices. This results in an irregular trailing edge and leads to an increase of the trailing edge thickness at several spanwise locations, which may be the reason for the increased trailing edge noise generation of the Reapor airfoil. Additionally, the open porosity of Reapor is also below that of most of the other porous materials, especially the foams.

The high frequency noise of the porous airfoils with medium air flow resistivities is less than that of the airfoils made of materials with low air flow resistivities. This further supports the theory that the high frequency part of the trailing edge noise of the porous airfoils is a contribution of surface roughness noise, since (as pointed out in Section 3.1.2) the airfoils with medium air flow resistivities in general have smaller pores than the airfoils with low air flow resistivities, and hence their surface is less rough.

As shown in Figure 4.10(c), the maximum trailing edge noise reduction which is possible using porous airfoils with high air flow resistivities is in the range of 10 to 15 dB and about the same as for airfoils with medium air flow resistivities (Figure 4.10(b)). At low frequencies some of the porous airfoils (for example the airfoil made of Porex, $r = 316,500$ Pa s/m², and the airfoil made of ArmaFoam Sound, $r = 112,100$ Pa s/m²) generate more trailing edge noise than the reference airfoil. The reason for the increased trailing edge noise of these airfoils is not clear yet.

Regarding the possibility of a contribution of surface roughness noise it can be seen that the porous airfoils with a high air flow resistivity (and hence small pores) lead to an even lower high frequency noise emission than that measured for the airfoils with medium and low air flow resistivities. This further supports the theory of the dominance of surface roughness noise in the trailing edge noise of the porous airfoils at high frequencies.

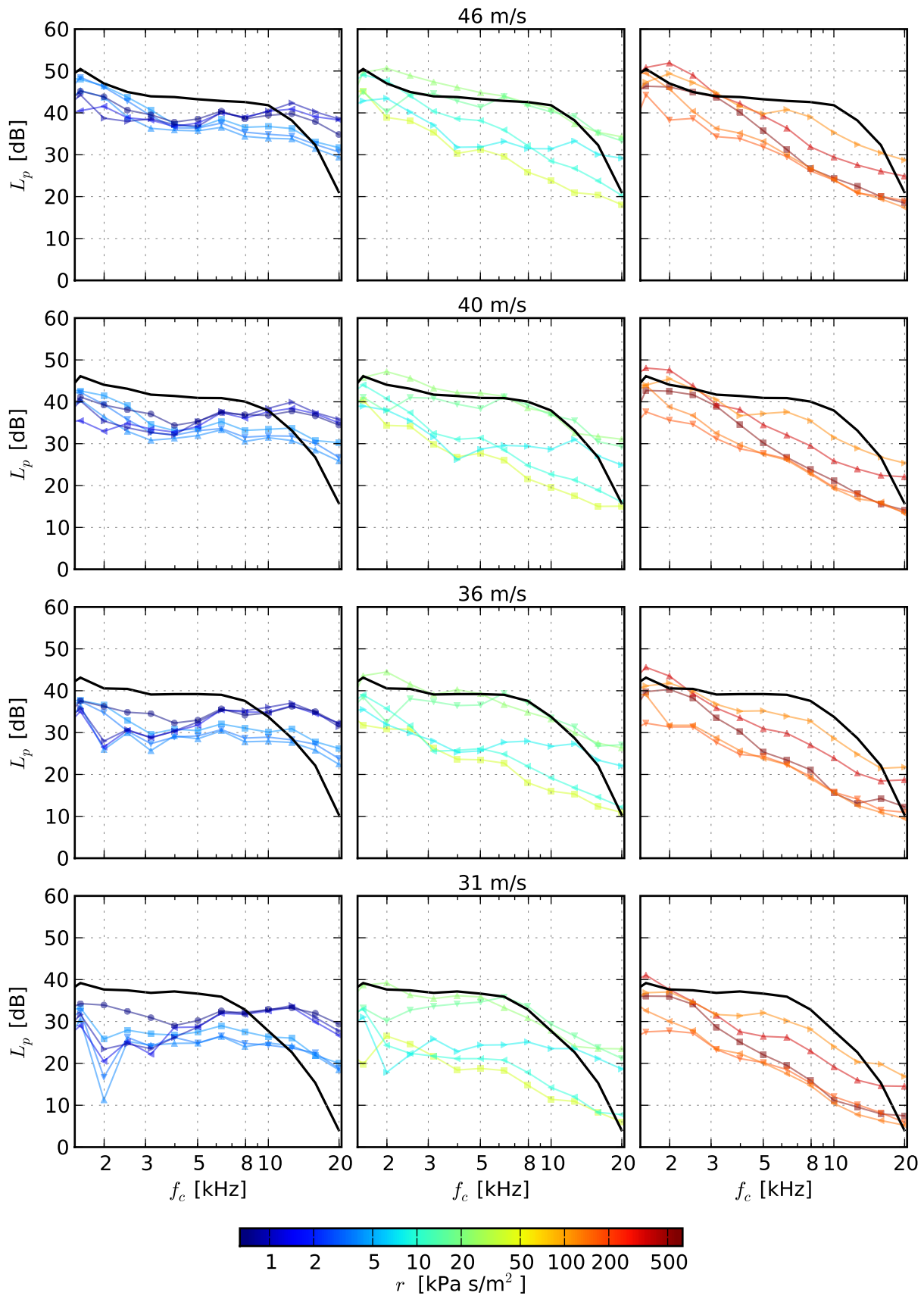


Figure 4.11: Third-octave band sound pressure levels (L_p) of the noise measured at the trailing edge of the airfoils at different flow speeds U_0 as a function of frequency, angle of attack $\alpha = 0^\circ$

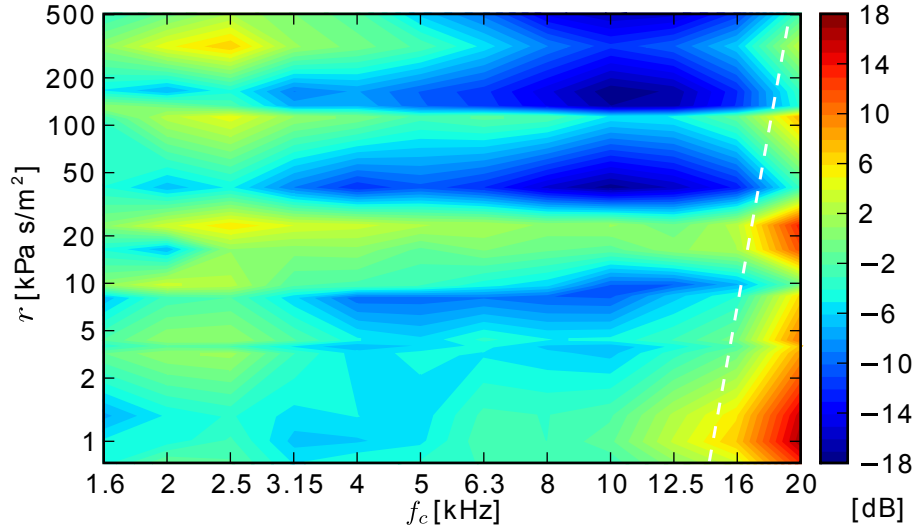


Figure 4.12: Trailing edge noise reduction of the porous airfoils compared to the non-porous airfoil ($L_{p,\text{por}} - L_{p,\text{ref}}$) in third-octave bands, angle of attack $\alpha = 0^\circ$, flow speed $U_0 = 50$ m/s

Similar to Figure 4.10, Figure 4.11 shows the trailing edge noise third-octave band sound pressure levels of all airfoils compared to the non-porous airfoil, but at different flow speeds U_0 from approximately 31 m/s to 46 m/s. The figures are given to point out that, apart from the shift of the bluntness noise peak center frequency of the reference airfoil, the spectral shape of the trailing edge noise is basically identical for all flow speeds in the examined range. At high flow speeds (as was observed for maximum flow speed) the porous airfoil made of Arpro, $r = 23,100$ Pa s/m², generates trailing edge noise that exceeds the trailing edge noise of the reference airfoil over nearly the complete range of frequencies analyzed, which does not occur at low flow speeds. The increased noise generation of the porous airfoils at high frequencies, especially the ones with low air flow resistivities, can again be seen. This becomes even more noticeable at low flow speeds due to the fact that the bluntness noise peak of the reference airfoil is shifted toward lower frequencies (and hence is the point where the spectrum starts decreasing strongly with increasing frequency).

The trailing edge noise reduction that can be achieved through the use of porous airfoils is given in Figure 4.12 exemplarily as a contour plot for a flow speed of 50 m/s and zero angle of attack. The noise reduction is given as the third-octave band sound pressure level difference between the trailing edge noise of the porous airfoils and the non-porous reference airfoil,

$$\Delta L_p = L_{p,\text{por}} - L_{p,\text{ref}} = 10 \cdot \log_{10} \left(\frac{\tilde{p}_{\text{ref}}^2}{\tilde{p}_{\text{por}}^2} \right), \quad (4.9)$$

where the index “ref” relates to the non-porous reference airfoil and the index “por” relates to the porous airfoils.

Figure 4.12 basically gives the same information as Figure 4.10(a) through 4.10(c), but it illustrates very well the frequency ranges where the porous airfoils lead to a noise reduction and the frequency ranges where the trailing edge noise of the porous airfoils exceeds that of the reference airfoil. At high frequencies the increase of noise supposedly due to the surface roughness of the porous airfoils becomes clearly visible. It is marked in Figure 4.12 by the dashed white line: The area to the right side of this line shows the assumed surface roughness noise contribution that exceeds the noise of the reference airfoil. The lower

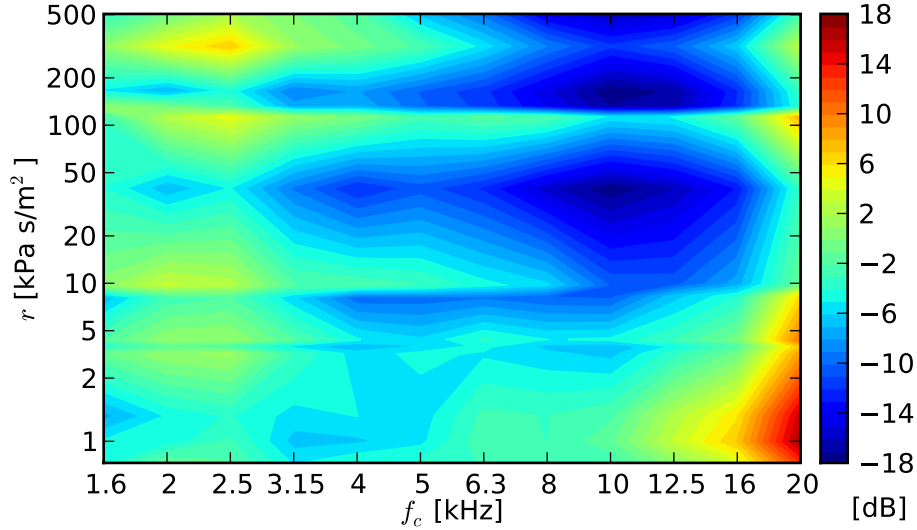


Figure 4.13: Trailing edge noise reduction of the porous airfoils, with the exception of the airfoils made of Arpro ($r = 23,100 \text{ Pa s/m}^2$) and Reapor ($r = 16,500 \text{ Pa s/m}^2$), compared to the non-porous airfoil ($L_{p,\text{por}} - L_{p,\text{ref}}$) in third-octave bands, angle of attack $\alpha = 0^\circ$, flow speed $U_0 = 50 \text{ m/s}$

frequency limit of this noise increases with increasing air flow resistivity and hence the white line has a positive slope.

Additional acoustic measurements on a set of porous airfoils with even higher air flow resistivities than the ones examined in the present study would be necessary to define the limit of the trailing edge noise reduction which is possible at medium frequencies. Obviously there has to be a drop in the noise reduction for further increasing air flow resistivities since the non-porous airfoil with $r = \infty$ does not provide any noise reduction at all.

When the sound pressure levels of the two porous airfoils made of Arpro and Reapor, that were found to result in an increased trailing edge noise level due to the very low volume porosity and the partly irregular trailing edge, respectively, are omitted, a possible noise reduction as given in Figure 4.13 can be achieved. The range of medium frequencies where the porous airfoils lead to a noticeable noise reduction can now be seen more clearly.

The third-octave band sound pressure levels of the trailing edge noise of all porous airfoils and the non-porous airfoil are presented in Figure 4.14 as a function of the chord based Strouhal number $f_c \cdot c_l / U_0$, scaled using Equation (4.8) with an exponent of $n = 4.5$. The same conclusions can be drawn as for the third-octave band spectra presented in Figure 4.10: Most of the porous airfoils generate trailing edge noise below that generated by the non-porous airfoil. At high Strouhal numbers the third-octave band sound pressure level of the non-porous airfoil decreases and the noise generated by the porous airfoils exceeds the noise of the reference airfoil, especially for airfoils with low air flow resistivities. Again, the porous airfoil made of Arpro ($r = 23,100 \text{ Pa s/m}^2$) generates more noise than the reference airfoil over a large range of Strouhal numbers, as already observed from Figure 4.10 and Figure 4.11.

It becomes evident that the chosen scaling approach, while giving good results for the non-porous airfoil, does not generally fit for the data of all porous airfoils. This can be concluded from the fact that the scaled trailing edge noise of the reference airfoil collapses to a smooth

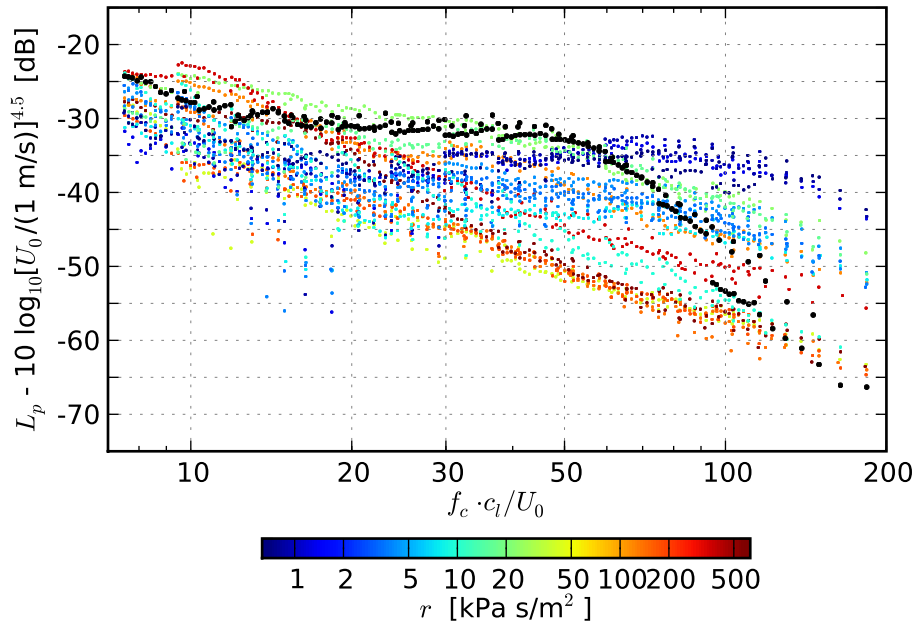


Figure 4.14: Trailing edge noise third–octave band sound pressure levels as a function of chord based Strouhal number, scaled based on $U_0^{4.5}$, angle of attack $\alpha = 0^\circ$.

curve while the curves of most of the porous airfoils are more scattered. Nevertheless, for some porous airfoils this approach seems to be a good first guess.

The curves of the scaled third–octave band sound pressure levels of the porous airfoils and the non–porous airfoil as a function of the chord based Strouhal number are again presented in Figure 4.15, but with separate plots for each airfoil. For the purpose of comparison, the trailing edge noise of the porous airfoils is also scaled with $U_0^{4.5}$ and the spectrum of the reference airfoil is indicated in each plot. The single figures indicate that the chosen scaling approach delivers smooth plots most notably for porous airfoils characterized by a high air flow resistivity. For porous airfoils with low air flow resistivities a noticeable scatter can be seen mainly for low Strouhal numbers.

When discussing the velocity scaling of the porous airfoils, the influence of the increased trailing edge thickness of the porous airfoils of 1.59 mm has to be taken into account. According to the study by Brooks and Hodgson [Brooks and Hodgson, 1981] a blunt trailing edge leads to a noticeable increase of the scaling exponent (for the 2.5 mm thick trailing edge Brooks and Hodgson found a scaling exponent of 5.3 compared to 5.07 for the sharp trailing edge).

Furthermore, Figure 4.15 shows that for many of the porous airfoils (e.g. M&K felt, 0.22 g/cm^3 , $r = 164,800 \text{ Pa s/m}^2$, Needlona felt, SO 2002, $r = 130,200 \text{ Pa s/m}^2$, Needlona felt, WO–PE 1958, $r = 40,100 \text{ Pa s/m}^2$, Recemat, $r = 8,200 \text{ Pa s/m}^2$, Balzer RG 3550, $r = 4,400 \text{ Pa s/m}^2$, Panacell 90 ppi, $r = 4,000 \text{ Pa s/m}^2$, Panacell 60 ppi, $r = 3,600 \text{ Pa s/m}^2$, M–Pore PU 45 ppi, $r = 1,500 \text{ Pa s/m}^2$, M–Pore Al 45 ppi, $r = 1,000 \text{ Pa s/m}^2$) there are noticeable deviations for a few single sound pressure levels measured at low flow speeds and low frequencies, especially at the 2 kHz third–octave band of the trailing edge noise of airfoils with low air flow resistivities (as also visible in Figure 4.11). These sound pressure levels are 5 to 10 dB lower than those of neighboring points at lower and higher Strouhal numbers and hence they clearly fall short of the expected spectral shape. The reason for

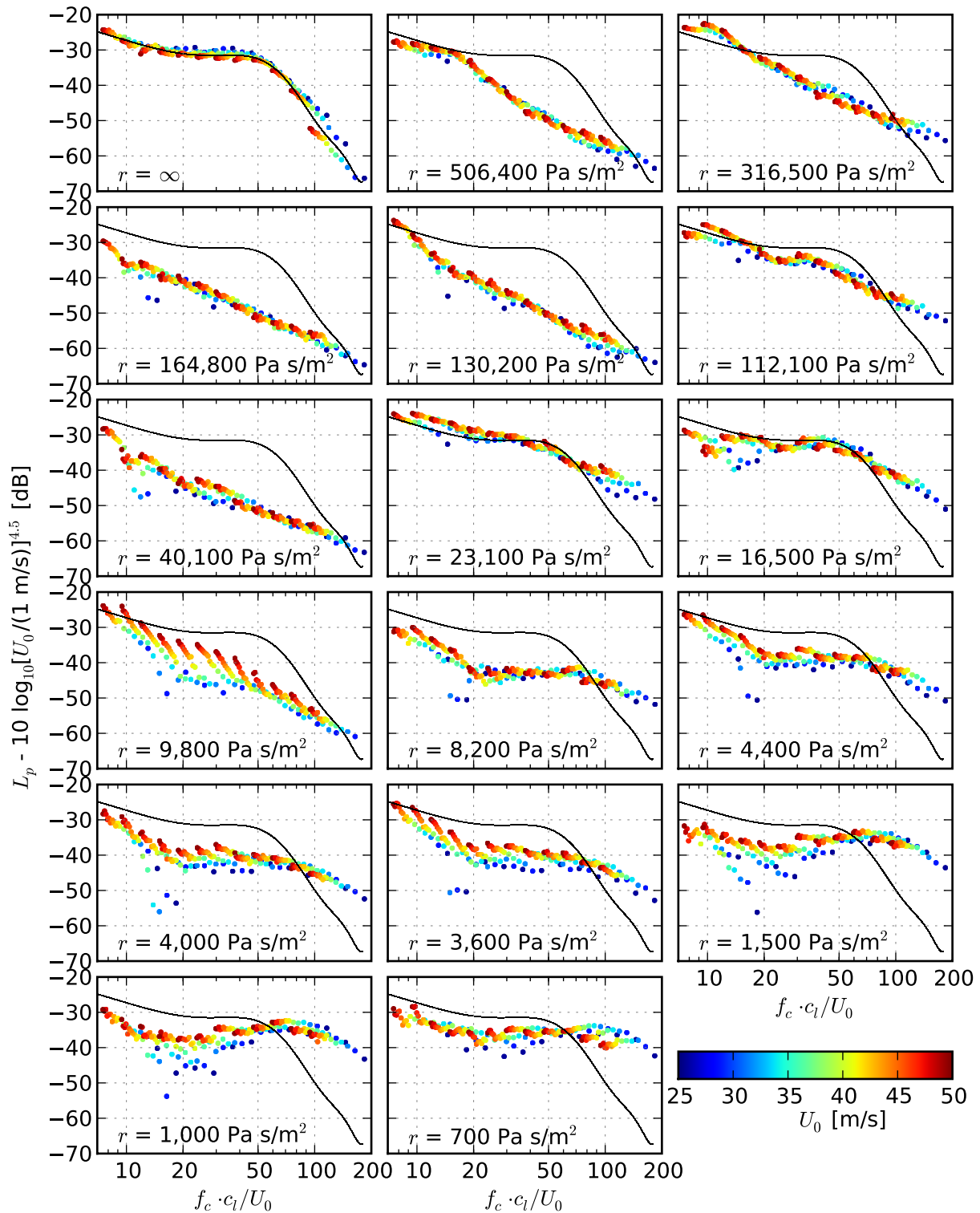


Figure 4.15: Trailing edge noise third-octave band sound pressure levels as a function of chord based Strouhal number, scaled based on $U_0^{4.5}$, angle of attack $\alpha = 0^\circ$ (the black line indicates the curve for the non-porous airfoil as a reference; the colors are assigned to the flow speed U_0)

these deviations is not clear. The examination of corresponding three-dimensional sample sound maps did not show any significant discrepancies that may explain the low trailing edge noise levels.

Additional measurements using the wind tunnel nozzle with a diameter of 0.35 m [Sarradj et al., 2009] would be reasonable since they would provide the opportunity to examine a larger trailing edge noise sector with an increased spanwise extent and would possibly lead to further conclusions regarding the cause of the drop of the measured noise levels.

To include in the analysis of the trailing edge noise generation the aerodynamic performance of the different airfoils, the third-octave band sound pressure levels were further scaled using the measured lift forces. This method was employed in different empirical flight noise studies (see Section 2.2.1), as for example in the work of Lasagna et al. [Lasagna et al., 1980], summarized by Equation (2.9), or in the work of Lilley [Lilley, 1998], summarized by Equation (2.15). The resulting scaling approach used in the present study is given by

$$L_{p,\text{scaled}} = L_p - 10 \cdot \log_{10} \left(\frac{U_0}{1 \text{ m/s}} \right)^{2.5} - 10 \cdot \log_{10} \left(\frac{F_L}{1 \text{ kg m/s}^2} \right) \text{ [dB]}. \quad (4.10)$$

As can be seen, this approach still contains the overall $U_0^{4.5}$ velocity scaling since $F_L \propto U_0^2$. The scaling allows for an evaluation of the trailing edge noise generation of the porous airfoils under consideration of their reduced lift force generation, because, as explained at the beginning of Section 4.1, the use of porous airfoils in technical applications can only be of interest if their aerodynamic efficiency is not much smaller than that of a common non-porous airfoil. The scaling given in Equation 4.10 takes into account the aerodynamic efficiency of the porous airfoils in terms of the measured lift force and hence yields the trailing edge noise generated by the corresponding airfoil per unit lift force (here equal to 1 N).

The resulting trailing edge noise third-octave band sound pressure levels of the airfoils, scaled using Equation (4.10), are presented in Figure 4.16. The inclusion of the lift force in the scaling shows that only porous airfoils with medium to high air flow resistivities r generate less trailing edge noise per unit lift force than the reference airfoil. As examined in Section 4.1, this is due to the fact that the generated lift force increases with increasing air flow resistivity. Porous airfoils with a low air flow resistivity may originally lead to a noticeable noise reduction at low and medium frequencies, as was shown above, but due to the severe losses in aerodynamic performance they generate more trailing edge noise per unit lift force than the non-porous airfoil. The porous airfoils that generate less trailing edge noise per unit lift force compared to the non-porous airfoil are airfoils with medium and high air flow resistivities, approximately starting with the airfoil made of Needlona felt SO 2002 ($r = 40,100 \text{ Pa s/m}^2$). The lower limit of the air flow resistivity of porous airfoils resulting in a reduction of the trailing edge noise radiation under consideration of the generated lift force is approximately between that of the airfoil made of Arpro and that of the airfoil made of the Needlona felt and hence between about $25,000 \text{ Pa s/m}^2$ and $40,000 \text{ Pa s/m}^2$.

For some of these porous airfoils with air flow resistivities above 25 to 40 kPa s/m² the maximum possible noise reduction is still in the order of 15 dB at medium chord based Strouhal numbers. Once again this gives evidence to the noticeable noise reduction capability inherent to the porous airfoils. Especially in applications for which the efficiency is not

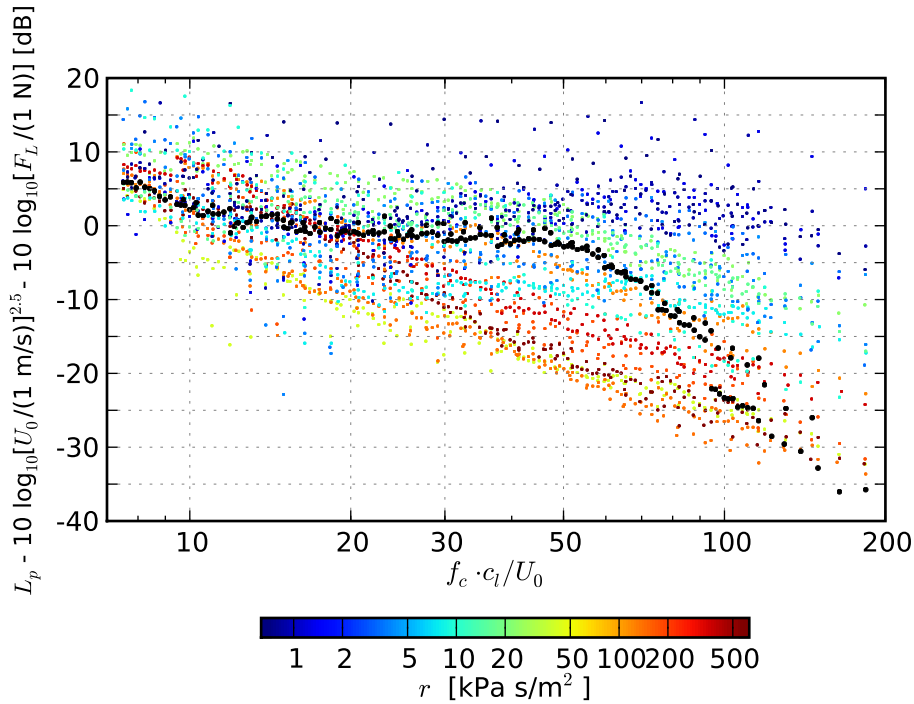


Figure 4.16: Trailing edge noise third-octave band sound pressure levels as a function of chord based Strouhal number, scaled based on $U_0^{2.5}$ and the measured lift force F_L , angle of attack $\alpha = 0^\circ$.

the crucial factor and for which a certain surface roughness of the trailing edge is tolerable, as for example fans in electrical systems or small wind turbines, the use of porous or partly porous airfoils (the latter referring to airfoils with a non-porous leading edge but a porous trailing edge) may provide an adequate way to reduce trailing edge noise.

A possible way to further increase the noise reduction of porous treatments may be the use of porous materials with an air flow resistivity that varies along the chordwise extent of the treatment, as already proposed by Fink and Bailey [Fink and Bailey, 1980]. It can be assumed that it is beneficial for the aerodynamic efficiency if the air flow resistivity of the porous airfoils decreases with increasing distance from the leading edge, so that a large extent of the airfoil is nearly non-permeable and only the aft part of the airfoil has a lower air flow resistivity.

What has to be kept in mind when analyzing the trailing edge noise generation of the porous airfoils in comparison to the non-porous airfoil is the absence of low frequency noise data below 1.5 kHz due to the non-compactness condition regarding the present measurement setup as formulated in Equation (1.2). Additionally, the increasing width of the array main lobe with decreasing frequency prevents accurate source separation at lower frequencies. This is especially important considering the small width of the trailing edge sector of 0.12 m.

Thus, it is not possible to examine the noise generation at frequencies below approximately 1.5 kHz. According to theory, the trailing edge noise spectra of common airfoils have a peak at a relatively low frequency (or Strouhal number). For example, according to the trailing edge noise model developed by Fink [Fink, 1977] the peak center frequency can be calculated from the flow speed, the boundary layer thickness and a Strouhal number (based

on boundary layer thickness) of approximately 0.1. The same peak Strouhal number was given by Schlinker and Amiet [Schlinker and Amiet, 1981] and subsequently also applied by Grosveld [Grosveld, 1985]. Using this relation and the turbulent boundary layer thickness as calculated by XFOIL [Drela, 1989] for the non-porous airfoil of the present study, which is approximately 6.5 mm for the suction side turbulent boundary layer, a peak frequency of approximately 770 Hz can be calculated for the maximum flow speed of 50 m/s. For lower flow speeds this peak frequency is even lower and clearly below the lower frequency limit of the acoustic measurement setup of the present study.

Interestingly, the use of a peak Strouhal number based on boundary layer thickness of 0.25 or 0.3, as proposed by Brooks and Marcolini [Brooks and Marcolini, 1985], would lead to a peak center frequency approximately between 2 kHz and 2.5 kHz as predicted by the BPM-model and shown in Figure 4.7(a). However, a distinct spectral peak at this frequency range cannot be observed in the measured trailing edge noise spectra presented in Figure 4.10.

Besides the fact that the trailing edge noise spectral peak of the non-porous airfoil is assumed to be below the lower frequency limit of the measurement setup, there is no information available in the literature on how the consistency of porous airfoils or porous trailing edges affects such a peak.

One possible scenario is that the peak frequency or peak Strouhal number is independent of the porous consistency and remains constant for each airfoil. The peak frequency would then be characterized only by the flow speed and a characteristic dimension (possibly in relation to the airfoil chord length) which can be assumed to be constant for all airfoils of constant shape and dimension and hence independent of the porous consistency. According to the trailing edge noise prediction models mentioned above, which are of course designed for common, non-porous airfoils only, this parameter may be the thickness of the turbulent boundary layer. Based on the present measurements, the assumption of a constant peak frequency would imply that the noise reduction measured at medium frequencies for most of the porous airfoils would be a mere detail of a general noise reduction over the complete range of frequencies. The trailing edge noise spectra of the porous airfoils would simply have a lower amplitude but they would not be shifted toward higher or lower frequencies compared to the non-porous airfoil.

Another possibility is that the spectral peak of the porous airfoils shifts toward higher frequencies compared to the peak measured for the non-porous airfoil. But this seems very unlikely since no such peak was detected in the measured spectra.

The third possibility, a shift of the spectral peak of the trailing edge noise generated by the porous airfoils toward lower frequencies, would indicate that the measured noise reduction at medium frequencies is accompanied by an increase of the trailing edge noise at very low frequencies (< 1.5 kHz). Low frequency noise contains much energy, which means that, considering the complete range of frequencies, the use of porous airfoils does not lead to a noise reduction but may even lead to an increase of the overall sound pressure level compared to the non-porous airfoil.

The absence of low frequencies in the measured trailing edge noise spectra is also the reason why no overall sound pressure level $L_{p,\text{tot}}$ was calculated from the three-dimensional beamforming results. And since several noise prediction models, first and foremost models for the prediction of flyover noise generated by complete aircraft (as discussed in Section

2.2), involve the knowledge of the overall sound pressure level or the knowledge of the frequency of the trailing edge peak, their usability cannot be tested for the porous airfoils.

One additional property which characterizes the porous materials and whose influence has yet to be discussed is the elasticity of the porous airfoils. A large number of the materials used for the manufacturing of the porous airfoils in the present study (given in Table 3.1) is elastic. These are mainly the airfoils made of felts and polyurethane foams. The only airfoils which are rigid even at the thin trailing edge are the airfoils made of Porex ($r = 316,500 \text{ Pa s/m}^2$), Reapor ($r = 16,500 \text{ Pa s/m}^2$), Recemat ($r = 8,200 \text{ Pa s/m}^2$), M-Pore PU 45 ppi ($r = 1,500 \text{ Pa s/m}^2$) and M-Pore Al 45 ppi ($r = 1,000 \text{ Pa s/m}^2$). For this reason, four of these airfoils were used for the hot-wire measurements.

As can be seen from the trailing edge noise spectra of the porous airfoils, especially when scaled with the measured lift force as presented in Figure 4.16, no noticeable dependence on the elasticity can be observed. This means that the airfoils which generate less trailing edge noise per unit lift force than the non-porous reference airfoil can clearly be characterized by their air flow resistivity (and to a lesser extent by their open porosity), but cannot easily be described as belonging to either elastic or rigid airfoils. The set of porous materials leading to the highest noise reduction per unit lift force consists of airfoils with medium and high air flow resistivities, meaning felts and synthetic foams. These airfoils may either be rigid (Porex) or elastic (M&K felts, Needlona felts).

Although additional experiments would be reasonable to exactly determine the elasticity of each airfoil and, more important, its impact on the trailing edge noise generation, it is concluded that within the scope of this thesis the elasticity is not considered being a basic parameter influencing the noise generation at the trailing edge. This assumption is further confirmed by the work of Bohn [Bohn, 1976], who performed acoustic measurements and vibration measurements on flat plates with porous trailing edge extensions and found that the decrease of the trailing edge noise caused by the porous edges is not related to the thickness or rigidity of the materials.

4.3 Constant temperature anemometry measurements

In the following section, the results of the hot-wire anemometry measurements that were performed in the turbulent boundary layer of four porous airfoils and the non-porous reference airfoil (see Table 3.2) will be presented. It is assumed that the trailing edge noise reduction that can be achieved through the use of porous airfoils instead of a non-porous airfoil of the same shape is accompanied by noticeable differences of the turbulent boundary layer parameters. Some of the results that will be shown in the following section were already presented in reference [Geyer et al., 2010b].

4.3.1 Velocity profiles

Figure 4.17 through Figure 4.21 show the velocity profiles $\bar{u}(z)$ near the surface of the five airfoils, measured at eleven positions along the chord and at two positions in the wake (measurement positions shown in Figure 3.27) for a flow speed of approximately 50 m/s and an angle of attack of 0° . The velocity profiles at the suction side of each airfoil are given in the upper figure, while the lower figure shows the velocity profiles measured at the pressure side of the airfoil.

The figures provide a qualitative overview of the boundary layer thickness δ , defined as the vertical distance z at which the velocity reaches 99 % of the (free stream) flow speed. Practically it is very difficult to calculate the exact value of the boundary layer thickness due to the asymptotic shape of the velocity profile near the edge of the boundary layer. However, it can be seen from the figures that the boundary layer thickness δ increases with decreasing air flow resistivity r of the porous airfoils. The non-porous airfoil, with an air flow resistivity of infinity, develops the smallest boundary layer thickness, while the porous airfoil with the lowest air flow resistivity (M-Pore Al 45 ppi, $r = 1,000 \text{ Pa s/m}^2$) develops the thickest turbulent boundary layer.

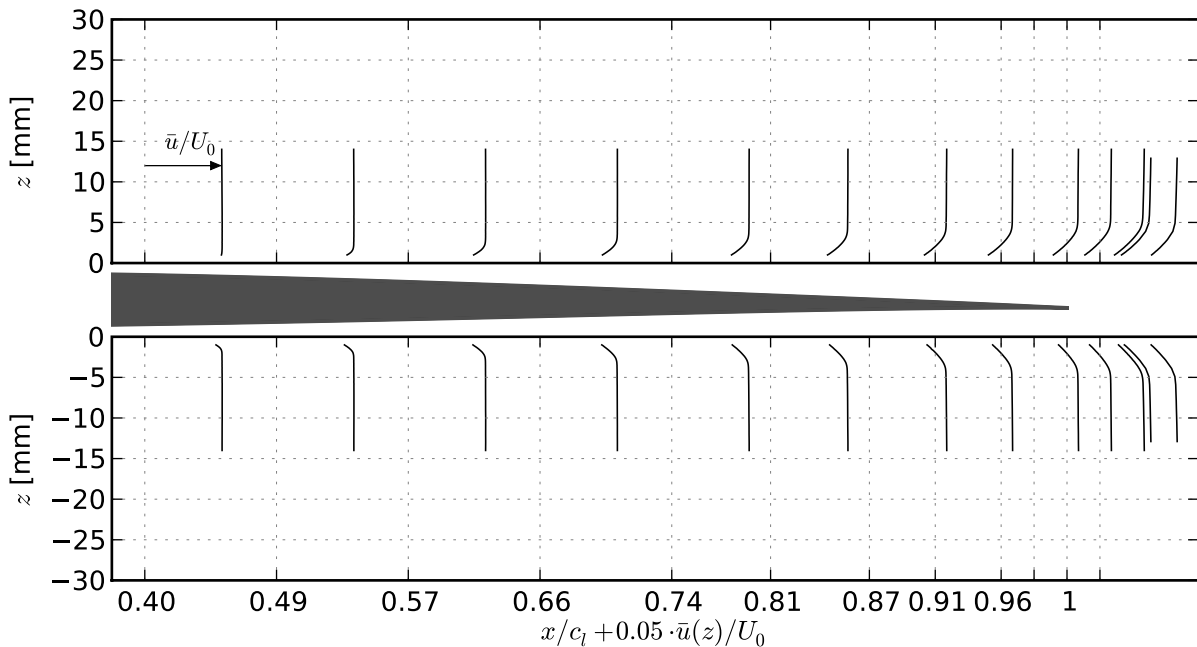


Figure 4.17: Measured boundary layer velocity profiles near the surface of the non-porous reference airfoil, $r = \infty$, flow speed $U_0 = 50 \text{ m/s}$, angle of attack $\alpha = 0^\circ$ (The gray shape in the middle of the figure indicates the airfoil relative to the chord (x -) position of the measurements. Note that this schematic is given for illustrative purposes only, the distance given on the ordinate refers to the airfoil surface as origin.)

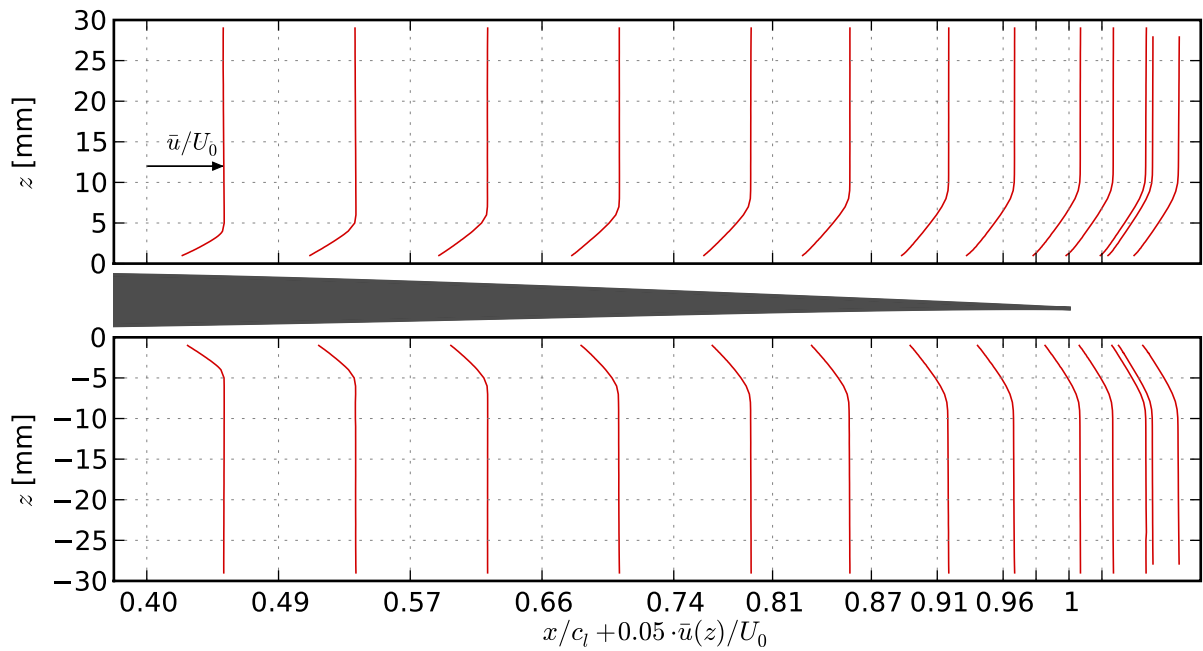


Figure 4.18: Measured boundary layer velocity profiles near the surface of the airfoil made of Porex, $r = 316,500 \text{ Pa s/m}^2$, flow speed $U_0 = 50 \text{ m/s}$, angle of attack $\alpha = 0^\circ$

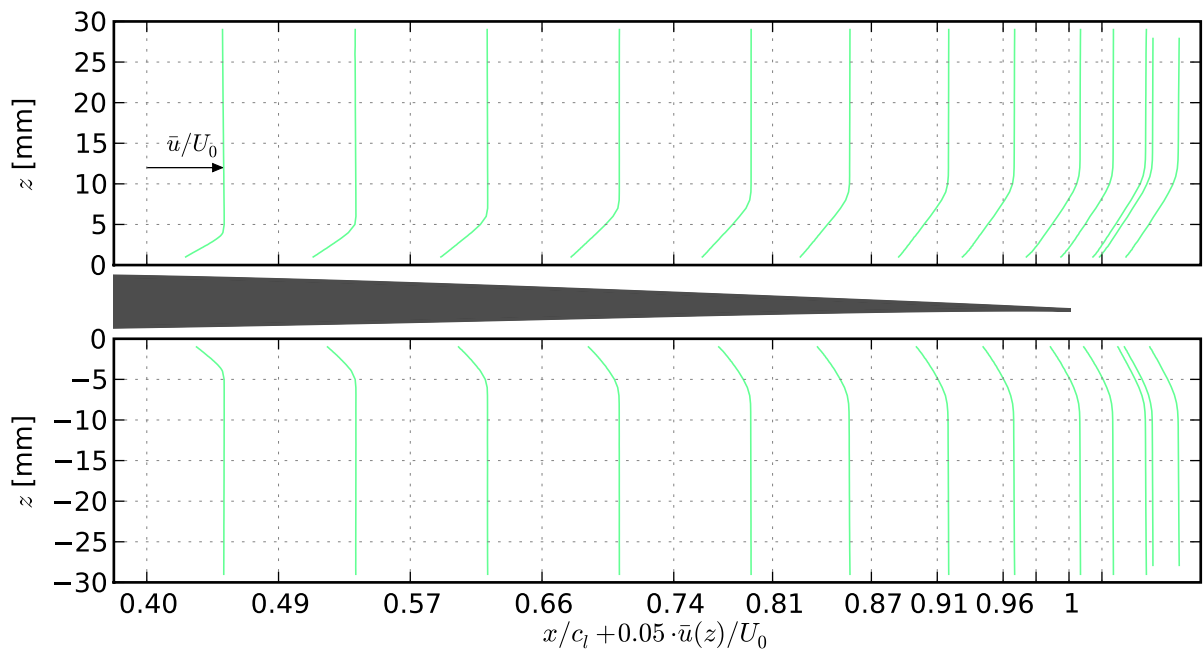


Figure 4.19: Measured boundary layer velocity profiles near the surface of the airfoil made of Reapor, $r = 16,500 \text{ Pa s/m}^2$, flow speed $U_0 = 50 \text{ m/s}$, angle of attack $\alpha = 0^\circ$

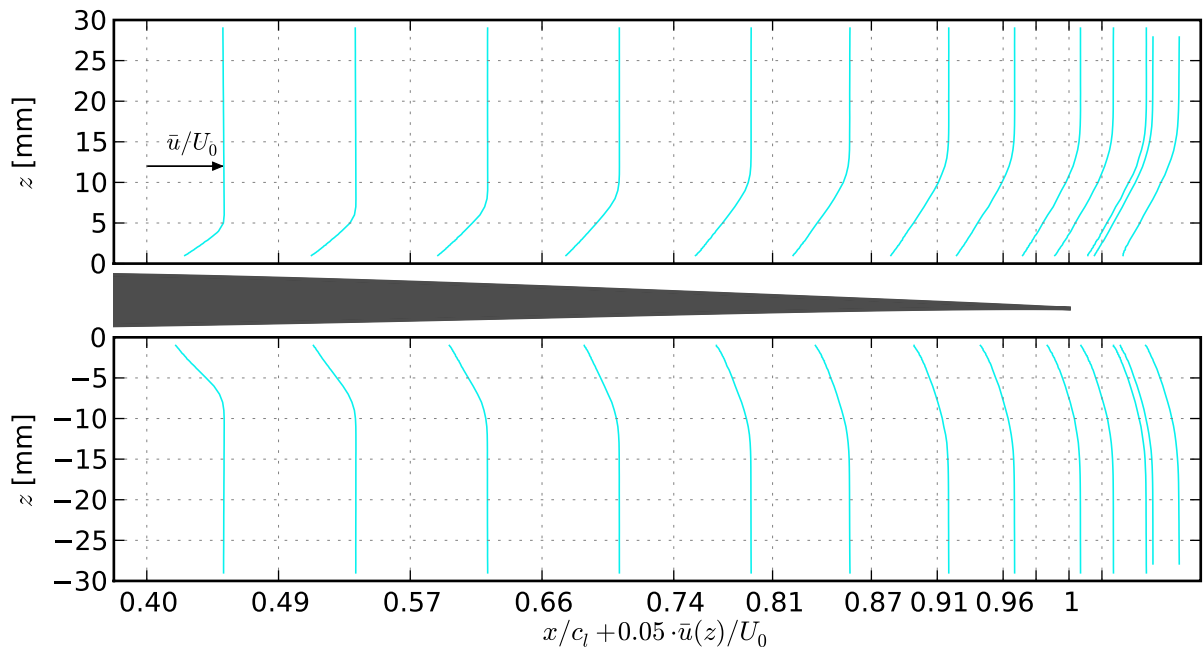


Figure 4.20: Measured boundary layer velocity profiles near the surface of the airfoil made of Recemat, $r = 8,200 \text{ Pa s/m}^2$, flow speed $U_0 = 50 \text{ m/s}$, angle of attack $\alpha = 0^\circ$

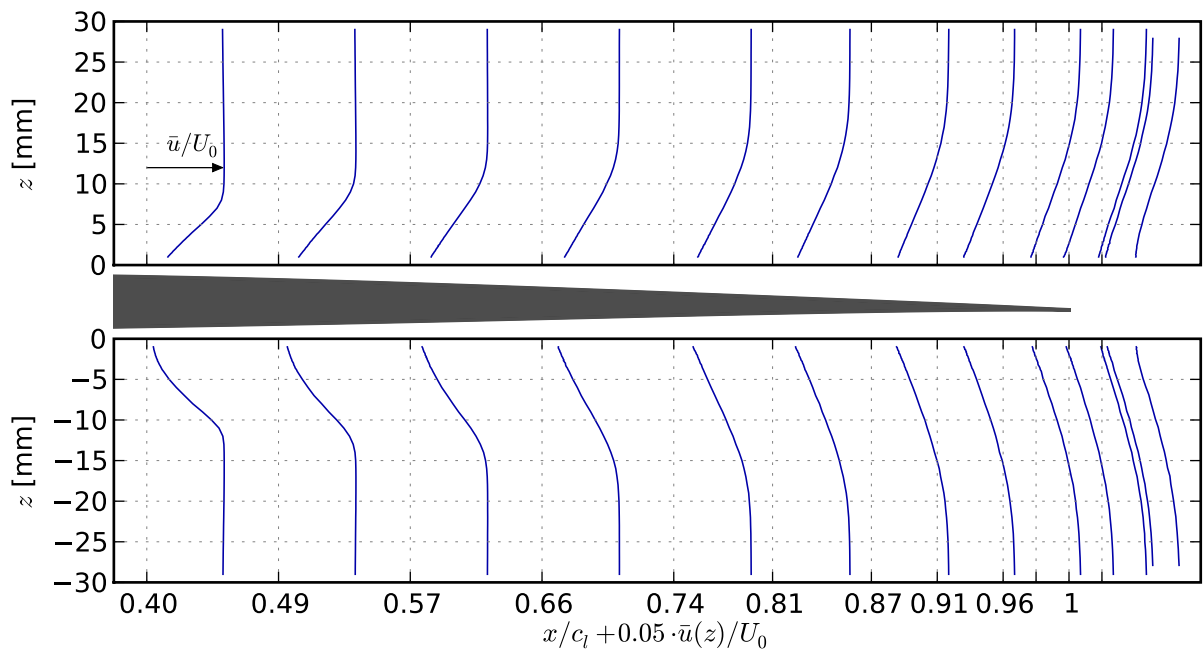


Figure 4.21: Measured boundary layer velocity profiles near the surface of the airfoil made of M-Pore Al 45 ppi, $r = 1,000 \text{ Pa s/m}^2$, flow speed $U_0 = 50 \text{ m/s}$, angle of attack $\alpha = 0^\circ$

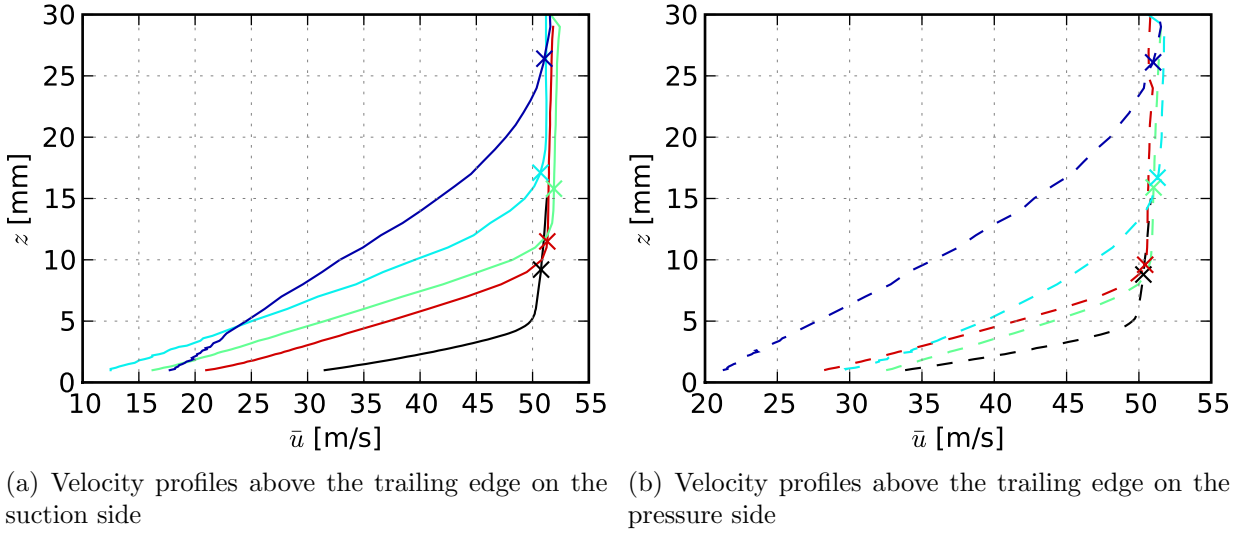


Figure 4.22: Measured velocity profiles above the trailing edge at $x/c_l = 1$, flow speed $U_0 = 50$ m/s, angle of attack $\alpha = 0^\circ$ ($r = \infty$, $\color{red}{\blacksquare}$ 316,500, $\color{green}{\blacksquare}$ 16,500, $\color{cyan}{\blacksquare}$ 8,200, $\color{blue}{\blacksquare}$ 1,000 Pa s/m²). The “x” markers denote the boundary layer thickness δ , obtained by a spline fit.

In order to overcome the difficulty of a direct calculation of the boundary layer thickness from the measured velocity profiles, the values of the turbulent boundary layer thickness were estimated using an interpolation of the measured velocity profiles $\bar{u}(z)$ above the trailing edge by a spline fit $U'(z)$. Subsequently, the distance from the airfoil surface where $U'(z) = 0.99 U_0$ was determined from the fitted curves. Figure 4.22 shows the velocity profiles measured directly above the trailing edge and the corresponding boundary layer thicknesses. Still, it has to be noted that the determination of the boundary layer thickness using this method remains a mere estimation.

The boundary layer thickness δ , measured at a flow speed of 50 m/s, is given in Figure 4.23(a) as a function of the viscous permeability k_v of the airfoils. Figure 4.23(b) then shows the turbulent boundary layer thickness measured at the trailing edge of the porous airfoils, δ_{por} , normalized to the boundary layer thickness of the reference airfoil at the same flow speed, δ_{ref} ,

$$\delta_n = \frac{\delta_{\text{por}}}{\delta_{\text{ref}}}, \quad (4.11)$$

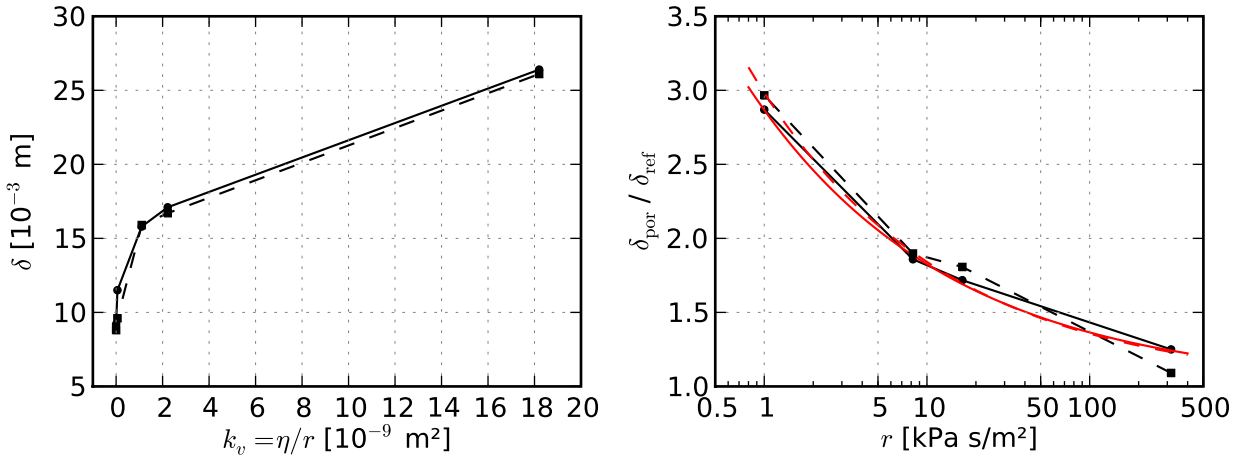
as a function of the air flow resistivity r for both suction side and pressure side. Figure 4.23(b) basically shows the same trend that was already qualitatively derived from the velocity profiles of the porous airfoils (Figure 4.17 through 4.21) and from Figure 4.22: For increasing air flow resistivity r of the porous airfoils the boundary layer thickness δ decreases.

Also given in Figure 4.23(b) is an exponential least squares fit to approximate the normalized turbulent boundary layer thickness of a porous airfoil as a function of its air flow resistivity r :

$$\delta_n(r) = 21.611 \cdot \exp(-0.816 \cdot \log_{10} r) + 1 = 21.611 \cdot r^{-\frac{0.816}{\ln 10}} + 1 \quad (4.12)$$

for the boundary layer thickness at the suction side and

$$\delta_n(r) = 26.006 \cdot \exp(-0.858 \cdot \log_{10} r) + 1 = 26.006 \cdot r^{-\frac{0.858}{\ln 10}} + 1 \quad (4.13)$$



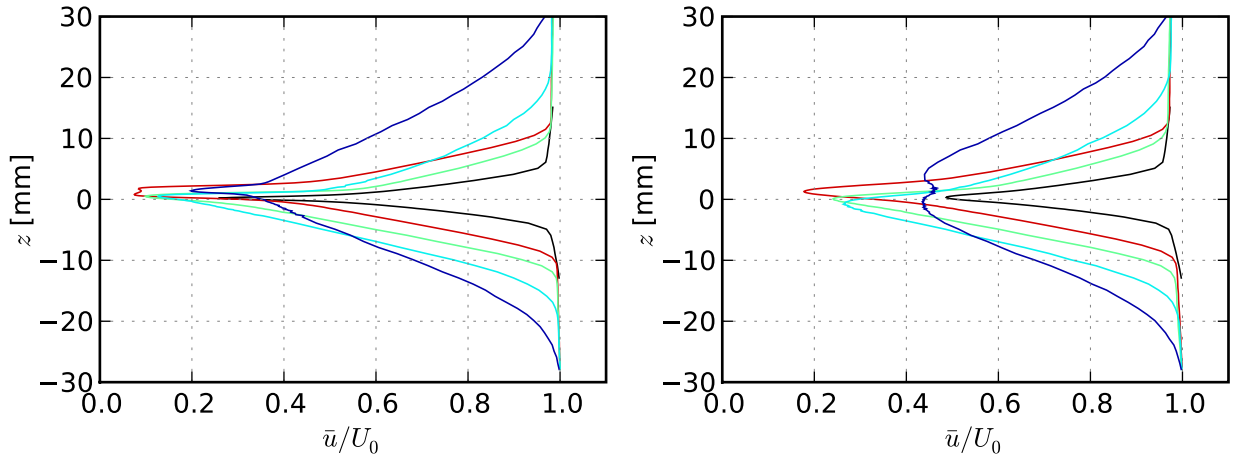
(a) Measured boundary layer thickness of the airfoils as a function of the viscous permeability k_v (with $\eta = 18.2 \cdot 10^{-6}$ kg/(m s) at 22°C) (b) Normalized boundary layer thickness δ_n according to Equation (4.11) \blacksquare and exponential fit $\color{red}\blacksquare$ as a function of air flow resistivity r

Figure 4.23: Boundary layer thickness δ of the airfoils, measured at zero angle of attack and a flow speed of 50 m/s (solid line: suction side, dashed line: pressure side)

for the thickness of the turbulent boundary layer measured at the pressure side of the airfoils. The boundary layer thickness above the trailing edge of the non-porous airfoil is approximately 9.2 mm for the suction side and 8.8 mm for the pressure side, corresponding to the values given in Figure 4.22 (the values predicted by XFOIL [Drela, 1989] would be 6.5 mm and 5.5 mm, respectively).

Equation (4.12) and (4.13) are basic estimations that were obtained for the examined range of air flow resistivities between approximately 700 Pa s/m² and 500 kPa s/m² at a flow speed of 50 m/s. A validity of these equations below or above this range of air flow resistivities was not tested and cannot be guaranteed.

The normalized velocity profiles $\bar{u}(z)/U_0$ measured in the wake of the airfoils are presented in Figure 4.24(a) for a distance of 1 mm behind the trailing edge and in Figure 4.24(b) for a distance of 5 mm behind the trailing edge. As also observed in Figure 4.17 through 4.21, it can be seen from Figure 4.24(a) and Figure 4.24(b) that the boundary layer thickness δ increases with decreasing air flow resistivity r of the porous materials. More precisely, at the pressure side ($z < 0$) the order of the measured boundary layer thicknesses (from lower to higher values: non-porous airfoil, Porex, Reapor, Recemat, M-Pore) is exactly consistent with the reversed order of the air flow resistivities r of the corresponding porous materials (see Table 3.2), while at the suction side ($z > 0$) the boundary layer thickness of the airfoil made of Porex ($r = 316,500$ Pa s/m²) is smaller than that of the airfoil made of Reapor ($r = 16,500$ Pa s/m²), despite its higher air flow resistivity. The exact cause of this effect is not clear yet, but one possibility may be some unevenness on the suction side surface of the airfoil made of Reapor, which could not be noticed visually. This is not implausible considering that Reapor consists of grouted porous glass pellets. Even differences in the microstructure of both materials may be responsible. Additionally, as was mentioned in Section 4.2.2, the trailing edge of the airfoil made of Reapor is not as regular as that of the other porous airfoils due to some of the pellets of the porous glass granulate breaking out during the assembling of the airfoil, which may add to the effect of its increased boundary layer thickness.



(a) Measured velocity profiles in the wake (1 mm behind the airfoil trailing edge) (b) Measured velocity profiles in the wake (5 mm behind the airfoil trailing edge)

Figure 4.24: Measured velocity profiles in the wake, flow speed $U_0 = 50$ m/s, angle of attack $\alpha = 0^\circ$ ($r = \infty$, $\color{red}{\blacksquare}$ 316,500, $\color{green}{\blacksquare}$ 16,500, $\color{cyan}{\blacksquare}$ 8,200, $\color{blue}{\blacksquare}$ 1,000 Pa s/m²). Note that the given distance in the vertical direction relates to the upper side of the trailing edge.

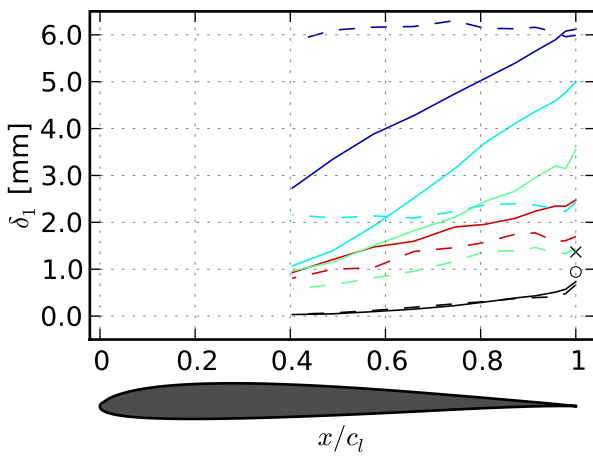
Another effect can be seen in Figure 4.24(a) and 4.24(b): The porous consistency of the airfoils has an influence on the shape of the wake velocity profiles. This is especially visible for the airfoil made of M-Pore Al 45 ppi, the material with the lowest air flow resistivity of 1,000 Pa s/m², where a noticeable increase of the flow velocity directly behind the trailing edge was measured. This increased velocity is assumed to be caused by an internal flow inside the porous airfoil. Some of the resulting wake velocity profiles therefore resemble, at least to a certain degree, the velocity profiles that may be achieved through airfoil trailing edge blowing [Winkler et al., 2009].

Figure 4.22 and especially Figure 4.24(a) and 4.24(b) indicate that despite a presumable flow inside the porous materials the velocity $\bar{u}(z)$ directly at the surface of the porous airfoils ($z = 0$) is very small, although not necessarily equal to zero as can be assumed according to aerodynamic theory for the non-porous reference airfoil.

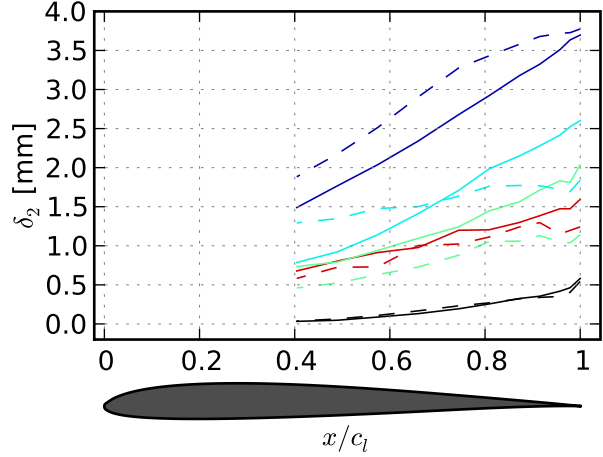
It remains to be fully clarified how much of the increase of the turbulent boundary layer thickness is due to the permeability of the materials and how much is solely due to the increased surface roughness of the porous airfoils compared to the non-porous airfoil. To this end, measurements on non-porous airfoils with an increased surface roughness similar to that of the porous airfoils would be necessary.

4.3.2 Boundary layer integral parameters

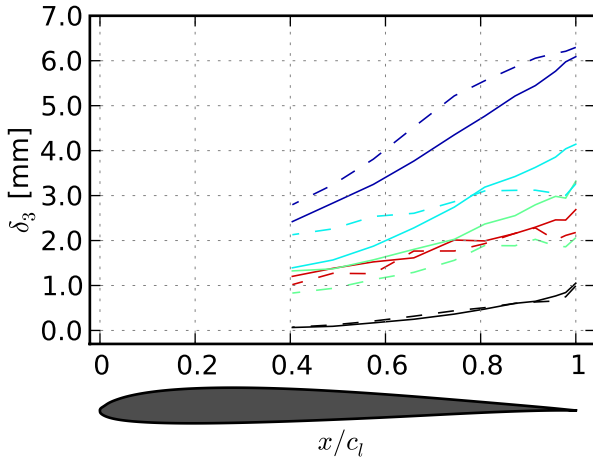
The statistical integral parameters boundary layer displacement thickness δ_1 , momentum thickness δ_2 and energy thickness δ_3 of the four porous airfoils and the reference airfoil, calculated according to Equation (3.39), (3.40) and (3.41), are presented in Figure 4.25(a), 4.25(b) and 4.25(c), respectively. In general, the same trend can be seen as for the turbulent boundary layer thickness: Airfoils made of materials with low air flow resistivities r result in higher displacement thicknesses δ_1 , momentum thicknesses δ_2 and energy thicknesses δ_3 than the non-porous reference airfoil.



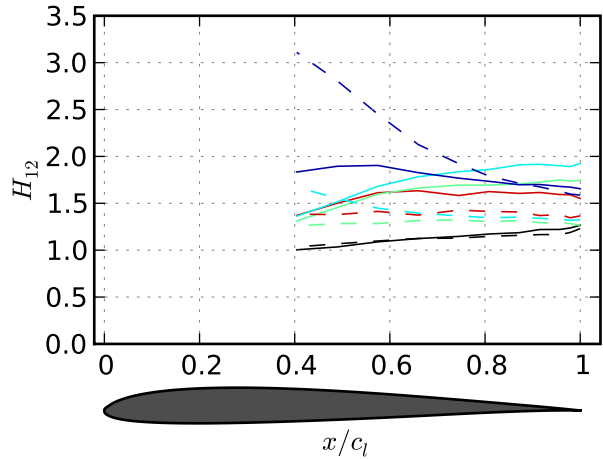
(a) Boundary layer displacement thickness, calculated using Equation (3.39) (The “x” and “o” denote the displacement thicknesses calculated using XFOIL [Drela, 1989] for suction side and pressure side, respectively.)



(b) Boundary layer momentum thickness, calculated using Equation (3.40)



(c) Boundary layer energy thickness, calculated using Equation (3.41)



(d) Shape factor, calculated using Equation (3.42)

Figure 4.25: Statistic flow parameters, angle of attack $\alpha = 0^\circ$ and flow speed $U_0 = 50$ m/s, the continuous line represents the results from the suction side, the dashed line those from the pressure side of each airfoil ($r = \blacksquare \infty$, \blacksquare 316,500, \blacksquare 16,500, \blacksquare 8,200, \blacksquare 1,000 Pa s/m²). Note that the schematic of the airfoil is given for illustrative purposes only, the distance given on the ordinate refers to the airfoil surface as origin.

The boundary layer displacement thickness δ_1 of the porous airfoils is considerably greater than that of the non-porous reference airfoil, as can be seen in Figure 4.25(a), for both suction side and pressure side. Due to the chosen range of the ordinate in Figure 4.25(a), the results of the non-porous reference airfoil seem to be quite similar for both suction side and pressure side, which is clearly not true for the porous airfoils. Of course the boundary layer displacement thickness δ_1 is also slightly different for suction and pressure side of the reference airfoil, as would be expected for a semi-symmetrical airfoil shape. However, this difference is not as noticeable as it is for the porous airfoils, partly due to their generally increased displacement thicknesses. Another possible reason for this difference may be the assumed fluid flow through the porous airfoils from the pressure to the suction side.

Basically, the displacement thickness at the trailing edge position of the different porous airfoils ($x/c_t = 1$) increases with decreasing air flow resistivity of the porous materials. While this is exactly true for the measurements at the suction side of the airfoils, there is one exception for the pressure side results: As for the velocity profiles measured in the wake of the airfoils, the displacement thickness of the airfoil made of Reapor ($r = 16,500 \text{ Pa s/m}^2$) is smaller than that of the airfoil made of Porex ($r = 316,500 \text{ Pa s/m}^2$), despite the lower flow resistivity of the latter material. This may have the same reasons as discussed above.

It can also be noticed that the curves in Figure 4.25(a) show different slopes. For most airfoils, the displacement thickness increases with increasing distance from the leading edge. But some measurements reveal a displacement thickness that remains almost constant over all measurement positions along the airfoil chord length, for example at the pressure side of the airfoil made of M-Pore Al 45 ppi ($r = 1,000 \text{ Pa s/m}^2$) and at the pressure side of the Recemat airfoil ($r = 8,200 \text{ Pa s/m}^2$) or, although less clearly, at the pressure side of the Reapor airfoil ($r = 16,500 \text{ Pa s/m}^2$). The reason for these differences compared to the other porous airfoils and the non-porous airfoil is not clear yet, but one possible cause could be some sort of surface irregularity at the pressure side of the airfoils. However, it has to be noted that obvious irregularities were not visible. It may also be possible, although not very likely, that this effect is caused by some inner inconsistencies of the porous materials beneath the pressure side surface, as for example some extent of clogging of the inner pores.

Regarding the comparison between measurement and prediction it is visible from Figure 4.25(a) that the measured displacement thicknesses of the non-porous reference airfoil are smaller than those calculated with XFOIL [Drela, 1989] for an SD7003 airfoil for both the suction side and the pressure side. The exact reason for this difference is not clear, but one possible cause might be the more approximative method used to determine the distance between the hot-wire probe and the airfoil surface in the measurements, as described in Section 3.5.

This difference between measured and predicted boundary layer displacement thickness may be the reason for the difference of the peak frequency of the trailing edge bluntness noise peak shown in Figure 4.7. However, since the measured displacement thickness is smaller than the calculated displacement thickness this would lead to a decrease in peak frequency, which was indeed observed, but according to [Brooks et al., 1989] also to an increase in peak level. The latter was not detected in the measured spectra compared to the predicted spectra.

According to [Eckert and Drake jr., 1959], the ratio of boundary layer displacement thickness to boundary layer thickness δ_1/δ at a flat plate at zero angle of attack is 0.125. This relation is often employed in order to scale trailing edge noise with the measured boundary layer displacement thickness instead of the boundary layer thickness, as mentioned at the end of Section 3.5, since it is difficult to exactly determine the boundary layer thickness from measured velocity profiles. In several models for the prediction of airfoil self noise or noise from wind turbines the value $\delta_1/\delta = 0.125$ is adopted for airfoils, as for example in the work of Grosveld [Grosveld, 1985]. Other studies on airfoil self noise use a corrected ratio larger than the flat plate value, taking into account the difference between a flat plate and a real airfoil shape. For example, Brooks, Pope and Marcolini [Brooks et al., 1989] use a ratio that depends on the chord based Reynolds number and according to Lowson [Lowson, 1992, Lowson, 1993] the flat plate value of 0.125 has to be multiplied with an

Table 4.1: Ratio of boundary layer displacement thickness to boundary layer thickness δ_1/δ and ratio of trailing edge thickness to boundary layer displacement thickness h/δ_1 for the airfoils given in Table 3.2 (The trailing edge thickness was taken to be 0.5 mm for the reference airfoil, as measured, and 1.59 mm for the porous airfoils.)

r [Pa s/m ²]	∞	316,500	16,500	8,200	1,000	
δ [mm]	9.2	11.5	15.8	17.1	26.4	suction side
δ_1 [mm]	0.7	2.5	3.6	5.0	6.1	
δ_1/δ	0.08	0.22	0.23	0.29	0.23	
h/δ_1	0.71	0.64	0.44	0.32	0.26	
δ [mm]	8.8	9.6	15.8	16.7	26.1	pressure side
δ_1 [mm]	0.7	1.7	1.4	2.4	6.0	
δ_1/δ	0.08	0.18	0.09	0.14	0.23	
h/δ_1	0.71	0.94	1.14	0.66	0.27	
δ [mm]	9.0	10.6	15.9	16.9	26.3	average
δ_1 [mm]	0.7	2.1	2.5	3.7	6.1	
δ_1/δ	0.08	0.20	0.16	0.22	0.23	
h/δ_1	0.71	0.76	0.64	0.43	0.26	

empirical factor between 2 and 4 to account for the increased boundary layer of an airfoil as opposed to the flat plate.

In the present study, the δ_1/δ ratio of the non-porous reference airfoil at zero angle of attack was found to be in the order of 0.08 for both suction side and pressure side, which is less than the theoretical value of 0.125 for a flat plate. It is assumed that the method used to determine the distance between hot-wire probe and airfoil surface employed in the present study is the main reason why the measured ratio of boundary layer displacement thickness to boundary layer thickness is less than 0.125. For the four porous airfoils this ratio is in the order of 0.22 to 0.29 for the suction side and 0.09 to 0.23 for the pressure side, and thus almost uniformly larger than for the non-porous airfoil. When averaged over the values obtained for the suction side and the pressure side, the δ_1/δ ratio is, in a first approximation, constant for the porous airfoils examined and takes a value of about 0.2. Table 4.1 lists the δ_1/δ ratio for each airfoil.

It is important to clarify that not only the absolute value of the displacement thickness is larger for the porous airfoils, but so is the displacement thickness in relation to the boundary layer thickness. This means that for an inviscid fluid, the distance that the external streamlines would have to be shifted outward in order to keep the flow field unchanged compared to the real flow field, is larger for the porous airfoils than for the non-porous airfoil. One possible reason for the relative increase of the boundary layer displacement thickness may be the surface porosity of the airfoils. Another possible reason is that the porous consistency allows for an internal fluid flow through the airfoil which leaves the airfoil along the surface and thus shifts the boundary layer outwards. This could be imagined as a multitude of small (and relatively weak) jets, where each jet originates from an open pore.

The ratios of boundary layer displacement thickness to boundary layer thickness indicate that the turbulent boundary layer of a porous airfoil cannot be correctly approximated using the common power-law velocity profiles (as for example given by Eckert and Drake

[Eckert and Drake jr., 1959] and Schlichting [Schlichting and Gersten, 2000]) used for flat plates and, by approximation, for non-porous airfoils. Therefore, the displacement thickness δ_1 should not be used as a substitute for the boundary layer thickness δ for the scaling of the trailing edge noise of both non-porous airfoils and airfoils made of porous materials alike. If, however, any such scaling approach would in fact differentiate between porous and non-porous airfoils, a δ_1/δ ratio may be employed since it is, in a first approximation, constant for the porous airfoils of the present study when averaged over the values for suction side and pressure side.

According to the suggestion of Blake [Blake, 1986], no vortex shedding sounds should be generated and hence no contribution of trailing edge bluntness noise should occur if the ratio of the trailing edge thickness h to the boundary layer displacement thickness δ_1 is less than approximately 0.3. Of course this design guideline was developed for rigid, non-porous airfoils only, but its validity will be tested for the porous airfoils nevertheless. Using the trailing edge thickness of 1.59 mm for the porous airfoils and 0.5 mm for the reference airfoil, the ratio h/δ_1 was calculated and is given in Table 4.1.

Judging from these results, all airfoils, with the exception of the porous airfoil made of M-Pore Al 45 ppi ($r = 1,000 \text{ Pa s/m}^2$), should emit trailing edge bluntness noise. No vortex shedding should occur at the trailing edge of the M-Pore Al 45 ppi airfoil, if any, since its displacement thickness is relatively high and the ratio h/δ_1 is slightly below 0.3. But as the measured trailing edge noise third-octave band sound pressure levels (Figure 4.10) show, a contribution of trailing edge bluntness noise to the total trailing edge noise was only detected for the non-porous reference airfoil. This further indicates that the porous consistency strongly influences the flow in the vicinity of the trailing edge. It can be assumed that the permeability of the material leads to interactions between the suction side boundary layer and the pressure side boundary layer upstream of the trailing edge. When turbulent eddies approach the trailing edge, the impedance of the boundary surface does not change abruptly as for the non-porous airfoil, but rather a more gradual change of the impedance occurs.

As can be seen from Figure 4.25(b), the dependence of the turbulent boundary layer momentum thickness δ_2 , calculated using Equation (3.40), on the air flow resistivity r of the porous materials is basically the same as for the boundary layer displacement thickness given in Figure 4.25(a): The momentum thickness δ_2 for suction and pressure side increases with decreasing air flow resistivity. Again, the momentum thickness of the airfoil made of Reapor is below that of the airfoil made of Porex at the pressure side of the airfoils.

As the boundary layer displacement thickness δ_1 and the momentum thickness δ_2 , the boundary layer energy thickness δ_3 , shown in Figure 4.25(c), basically increases with decreasing air flow resistivity r of the porous airfoils (with the exception of the values for the airfoils made of Reapor and Porex at the pressure side, where again the order is not the same as for the suction side).

The shape factor H_{12} of the airfoils is shown in Figure 4.25(d). It remains nearly constant for all airfoils except for the airfoil made of M-Pore Al 45 ppi ($r = 1,000 \text{ Pa s/m}^2$), where the shape factor from the pressure side measurement is higher at the position nearest to the leading edge (at $x/c_l = 0.4$) and then decreases strongly. This decrease is caused by the boundary layer displacement thickness δ_1 at the pressure side of the M-Pore airfoil that, instead of increasing toward the trailing edge, remains nearly constant in the streamwise direction (shown in Figure 4.25(a)).

According to Eckert and Drake [Eckert and Drake jr., 1959], the shape factor takes a value of approximately 1.3 in case of a turbulent boundary layer flow over a flat plate and a considerably larger value (approximately 2.3) in case of a laminar boundary layer (see Section 3.5). For the non-porous airfoil, the shape factor of both suction and pressure side slightly increases from about 1 at the measurement position nearest to the leading edge to about 1.3 directly at the trailing edge, with the pressure side shape factor being slightly lower than the suction side shape factor. This further confirms, as could already be observed qualitatively from the velocity profiles shown in Figure 4.17, that the boundary layer is fully turbulent at the position of the trailing edge.

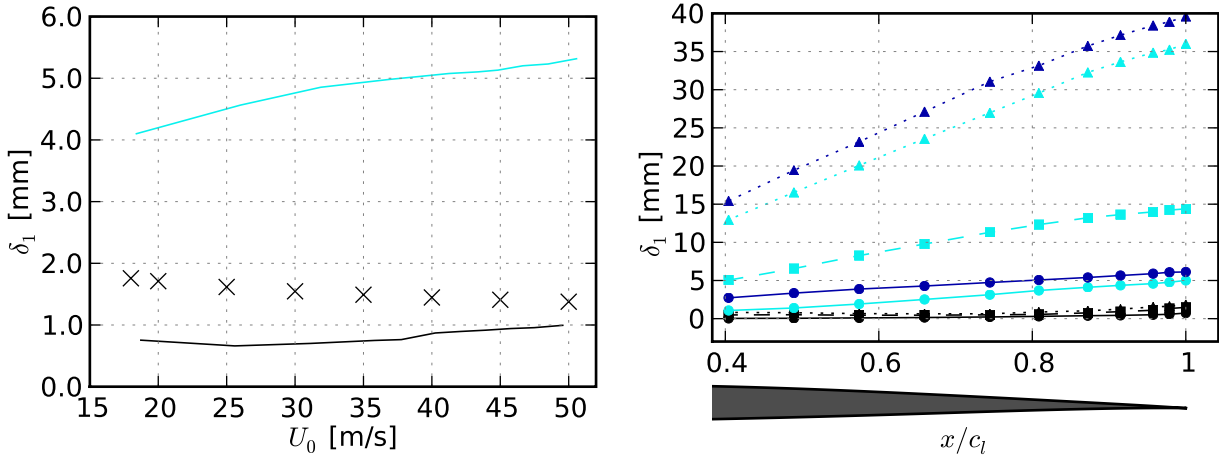
The shape factor of the porous airfoils is generally larger than that of the non-porous airfoil. It increases with decreasing air flow resistivities, from about 1.3 to 1.6 for the airfoil made of Porex ($r = 316,500 \text{ Pa s/m}^2$) to about 1.6 to 3.1 for the airfoil made of M-Pore Al 45 ppi ($r = 1,000 \text{ Pa s/m}^2$). But, as mentioned above, the results measured at the pressure side of the M-Pore Al 45 ppi airfoil are different from the results of the remaining airfoils due to the nearly constant boundary layer displacement thickness in streamwise direction. At the suction side of this airfoil, the maximum value of the shape factor is about 1.9. As is the case for the non-porous airfoil, the shape factor at the pressure side of the porous airfoils is slightly smaller than that at the suction side, with the exception of the airfoil made of M-Pore Al 45 ppi. So, although the boundary layer of the porous airfoils is fully turbulent, as can be seen from the velocity profiles given in Figure 4.18 through Figure 4.21, the shape factor is generally equal to or larger than the theoretical value of 1.3. This is caused by the increased boundary layer displacement thickness of the porous airfoils. However, with the exception of the airfoil made of M-Pore Al 45 ppi, at least at the upstream measurement positions, the shape factor of the porous airfoils is still below 2.3, the theoretical value for a laminar boundary layer at a flat plate or a non-porous airfoil.

Since the turbulent boundary layer displacement thickness δ_1 is the one boundary layer parameter used most often in airfoil self noise theories for the scaling of turbulent boundary layer trailing edge noise, its dependence on the flow speed U_0 and on the angle of attack α will be further examined for one porous airfoil and the non-porous reference airfoil. Figure 4.26(a) gives the boundary layer displacement thickness as a function of the flow speed for the porous airfoil made of Recemat ($r = 8,200 \text{ Pa s/m}^2$) and the non-porous airfoil, measured at zero angle of attack. And while δ_1 is more than four times greater for the porous airfoil compared to the non-porous airfoil, it slightly increases with increasing flow speed for both airfoils.

For the purpose of comparison, Figure 4.26(a) also contains the results obtained with XFOIL [Drela, 1989] for an SD7003 airfoil of the same chord length. It can be assumed that the XFOIL boundary layer prediction takes into account basic flat plate theory. According to this theory [Eckert and Drake jr., 1959], the boundary layer thickness decreases with increasing flow speed according to

$$\delta/c_l = 0.37 \cdot Re^{-0.2}. \quad (4.14)$$

The differences between the measured boundary layer displacement thickness and the XFOIL prediction may be caused by differences between the flow field around a technical airfoil with finite dimensions and the merely theoretic flow field employed by XFOIL. The increase of the boundary layer displacement thickness with increasing flow speed examined in the present study is supported by the boundary layer thicknesses measured



(a) Dependence of the boundary layer displacement thickness δ_1 on the mean flow speed U_0 (The “x”-markers denote the displacement thicknesses calculated using XFOIL [Drela, 1989] for the suction side)

(b) Dependence of the boundary layer displacement thickness δ_1 on the angle of attack α , solid line, circles: 0° , dashed line, squares: $+4^\circ$, dotted line, triangles: $+8^\circ$)

Figure 4.26: Dependence of the (suction side) boundary layer displacement thickness on the flow speed U_0 and the angle of attack α for three airfoils ($r = \infty$, $8,200$, $1,000$ Pa s/m²). Note that the schematic of the airfoil is given for illustrative purposes of the chordwise position only, the distance given on the ordinate refers to the airfoil surface.

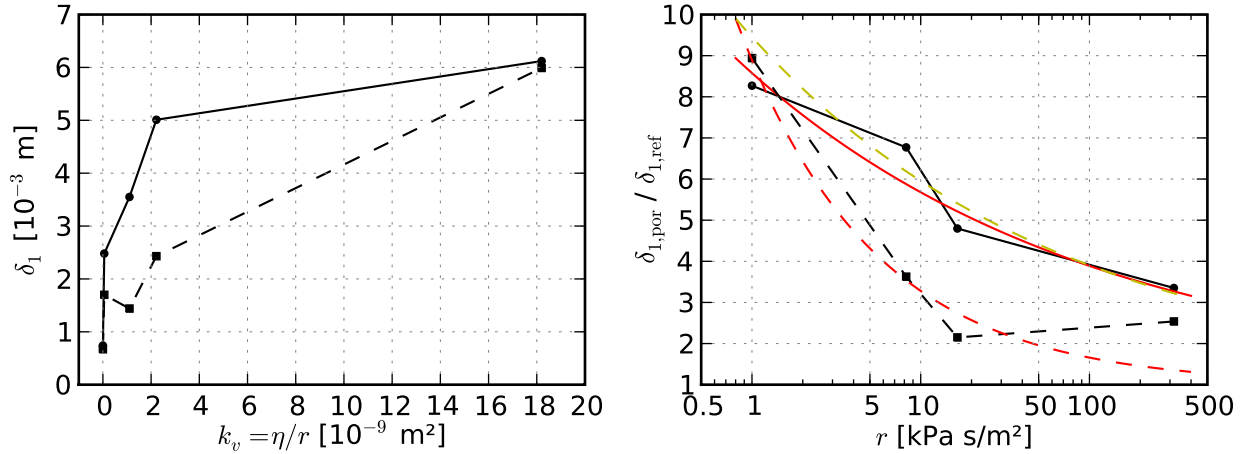
at a helicopter blade segment and the corresponding flat plate predictions described by Schlinker and Amiet [Schlinker and Amiet, 1981]. They found a slight increase of the measured boundary layer thickness with increasing flow speed for the suction side of the airfoil in the examined range of Mach numbers between approximately 0.14 and 0.4. According to theory, this would be consistent to an increase of the boundary layer displacement thickness.

The dependence of δ_1 on the geometric angle of attack α is shown in Figure 4.26(b) for the reference airfoil and two porous airfoils (Recemat, $r = 8,200$ Pa s/m², and M-Pore Al 45 ppi, $r = 1,000$ Pa s/m²) for a flow speed of 50 m/s. As would be expected, the turbulent boundary layer displacement thickness δ_1 increases with increasing angle of attack. While this increase is barely visible for the reference airfoil in Figure 4.26(b) due to the chosen range of the ordinate, it is considerable for the porous airfoils.

Figure 4.27(a) shows the boundary layer displacement thickness of the airfoils as a function of the viscous permeability k_v and Figure 4.27(b) shows the normalized boundary layer displacement thickness $\delta_{1,n}$ at the trailing edge of the porous airfoils as a function of the air flow resistivity r :

$$\delta_{1,n} = \frac{\delta_{1,\text{por}}}{\delta_{1,\text{ref}}}, \quad (4.15)$$

where $\delta_{1,\text{por}}$ is the boundary layer displacement thickness of the porous airfoils and $\delta_{1,\text{ref}}$ is the displacement thickness of the non-porous reference airfoil. The general trend of a decreasing displacement thickness for increasing air flow resistivities is confirmed. To enable the determination of the normalized boundary layer displacement thickness $\delta_{1,n}$ for a porous airfoil based on its air flow resistivity similar to the method described above for the boundary layer thickness (Figure 4.23(b)), a least squares fit to an exponential function was performed on the data from Figure 4.27(b) for both suction side and pressure side.



(a) Measured boundary layer displacement thickness of the airfoils as a function of the viscous permeability k_v (with $\eta = 18.2 \cdot 10^{-6}$ kg/(m s) at 22°C)

(b) Normalized turbulent boundary layer displacement thickness according to Equation (4.15) as a function of air flow resistivity, **—** exponential fit (**- - -** second exponential fit, obtained when the values of δ_1 from the pressure side of Reapor, $r = 16,500$ Pa s/m², and Recemat, $r = 8,200$ Pa s/m², are replaced by the corresponding suction side values)

Figure 4.27: Boundary layer displacement thickness of the airfoils, measured at zero angle of attack and a flow speed of 50 m/s (solid line: suction side, dashed line: pressure side)

The resulting exponential equations, although based on four data points only, yield a rough estimation of the boundary layer displacement thickness for an airfoil made completely out of a porous material characterized by the air flow resistivity r :

$$\delta_{1,n}(r) = 32.190 \cdot \exp(-0.482 \cdot \log_{10} r) + 1 = 32.190 \cdot r^{\frac{-0.482}{\ln 10}} + 1 \quad (4.16)$$

for the suction side and

$$\delta_{1,n}(r) = 327.191 \cdot \exp(-1.242 \cdot \log_{10} r) + 1 = 327.191 \cdot r^{\frac{-1.242}{\ln 10}} + 1 \quad (4.17)$$

for the pressure side (in accordance to Figure 4.25(a), the displacement thickness above the trailing edge of the non-porous airfoil is approximately 0.74 mm for the suction side and 0.67 mm for the pressure side). Again, Equation (4.16) and (4.17) are valid only for the examined range of air flow resistivities between approximately 700 Pa s/m² and 500 kPa s/m².

The boundary layer displacement thickness calculated for the pressure side of the airfoil made of Reapor ($r = 16,500$ Pa s/m²) is smaller than what would be expected compared to the suction side results. Additionally, the pressure side boundary layer displacement thickness of the airfoil made of Recemat is also clearly below the value obtained for the suction side. Therefore, the curve describing the pressure side displacement thickness of the porous airfoils as a function of the air flow resistivity is not a strictly monotonically decreasing function as is the curve for the suction side boundary layer displacement thicknesses.

When the values of the boundary layer displacement thickness for the pressure side of the Reapor airfoil and the Recemat airfoil are replaced by the corresponding suction side values in order to obtain a more coherent mathematical model, Equation (4.17) can be replaced

by

$$\delta_{1,n}(r) = 41.993 \cdot \exp(-0.534 \cdot \log_{10}r) + 1 = 41.993 \cdot r^{\frac{-0.534}{\ln 10}} + 1. \quad (4.18)$$

Taking into account that the displacement thicknesses measured at the pressure side of some porous airfoils may be influenced by some sort of surface irregularity, Equation (4.18) seems to be a more fitting model in comparison to the model for the suction side boundary layer displacement thickness.

4.3.3 Turbulence parameters in the wake

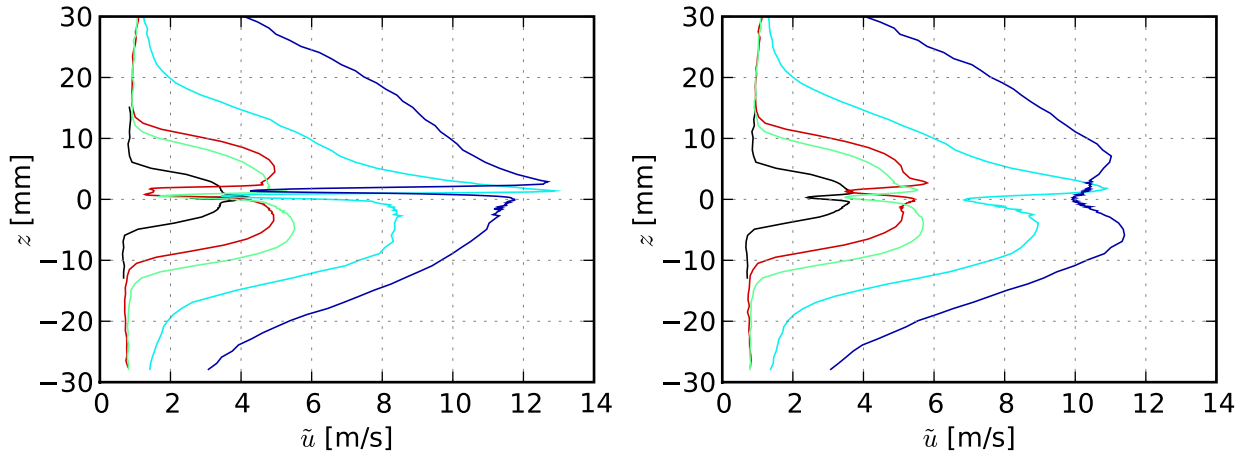
In this section, the turbulence parameters in the wake of the airfoils shall be further examined in addition to the velocity profiles given in Figure 4.24(a) and 4.24(b). To better understand the characteristics of the flow behind the trailing edge of the airfoils, not only normalized parameters as the turbulence intensity Tu will be examined, but also absolute values of the measured quantities.

Figure 4.28(a) and Figure 4.28(b) show the root-mean-square of the turbulent velocity fluctuations $\sqrt{u^2}$, measured at a distance of 1 mm and 5 mm behind the airfoil trailing edge, respectively. The basic shape of the curves is the same for all airfoils. Starting outside of the turbulent boundary layer, the velocity increases with decreasing vertical distance toward the trailing edge position ($z \rightarrow 0$), with a sharp drop of the velocity directly behind the trailing edge ($z = 0$). At a distance of 1 mm behind the trailing edge (Figure 4.28(a)) this drop in velocity is sharper than 5 mm behind the trailing edge (Figure 4.28(b)), where the rms velocity of the porous airfoils with lower air flow resistivities decreases more gradually.

The rms velocity measured in the wake of the porous airfoils is generally higher than that in the wake of the non-porous airfoil, which may again be an indicator that either a fluid flow through the porous airfoils exists or that the velocity is increased due to the increased surface roughness of the porous airfoils.

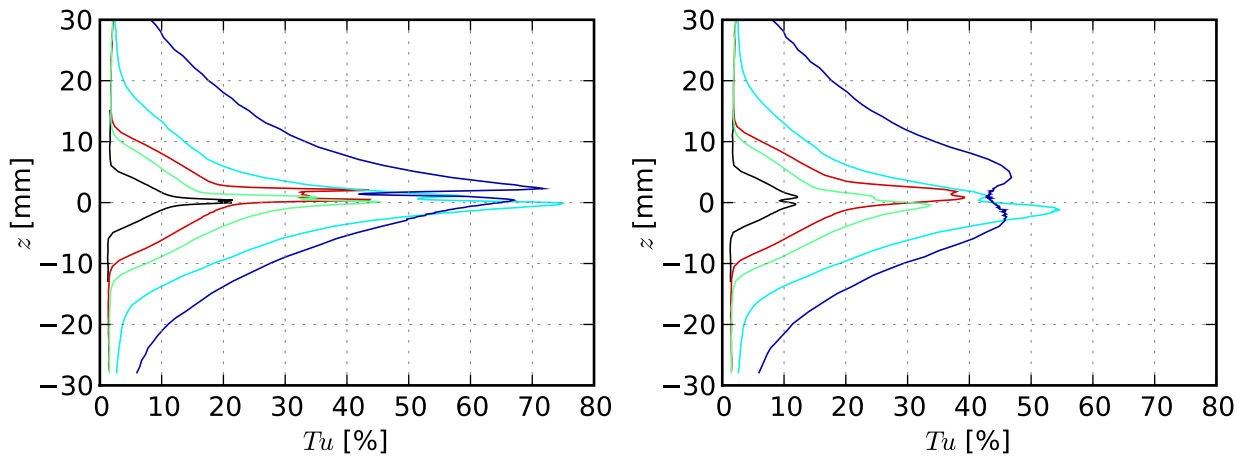
According to Equation (3.15) the root-mean-square of the turbulent velocity fluctuations is then normalized using the mean flow velocity \bar{u} measured at the corresponding measurement position (Figure 4.24(a) and 4.24(b)) to obtain the turbulence intensity in the wake, given in Figure 4.28(c) and 4.28(d).

Not very different from the root-mean-square of the turbulent velocity fluctuations, the turbulence intensity Tu first increases with decreasing distance toward $z = 0$ and then strongly decreases directly behind the trailing edge. As the rms velocity fluctuations, the turbulence intensity measured in the wake of the porous airfoils is larger than that in the wake of the reference airfoil. This is a direct consequence of both the larger rms velocity fluctuations $\sqrt{u^2}$ and the smaller mean flow velocity \bar{u} of the porous airfoils compared to the non-porous airfoil.



(a) Root-mean-square of the turbulent velocity fluctuations $\tilde{u} = \sqrt{u'^2}$ measured 1 mm behind the airfoil trailing edge

(b) Root-mean-square of the turbulent velocity fluctuations $\tilde{u} = \sqrt{u'^2}$ measured 5 mm behind the airfoil trailing edge



(c) Measured turbulence intensity Tu 1 mm behind the airfoil trailing edge

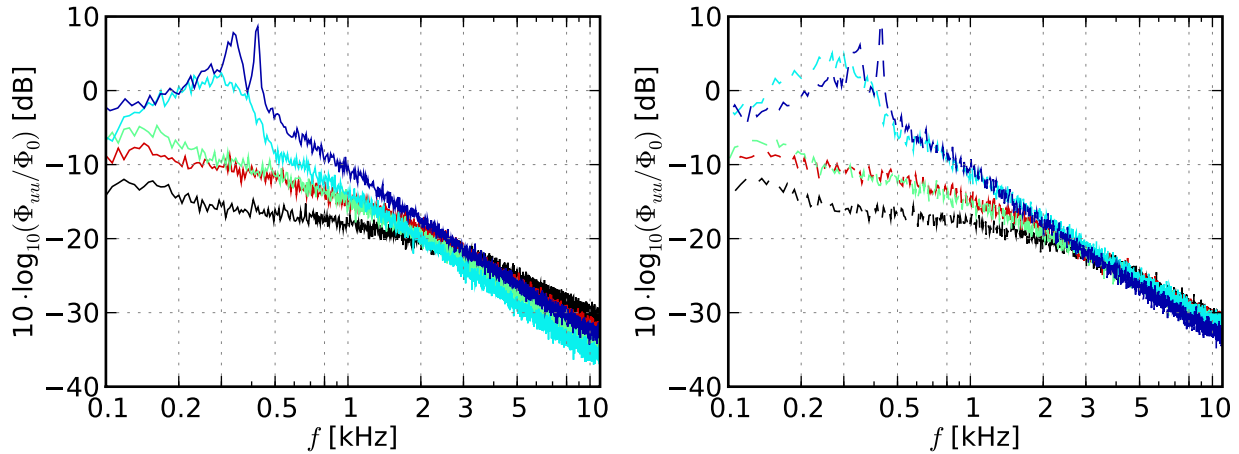
(d) Measured turbulence intensity Tu 5 mm behind the airfoil trailing edge

Figure 4.28: Turbulence parameters in the wake of the airfoils, flow speed $U_0 = 50$ m/s, angle of attack $\alpha = 0^\circ$ ($r = \blacksquare \infty$, \blacksquare 316,500, \blacksquare 16,500, \blacksquare 8,200, \blacksquare 1,000 Pa s/m²). Note that the given distance in the vertical direction relates to the upper side of the trailing edge.

4.3.4 Turbulence spectra

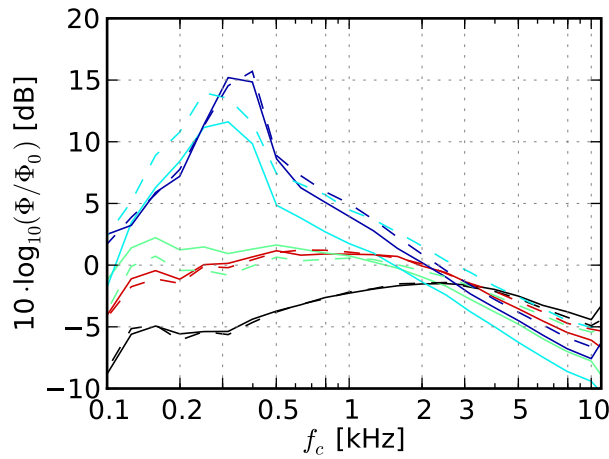
To enable a further examination of correlations between the trailing edge noise and the properties of the turbulent boundary layer flow above the surface and the trailing edge of the porous airfoils, the spectral shape of the velocity fluctuations, the turbulence power spectral density (in the remaining part of this thesis referred to as turbulence spectrum), has to be analyzed.

Figure 4.29(a) shows the power spectral density of the velocity fluctuations Φ_{uu} at a flow speed of 50 m/s at zero angle of attack, measured within the turbulent boundary layer approximately 1 mm above the trailing edge ($x/c_l = 1$) on the suction side of the airfoils from Table 3.2. The power spectral densities are given with a frequency step size of 6.25 Hz due to the chosen sample frequency and block size, and are normalized with $\Phi_0 = 1$ m²s⁻¹. The results for the pressure side of the airfoils can be seen in Figure 4.29(b). The corre-



(a) Measured power spectral density of the turbulent velocity fluctuations Φ_{uu} re $1 \text{ (m/s)}^2/(6,25 \text{ Hz})$, normalized with $\Phi_0 = 1 \text{ m}^2\text{s}^{-1}$, suction side

(b) Measured power spectral density of the turbulent velocity fluctuations Φ_{uu} re $1 \text{ (m/s)}^2/(6,25 \text{ Hz})$, normalized with $\Phi_0 = 1 \text{ m}^2\text{s}^{-1}$, pressure side



(c) Measured third-octave band turbulence spectra Φ , normalized with $\Phi_0 = 1 \text{ m}^2\text{s}^{-1}$

Figure 4.29: Power spectral density of the turbulent velocity fluctuations and third-octave band turbulence spectra of the airfoils measured at $x/c_l = 1$ approximately 1 mm above the trailing edge, $\alpha = 0^\circ$ and $U_0 = 50 \text{ m/s}$, the continuous line represents the results from the suction side, the dashed line those from the pressure side of each airfoil ($r = \blacksquare \infty$, $\blacksquare 316,500$, $\blacksquare 16,500$, $\blacksquare 8,200$, $\blacksquare 1,000 \text{ Pa s/m}^2$).

sponding third-octave band turbulence spectra Φ derived from the power spectral densities and again normalized with $\Phi_0 = 1 \text{ m}^2\text{s}^{-1}$ for both suction side and pressure side of the four porous airfoils and the non-porous airfoil are then presented in Figure 4.29(c).

The measurements were performed using a single-wire probe and therefore the corresponding spectra contain both streamwise velocity fluctuations as well as fluctuations in the vertical direction. For a more exact analysis of the turbulence within the turbulent boundary layer, hot-wire measurements using multi-wire probes would be required (for example X-wire probes).

In general, the spectra measured at suction side and pressure side do collapse well for each airfoil. Both the power spectral density and the third-octave band turbulence spectra of two of the porous airfoils with the lowest air flow resistivities (M-Pore Al 45 ppi,

$r = 1,000 \text{ Pa s/m}^2$, and Recemat, $r = 8,200 \text{ Pa s/m}^2$) show a strong spectral peak, with the maximum around 300 Hz. The peak frequency is approximately the same at suction side and pressure side for both airfoils. This strong peak cannot be caused by the airfoil shape because then it would also be visible for the other airfoils. Since the M-Pore Al 45 ppi airfoil is assembled from porous plates of 15 mm thickness and the Recemat airfoil from plates of 5 mm thickness, it is not likely that the peak is caused by flow effects induced by the thickness of the porous plates. It is rather possible that the strong spectral peaks are a result of the porous material characteristics, presumably the pore size or the air flow resistivity. The spectra of the remaining three airfoils only show a small spectral hump between 100 Hz and 200 Hz.

Garcia-Sagrado et al. [Garcia-Sagrado et al., 2006] measured a peak in the turbulence spectrum behind a blunt trailing edge that they related to the peak of the bluntness noise contribution. The spectral peak was observed at approximately 1.1 kHz for a blunt NACA 0012 airfoil with a chord length of 300 mm and a trailing edge thickness of 1.6 mm, which is roughly comparable to the dimensions of the porous airfoils of the present study. But a distinct spectral peak in this frequency range cannot be seen from the turbulence spectra presented in Figure 4.29. Additionally, no contribution of bluntness noise was observed in the trailing edge noise spectra of the porous airfoils.

The spectrum of the reference airfoil has a flat peak at approximately 2 kHz to 3 kHz. No such peak at this frequency was found in the acoustic spectra, but a spectral peak in this range of frequencies was predicted by the BPM-model, as shown in Figure 4.7(a). The peak predicted by the BPM-model is a result of the assumed peak Strouhal number (based on boundary layer displacement thickness) of 0.25 or 0.3 according to the results of Brooks and Marcolini [Brooks and Marcolini, 1985].

The corresponding spectral peaks of the porous airfoils made of Porex ($r = 316,500 \text{ Pa s/m}^2$) and Reapor ($r = 16,500 \text{ Pa s/m}^2$) have a lower peak frequency between 500 Hz and 1 kHz. The amplitudes of the turbulence spectra are different for the different airfoils. The spectrum measured above the trailing edge of the reference airfoil has the smallest amplitude at low and medium frequencies up to approximately 3 kHz. For higher frequencies the spectrum takes values above those measured for the porous airfoils. It is quite possible that this shift of the amplitude of the non-porous reference airfoil is responsible for the increased trailing edge noise generation at medium and high frequencies compared to the porous airfoils. The spectra measured above the trailing edge of the porous airfoils in general have higher amplitudes at low frequencies (approximately below 2 or 3 kHz), but the amplitude then decreases more strongly with increasing frequency.

Based on these observations it can be assumed that the small scale turbulent structures which are associated with the high frequency part of the turbulence spectra are damped when they convect over the surface of the porous airfoils. This effect, which is called hydrodynamic damping, is likely to be caused by interactions between the small scale velocity fluctuations of the turbulence with the pores of the porous materials and thus by a transfer from energy contained in the high frequency range of the turbulence spectra into heat.

In the frequency range below 3 kHz, the amplitudes approximately match the reversed order of the air flow resistivities r of the airfoils, with the lowest air flow resistivity leading to the maximum amplitude of the turbulence spectrum and the maximum air flow resistivity

leading to the smallest amplitude. If it is assumed that trailing edge noise is basically generated through the mechanism of scattering of the turbulent structures that are convected within the boundary layer flow at the trailing edge, and that hence the turbulence spectra are somehow related to the spectra of the trailing edge noise, this may even be an indicator that the porous airfoils generate more noise at frequencies below the lower frequency limit of the acoustic measurement setup.

What has to be considered is that the turbulence spectra shown in Figure 4.29(c) were measured at the same distance of 1 mm from the airfoil surface and hence at different positions relative to the turbulent boundary layer thickness of the corresponding airfoil. In order to achieve a more significant estimation of the energy contained in the turbulent boundary layer and to enable a comparison between the different airfoils, the turbulence spectra have to be normalized by taking into account the measurement position inside the turbulent boundary layer.

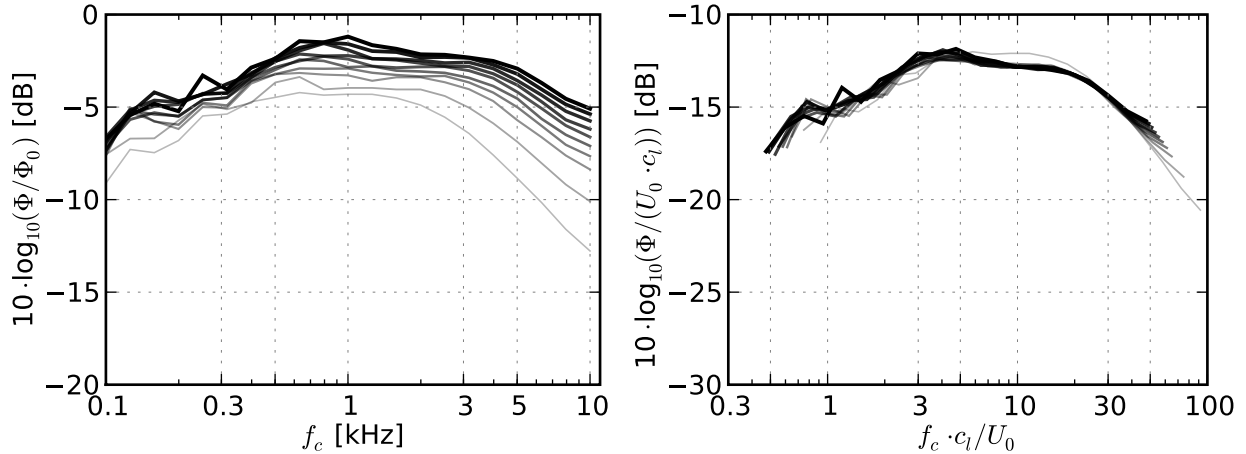
In order to develop a normalization for the turbulence spectra, results from measurements at different flow speeds are compared. Figure 4.30 shows the third-octave band turbulence spectra of the non-porous airfoil and one porous airfoil, measured 1 mm above the trailing edge at $x/c_l = 1$ at different flow speeds between approximately 25 m/s and 50 m/s. First, the spectra are presented as a function of frequency (Figure 4.30(a) and 4.30(c)). Second, the third-octave band turbulence spectra are normalized and plotted as a function of the chord based Strouhal number (Figure 4.30(b) and 4.30(d)). The spectra are normalized using the flow speed U_0 and the chord length c_l , both parameters that are identical for all airfoils examined and thus independent of the properties of the porous materials.

It is visible from Figure 4.30 that the turbulence spectra indeed show a dependence on the chord based Strouhal number, since the spectral peak of both airfoils collapses when plotted versus $f_c \cdot c_l / U_0$. Regarding the amplitude of the spectra it is found that this normalization is useful for the non-porous airfoil, for which the spectra collapse well, but not for the porous airfoil, for which the amplitude increases noticeably with increasing flow speed.

Other normalization approaches that were tested include a normalization employing the turbulent boundary layer displacement thickness δ_1 , which did not lead to a considerably better collapse of the turbulence spectra than the approach shown in Figure 4.30. The results are given in Figure E.2 of Appendix E. An approach that employs the boundary layer thickness δ does not seem to be practicable due to the described difficulties to exactly determine the thickness of the turbulent boundary layer.

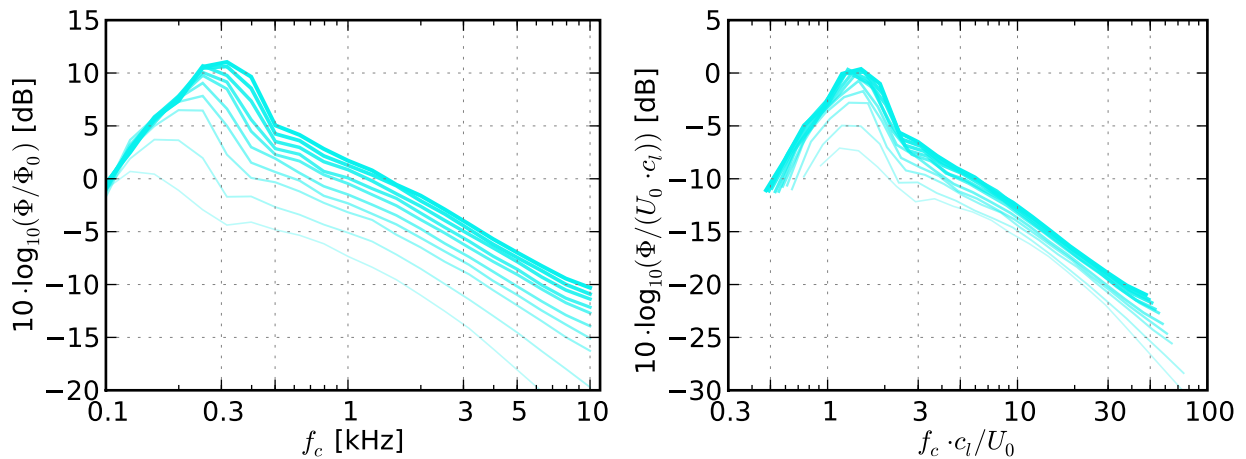
Figure 4.31(a) shows the third-octave band turbulence spectra of all five airfoils, obtained from the measurements performed 1 mm above the trailing edge at $x/c_l = 1$ at both suction side and pressure side, normalized using the approach shown in Figure 4.30.

Another normalization that was tested on the measured turbulence spectra of the porous airfoils and the non-porous airfoil is the method used by Garcia-Sagrado et al. [Garcia-Sagrado et al., 2006], who present the normalized turbulence spectrum $10 \cdot \log_{10}[\Phi / (U_0 \cdot \delta_1)]$ as a function of the Strouhal number based on the turbulent boundary layer displacement thickness, $f \cdot \delta_1 / U_0$. This normalization is consistent with the approach tested for the normalization of the turbulence spectra measured at different flow speeds as shown in Figure E.2 of Appendix E (although these spectra are plotted versus the Strouhal number based on chord length). The resulting turbulence spectra for the four porous airfoils and the non-porous reference airfoil are shown in Figure 4.31(b).



(a) Measured turbulence spectra of the non-porous reference airfoil ($r = \infty$), from thinnest to thickest line: $U_0 \approx 26, 31, 36, 38, 40, 42, 44, 46, 48, 50$ m/s

(b) Normalized spectra of the non-porous reference airfoil ($r = \infty$), from thinnest to thickest line: $U_0 \approx 26, 31, 36, 38, 40, 42, 44, 46, 48, 50$ m/s

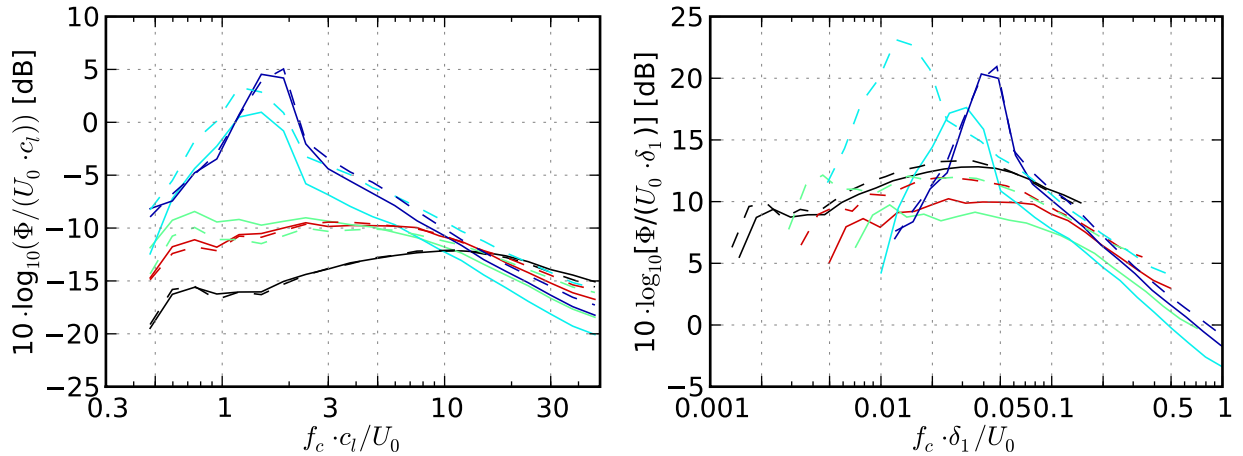


(c) Measured turbulence spectra of the airfoil made of Recemat ($r = 8,200$ Pa s/m²), from thinnest to thickest line: $U_0 \approx 26, 31, 36, 38, 40, 42, 44, 46, 48, 50$ m/s

(d) Normalized spectra of the airfoil made of Recemat ($r = 8,200$ Pa s/m²), from thinnest to thickest line: $U_0 \approx 26, 31, 36, 38, 40, 42, 44, 46, 48, 50$ m/s

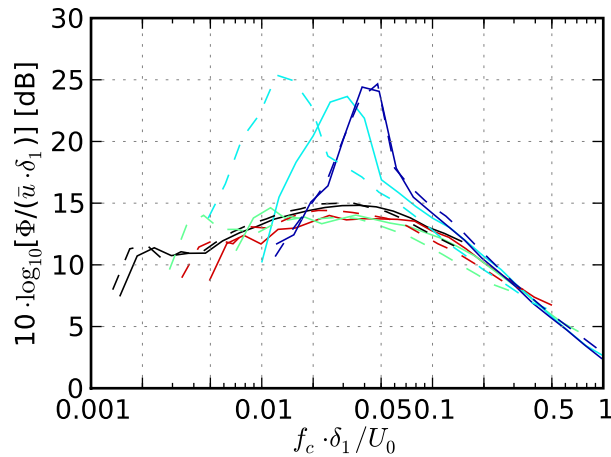
Figure 4.30: Comparison of measured third-octave band turbulence spectra with normalized turbulence spectra for different flow speeds between $U_0 = 25$ m/s (thinnest, most transparent line) and $U_0 = 50$ m/s (thickest, most opaque line), angle of attack $\alpha = 0^\circ$. Note the different scales of the ordinate for porous airfoil and reference airfoil.

With the exception of the results obtained at the suction side and, even more noticeable, the pressure side of the airfoil made of Recemat ($r = 8,200$ Pa s/m²), the corresponding spectra collapse reasonably well regarding the Strouhal numbers of the spectral peaks, but not regarding the absolute level. The peak Strouhal number of the spectrum measured at the pressure side of the airfoil made of Recemat differs from that measured at the suction side, which does not occur when using the normalization shown in Figure 4.31(a). The differences of the peak Strouhal number at the airfoil made of Recemat are caused by the boundary layer displacement thickness δ_1 measured at this particular airfoil, especially at the pressure side, which is smaller than what would be expected in comparison to the suction side result and to the results of the remaining porous airfoils. This was shown in Figure 4.25(a) and discussed in Section 4.3.2.



(a) Normalization employing the flow speed U_0 and the chord length c_l

(b) Normalization used by Garcia-Sagrado et al. [Garcia-Sagrado et al., 2006], employing the flow speed U_0 and the boundary layer displacement thickness δ_1



(c) Normalization employing the mean flow velocity \bar{u} and the boundary layer displacement thickness δ_1

Figure 4.31: Comparison of different normalization approaches: normalized third-octave band turbulence spectra of the airfoils measured at $x/c_l = 1$ (above the trailing edge), $\alpha = 0^\circ$ and $U_0 = 50$ m/s, the solid line represents the results from the suction side, the dashed line those from the pressure side of each airfoil ($r = \infty$, 316,500, 16,500, 8,200, 1,000 Pa s/m²).

A third approach that was tested is inspired by the approach employed by Garcia-Sagrado et al., but instead of using the flow speed U_0 for the normalization of the spectra, the mean velocity \bar{u} measured at the corresponding position at a distance of 1 mm above the trailing edge of the particular airfoil is used. This is due to the fact that in the present measurements the fixed distance of the hot-wire probe from the surface of the airfoil corresponds to a different mean velocity due to the different boundary layer thicknesses. Hence the normalized turbulence spectrum $10 \cdot \log_{10}[\Phi / (\bar{u} \cdot \delta_1)]$ is plotted versus the Strouhal number based on boundary layer displacement thickness δ_1 and flow speed U_0 .

Regarding the amplitude at high Strouhal numbers the resulting normalized spectra, shown in Figure 4.31(c), do collapse better than the spectra normalized using the method employed by Garcia-Sagrado et al. as shown in Figure 4.31(b). Again, with the exception of

the spectra measured at the Recemat airfoil, the spectral peaks from the different airfoils collapse reasonably well. No better collapse of the turbulence spectra was achieved when using the mean flow velocity \bar{u} to calculate a Strouhal number $f_c \cdot \delta_1 / \bar{u}$.

In general, the presentation of the spectra based on δ_1 and \bar{u} complicates the analysis of the data and the discussion of differences between the turbulence spectra of different airfoils since these parameters are not known a priori (as are for example the flow speed and the chord length).

In the remaining part of this chapter, the third-octave band turbulence spectra will be normalized using the flow speed U_0 and the airfoil chord length c_l , and presented as a function of the Strouhal number based on chord length and flow speed, as shown in Figure 4.31(a). This normalization is chosen since it uses parameters that are readily available for all airfoils and the turbulence spectra were found to collapse well regarding the spectral peaks as shown in Figure 4.30.

In order to gain knowledge on the development of the turbulent structures that move over the surface of the airfoils within the turbulent boundary layer and, possibly, on the assumed damping effect, turbulence spectra measured at different stations along the chord of the airfoils have to be examined. Figure 4.32 shows the comparison of the normalized turbulence spectra of the five airfoils at six different chord positions, from $x/c_l = 0.49$ to $x/c_l = 0.96$. The spectra measured at the last chord position $x/c_l = 1$ are given in Figure 4.31(a).

The comparison of the different plots from Figure 4.32 shows that with decreasing distance of the measurement position from the trailing edge the turbulence spectra measured at suction side and pressure side of most airfoils draw nearer to each other and finally collapse. This is most likely due to the semi-symmetric SD7003 shape, which is only slightly cambered. (For a symmetric airfoil shape, like the NACA 0012, the spectra for suction side and pressure side should be similar at each chord position.) While this is especially true for the non-porous airfoil and the airfoil made of M-Pore Al 45 ppi ($r = 1,000 \text{ Pa s/m}^2$), the pressure side and suction side turbulence spectra of the airfoil made of Porex ($r = 316,500 \text{ Pa s/m}^2$) are more or less similar at each chord position presented. The reason for this similarity is not clear yet.

With increasing chord position, the peak Strouhal number for both suction side and pressure side of the non-porous airfoil slightly shifts toward lower Strouhal numbers, while the small spectral hump at $f_c \cdot c_l / U_0 \approx 0.7$ develops gradually. As the measurement position draws nearer toward the trailing edge, the strong spectral peaks observed for the two porous airfoils (M-Pore Al 45 ppi, $r = 1,000 \text{ Pa s/m}^2$, and Recemat, $r = 8,200 \text{ Pa s/m}^2$) develop gradually. The peaks are not visible at the first chord position displayed, but can clearly be distinguished between $x/c_l = 0.66$ and $x/c_l = 0.74$. This may be an indicator for the hypothesis that these peaks are related to the bluntness of the trailing edge, although this would raise the question why such a peak cannot be seen in the turbulence spectra of the other porous airfoils. Due to the partly irregular trailing edge of the Reapor airfoil ($r = 16,500 \text{ Pa s/m}^2$) it is possible that no such peak can be observed in the corresponding turbulence spectra, but at least the porous airfoil made of Porex ($r = 316,500 \text{ Pa s/m}^2$) should feature a similar peak.

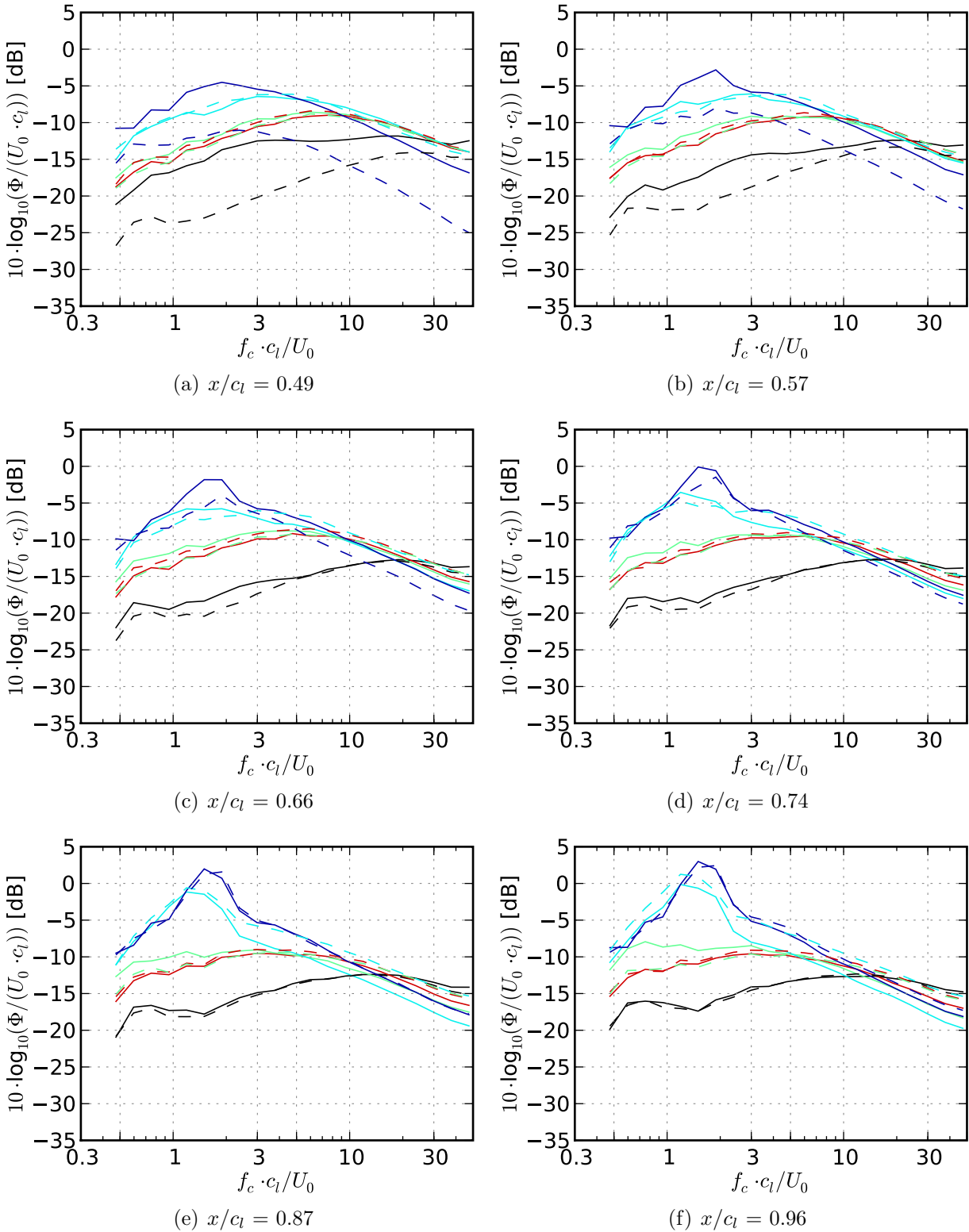


Figure 4.32: Normalized turbulence spectra (in third-octave bands) of the airfoils, measured at different positions along the chord on the suction side (solid lines) and pressure side (dashed lines) approximately 1 mm above the surface, $\alpha = 0^\circ$ and $U_0 = 50$ m/s ($r = \infty$, \blacksquare 316,500, \blacksquare 16,500, \blacksquare 8,200, \blacksquare 1,000 Pa s/m²).

Another way to illustrate the spectral differences of the boundary layer turbulence at different positions along the chord is given in Figure 4.33, where the turbulence spectra for each airfoil from Table 3.2 are shown individually. Normalized third–octave band spectra are presented for eight chord positions from $x/c_l = 0.49$ to $x/c_l = 1$.

From the single plots in Figure 4.33 it is visible that with decreasing distance from the trailing edge the turbulence spectra of the non–porous airfoil are shifted toward lower Strouhal numbers, resulting in a virtual increase of the amplitude at Strouhal numbers below $f_c \cdot c_l/U_0 \approx 20$ and a minor decrease of the amplitude at higher Strouhal numbers. But the resulting third–octave band level differences are relatively small, taking maximum values of about 5 dB at low Strouhal numbers.

Wyganski et al. [Wyganski et al., 1986] measured the spectra of the streamwise component of the velocity fluctuations, but at several locations in the wake behind a flat plate. They found that, with increasing distance from the trailing edge, the frequency range related to the most energetic eddies gradually moves toward lower frequencies as the flow develops in the downstream direction. Assuming that the turbulence spectra in the wake of the airfoils develop from the spectra in the turbulent boundary layer, the observations of Wyganski et al. are supported by the measurements on the non–porous airfoil of the present study, although the shift of the peak is less strong.

A shift of the turbulence spectra can also be observed for the porous airfoils, but much more noticeable than for the reference airfoil. This is partly due to the fact that the peak Strouhal numbers of the turbulence spectra of the porous airfoils are already lower than that of the reference airfoil in the first place. With increasing chord position the spectra of the porous airfoils are shifted toward lower Strouhal numbers, leading to an increase of the amplitude at low Strouhal numbers, but a strong decrease at medium and high Strouhal numbers approximately above $f_c \cdot c_l/U_0 = 3$. The level differences for some of the porous airfoils noticeably exceed that of the non–porous airfoil. Most notably, the difference of the amplitudes measured at the Recemat airfoil reaches values of up to 10 dB at the peak and more than 5 dB at the highest Strouhal number examined.

This illustrates that when the turbulence convects over the surface of the porous airfoils, the high frequency range of the spectrum and the eddies associated with this frequency range decrease more strongly than for the non–porous reference airfoil, while the amplitude of the low frequency range increases. In other words, the energy contained in the turbulence is gradually shifted toward the lower frequency range, an effect which is stronger for the porous airfoils than for the non–porous reference airfoil.

Regarding absolute level differences of the turbulence spectra it has to be kept in mind that the fixed distance of 1 mm between the hot–wire probe and the airfoil surface corresponds to different positions relative to the boundary layer thickness of the particular airfoil. Therefore, Figure E.3 in Appendix E shows the turbulence spectra measured at different chord positions similar to Figure 4.33, but normalized using the mean velocity $\bar{u}(x, z)$ at each measurement position instead of the flow speed U_0 .

The basic behavior obtained from Figure E.3 regarding the development of the turbulence when convected above the surface of the airfoils is the same as was concluded from Figure 4.33: Both the spectra measured at the non–porous airfoil and at the porous airfoils are shifted toward lower Strouhal numbers. But this effect is much stronger for the porous airfoils, leading to a noticeable decrease of the third–octave band level of the turbulent

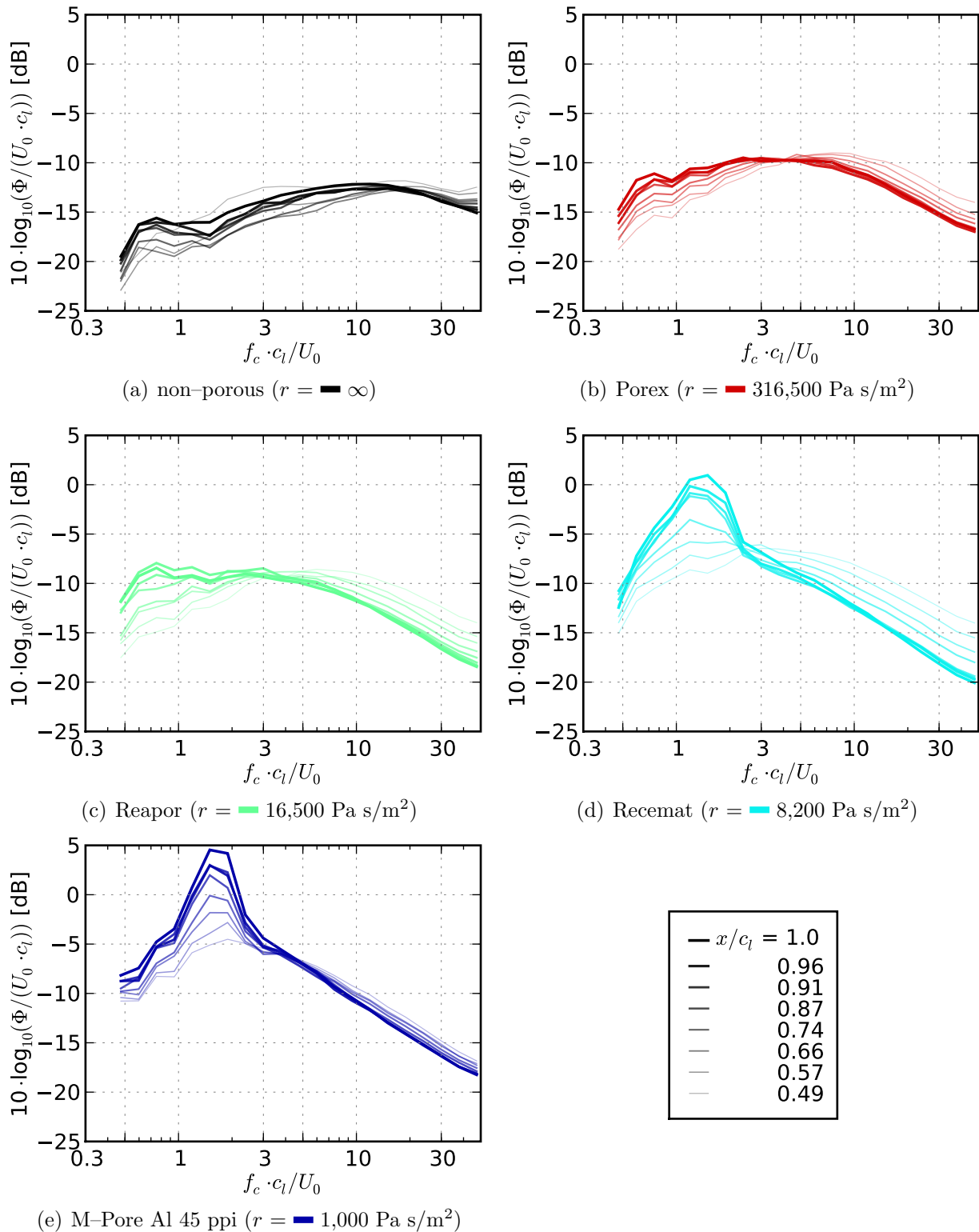
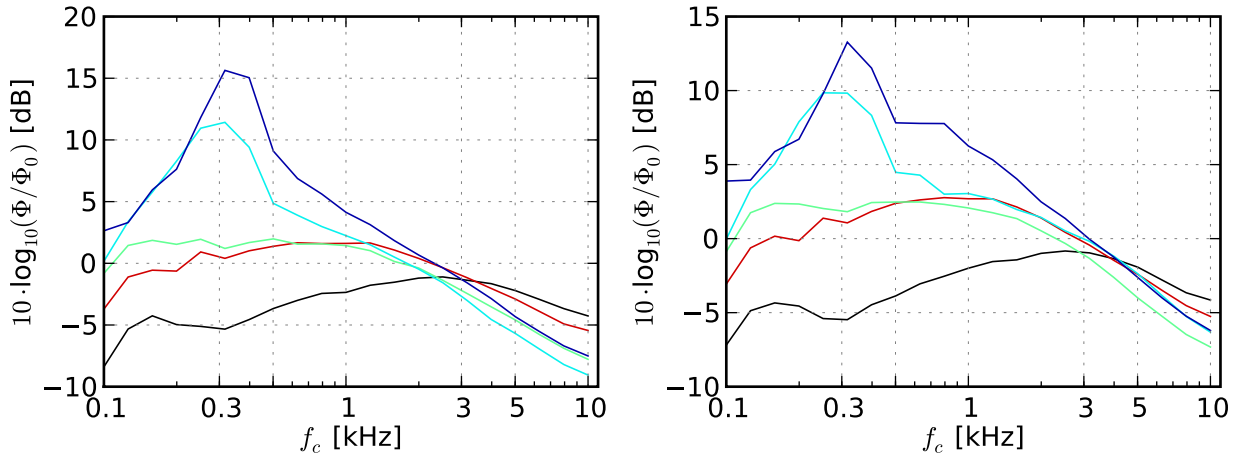


Figure 4.33: Normalized turbulence spectra (in third-octave bands) of the airfoils, measured at different positions along the chord on the suction side approximately 1 mm above the surface, $\alpha = 0^\circ$ and $U_0 = 50 \text{ m/s}$ (The line width and the opacity of the solid lines increase with decreasing distance of the measurement position from the airfoil trailing edge.)



(a) Measured turbulence spectra 1 mm behind the airfoil trailing edge

(b) Measured turbulence spectra 5 mm behind the airfoil trailing edge

Figure 4.34: Third-octave band turbulence spectra Φ , normalized with $\Phi_0 = 1 \text{ m}^2\text{s}^{-1}$, measured in the wake of the airfoils behind the trailing edge, $\alpha = 0^\circ$ and $U_0 = 50 \text{ m/s}$ ($r = \infty$, $\color{red}{\blacksquare}$ 316,500, $\color{green}{\blacksquare}$ 16,500, $\color{cyan}{\blacksquare}$ 8,200, $\color{blue}{\blacksquare}$ 1,000 Pa s/m^2).

velocity fluctuations at Strouhal numbers approximately above 3. For the reference airfoil, this decrease in amplitude is much weaker and can only be seen for higher Strouhal numbers above approximately $f_c \cdot c_l / U_0 = 20$.

Figure 4.34 shows the third-octave band turbulence spectra measured at two positions in the wake of the airfoils. The spectra are given without any normalization as a function of frequency and basically show the same spectral shape as the turbulence spectra measured in the turbulent boundary layer.

The comparison of the turbulence spectra measured above the trailing edge of the porous airfoils with the turbulence spectra of the reference airfoil showed that the amplitude of the turbulence spectra of the porous airfoils exceeds that of the reference airfoil at low frequencies. But at high frequencies the amplitude of the turbulence of the porous airfoils is clearly below that of the non-porous airfoil. This is assumed to be the reason for the measured trailing edge noise reduction of the porous airfoils in the examined range of frequencies above 1.5 kHz. The analysis of turbulence spectra measured at different chord positions showed that the range of medium and high frequencies of the turbulence spectra decreases noticeably with increasing chord position for the porous airfoils, which may be caused by hydrodynamic damping of high frequency velocity fluctuations and the turbulent structures associated with this frequency range. This damping effect can also be seen for the non-porous airfoil, but to a much lesser extent.

The results also show that at frequencies clearly below the limit of the acoustic measurements the turbulence spectra of the porous airfoils contain more energy than the non-porous airfoil, resulting in high-amplitude spectral peaks. It can therefore be assumed that the trailing edge noise generation of the porous airfoils exceeds that of the non-porous airfoil in this range of low frequencies.

To answer the question whether or not the porous airfoils lead to a reduction of the overall sound pressure level, acoustic measurements would be reasonable employing a setup that allows for the detection of low frequencies in the range of the peak frequencies detected in

the measured turbulence spectra of the porous airfoils. However, reliable acoustic measurements on the porous airfoils of the present study at frequencies well below 1.5 kHz were not possible using the present setup due to the compactness condition given in Equation (1.2) and due to the properties of the microphone array described in Section 3.4.

Chapter 5

Development of a basic trailing edge noise prediction model

In this chapter, a first approach toward a basic empirical trailing edge noise prediction model for porous airfoils will be developed, which is based on the third-octave band power spectral density of the velocity fluctuations Φ measured above the trailing edge of the airfoils, as presented in the previous chapter.

5.1 Development of the model

5.1.1 Theory

The underlying theory, which is the basis for the trailing edge noise model to be developed, is that the hydrodynamic disturbances (turbulent eddies) are transported within the turbulent boundary layer over the surface of the airfoils and then scattered at the trailing edge, where they are radiated into the far field as acoustic waves.

The prediction of the trailing edge noise generation is based on the edge noise formulation by Ffowcs Williams and Hall [Ffowcs Williams and Hall, 1970] as given in Equation (2.3) and Equation (2.4). When comparing different trailing edge noise models that make use of the basic formulations by Ffowcs Williams and Hall, it can be seen that one central issue seems to be the calculation of the convection velocity of the eddies. This velocity is described by Ffowcs Williams and Hall simply as the typical fluid velocity U . Another central issue is the determination of the correlation length ℓ of the turbulence in the vicinity of the edge. As discussed before, in many trailing edge noise studies the unknown turbulence correlation length ℓ is most often substituted by the boundary layer thickness δ or the boundary layer displacement thickness δ_1 , based on the assumption of a constant ratio δ_1/δ .

However, common to most trailing edge noise models is the hypothesis that the characteristic velocity scale of the turbulence, the turbulence correlation length ℓ and the characteristic frequency of the turbulence are related to each other. Ffowcs Williams and Hall state that the typical frequency of the turbulent source is in the order of $U/(2\ell)$. A basic formulation that expresses this relation between the characteristic velocity scale u_0 of turbulence, the turbulence correlation length ℓ and the characteristic source frequency ω_0 of the turbulence

is given by Lilley [Lilley, 2001] as

$$\frac{\omega_0 \ell}{u_0} \approx \text{const.} \quad (5.1)$$

The relation described by Equation (5.1) is, for example, used by Hosder et al. [Hosder et al., 2004], who then calculate both ℓ and u_0 from the turbulent kinetic energy obtained from computational fluid dynamics (CFD) simulations.

A reasonable and common approach regarding the determination of the convection velocity of the turbulent velocity fluctuations is the assumption that the convection velocity is proportional to the flow speed U_0 . In several trailing edge noise or aircraft noise models, an additional factor, or an additional summand when given logarithmic as sound pressure level, is then employed to finally adjust the amplitude of the resulting noise to match the measured noise.

Amiet [Amiet, 1976] assumes that the convection velocity of the turbulence is given by $U_c = 0.8 \cdot U_0$, an approach that is subsequently also used in the noise prediction models by Schlinker and Amiet [Schlinker and Amiet, 1981] and Grosveld [Grosveld, 1985]. Blake [Blake, 1986] gives a value of $U_c \approx 0.9 \cdot U_0$ in his review on the noise generation by lifting surfaces. In his study on the silent flight of the owl, Lilley [Lilley, 1998] assumes a ratio of $u_v/U_0 = 0.1$, where u_v is a measure of the turbulent velocity fluctuations in the unsteady vortical flow over an airfoil or wing. In the review on airframe noise reduction studies by Lockard and Lilley [Lockard and Lilley, 2004] they give a constant ratio of the characteristic velocity scale of the turbulence to the flight speed of 0.066 to calculate the noise from clean aircraft.

It can be noticed that several notations are used in the literature to classify the velocity of the turbulent eddies moving along the surface of a wing or an airfoil past its trailing edge. It is either described by a characteristic velocity scale of the turbulence u_0 (for example in the work of Lilley [Lilley, 1998]), as a fluid velocity U (as in the work of Ffowcs Williams and Hall [Ffowcs Williams and Hall, 1970]) or as a turbulence convection velocity U_c (as in the work of Amiet [Amiet, 1976]). All these velocity scales are assumed to be proportional to the flow speed U_0 outside the boundary layer. For the present development of a noise prediction model, the term “convection velocity U_c ” will be used, since it is found to be the most appropriate notation to characterize the velocity at which the turbulent eddies move past the trailing edge of the airfoils.

The formula that is used for the prediction of the maximum trailing edge noise at a certain observer position, based on the formula by Ffowcs Williams and Hall (Equation (2.3) and (2.4) with $U = U_c$), is given by

$$\bar{p}^2 = \frac{\rho^2 \cdot U_c^5 \cdot b^2 \cdot (\Phi/U_c^2) \cdot \sin^2 \frac{\Psi}{2}}{c \cdot R^2}. \quad (5.2)$$

Here, $R = 0.73$ m is the distance between the trailing edge at mid-span and the microphone array center, $\Psi = 68.5^\circ$ is the according angle between extended chordline and observer as shown in Figure 4.7(b) and $b = 0.12$ m is the spanwise extent analyzed in the acoustic measurements. As described by Ffowcs Williams and Hall, the volume of the turbulent eddy near the trailing edge in Equation (2.3) is taken as that of a cylinder of diameter 2ℓ and height b centered on the edge of the half plane. Since the typical frequency of the turbulent source f is said to be in the order of $U_c/(2\ell)$, the unknown turbulence correlation length ℓ is substituted by a frequency dependent term $\ell = U_c/(2f)$ and hence some sort of

velocity wavelength. The square of the third–octave band turbulence spectrum Φ , divided by the turbulence convection velocity U_c , gives the normalized turbulence intensity γ , which determines the spectral shape of the resulting trailing edge noise (resulting in a U_c^3 term in the numerator of Equation (5.2)). The exact value of the turbulence convection velocity U_c will be examined in the course of developing an appropriate trailing edge noise model.

In accordance to the work of Brooks et al. [Brooks et al., 1989], the total predicted trailing edge noise third–octave band sound pressure level L_p consists of contributions from noise predicted from the suction side turbulence spectrum, $L_{p,s}$, and noise predicted from the pressure side turbulence spectrum, $L_{p,p}$:

$$L_p = 10 \cdot \log_{10} (10^{L_{p,s}/10} + 10^{L_{p,p}/10}) \text{ dB.} \quad (5.3)$$

The contribution of trailing edge bluntness noise to the total trailing edge noise cannot be included in the prediction given in Equation (5.2), since that would require the knowledge of the flow field behind the airfoil, whereas only the hot–wire measurements performed above the trailing edge on both the suction side and the pressure side of each airfoil will be used as input to the model. The model also cannot include the total contribution of surface roughness noise which is assumed to be radiated not only from the trailing edge position of the porous airfoils, but from the complete surface of the airfoils. But it is quite possible that the prediction of trailing edge noise will contain at least some minor surface roughness noise contribution, because it can be assumed that the measured turbulence spectra Φ contain turbulent velocity fluctuations caused by the surface roughness of the porous airfoils near the trailing edge as well.

In general, the use of the prediction method given in Equation (5.2) requires the following assumptions: Based on the measured turbulence spectra discussed in Section 4.3.4, it is believed that the spectral shape of the trailing edge noise generated by each airfoil is determined by the spectral shape of the turbulent velocity fluctuations alone, while the according amplitude is determined by the associated turbulence convection velocity U_c . This means that the noise generated at the trailing edge of the airfoils supposedly has the same spectral shape as the turbulence spectra Φ measured above the edge, considering the missing bluntness noise contribution and, to some extent, a possible contribution of surface roughness noise to the predicted spectra.

Further, it is assumed that the turbulent eddies are not affected when they convect past the trailing edge, which is described as the “frozen turbulence” hypothesis by Taylor (see for example [Hinze, 1975]). This hypothesis basically states that the shape of the turbulent eddies can be viewed as constant if their lifespan is at least one order of magnitude larger than the time it takes the eddy to move past the edge.

To some extent, the assumption of a similarity between the spectral shape of turbulence and trailing edge noise is an approximation, at least in the present case. It has already been discussed that, for example, the turbulence spectrum measured above the trailing edge of the reference airfoil shows a peak between 2 kHz and 3 kHz that cannot be seen in the corresponding measured trailing edge noise spectrum (although it is also predicted by the BPM–model). However, the present approach is still considered useful, and the underlying theory is assumed to be reasonable and physical. The aim of the present work is the development of a rather simple empirical trailing edge noise model, and hence the use of the measured turbulence spectra is assumed to result in a sufficient overall accuracy compared to the results of the acoustic measurements.

The development of a trailing edge noise prediction model based on the power spectral density of the velocity fluctuations within the turbulent boundary layer requires the handling of two main issues:

1. the acquisition of the characteristic turbulent velocity fluctuations (turbulence spectra) from the hot-wire measurements within the turbulent boundary layer of the airfoils, and hence the determination of Φ in Equation (5.2) and
2. the determination of the characteristic velocity of the turbulent structures within the boundary layer, the turbulence convection velocity U_c in Equation (5.2).

In other words, the development of a trailing edge noise prediction model based on the formulation by Ffowcs Williams and Hall according to Equation (5.2), that uses turbulence spectra measured inside the turbulent boundary layer in the vicinity of the trailing edge, basically has two adjustable parameters (or degrees of freedom) that have an influence on both spectral shape and amplitude of the resulting trailing edge noise spectra. First, turbulence spectra Φ that are characteristic for each airfoil have to be determined. In order to expand the usability of the intended noise prediction model for other airfoils, without the necessity of detailed hot-wire measurements, the turbulence spectra should be modeled based on basic airfoil parameters and flow parameters. Second, the convection velocity U_c has to be determined. With the objective of a more universal trailing edge noise model, the turbulence convection velocity should also be modeled based on basic airfoil and flow parameters.

5.1.2 Trailing edge noise prediction based on measured turbulence spectra and measured mean velocity

In this section, the trailing edge noise of the five airfoils from Table 3.2 will be predicted using the velocities measured in the corresponding turbulent boundary layers.

Assessment of the characteristic turbulence spectra

To obtain the first input for the intended trailing edge noise model, a spectrum of the velocity fluctuations inside the turbulent boundary layer has to be determined, which is characteristic for each airfoil.

It is obvious that the exact position, at which the turbulence spectra were measured relative to the airfoil surface, has a large influence on the measured spectra. In the present case of the development of a trailing edge noise prediction model based on velocity fluctuations within the turbulent boundary layer, it is assumed that it is advantageous when the turbulence spectra are measured as close to the airfoil surface as possible. As discussed in Section 3.5, it is difficult to exactly determine the distance of the hot-wire probe from the surface of porous airfoils, especially for airfoils with large pores and a very coarse surface, since it is not possible to detect $z = 0$ for a rough surface.

Considering that the intended model will be used for the trailing edge noise prediction of porous airfoils in comparison to a reference airfoil, the turbulence spectra should be measured at approximately identical distances from the surface of the airfoils. If possible,

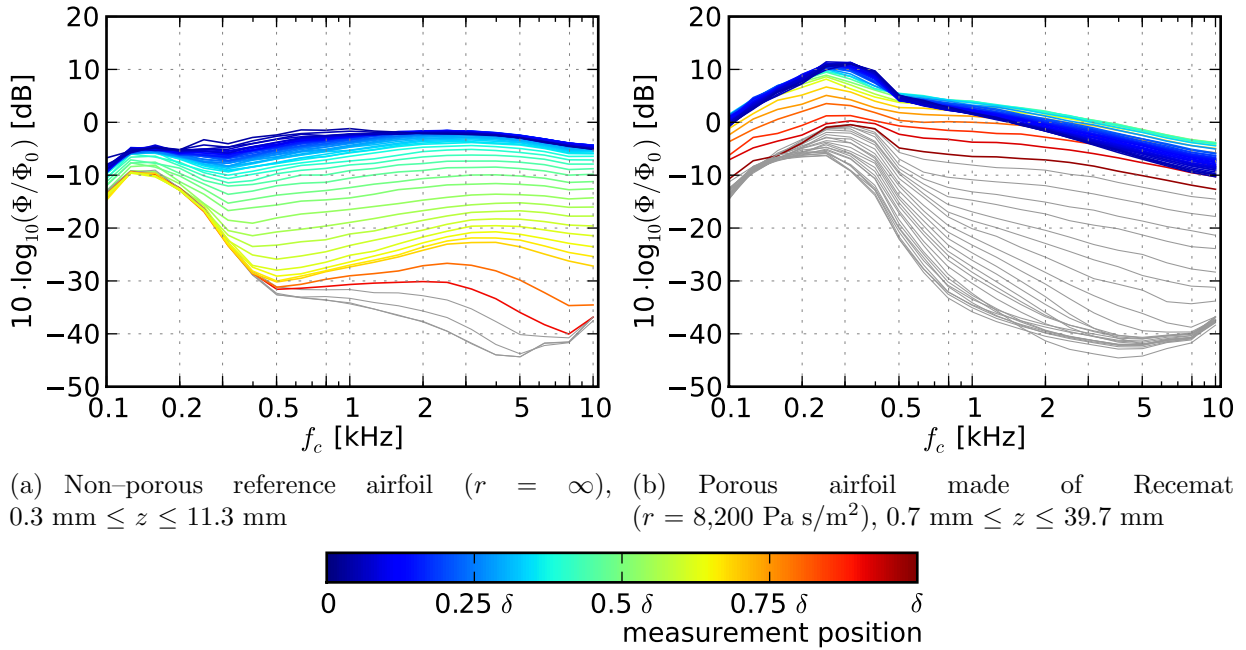


Figure 5.1: Turbulence spectra measured at different distances z above the trailing edge of two airfoils at a flow speed of 50 m/s and zero angle of attack (colored lines indicate measurement positions within a distance equal to the corresponding boundary layer thickness, estimated according to the method described at the end of Section 4.3.1, from the airfoil surface, gray lines indicate measurement positions further away from the surface)

variations of the probe position relative to the surface between measurements at different airfoils should be minimized.

To illustrate the influence of the measurement position on the resulting turbulence spectra, Figure 5.1 shows the third-octave band turbulence spectra measured at different heights above the surface of two airfoils.

It can be observed that for measurement positions close to the surface of the airfoils, the spectral shape of the turbulence does not change significantly and the differences in amplitude are small. In the corresponding measurements, the vertical step size between measurement positions closest to the surface was 0.1 mm for at least the first 22 measurements and hence a distance of at least 2.2 mm from the initial position.

Additionally, the spectra presented in Figure 5.1 indicate that the turbulence at very low frequencies may be influenced by other mechanisms than the turbulent boundary layer of the airfoil, since the low frequency range of the spectra for both airfoils (approximately below 200 Hz to 300 Hz) are characterized by a noticeable spectral hump which is also visible for measurement positions outside of the turbulent boundary layer. This spectral hump was already observed in the turbulence spectra shown in Section 4.3.4 of the last chapter.

The influence of variations of the distance, at which the hot-wire measurements were performed, on the third-octave band turbulence spectra and the resulting trailing edge noise predictions will be examined in more detail in the following sections.

Finally, it was decided to use the third-octave band turbulence spectra measured at the closest distance of 1 mm from the airfoil surface for both the non-porous airfoil and the

porous airfoils. The resulting turbulence spectra that will be used for the prediction of trailing edge noise are hence the ones that are shown in Figure 4.29 of Chapter 4.

Other methods have been tested to obtain characteristic turbulence spectra for the examined airfoils. This included an approach which consisted of an averaging of the turbulence spectra over a region with a certain height above the airfoil surface, for example a height of $2 \delta_1$. The resulting averaged turbulence spectra did not show any significant differences in amplitude at high frequencies, which would lead to only insignificant differences in the resulting predicted trailing edge noise spectra (if not completely different turbulence convection velocities would be chosen for each airfoil). Another approach that was tested also contained an averaging of the turbulence spectra measured above the airfoil surfaces, but with a frequency dependent upper limit, such as a constant fraction of the hydrodynamic wavelength U_0/f_c . This approach is similar to the method described by Chase [Chase, 1972], who developed a theoretical trailing edge noise model based on surface pressures, and considers sources only that are located within a distance z equal to a small fraction of an acoustic wavelength from the edge so that $kz \ll 1$. However, the approach did not lead to a particularly good agreement between predicted and measured trailing edge noise spectra.

Assessment of the mean flow velocities

The aim of this section is the development of a method to determine a characteristic value for the turbulence convection velocity U_c needed for the intended trailing edge noise model based on Equation (5.2).

According to theory, the convection velocity is proportional to the flow speed, $U_c \propto U_0$. It is assumed in the present study, that the convection velocity is approximately consistent with a velocity proportional to the mean flow speed $\bar{u}(z)$ at the distance z from the surface of the airfoils at which the corresponding turbulence spectra have been measured. In the present case, this refers to a distance of $z = 1$ mm, corresponding to the turbulence spectra shown in Figure 4.29(c). The resulting turbulence convection velocity U_c will then be calculated according to

$$U_c = g \cdot \bar{u}(z), \quad (5.4)$$

with $z = 1$ mm. In Equation (5.4), g is a constant factor. This approach has the advantage that the characteristic turbulence spectrum is strongly related to the convection velocity U_c , since both are derived from measurements at the same position inside the boundary layer.

The use of a constant proportionality factor g for all airfoils includes the assumption that the mean velocity at the position, where the noise is generated due to the interaction of the turbulence with the trailing edge, is nearly constant for all airfoils. Yet the velocity profiles measured above the trailing edge and in the wake of the airfoils, as shown in Section 4.3.1, indicate that the velocity directly at the surface is small for the porous airfoils, but not necessarily zero as can be assumed for the non-porous airfoil according to theory. Thus, the assumption of a constant factor will introduce a minor error. However, with the intention of developing a simple trailing edge noise prediction model, a constant value of g will be used for both porous airfoils and non-porous airfoils. The proportionality factor g will finally be adjusted to result in the best agreement between measured and predicted third-octave band sound pressure levels.

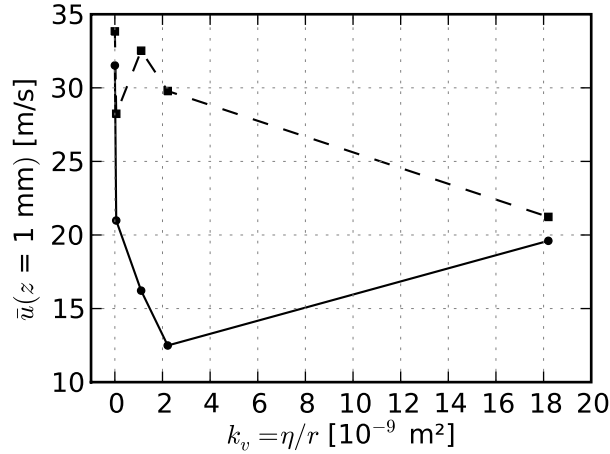


Figure 5.2: Mean flow velocity $\bar{u}(z)$ measured at a distance of $z = 1$ mm above the trailing edge of the airfoils as a function of the viscous permeability k_v (with $\eta = 18.2 \cdot 10^{-6}$ kg/(m s) at 22°C) of the airfoils

Due to the coupling of the turbulence spectrum and the mean flow velocity, measurements at different distances than $z = 1$ mm from the airfoil surface would not only result in different characteristic turbulence spectra, but also in different mean flow velocities $\bar{u}(z)$, and the resulting differences in the amplitude of the predicted trailing edge noise may be corrected by adjusting the proportionality factor g . But again, the underlying theory of the intended trailing edge noise model is that the velocity fluctuations are measured in the vicinity of the trailing edge in order to be correlated to the generated trailing edge noise, and hence measurements should be performed close to the trailing edge.

In the course of the development of the model, different other approaches were tested regarding the appropriate convection velocity U_c . This included the use of the mean velocity at a distance z relative to the boundary layer thickness of the different airfoils (more precisely, a distance of $z = \frac{1}{4} \cdot \delta$), which lead to a turbulence convection velocity $U_c = g \cdot \bar{u} (z = \frac{1}{4} \cdot \delta)$. Another approach was tested that involved a frequency-dependent distance as a constant fraction of the hydrodynamic wavelength U_0/f_c , similar to the approach tested for the upper limit of the averaging of the turbulence spectra as described in the last section. However, the approach lead to a strong decrease of the resulting trailing edge noise spectra with increasing frequency that exceeded the decrease of the measured spectra.

Finally, the chosen method, that uses the mean flow velocity at the same measurement position at which the corresponding turbulence spectra were measured, seems to be the most physically meaningful approach. The measured mean flow velocities at the fixed distance $z = 1$ mm above the airfoil surface are shown in Figure 5.2 as a function of the viscous permeability k_v of the airfoils. It is visible that the corresponding values of $\bar{u}(z = 1 \text{ mm})$ for suction side and pressure side differ noticeably for some airfoils (especially Recemat and Reapor). This is assumed to be due to the semi-symmetric shape of the airfoils. As discussed in Section 4.1, the semi-symmetric shape of the SD7003 airfoil causes a positive lift force even at a geometrical angle of attack of 0° , which may be accounted for by introducing an effective angle of attack. Hence, in the present case of nominally zero angle of attack, the effective angle of attack is greater zero, which may be the reason for the differences between the mean flow velocity of suction side boundary layer and pressure side boundary layer.

In order to obtain a more detailed view of the turbulent boundary layer of the porous airfoils, the shape of the measured velocity profiles will be further examined. The velocity profiles above the trailing edge were presented in Figure 4.22 for both the suction side and the pressure side of the five airfoils from Table 3.1.

According to flat plate theory [Eckert and Drake jr., 1959], the turbulent boundary layer consists of a thin viscous sublayer directly at the wall, also called laminar sublayer, and a range which can be described by a logarithmic function, known as the “log law of the wall” [Bradshaw and Huang, 1995]. It is of interest for the present study how the consistency of the porous airfoils changes the velocity profile of the boundary layer with respect to these single layers. It was already stated that the thickness of the turbulent boundary layer increases with decreasing air flow resistivity, as does the boundary layer displacement thickness. However, the ratio of displacement thickness to boundary layer thickness, δ_1/δ , was found to be different for the porous airfoils compared to the reference airfoil. This indicates that the shape of the corresponding velocity profiles may be generally different.

The viscous sublayer of the turbulent boundary layer is characterized by a linear relation between the mean velocity $\bar{u}(z)$ and the wall distance z , the characteristic parameters of the viscous sublayer being the laminar sublayer thickness δ_b and the mean velocity \bar{u}_b at the distance $z = \delta_b$. For flat plates the sublayer thickness δ_b can be estimated as

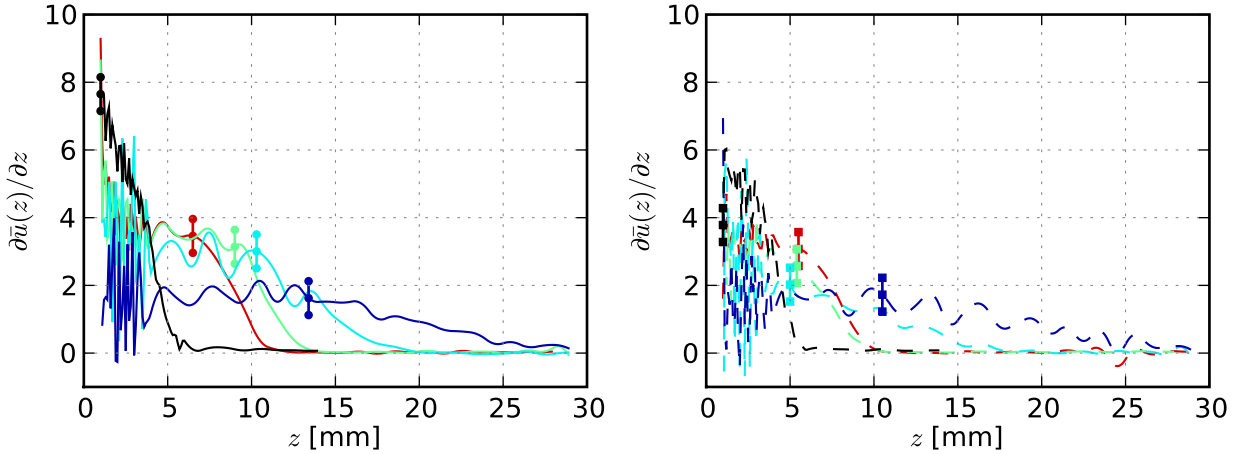
$$\frac{\delta_b}{\delta} = \frac{194}{Re_x^{0.7}}, \quad (5.5)$$

with Re_x being the Reynolds number based on plate length [Eckert and Drake jr., 1959]. Using this equation to obtain a first estimate of the sublayer thickness of the reference airfoil yields a value of $\delta_b \approx 0.13$ mm for both suction side and pressure side when using the Reynolds number based on chord length at $U_0 = 50$ m/s. The distance of the hot-wire probe of approximately 1 mm would hence be outside of the viscous sublayer.

Equation (5.5) cannot be assumed to be valid for the porous airfoils. Another method to determine the sublayer thickness of the boundary layer is the calculation of the velocity gradient $\partial\bar{u}(z)/\partial z$, which is constant inside the laminar sublayer. The gradient of the velocity is given in Figure 5.3 for the suction side and the pressure side of the five airfoils from Table 3.2. It is calculated based on the interpolation of the measured velocity profiles by a spline fit $U'(z)$, as described in Section 4.3.1.

In general, the gradient $\partial\bar{u}(z)/\partial z$ in the boundary layer should be constant in the proximity of the wall up to a distance of $z = \delta_u$. With further increasing distance the gradient should decrease to a value of zero at the edge of the turbulent boundary layer, where $\bar{u}(\delta) = U_0 = \text{const}$. The sublayer thickness can hence be estimated from the velocity gradient as the distance where the curves begin to decrease from a constant value. An approximate value for the viscous sublayer thickness, derived visually from the curves of the velocity gradient, is indicated in Figure 5.3 for each airfoil.

In accordance with the rough estimate from Equation (5.5), it can be seen that the sublayer thickness of the non-porous airfoil is smaller than (or at the maximum equal to) the minimum distance of the measurements of 1 mm, while for the porous airfoils the sublayer thickness is much larger. Furthermore, although the velocity gradient obtained from the spline fit is subject to fluctuations near the surface of the airfoils, a trend can be obtained: For both suction side and pressure side the gradient at the non-porous airfoil is higher than that measured at the porous airfoils, which can be roughly divided into two groups: Porous



(a) Gradient of the velocity from the suction side as shown in Figure 4.22(a)

(b) Gradient of the velocity from the pressure side as shown in Figure 4.22(b)

Figure 5.3: Gradient $\partial\bar{u}(z)/\partial z$ of the velocity in the boundary layer above the trailing edge at $x/c_l = 1$, obtained by a spline fit as explained in Section 4.3.1, flow speed $U_0 = 50$ m/s, angle of attack $\alpha = 0^\circ$ ($r = \infty, 316,500, 16,500, 8,200, 1,000$ Pa s/m²). The markers denote the estimate of the thickness δ_b of the laminar sublayer.

airfoils made of materials with medium and high air flow resistivities ($r = 316,500, 16,500$ and $8,200$ Pa s/m²) show a velocity gradient clearly above that measured in the laminar sublayer of the porous airfoil with a considerably lower air flow resistivity of $1,000$ Pa s/m². This trend can also be observed from the velocity profiles shown in Figure 4.22.

Figure 5.3 shows that there exist differences between the sublayer thicknesses of suction side and pressure side, especially for the airfoils made of Reapor and Recemat ($r = 16,500$ and $8,200$ Pa s/m²). In general, the estimated sublayer thickness at the pressure side of all four porous airfoils is smaller than that of the suction side, but for these two airfoils the difference is larger than for the other airfoils. As a result, the order of the laminar sublayer thickness changes. While it is consistent to the reversed order of air flow resistivities at the suction side (δ_b increases with decreasing r), this is not true for the pressure side.

The results of the examination of the velocity within the turbulent boundary layer of the porous airfoils give evidence that the hot-wire measurements, performed at a constant distance of approximately 1 mm, were conducted within the laminar sublayer of the porous airfoils. The measurement in the boundary layer of the non-porous reference airfoil was either performed just outside or at the edge of the laminar sublayer.

Evaluation of the method using measured turbulence spectra and measured convection velocities

As a first evaluation of the trailing edge noise model, Figure 5.4 shows the comparison between the measured third-octave band sound pressure levels with those predicted by Equation (5.2). The prediction is based on the measured turbulence spectra, presented in Figure 4.29, as well as the mean flow velocity $\bar{u}(z)$, measured at a distance of 1 mm above the trailing edge of the airfoils at a flow speed of 50 m/s, as presented in Figure 5.2.

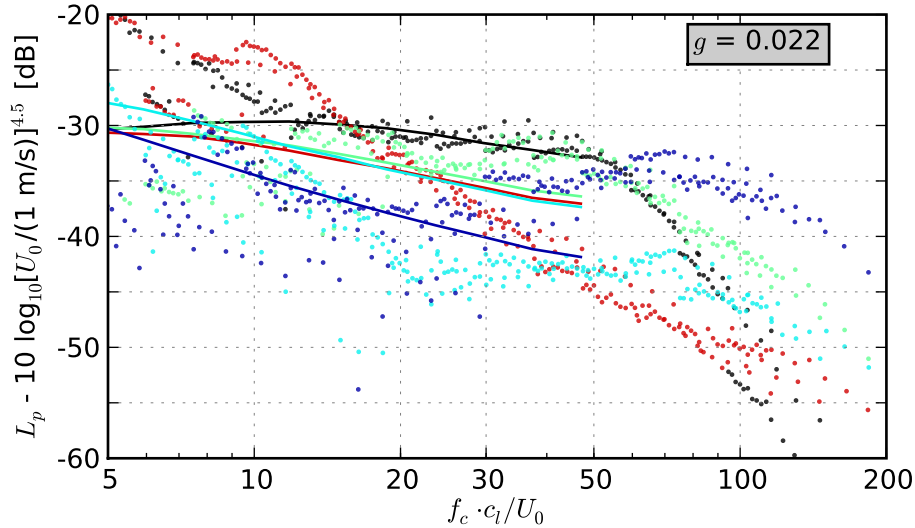


Figure 5.4: Comparison of predicted and measured trailing edge noise third-octave band sound pressure levels as a function of chord based Strouhal number, scaled based on $U_0^{4.5}$, for the airfoils from Table 3.2 ($r = \infty$, $316,500$, $16,500$, $8,200$, $1,000$ Pa s/m²), angle of attack $\alpha = 0^\circ$ (prediction is based on measured third-octave band turbulence spectra Φ and turbulence convection velocity $U_c = 0.022 \cdot \bar{u}(z)$ at $z = 1$ mm for a flow speed of 50 m/s)

The ambient temperature measured during the hot-wire measurements is used for the correction of the speed of sound in Equation (5.2).

The proportionality factor g , needed to scale the turbulence convection velocity, is set to 0.022, which was found to result in the best agreement between the predicted and the measured sound pressure levels of the non-porous reference airfoil. Hence, the turbulence convection velocity U_c is assumed to be equal to $0.022 \cdot \bar{u}(z = 1 \text{ mm})$.

The sound pressure levels in Figure 5.4 are presented as a function of the chord based Strouhal number and scaled with the 4.5th power of the flow speed U_0 . This way of presentation, as a function of Strouhal number instead of frequency at the flow speed used for the hot-wire measurements, has been chosen since more data points are available, which allows for a comparison that concentrates on the basic reproduction of the measured spectra rather than the analysis of minor differences that cannot be correctly predicted by the basic trailing edge noise model in the first place.

Since the prediction is based on the measured turbulence spectra, the upper frequency limit of the resulting sound pressure level spectra is equal to the upper limit of the hot-wire measurements of 10 kHz. On the other hand, the lower frequency limit of the acoustic measurements is 1.5 kHz, resulting in only a small range of frequencies available for the comparison of the predicted results with the measured results. Most notably, as discussed before, this means that the spectral peak of the predicted trailing edge noise for the porous airfoils cannot be verified. The spectral peak predicted for the non-porous airfoil at a Strouhal number of approximately 10 to 15 cannot be observed in the measured trailing edge noise spectra. However, for this admittedly simple trailing edge noise prediction method, the comparison shown in Figure 5.4 is seen as a rather satisfying result.

Due to the missing of high frequencies in the measured turbulence spectra, and subsequently also in the predicted trailing edge noise spectra, the drop of the measured third-octave band spectrum of the non-porous airfoil at high frequencies cannot be predicted. The

same applies to the prediction of the assumed contribution of surface roughness noise of the porous airfoils in this frequency range.

It can be seen that the measured sound pressure levels of the porous airfoils with low air flow resistivities are noticeably scattered, making it difficult to exactly analyze the agreement between measurement and prediction for these airfoils. The predicted spectra can be roughly divided into three groups: the non-porous airfoil, airfoils with medium and high air flow resistivities and airfoils with low air flow resistivities. The predicted trailing edge noise of the non-porous airfoil has the highest amplitude at medium and high Strouhal numbers. The noise generated at the trailing edge of the airfoils with high and medium air flow resistivities ($r = 316,500$, $16,500$ and $8,200$ Pa s/m²) is lower than that of the reference airfoil, with a maximum difference of about 5 dB at high Strouhal numbers, while the porous airfoil with the lowest air flow resistivity ($r = 1,000$ Pa s/m²) generates even less trailing edge noise with differences in the order of 10 dB compared to the non-porous airfoil.

It appears that the general agreement between predicted and measured trailing edge noise is better at medium frequencies, corresponding to Strouhal numbers approximately between 10 and 30 in Figure 5.4. It may be assumed that at higher Strouhal numbers the trailing edge noise spectra of the porous airfoils, especially those with low air flow resistivities, are already influenced by surface roughness noise, which cannot be correctly predicted by the trailing edge noise model. Furthermore, as was discussed in Section 3.4.4, the three-dimensional sound maps obtained for some of the porous airfoils indicate the potential existence of another noise source mechanism. This mechanism, which currently cannot be explained, is not taken into account in the prediction model.

The shape of the predicted spectra is derived from the shape of the measured turbulence spectra, which was one of the initial assumptions for the development of the prediction model. The resulting slope of the predicted trailing edge noise shows differences compared to the shape of the measured trailing edge noise spectra. For example, for the airfoil made of Porex ($r = 316,500$ Pa s/m²) the slope of the measured spectra is smaller than that of the predicted spectra, while for the remaining porous airfoils the predicted slope seems to be smaller than the overall slope of the measured spectra. The reasons are the same as mentioned above, the contribution of surface roughness noise and, possibly, noise from another noise source mechanism, to the measured trailing edge noise. Additionally, some of the porous airfoils that were subject to the hot-wire measurements generated a noticeably increased trailing edge noise compared to the reference airfoil, such as the airfoil made of Reapor ($r = 16,500$ Pa s/m²) due to its partly irregular trailing edge. Such distinct features of the trailing edge noise spectral shape are not included in the prediction model. However, considering the basic approach of the model and the scattering of the measured trailing edge noise spectra, the general agreement between measurement and prediction is quite adequate.

Influence of the distance of the measurement position from the airfoil surface

In this section, the influence of the distance of the hot-wire measurement location from the surface of the airfoil, for example due to the inaccurate positioning or misalignment of the hot-wire probe, will be addressed.

A basic requirement for the development of the trailing edge noise model of the present study is the performance of hot-wire measurements within the turbulent boundary layer very close to the trailing edge, in order to be a characteristic measure for the generated trailing edge noise. Furthermore, it is assumed that the hot-wire measurements were performed at similar distances from the surface of each airfoil. However, this assumption cannot be verified due to the surface roughness of the porous airfoils and the subsequent rather approximative method used to determine the distance of the hot-wire probe from the airfoil surface. It is therefore likely that the measured distances contain some errors. This is especially true for porous materials with a very low air flow resistivity, large pores and hence a very coarse surface.

Different measurement locations within the turbulent boundary layer of the airfoils result in differences of the turbulence spectra, an effect which was shown in Figure 5.1, and differences of the mean flow velocity $\bar{u}(z)$. The latter may have a stronger effect on the resulting noise prediction, since the trailing edge noise model according to Equation (5.2) contains the mean velocity to the third power.

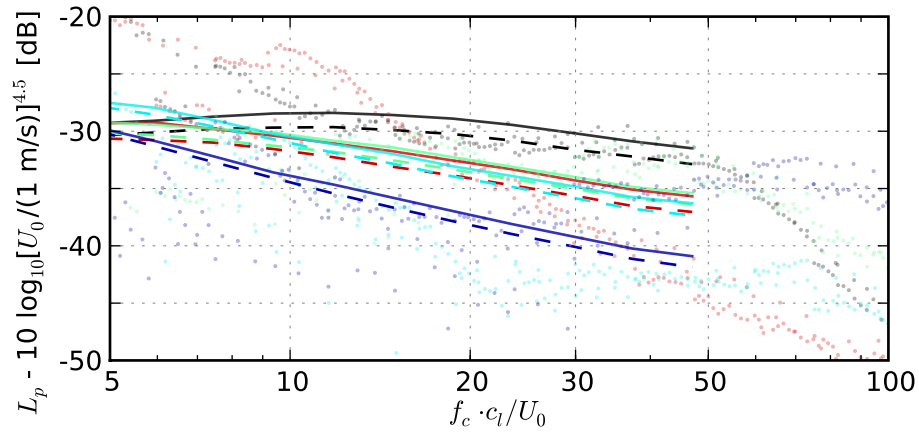
The influence of variations of the measurement distance on the resulting noise prediction will be examined using a relatively simple method: Figure 5.5 presents trailing edge noise spectra which are predicted from measurements at distances other than 1 mm, but with the same proportionality factor g of 0.022 as used for the prediction shown in Figure 5.4. The predicted spectra obtained from measurements at a distance of 1.5 mm are given in Figure 5.5(a), those obtained from measurements 2 mm from the airfoil surface are shown in Figure 5.5(b) and those calculated based on measurements 3 mm from the surface are given in Figure 5.5(c). This means that a positioning error of 0.5 mm, 1 mm and 2 mm compared to the “reference” prediction (based on measurements 1 mm from the surface of the airfoils) is assumed, respectively. For the means of comparison, each figure contains the reference spectra from Figure 5.4.

As can be obtained from Figure 5.5(a), a deviation of 0.5 mm from the assumed measurement distance of 1 mm from the surface of the airfoils would lead to a maximum deviation of approximately less than 2 dB for the non-porous airfoil and the porous airfoils made of Porex ($r = 316,500 \text{ Pa s/m}^2$) and Recemat ($r = 8,200 \text{ Pa s/m}^2$). For the porous airfoils with lower air flow resistivities the maximum deviation is even slightly lower and in the order of 1 dB.

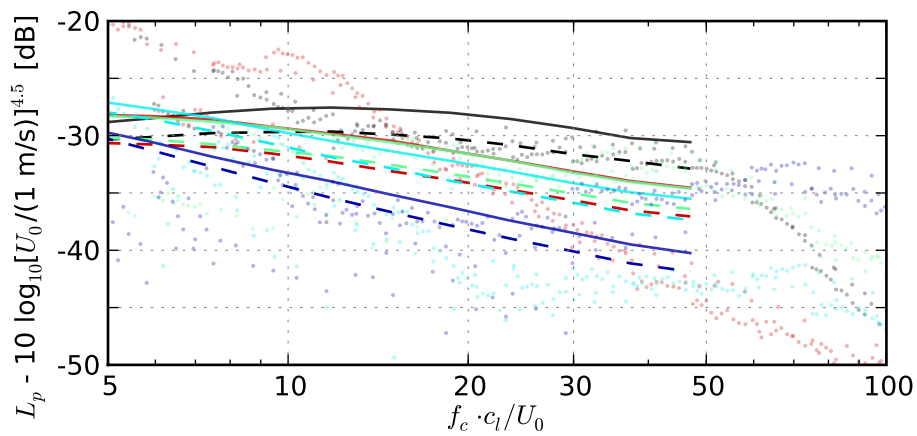
A deviation of 1 mm from the assumed distance leads to an increased deviation of the resulting predicted spectra, as presented in Figure 5.5(b). The maximum deviation for the non-porous airfoil and porous airfoils with high air flow resistivities is now in the order of approximately 3 dB, that for the porous airfoils with low air flow resistivities is smaller and about 2 dB to 3 dB.

Finally, a deviation of the measurement distance of 2 mm would lead to the results presented in Figure 5.5(c). The maximum difference between the predicted trailing edge noise levels are in the order of approximately 4 to 5 dB for all airfoils examined.

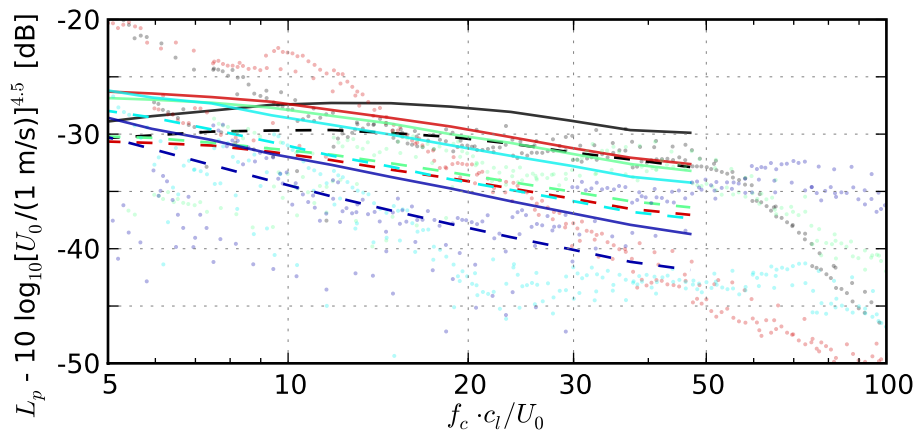
Thereby, it has to be noted that the differences in amplitude have the same tendency for all airfoils, meaning that a measurement position further away from the surface results in an increase of the trailing edge noise level for all airfoils when the same proportionality factor g is used. Thus, a systematic positioning error would only have a minor effect on the prediction of level differences between different airfoils.



(a) Measurement position $z = 1.5$ mm above airfoil surface, positioning error $\Delta z = 0.5$ mm



(b) Measurement position $z = 2$ mm above airfoil surface, positioning error $\Delta z = 1$ mm



(c) Measurement position $z = 3$ mm above airfoil surface, positioning error $\Delta z = 2$ mm

Figure 5.5: Influence of the distance of the measurement position from the airfoil surface on the noise prediction, $g = 0.022$, flow speed $U_0 = 50$ m/s, angle of attack $\alpha = 0^\circ$, solid line: predicted spectra based on the indicated measurement position, dashed line: predicted spectra based on the measurements 1 mm above the airfoil surface as shown in Figure 5.4 as a reference ($r = \infty, 316,500, 16,500, 8,200, 1,000$ Pa s/m²)

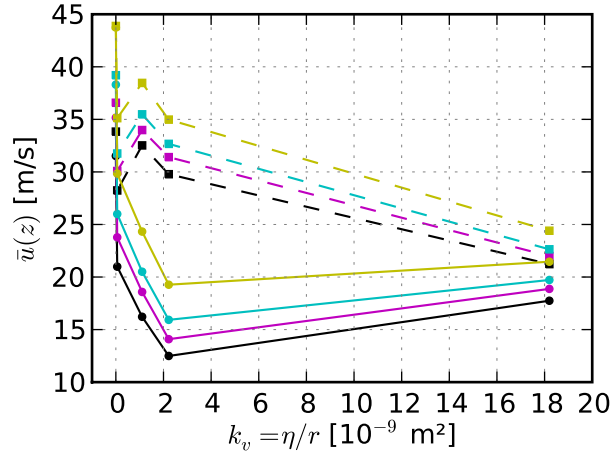


Figure 5.6: Influence of the distance of the measurement position from the airfoil surface on the mean flow velocity $\bar{u}(z)$ as a function of the viscous permeability k_v of the airfoils ($z = \blacksquare$ 1 mm, \blacksquare 1.5 mm, \blacksquare 2 mm, \blacksquare 3 mm)

The examination of the influence of a potential positioning error of the hot-wire probe yielded satisfying results regarding the basic approach of the trailing edge noise prediction model. A level difference of less than 5 dB in case of a deviation of the probe position of 2 mm is taken to be quite acceptable. Besides, if the hot-wire measurements are carefully prepared and the probe is positioned as accurately as possible, it can be assumed to be unlikely that the differences of the distance are larger than 0.5 mm or 1 mm even for relatively rough surfaces.

As mentioned before, it is assumed that the main reason for the differences in amplitude of the predicted spectra due to deviations of the probe position is the mean flow velocity $\bar{u}(z)$ within the turbulent boundary layer. The amplitude of the corresponding third-octave band turbulence spectra was found to be only minimally affected by changes of the probe position (when within a small range close to the surface of the airfoils), as was shown in Figure 5.1.

The influence of the hot-wire measurement position on the mean flow velocity is presented in Figure 5.6 for the distances of 1 mm, 1.5 mm, 2 mm and 3 mm that were used for the predictions shown in Figure 5.4 and Figure 5.5. The information presented in Figure 5.6 is basically also contained in the velocity profiles shown in Figure 4.22.

A rough estimate for the influence of differences in the mean flow velocity on the resulting level differences of the predicted trailing edge noise will be given for the case of a noticeable positioning error of 2 mm, corresponding to the differences in the predicted sound pressure levels shown in Figure 5.5(c). The resulting differences of the mean flow velocity between the measurement 1 mm and 3 mm from the surface of the airfoils are, for example, 12.2 m/s and 10.0 m/s for the suction side and pressure side of the non-porous airfoil, respectively, which is the maximum difference. For the porous airfoil with the lowest air flow resistivity, M-Pore Al 45 ppi ($r = 1,000 \text{ Pa s/m}^2$), the corresponding differences are 3.7 m/s and 3.1 m/s. These deviations would cause differences of the predicted sound pressure levels of 4.3 dB and 3.4 dB for suction side and pressure side of the non-porous airfoil and 2.5 dB and 1.8 dB for the porous airfoil. These differences are still smaller than the level differences obtained from Figure 5.5(c).

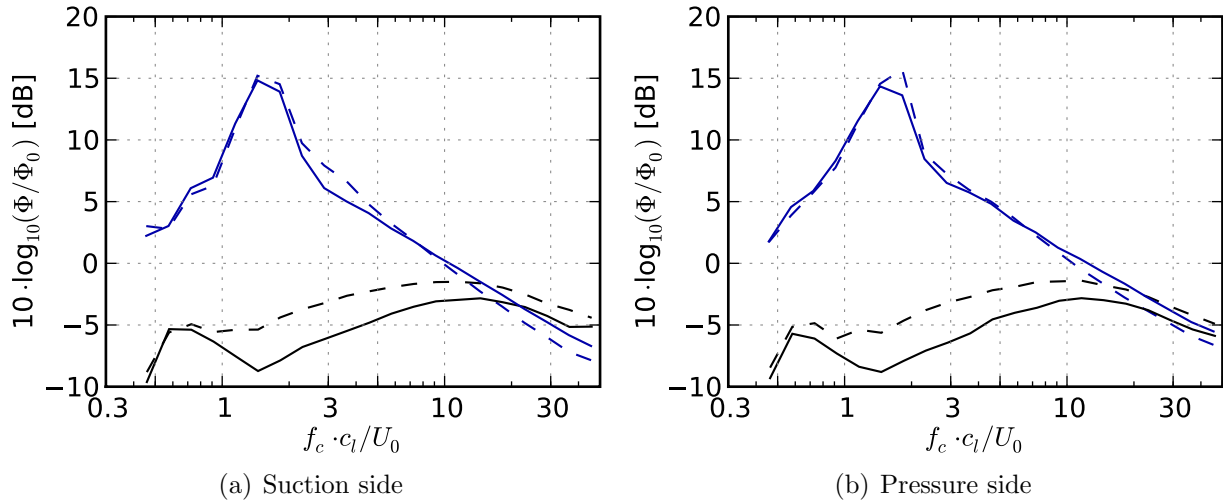


Figure 5.7: Influence of the distance of the measurement position from the airfoil surface on the turbulence spectra measured above the trailing edge of two airfoils, flow speed $U_0 = 50$ m/s, angle of attack $\alpha = 0^\circ$, solid line: $z = 3$ mm, dashed line: $z = 1$ mm ($r = \infty$, \blacksquare 1,000 Pa s/m²)

Although it was found that the influence of the measurement position on the resulting turbulence spectra is relatively small when within a reasonable distance from the surface of the airfoil, it will be further examined for the two airfoils considered above. Figure 5.7 shows the corresponding third-octave band turbulence spectra for both suction side and pressure side of the non-porous airfoil and the porous airfoil made of M-Pore Al 45 ppi, measured at the reference distance of 1 mm and a distance of 3 mm (again assuming a noticeable positioning error of 2 mm).

The spectra of the porous airfoil presented in Figure 5.7 show only minor differences for both suction side and pressure side, with maximum deviations of approximately 1 dB to 2 dB. With increasing distance from the surface, the amplitude of the spectrum slightly decreases around the peak, but increases at higher Strouhal numbers approximately above 5. For the non-porous reference airfoil the differences in amplitude are larger, reaching maximum values of about 3 dB. It can be seen that for the reference airfoil the shifting of the measurement position further away from the surface leads to a decrease in amplitude. For the examined measurement positions this effect leads to an interaction of the trailing edge noise increase due to the increasing mean flow velocity $\bar{u}(z)$ (Figure 5.6) with the trailing edge noise reduction due to the decreasing amplitude of the corresponding trailing edge noise spectra (Figure 5.7).

The examination of the cause for the differences of the predicted trailing edge noise spectra, due to deviations of the measurement position within the turbulent boundary layer, lead to the conclusion that the differences are both a consequence of the changing mean flow velocity and the changing amplitude of the turbulence spectra. An increasing distance from the surface naturally leads to an increase of the mean flow velocity $\bar{u}(z)$ and hence an increase of the resulting trailing edge noise. The dependence of the turbulence spectra on the measurement position is more complex when relatively close to the surface. An increase in distance may lead to a decrease in amplitude of the turbulence spectrum or even to an increase, thus interfering with the trailing edge noise increase due to the increasing mean

flow velocity. Additionally, different measurement positions inside the turbulent boundary layer potentially lead to different shapes of the according turbulence spectra.

5.1.3 Trailing edge noise prediction based on modeled turbulence spectra and mean velocity

After it was shown that the trailing edge noise model given by Equation (5.2) provides satisfying results for the prediction based on measured turbulence spectra and mean velocities, it will be further developed to enable the trailing edge noise prediction for the remaining porous airfoils without the necessity of detailed hot-wire measurements. This will be achieved by deriving approximative equations for the estimation of the characteristic turbulence spectra as well as the characteristic mean flow velocity.

To this end, a simplified approach will be used: Instead of approximating the turbulence spectra and mean flow velocities for both suction side and pressure side separately, the corresponding data will be averaged prior to the approximation. Complex tasks like the analytic description of the mean flow velocity $\bar{u}(z = 1 \text{ mm})$, which features completely different curve shapes for suction side and pressure side (Figure 5.2), can hence be avoided. Moreover, this approach seems to be reasonable since the trailing edge noise contributions from suction side and pressure side will finally be summed up, and contrary effects, originating from velocity fluctuations at the suction side and at the pressure side, on the far field noise may eventually be cancelled.

Estimation of characteristic turbulence spectra

In order to obtain a basic trailing edge noise prediction model that does not require the measurement of velocity fluctuations inside the boundary layer, the basic shape of the turbulence spectra will be approximated using known airfoil and flow parameters. Therefore, it is reasonable to model the shape of the turbulence spectra with as few parameters as possible.

In the present work, the third-octave band turbulence spectra measured at a distance of 1 mm above the trailing edge of the airfoils, and averaged over suction side and pressure side, were found to be approximately even functions when plotted versus the Strouhal number based on boundary layer displacement thickness, $f_c \cdot \delta_1 / U_0$. This means that the spectra are, in first approximation, symmetric with respect to the peak Strouhal number $St_{\delta_1, \text{peak}}$.

As can be concluded from the normalized turbulence spectra shown in Figure 4.31(b) and Figure 4.31(c) of the last chapter, the assumption of an even function, with $\text{func}(x) = \text{func}(-x)$, is a simplification. This is especially true for the low frequency range of the spectra. However, the following arguments suggest that this approach will nevertheless prove successful for the desired prediction model: First, the frequency range of the turbulence spectra below the peak is practically of no importance for the present objective to develop a basic trailing edge noise model which, finally, will be compared to the measured trailing edge noise of the non-porous reference airfoil and the porous airfoils. Measured trailing edge noise spectra are available only for frequencies above 1.5 kHz. Second, as can be concluded from Figure 5.1, there may be other mechanisms that have an effect on the

turbulence spectra at very low frequencies, which should not be integrated in the trailing edge noise model.

With the objective of a preferably simple prediction model, it is assumed that the spectral shape of the turbulence spectra, when given as a function of the Strouhal number based on boundary layer displacement thickness, $f_c \cdot \delta_1 / U_0$, with a logarithmically plotted abscissa, can be approximated by three curve segments: a linear function with a positive slope at low Strouhal numbers, a quadratic function for Strouhal numbers around the peak and again a linear function, but with a negative slope, at high Strouhal numbers.

The according functions are determined taking into account the following requirements: First, the positive slope of the linear function at low Strouhal numbers should have the same absolute value as the negative slope of the linear function at high Strouhal numbers, since the resulting function should be an even function. Second, the peak Strouhal number of the quadratic function should be identical to the peak Strouhal number of the averaged turbulence spectrum, while the resulting function should be a continuous function without points of discontinuity. The latter requirement may lead to the fact that the peak amplitude of the fitted function is not necessarily identical to the peak amplitude of the original turbulence spectrum, which is acknowledged in order to obtain a relatively simple fit.

The corresponding Strouhal numbers of the boundaries between the three segments were found to be best approximated by $2/3 \cdot Sr_{\delta_1, \text{peak}}$ and $3/2 \cdot Sr_{\delta_1, \text{peak}}$ for the lower and upper boundary, respectively.

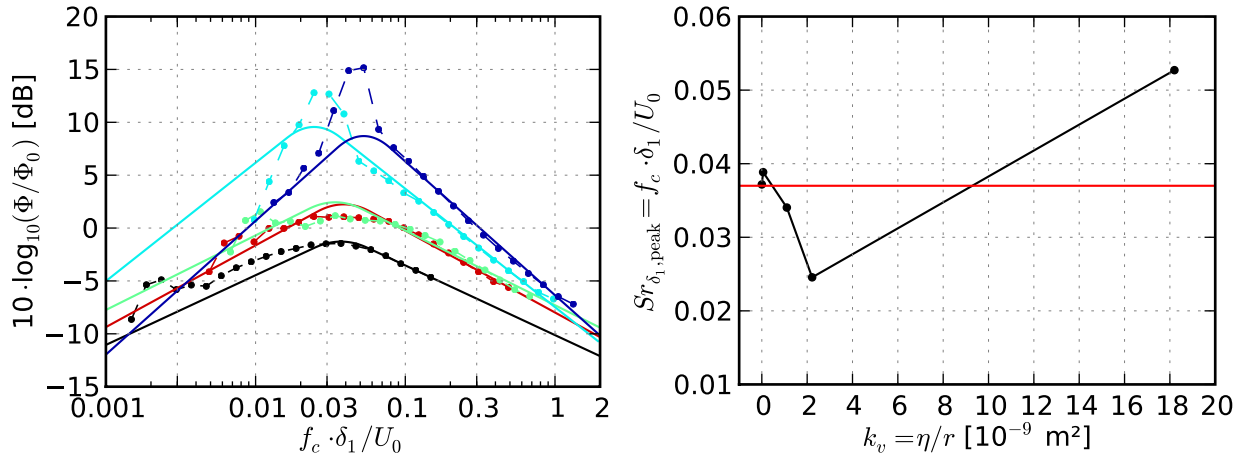
The turbulence spectra of the airfoils can then be modeled as a function of the Strouhal number based on boundary layer displacement thickness using the following equations:

$$10 \cdot \log_{10}(\Phi/\Phi_0) = \begin{cases} m_1 \cdot \log_{10} Sr_{\delta_1} + n_1 & \text{for } Sr_{\delta_1} \leq \frac{2}{3} \cdot Sr_{\delta_1, \text{peak}} \\ a_p \cdot (\log_{10} Sr_{\delta_1} - \log_{10} Sr_{\delta_1, \text{peak}})^2 + b_p & \text{for } \frac{2}{3} \cdot Sr_{\delta_1, \text{peak}} < Sr_{\delta_1} < \frac{3}{2} \cdot \log_{10} Sr_{\delta_1, \text{peak}} \\ m_2 \cdot Sr_{\delta_1} + n_2 & \text{for } Sr_{\delta_1} \geq \frac{3}{2} \cdot Sr_{\delta_1, \text{peak}} \end{cases}, \quad (5.6)$$

with $m_2 = -m_1$ and $\Phi_0 = 1 \text{ m}^2\text{s}^{-1}$.

Figure 5.8(a) shows both the mean turbulence spectra (as an average of suction side and pressure side spectra) of the five airfoils from Table 3.2, measured 1 mm above the trailing edge, and the resulting fits according to Equation (5.6). To achieve a more consistent model, the low frequency range of the turbulence spectra for the porous airfoils made of Reapor ($r = 16,500 \text{ Pa s/m}^2$) and Porex ($r = 316,500 \text{ Pa s/m}^2$) was omitted for the calculation of the fit functions. Otherwise the peak of the spectra would have been located at a much lower Strouhal number corresponding to the spectral humps already observed in Figure 4.29(c), which are assumed to be influenced by other mechanisms than the velocity fluctuations within the turbulent boundary layer of the airfoils.

It can be seen that the agreement between the original spectra and the fitted functions is relatively poor at low Strouhal numbers, described by the first linear function from Equation (5.6), while the agreement is much better at medium and high Strouhal numbers. With the exception of the two strong spectral peaks measured at the airfoils made of Recemat ($r = 8,200 \text{ Pa s/m}^2$) and M-Pore Al 45 ppi ($r = 1,000 \text{ Pa s/m}^2$), the peak levels of the averaged turbulence spectra are approximated sufficiently well. However, as explained above, in the present work mainly the high Strouhal number range of the turbulence spectra



(a) Turbulence spectra measured 1 mm above the trailing edge of the airfoils, averaged over suction side and pressure side, dashed lines: measurement, solid lines: prediction according to Equation (5.6) ($r = \blacksquare \infty$, \blacksquare 316,500, \blacksquare 16,500, \blacksquare 8,200, \blacksquare 1,000 Pa s/m²)

(b) Peak Strouhal number of the turbulence spectra shown in Figure 5.8(a), plotted versus the viscous permeability k_v of the airfoils (\blacksquare measured values, \blacksquare mean value of 0.037)

Figure 5.8: Approximation of the characteristic turbulence spectra (based on measurements at $U_0 = 50$ m/s and zero angle of attack) and corresponding peak Strouhal numbers based on boundary layer displacement thickness, $Sr_{\delta_1, \text{peak}} = f_{c, \text{peak}} \cdot \delta_1 / U_0$

is of interest (and is needed for the final comparison of the predicted trailing edge noise spectra with the measured spectra). In this Strouhal number range, the relatively simple approximation is found to be in satisfying agreement with the measured spectra.

Due to the additional conditions regarding the shape of the fit function mentioned above, all three curve segments can be calculated if, besides the peak Strouhal number, one of the linear functions is known. Presumably, this would be the linear function at high Strouhal numbers, since it can be fitted more accurately due to the larger number of data points. Thus, the coefficients m_2 and n_2 of the linear function are obtained from fitting a linear function to the averaged turbulence spectra at high Strouhal numbers. The second linear function can then be determined since it is demanded that the value at the intersection between the linear functions and the quadratic function (at $2/3 \cdot Sr_{\delta_1, \text{peak}}$ and $3/2 \cdot Sr_{\delta_1, \text{peak}}$) is the same in order to yield an even function. To this end, the coefficient n_1 can be calculated from the known parameters m_2 and n_2 using the following equation:

$$-m_2 \cdot \log_{10}\left(\frac{2}{3} \cdot Sr_{\delta_1, \text{peak}}\right) + n_1 = m_2 \cdot \log_{10}\left(\frac{3}{2} \cdot Sr_{\delta_1}\right) + n_2, \quad (5.7)$$

taking into account that the absolute value of the slope of the second linear function is identical to that of the first linear function, but has the opposite sign. The coefficients a_p and b_p of the quadratic function, used to approximate the peak of the turbulence spectra, can then be determined based on the facts that, first, the value of the quadratic function has to be equal to the values of the linear functions at the intersections between the curves (at $2/3 \cdot Sr_{\delta_1, \text{peak}}$ and $3/2 \cdot Sr_{\delta_1, \text{peak}}$), second, the derivative of the quadratic function has to be equal to the derivative of the linear functions at these points (in order to obtain a continuous curve) and, third, the derivative at the peak Strouhal number has to be equal to zero. The coefficients a_p and b_p can then be calculated as the solution to the resulting system of equations.

Table 5.1: Coefficients m_2 and n_2 determined for the modeling of the third–octave band turbulence spectra according to Equation (5.6)

r [Pa s/m ²]	∞	316,500	16,500	8,200	1,000	Strouhal number range
m_2 [dB]	−6.591	−7.730	−7.052	−11.195	−12.646	$Sr_{\delta_1} \geq \frac{3}{2} \cdot Sr_{\delta_1, \text{peak}}$
n_2 [dB]	−10.123	−7.984	−7.295	−7.477	−6.351	

In order to model the turbulence spectra of the porous airfoils using Equation (5.6), it is necessary to know the according peak Strouhal numbers of the turbulence spectra (or at least an estimate for the peak Strouhal numbers). It is therefore convenient that, as described in Section 4.3.4, the peaks are found to collapse reasonably well when the spectra are plotted as a function of the Strouhal number based on boundary layer displacement thickness. One airfoil whose peak Strouhal number is found to be noticeably different from those of the remaining airfoils is the porous airfoil made of Recemat ($r = 8,200$ Pa s/m²).

The peak Strouhal numbers $Sr_{\delta_1, \text{peak}} = f_{c, \text{peak}} \cdot \delta_1 / U_0$ of the turbulence spectra from Figure 5.8(a) are plotted in Figure 5.8(b) versus the viscous permeability k_v of the airfoils. It can be seen that the variation of the peak Strouhal number is larger for the two porous airfoils with the lowest air flow resistivities, Recemat ($r = 8,200$ Pa s/m², $k_v = 2.22 \cdot 10^{-9}$ m² with $\eta = 18.2 \cdot 10^{-6}$ kg/(m s) at 22°C) and M–Pore Al 45 ppi ($r = 1,000$ Pa s/m², $k_v = 1.82 \cdot 10^{-8}$ m²). However, although the peak Strouhal number is not constant for all airfoils but rather shows noticeable variations, it will be approximated by a single mean peak Strouhal number in order to obtain a simple trailing edge noise model. This mean peak Strouhal number is found to be equal to 0.037 and is indicated in Figure 5.8(b).

Thus, the third–octave band turbulence spectra of the porous airfoils and the non–porous airfoil can be described based on six parameters: the peak Strouhal number $Sr_{\delta_1, \text{peak}}$, the slope $m_1 = -m_2$ and the offset n_1 and n_2 of the linear functions as well as the coefficients a_p and b_p of the quadratic function that model the peak of the fitted curve. As mentioned above, the five parameters characterizing the turbulence spectra can be calculated when the coefficients m_2 and n_2 of the linear function at high Strouhal numbers are known (for example through a linear fit to measured data), assuming a continuous and even curve shape when the abscissa is plotted logarithmically. The according coefficients m_2 and n_2 for the high Strouhal number segment of the fitted functions shown in Figure 5.8(a) are given in Table 5.1.

The slope m_2 and the offset n_2 of the linear functions used to fit the high Strouhal number range of the turbulence spectra are presented in Figure 5.9(a) and Figure 5.9(b) as a function of the viscous permeability k_v of the airfoils. In order to model the third–octave band turbulence spectra for all porous airfoils of the present study, without the necessity for hot–wire measurements, both m_2 and n_2 will be described as functions of the air flow resistivity or the viscous permeability of the porous materials.

It can be concluded from Figure 5.9(a) that the curve of the slope m_2 might best be approximated using a monotonically decreasing exponential function. According to the fit included in Figure 5.9(a), the slope m_2 of the linear function at high Strouhal numbers can be estimated by

$$m_2 = 5.976 \text{ dB} \cdot \exp(-3.488 \cdot 10^8 \text{ m}^{-2} \cdot k_v) - 12.8 \text{ dB}. \quad (5.8)$$

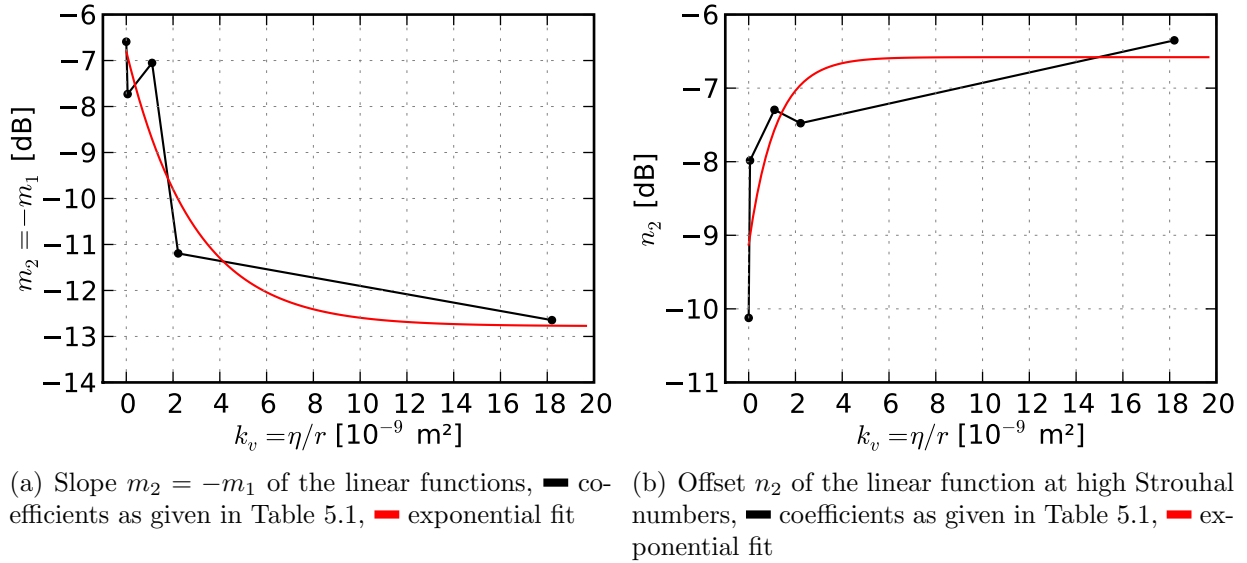


Figure 5.9: Parameters m_2 and n_2 needed for the modeling of the third–octave band turbulence spectra according to Equation (5.6) for high Strouhal numbers ($Str_{\delta_1} \geq \frac{3}{2} \cdot Str_{\delta_1, \text{peak}}$) as a function of the viscous permeability k_v of the airfoils

In the same way, the offset n_2 as a function of the viscous permeability, presented in Figure 5.9(b), may be approximated by the monotonically increasing exponential fit

$$n_2 = -2.547 \text{ dB} \cdot \exp(-8.609 \cdot 10^8 \text{ m}^{-2} \cdot k_v) - 6.6 \text{ dB}, \quad (5.9)$$

which is included in Figure 5.9(b).

As can be obtained from Figure 5.9, the exponential fits used to estimate both m_2 and n_2 may lead to some errors at very low viscous permeabilities k_v , since the exponential functions cannot approximate the large decrease of m_2 or the large increase of n_2 in this range of permeabilities. Hence, predicted differences between the coefficients for porous airfoils with very high air flow resistivities may be too small.

The resulting turbulence spectra, predicted for all airfoils of the present study using Equation (5.8) and (5.9), are given in Figure 5.10. Comparing the predicted turbulence spectra from Figure 5.10 with the original turbulence spectra shown in Figure 5.8(a), it can be seen that the basic trend is correctly predicted: The amplitudes of the turbulence spectra decrease with increasing air flow resistivity of the porous materials, a behavior consistent to that of the measured third–octave band turbulence spectra of the airfoils. It is also visible that the turbulence levels are not predicted correctly, and that differences in amplitude between the single airfoils are not correct.

For example, the peak of the fitted turbulence level of the non–porous airfoil according to Figure 5.8(a) is approximately -2 dB, that of the porous airfoils made of Porex and Reapor ($r = 316,500 \text{ Pa s/m}^2$ and $16,500 \text{ Pa s/m}^2$) is approximately $+2$ dB and that of the porous airfoils made of Recemat and M–Pore Al 45 ppi ($r = 8,200 \text{ Pa s/m}^2$ and $1,000 \text{ Pa s/m}^2$) is about 8 to 10 dB. The predicted peak of the non–porous airfoil is at 0 dB in Figure 5.10 and hence slightly larger than the original value. This is due to the aforementioned error caused by the approximation of m_2 and, even more, n_2 , using exponential fits for the lower range of viscous permeabilities. The same conclusion can be drawn for the materials with high air flow resistivities, for which the predicted amplitudes are in the order of 0 dB to

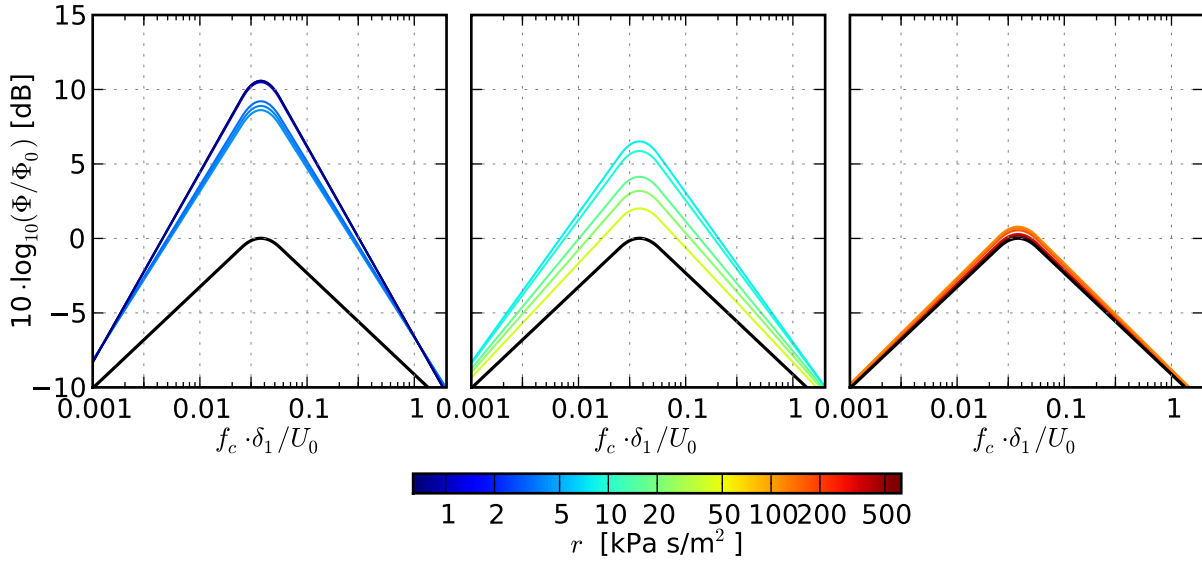


Figure 5.10: Third-octave band turbulence spectra predicted for all airfoils of the present study, using exponential fits to approximate the slope m_2 and the offset n_2 at high Strouhal numbers, peak Strouhal number $f_c \cdot \delta_1 / U_0 = 0.037$ (left column: low air flow resistivities, center column: medium air flow resistivities, right column: high air flow resistivities)

1 dB, clearly lower than those shown in Figure 5.8(a). The predicted amplitudes for the materials with low air flow resistivities, on the other hand, are in the order of 8 dB to 11 dB, which is in good agreement with the amplitudes of the fitted turbulence spectra from Figure 5.8(a).

Hence, for porous airfoils with low air flow resistivities, the predicted level differences compared to the non-porous reference airfoil are approximately equal to or slightly higher than the level differences of the fitted turbulence spectra, while for airfoils made of porous materials with high air flow resistivities the level differences are too small. This will have an effect on the predicted trailing edge noise levels, where it may lead to sound pressure levels that are too small for airfoils with low air flow resistivities and sound pressure levels that are too high for porous airfoils with high air flow resistivities.

However, due to the fact that the basic trend is correctly predicted, the first step toward a simple trailing edge noise prediction model seems to be successful.

Estimation of the turbulence convection velocity

Similar to the procedure described in the last section for the approximation of the characteristic turbulence spectra of the airfoils as a function of their viscous permeability, in this section a method will be developed to approximate the mean flow velocities that correspond to the turbulence spectra.

As described above, in order to obtain a rather simple model, the mean flow velocities $\bar{u}(z)$ at the measurement position approximately 1 mm above the trailing edge of the airfoils are averaged over suction side and pressure side. The resulting flow velocities are presented in Figure 5.11. As was the case for the slope m_2 and the offset n_2 of the linear segment of the turbulence spectra at high Strouhal numbers (Figure 5.9(a) and 5.9(b)), the mean flow

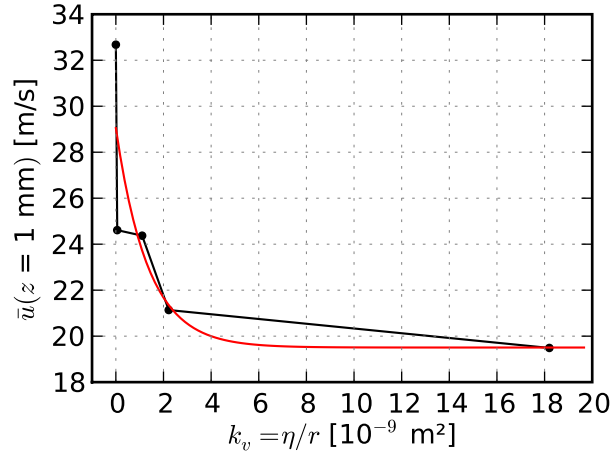


Figure 5.11: Mean velocity as a function of the viscous permeability k_v of the airfoils, averaged over the velocities measured at suction side and pressure side at a flow speed of 50 m/s and zero angle of attack, **—** measured, **—** exponential fit

velocity $\bar{u}(z = 1 \text{ mm})$ will be approximated by an exponential function, which is included in Figure 5.11.

According to this exponential fit, the mean flow velocity at a distance of 1 mm from the surface of the airfoils at $x/c_l = 1$ can be estimated as

$$\bar{u}(z = 1\text{mm}) = 9.544 \text{ m/s} \cdot \exp(-7.402 \cdot 10^8 \text{ m}^{-2} \cdot k_v) + 19.5 \text{ m/s}. \quad (5.10)$$

Again, the use of an exponential function is assumed to lead to some errors for the mean velocity estimated for airfoils with low viscous permeabilities k_v , since the exponential fit cannot predict the large negative slope in this range of permeabilities. However, considering the aim of the present study to develop a basic trailing edge noise model, Equation (5.10) is assumed to deliver a sufficiently accurate estimation for the characteristic mean flow velocity.

Thus, the turbulence convection velocity U_c needed for the trailing edge noise prediction will be calculated as proportional to the mean flow velocity $\bar{u}(z = 1 \text{ mm})$ obtained by Equation (5.10) in the present work. To determine the absolute level of the predicted trailing edge noise spectra, the resulting values of the mean velocity will be multiplied by an additional factor g to obtain a measure for the turbulence convection velocity as an input to the empirical trailing edge noise prediction model given by Equation (5.2).

5.2 Prediction of the trailing edge noise of porous airfoils

In this section, the trailing edge noise third-octave band sound pressure levels of the airfoils, predicted using Equation (5.2), will be briefly compared to measured sound pressure levels as presented in Section 4.2.2.

5.2.1 Comparison of predicted and measured trailing edge noise

A comparison of the measured and the predicted third–octave band sound pressure levels for the trailing edge noise of all sixteen porous airfoils and the reference airfoil from Table 3.1 is presented in Figure 5.12. The predicted trailing edge noise levels were obtained using the air flow resistivity r of the porous airfoils and the boundary layer thickness and boundary layer displacement thickness of the non–porous reference airfoil as the only input.

The trailing edge noise prediction shown in Figure 5.12 resulted from the following steps:

1. the prediction of the characteristic turbulence spectra at high Strouhal numbers $f_c \cdot \delta_1/U_0$ according to the third equation from Equation (5.6), using Equation (5.8) for the estimation of the slope m_2 and Equation (5.9) for the estimation of the offset n_2 ,
2. the subsequent prediction of the turbulence spectra at low and medium Strouhal numbers Sr_{δ_1} , based on a peak Strouhal number of 0.037 and the assumptions given in Section 5.1.2 regarding the shape of the fit functions used to approximate the measured turbulence spectra,
3. if necessary, the conversion of the Strouhal number based on boundary layer displacement thickness, $Sr_{\delta_1} = f_c \cdot \delta_1/U_0$, in frequency or Strouhal number based on chord length, $Sr_{c_l} = f_c \cdot c_l/U_0$, using Equation (4.16) and (4.18) for the estimation of the boundary layer displacement thickness of the porous airfoils at suction side and pressure side, which then have to be averaged,
4. the estimation of the mean flow velocity $\bar{u}(z)$ at a distance of $z = 1$ mm from the surface of the airfoils, using Equation (5.10),
5. the selection of the proportionality factor g to calculate the turbulence convection velocity $U_c = g \cdot \bar{u}(z = 1 \text{ mm})$, which was chosen to be equal to 0.022 as used for the prediction shown in Figure 5.4,
6. the prediction of the third–octave band sound pressure level L_p according to Equation (5.2).
7. If measured trailing edge noise levels are available for the non–porous airfoil, the proportionality factor g may be subsequently adjusted to result in the best agreement between measured and predicted sound pressure level spectra for this airfoil.

Basically, the same conclusions can be drawn from the comparison shown in Figure 5.12 as from that presented in Figure 5.4. The agreement between measured and predicted trailing edge noise spectra generated by the porous airfoils is satisfying, especially when the rather simple prediction model, based on hot–wire measurements on only five airfoils, and the small range of frequencies available for the evaluation of the method, are considered.

As discussed in Section 5.1.2, neither the sharp drop of the sound pressure level of the non–porous airfoil nor the contribution of surface roughness noise of the porous airfoils at high Strouhal numbers can be predicted by the model, since no measured turbulence spectra are available in this frequency range.

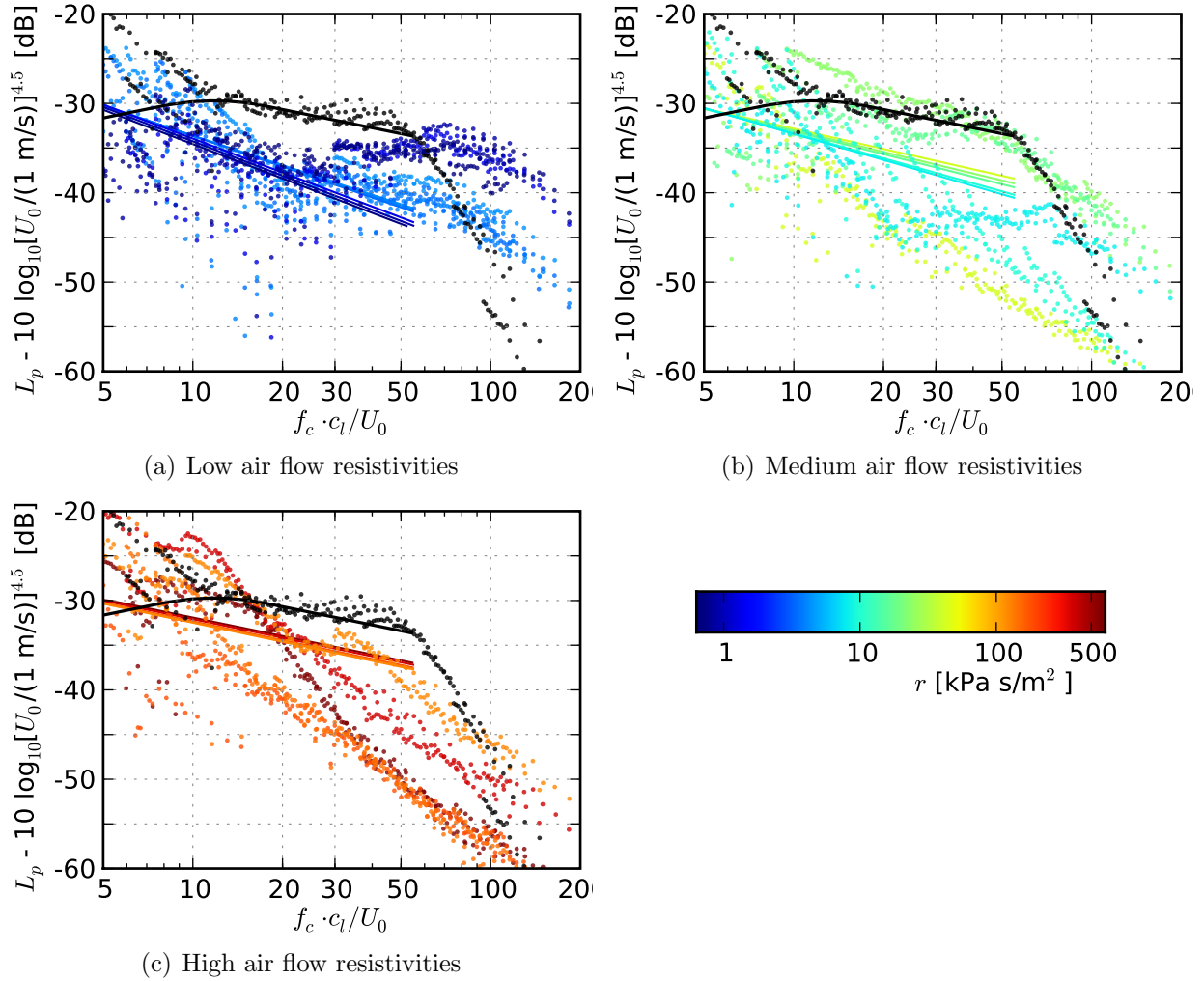


Figure 5.12: Comparison of predicted third-octave band sound pressure levels with measured sound pressure levels of the trailing edge noise of porous airfoils, scaled with $U_0^{4.5}$, angle of attack $\alpha = 0^\circ$ (prediction is based on Equation (5.2) and uses predicted turbulence spectra as well as the estimated mean flow velocity $\bar{u}(z = 1 \text{ mm})$ with a proportionality factor of 0.022 as a measure for the turbulence convection velocity)

Due to the approximation of both the turbulence spectra and the mean flow velocities using exponential functions, the agreement between measured and predicted sound pressure levels is better for airfoils with low air flow resistivities than for airfoils with high air flow resistivities. Basically, the difference between the predicted trailing edge noise of the porous airfoils and that of the reference airfoil decreases with increasing air flow resistivity.

More exact features of the measured trailing edge noise spectra cannot be predicted using the basic model developed herein, including narrow band characteristics such as spectral peaks. However, this is beyond the scope of the present work anyway. It is still assumed that the model developed herein may be useful for a first estimation of the possible noise reduction that can be achieved by a porous airfoil with a known air flow resistivity.

The semi-empiric trailing edge noise prediction model developed in this thesis is based completely on measurements on SD7003-shaped airfoils (with a slightly increased trailing edge thickness for the porous airfoils) with a chord length of 235 mm. Although it is

assumed that the model may give useful results also for other airfoils in a subsonic flow, including symmetric airfoils, this was not examined within the present study.

Future work should include detailed comparisons of the trailing edge model developed in the present thesis with other models, possibly including the measurement of surface pressures at least for a non-porous airfoil. As mentioned before, acoustic measurements and hot-wire measurements should be performed on non-porous airfoils with increased surface roughnesses to identify the influence of the surface roughness on the noise generation in comparison to the influence of the permeability of the porous airfoils.

5.2.2 Discussion of the results and possible improvements to the model

As was mentioned before, the resulting model is relatively sensitive to the input of the turbulence convection velocity, and hence to errors regarding the estimation of the mean flow velocity $\bar{u}(z)$ at the distance of 1 mm. This is due to the fact that the noise prediction model given by Equation (5.2) contains the convection velocity to the third power (not the fifth power since the convection velocity is also used to normalize the turbulence spectra in order to obtain the turbulence intensity γ as described in [Ffowcs Williams and Hall, 1970]).

Errors that occurred during the hot-wire measurements, which possibly lead to incorrect boundary layer parameters of the porous airfoils, are assumed to be an additional source of error with a noticeable influence on the resulting predicted trailing edge noise spectra. Most notably, it is possible that the results obtained from the constant temperature anemometry measurements at the suction side of the porous airfoil made of Recemat ($r = 8,200 \text{ Pa s/m}^2$) may contain errors, possibly due to some surface irregularity.

Hence, it can be assumed that detailed hot-wire measurements on a larger set of porous airfoils would be the most promising way to improve the present trailing edge noise model. Such measurements would require the manufacturing of additional rigid porous airfoils in order to enable the positioning of the hot-wire probe near the thin trailing edge. Potential improvements to the present trailing edge noise model could then aim at a more accurate prediction of the mean flow velocity $\bar{u}(z)$ and the parameters m_2 and n_2 used to approximate the turbulence spectra. Additionally, future work could include hot-wire measurements at a larger number of flow speeds U_0 to obtain a higher statistical reliability of the approximations derived for the prediction of $\bar{u}(z = 1 \text{ mm})$, m_2 and n_2 .

Several airfoil self noise studies make use of the so-called “upwash” velocity above the trailing edge to describe the flow field and predict the noise radiation from the trailing edge, for example [Hayden, 1972, Howe, 1999]. It can therefore be assumed that the use of a multi-wire probe for the constant temperature anemometry measurements within the turbulent boundary layer of the airfoils, and the subsequent focus on the vertical component of the turbulent velocity fluctuations in the analysis and prediction of the turbulence spectra, would possibly lead to a further improvement of the present trailing edge noise model.

Future acoustic measurements that include a wider range of low frequencies and hot-wire measurements that include high frequencies above 10 kHz would be reasonable to further validate and improve the prediction model.

Some improvement may also be achieved when additional parameters of the porous materials, as for example the tortuosity, are taken into account, although this is believed to result in a minor improvement only. Another approach, which would possibly lead to a noticeable improvement of the trailing edge noise model, would be to take into account the non-linearity of the air flow resistance, as was done by Revell et al. [Revell et al., 1997]. Of course, this would require detailed measurements on the porous materials used in the present study.

For a further refinement of the noise prediction model, acoustic measurements and hot-wire measurements on a larger number of airfoils of different chord length, leading to different chord based Reynolds numbers, and, possibly, also different shape would be helpful. Additional experiments on partly-porous airfoils may be conducted to include into the model the streamwise extent of the porous treatment necessary to achieve a certain trailing edge noise reduction.

Chapter 6

Conclusion

Detailed acoustic measurements have been performed on a non-porous reference airfoil and a set of 16 porous airfoils at various flow speeds in an open jet wind tunnel in order to investigate the potential reduction of trailing edge noise that can be achieved by using airfoils made completely out of an open-porous material. The reference airfoil has an SD7003 shape, while the shape of the porous airfoils is basically that of an SD7003 airfoil with a slightly increased trailing edge thickness. The chord length of all airfoils is 0.235 m. All measurements were performed in subsonic flow with a corresponding maximum chord based Reynolds number of approximately 780,000.

The porous materials are characterized by their air flow resistivity and, to a lesser extent, by their open volume porosity. Additionally, the porous materials have an increased surface roughness compared to the rather smooth surface of the reference airfoil.

The acoustic measurements were performed using microphone array technology, and the resulting data were processed by the application of an advanced three-dimensional beam-forming algorithm. The acoustic measurement setup has a lower frequency limit of approximately 1.5 kHz. To include the aerodynamic efficiency of the porous airfoils in the analysis of the potential trailing edge noise reduction, the corresponding lift forces and drag forces have been measured. Additional hot-wire measurements in the turbulent boundary layer of a subset of the airfoils were performed to enable conclusions on the mechanisms that are responsible for the trailing edge noise reduction. The results of the measurements allow for the following conclusions:

1. In the examined range of frequencies, a noticeable trailing edge noise reduction can be achieved through the use of porous airfoils despite losses in aerodynamic efficiency. This trailing edge noise reduction was observed mainly at medium frequencies.
2. The highest noise reduction per unit lift force was measured for porous airfoils with medium to high air flow resistivities approximately above 40,000 Pa s/m².
3. The trailing edge noise spectra of porous airfoils with low and medium air flow resistivities were found to exceed the trailing edge noise of the reference airfoil at high frequencies, which is assumed to be a contribution of surface roughness noise.
4. The investigation of three-dimensional sound maps indicates that for the porous airfoils another noise source mechanism may be present, which leads to noise sources

located above the surface and trailing edge of the airfoils, and even outside of the open jet of the wind tunnel, that contribute to the total noise emission. It is presently not clear what this mechanism may be.

5. The boundary layer thickness δ as well as the boundary layer displacement thickness δ_1 of the porous airfoils are noticeably larger than that measured at the reference airfoil.
6. The examination of spectra of the turbulent velocity fluctuations showed that the peak measured above the trailing edge of the porous airfoils is at a noticeably lower frequency than that measured at the reference airfoil.
7. Turbulence spectra measured at different chord positions along the surface of the airfoils revealed that the cause of the measured trailing edge noise reduction at medium and high frequencies may be a shift of the spectra toward lower frequencies with increasing chord position. This shift is notably stronger for the porous airfoils, which may indicate that the use of porous airfoils does not result in a reduction of the overall sound pressure level compared to the reference airfoil, but may even lead to an increase of the overall sound pressure level.

Based on turbulence spectra measured above the trailing edge of five airfoils, a simple trailing edge noise prediction model was developed following the fundamental theory by Ffowcs Williams and Hall on the generation of noise in the vicinity of the edge of a semi-infinite flat plate [Ffowcs Williams and Hall, 1970]. In the present thesis it is thereby assumed that the spectral shape of the trailing edge noise is related to the spectral shape of the turbulent velocity fluctuations in close proximity to the trailing edge, while the overall amplitude is determined by a convection velocity that is proportional to the mean flow velocity of the fluctuations.

One possible application of the resulting model is the prediction of the trailing edge noise based on the input of the measured turbulence spectrum and the corresponding mean flow velocity close to the trailing edge of an airfoil. A more convenient application of the model is the trailing edge noise prediction based on an estimated turbulence spectrum and the corresponding mean flow velocity based on approximations developed in the present thesis, without the necessity of detailed constant temperature anemometry measurements. Comparisons between predicted and measured trailing edge noise spectra lead to the following conclusions:

8. The agreement between prediction and measurement is satisfying for both cases, especially when considering the rather basic approach of the model.
9. When using the estimated turbulence spectra and the estimated mean flow velocity, the trailing edge noise prediction shows a clear trend: Porous airfoils with low air flow resistivities lead to a lower noise generation than airfoils with medium and high air flow resistivities. The level differences between the trailing edge noise predicted for porous airfoils with high air flow resistivities compared to the noise of the reference airfoil are too small, which is partly a consequence of the use of exponential functions for the approximation of both the characteristic turbulence spectra and the mean flow velocity close to the airfoil surface.

10. The results of the acoustic measurements cannot entirely confirm the clear trend obtained from the prediction model, which is to some extent due to the fact that the measured trailing edge noise is assumed to contain contributions of surface roughness noise and noise from another potential noise source mechanism than turbulent boundary layer - trailing edge noise.

It is assumed that the most promising way to improve the present trailing edge noise model would be the performance of additional hot-wire measurements on a larger set of porous airfoils and at a larger number of flow speeds. For the development of the trailing edge noise model based on the spectra of measured turbulent velocity fluctuations, the absence of low frequencies in the measured trailing edge noise spectra is a clear limitation, as is the absence of high frequencies in the measured turbulence spectra. Regarding a further improvement of the noise prediction model developed in the present study, acoustic measurements at considerably lower frequencies as well as hot-wire measurements at higher frequencies would be useful.

Chapter 7

Zusammenfassung

Um die mögliche Minderung der Hinterkantenschallerzeugung von Tragflügelprofilen aus offenporösen Materialien zu untersuchen, fanden umfangreiche Messungen an einem nichtporösen Referenzprofil und 16 porösen Profilen in einem Freistrahwindkanal bei subsonischen Strömungsgeschwindigkeiten statt. Das verwendete nichtporöse Profil besitzt eine SD7003-Geometrie, während die Geometrie der porösen Tragflügel aus Fertigungsgründen der eines SD7003-Profiles mit einer etwas dickeren Hinterkante entspricht. Die Sehnenlänge der Profile beträgt 0,235 m.

Die porösen Materialien werden durch ihren längenbezogenen Strömungswiderstand und ihre offene Porosität charakterisiert. Gegenüber der glatten Oberfläche des nichtporösen Referenzprofils weisen die porösen Profile außerdem eine erhöhte Oberflächenrauigkeit auf.

Akustische Messungen im Windkanal wurden mit Hilfe der Mikrofonarraymesstechnik durchgeführt, die Verarbeitung der Messdaten erfolgte mit Hilfe eines dreidimensionalen Beamforming-Algorithmus. Der gewählte Messaufbau hat eine untere Frequenzgrenze von etwa 1,5 kHz. Um die aerodynamische Effizienz der porösen Profile in die Auswertung einzubeziehen, erfolgte die Messung von Auftriebskraft und Widerstandskraft. Um Rückschlüsse auf die zugrunde liegenden Mechanismen der Schallreduktion zu erlauben, wurden zusätzliche Hitzdrahtmessungen in der Grenzschicht ausgewählter Profile durchgeführt. Aus den Ergebnissen der Messungen können folgende Schlussfolgerungen gezogen werden:

1. Durch den Einsatz poröser Profile lässt sich, trotz aerodynamischer Verluste, eine deutliche Minderung des Hinterkantenschalls im betrachteten Frequenzbereich erzielen. Diese Schallreduktion ergibt sich hauptsächlich bei mittleren Frequenzen.
2. Die größte Schallreduktion pro Auftriebskraft konnte für poröse Profile mit mittleren und hohen längenbezogenen Strömungswiderständen ab etwa 40.000 Pa s/m² gemessen werden.
3. Bei sehr hohen Frequenzen erzeugen poröse Profile mit geringen und mittleren längenbezogenen Strömungswiderständen zum Teil einen gegenüber dem Referenzprofil erhöhten Schalldruckpegel, wobei vermutet wird, dass dies ein Effekt der Oberflächenrauigkeit der porösen Profile und damit ein Beitrag von Rauigkeitslärm ist.

4. Die Untersuchung dreidimensionaler Schallkartierungen legt die Vermutung nahe, dass im Fall der porösen Tragflügelprofile ein möglicher weiterer Schallentstehungsmechanismus vorhanden ist. Dieser resultiert in Schallquellen über der Oberfläche und Hinterkante der Profile, zum Teil außerhalb des Freistrahls des Windkanals, und trägt zur Gesamtschallabstrahlung bei. Zum jetzigen Zeitpunkt ist unklar, um was für einen Mechanismus es sich dabei handelt.
5. Poröse Profile weisen gegenüber dem nichtporösen Profil eine größere Grenzschichtdicke δ als auch eine größere Grenzschichtverdrängungsdicke δ_1 auf.
6. Die Untersuchung der Spektren der Schwankungsgeschwindigkeit innerhalb der turbulenten Grenzschicht über der Hinterkante der Profile zeigte, dass das Maximum der Turbulenz für die porösen Profile bei deutlich tieferen Frequenzen liegt als das Maximum der über der Hinterkante des Referenzprofils gemessenen Turbulenz.
7. Messungen der Turbulenzspektren an verschiedenen Positionen entlang der Oberfläche der Profile in Strömungsrichtung ergaben, dass die mutmaßliche Ursache der Schallminderung durch die porösen Profile eine Verschiebung der Turbulenzspektren mit zunehmendem Abstand von der Vorderkante hin zu niedrigeren Frequenzen ist. Diese Verschiebung ist im Fall der porösen Profile viel deutlicher ausgeprägt als für das Referenzprofil, was vermuten lässt, dass die Verwendung poröser Profile aufgrund der höheren Schallenergie im tieffrequenten Bereich nicht zu einer Reduktion des Gesamtschalldruckpegels führen könnte. Es wäre sogar möglich, dass der Gesamtschalldruckpegel für die porösen Profile im Vergleich zu dem des Referenzprofils höher ist.

Basierend auf über der Hinterkante von fünf Profilen gemessenen Turbulenzspektren wurde in Anlehnung an die Theorie von Ffowcs Williams und Hall [Ffowcs Williams and Hall, 1970] über die Schallentstehung an einer halbunendlichen Platte ein einfaches Modell zur Vorhersage von Hinterkantenschall entwickelt. Die dabei zugrunde liegende Annahme ist, dass die Spektren des Hinterkantenschalls von den gemessenen Turbulenzspektren abgeleitet werden können, während die Amplituden eine Folge der zugehörigen Turbulenzkonvektionsgeschwindigkeiten sind.

Ein möglicher Einsatz des Vorhersagemodells ist die Berechnung des Hinterkantenschalls aus gemessenen Turbulenzspektren und den entsprechenden gemessenen mittleren Geschwindigkeiten in der Nähe der Hinterkante. Eine zweckmäßigere Einsatzmöglichkeit ist jedoch die Berechnung des Hinterkantenschalls aus modellierten Turbulenzspektren und Konvektionsgeschwindigkeiten, ohne die Notwendigkeit von detaillierten Hitzdrahtmessungen. Vergleiche zwischen vorhergesagten und gemessenen Hinterkantenschalldruckspektren erlauben folgende Rückschlüsse:

8. Die Übereinstimmung zwischen Modell und Messung ist generell zufriedenstellend, vor allem vor dem Hintergrund des relativ einfachen Modellansatzes.
9. Wenn die Turbulenzspektren sowie die mittlere Geschwindigkeit mit Hilfe des Modells geschätzt werden, ergibt sich ein klarer Trend: Poröse Profile mit niedrigen längenbezogenen Strömungswiderständen führen generell zu niedrigeren Schalldruckpegeln als Profile mit hohen längenbezogenen Strömungswiderständen. Dabei werden Unterschiede zwischen den Schalldruckpegeln für Profile mit hohen längenbezogenen

Strömungswiderständen gegenüber dem Referenzprofil zu niedrig berechnet, was zum Teil eine Folge der zur Modellierung verwendeten Exponentialfunktionen ist.

10. Der klare Trend der Vorhersage kann durch die gemessenen Hinterkantenschalldruckpegel nicht ohne Einschränkungen bestätigt werden, was aber auch teilweise durch den Beitrag von Rauigkeitslärm als auch von Lärm, welcher durch den vermuteten zweiten Schallentstehungsmechanismus erzeugt wird, zum gemessenen Hinterkantenschall verursacht wird.

Es wird vermutet, dass der vielversprechendste Weg zur Verbesserung des entwickelten Hinterkantenschallmodells die Durchführung von Hitzdrahtmessungen an zusätzlichen Profilen und bei mehreren Strömungsgeschwindigkeiten ist. Zur weiteren Verbesserung des Modells wären zudem akustische Messungen bei tieferen Frequenzen und Hitzdrahtmessungen bei höheren Frequenzen hilfreich.

Bibliography

- [Abdel-Rahman et al., 1987] Abdel-Rahman, A., Tropea, C., Slawson, P., and Strong, A. (1987). On temperature compensation in hot-wire anemometry. *Journal of Physics E: Scientific Instruments*, 20:315 – 319.
- [Alfredsson et al., 1988] Alfredsson, P. H., Johansson, A. V., Haritonidis, J. H., and Eckelmann, H. (1988). The fluctuating wall-shear stress and the velocity field in the viscous sublayer. *Physics of Fluids*, 21 (5):1026 – 1033.
- [Amiet, 1976] Amiet, R. K. (1976). Noise due to turbulent flow past a trailing edge. *Journal of Sound and Vibration*, 47(3):387–393.
- [Amiet, 1978] Amiet, R. K. (1978). Refraction of sound by a shear layer. *Journal of Sound and Vibration*, 58:467 – 482.
- [Anderson, 1984] Anderson, jr., J. D. (1984). *Fundamentals of Aerodynamics*. McGraw-Hill Book Company, New York.
- [Blake, 1986] Blake, W. K. (1986). *Mechanics of Flow-Induced Sound and Vibration, Volume II: Complex Flow-Structure Interactions*. Academic Press, Inc.
- [Bohn, 1976] Bohn, A. J. (1976). Edge noise attenuation by porous-edge extensions. *AIAA 14th Aerospace Sciences Meeting, AIAA Paper 76-80*.
- [Bradshaw and Huang, 1995] Bradshaw, P. and Huang, G. P. (1995). The law of the wall in turbulent flow. *Proceedings of the Royal Society in London A*, pages 165 – 188.
- [Bremhorst, 1985] Bremhorst, K. (1985). Effect of fluid temperature on hot-wire anemometers and an improved method of temperature compensation and linearisation without use of small signal sensitivities. *Journal of Physics E: Scientific Instruments*, 18:44 – 49.
- [Brooks and Hodgson, 1981] Brooks, T. F. and Hodgson, T. H. (1981). Trailing edge noise prediction from measured surface pressures. *Journal of Sound and Vibration*, 78:69 – 117.
- [Brooks and Humphreys, 1999] Brooks, T. F. and Humphreys, W. M. (1999). Effect of directional array size on the measurement of airframe noise components. *5th AIAA/CEAS Aeroacoustics Conference, AIAA paper 99-1958*.
- [Brooks and Humphreys, 2004] Brooks, T. F. and Humphreys, W. M. (2004). A deconvolution approach for the mapping of acoustic sources (DAMAS) determined from phased

- microphone arrays. *10th AIAA/CEAS Aeroacoustics Conference, AIAA paper 2004-2954*.
- [Brooks and Marcolini, 1985] Brooks, T. F. and Marcolini, M. A. (1985). Scaling of airfoil self-noise using measured flow parameters. *AIAA Journal*, 23(2):207 – 213.
- [Brooks et al., 1984] Brooks, T. F., Marcolini, M. A., and Pope, D. S. (1984). Airfoil trailing edge flow measurements and comparison with theory incorporating open wind tunnel corrections. In *9th AIAA/NASA Aeroacoustics Conference, AIAA paper 84-2266*.
- [Brooks et al., 1986] Brooks, T. F., Marcolini, M. A., and Pope, D. S. (1986). Airfoil trailing-edge flow measurements. *AIAA Journal*, 24(8).
- [Brooks et al., 1989] Brooks, T. F., Pope, D. S., and Marcolini, M. A. (1989). Airfoil self-noise and prediction. Technical report, NASA Reference Publication 1218.
- [Chanaud, 1972] Chanaud, R. C. (1972). Noise reduction in propeller fans using porous blades at free-flow conditions. *The Journal of the Acoustical Society of America*, 51:15 – 18.
- [Chanaud et al., 1976] Chanaud, R. C., Kong, N., and Sitterding, R. B. (1976). Experiments on porous blades as a means of reducing fan noise. *The Journal of the Acoustical Society of America*, 59:564 – 575.
- [Chase, 1972] Chase, D. M. (1972). Sound radiated by turbulent flow off a rigid half-plane as obtained from a wavevector spectrum of hydrodynamic pressure. *Journal of the Acoustical Society of America*, 52 (3):1011 – 1023.
- [Crighton, 1995] Crighton, D. G. (1995). *Chapter on Airframe Noise in Aeroacoustics of Flight Vehicles: Theory and Practise, Volume 1: Noise Sources*. Acoustical Society of America.
- [Dassen et al., 1996] Dassen, T., Parchen, R., Bruggeman, J., and Hagg, F. (1996). Results of a wind tunnel study on the reduction of airfoil self-noise by the application of serrated blade trailing edges. Technical report, National Aerospace Laboratory NLR TP 96350.
- [Dougherty, 2002] Dougherty, R. (2002). *Chapter on Beamforming in Acoustic Testing in Aeroacoustic Measurements*. pages 62 - 97, Springer Science+Business Media, Berlin.
- [Drela, 1989] Drela, M. (1989). XFOIL: An analysis and design system for low Reynolds number airfoils. In *Conference on Low Reynolds Number Aerodynamics, University of Notre Dame*.
- [Eckert and Drake jr., 1959] Eckert, E. R. G. and Drake jr., R. M. (1959). *Heat and Mass Transfer, 2nd Edition*. McGraw–Hill Series in Mechanical Engineering, New York.
- [Ffowcs Williams and Hall, 1970] Ffowcs Williams, J. E. and Hall, L. H. (1970). Aerodynamic sound generation by turbulent flow in the vicinity of a scattering halfplane. *Journal Fluid Mechanics*, 40(4):657 – 670.
- [Fink, 1976] Fink, M. R. (1976). Approximate prediction of airframe noise. *Journal of Aircraft*, 13 (2):833 – 834.

- [Fink, 1977] Fink, M. R. (1977). Airframe noise prediction method. Technical report, United Technologies Research Center, East Hartford, CT., FAA-RD-77-29, Contract number DOTFA76WA3821.
- [Fink, 1979] Fink, M. R. (1979). Noise component method for airframe noise. *Journal of Aircraft*, 16 (10):659 – 665.
- [Fink and Bailey, 1980] Fink, M. R. and Bailey, D. A. (1980). Airframe noise reduction studies and clean-airframe noise investigation. Technical report, NASA Contractor Report 159311.
- [Fink and Schlinker, 1979] Fink, M. R. and Schlinker, R. H. (1979). Airframe noise component interaction studies. Technical report, NASA Contractor Report 3110.
- [Fritzsche et al., 2010] Fritzsche, C., Sarradj, E., and Geyer, T. (2010). Akustische Polaren. *36. Jahrestagung für Akustik (DAGA 2010)*.
- [Garcia-Sagrado et al., 2006] Garcia-Sagrado, A., Hynes, T., and Hodson, H. (2006). Experimental investigation into trailing edge noise sources. *12th AIAA/CEAS Aeroacoustics Conference, AIAA paper 2006-2476*.
- [Gentle, 2007] Gentle, J. E. (2007). *Matrix Algebra - Theory, Computations, and Applications in Statistics*. Springer Science+Business Media, New York.
- [Geyer et al., 2010a] Geyer, T., Sarradj, E., and Fritzsche, C. (2010a). Measurement of the noise generation at the trailing edge of porous airfoils. *Experiments in Fluids*, 48 (2):291 – 308.
- [Geyer et al., 2010b] Geyer, T., Sarradj, E., and Fritzsche, C. (2010b). Porous airfoils: Noise reduction and boundary layer effects. *International Journal of Aeroacoustics*, 9 (6):787 – 820.
- [Glauert, 1983] Glauert, H. (1983). *The Elements of Aerofoil and Airscrew Theory - 2. Edition*. Cambridge University Press.
- [Goldstein, 1976] Goldstein, M. E. (1976). *Aeroacoustics*. McGraw-Hill, New York.
- [Grissom, 2007] Grissom, D. L. (2007). *A Study of Sound generated by a Turbulent Wall Jet Flow over Rough Surfaces*. PhD thesis, Virginia Polytechnic Institute and State University.
- [Grosveld, 1985] Grosveld, F. W. (1985). Prediction of broadband noise from horizontal axis wind turbines. *Journal of Propulsion*, 1:292 – 299.
- [Gruber et al., 2010] Gruber, M., Joseph, P. F., and Chong, T. P. (2010). Experimental investigation of airfoil self noise and turbulent wake reduction by the use of trailing edge serrations. *16th AIAA/CEAS Aeroacoustics Conference, AIAA Paper 2010-3803*.
- [Hardin et al., 1975] Hardin, J. C., Fratello, D. J., Hayden, R. E., Kadman, Y., and Africk, S. (1975). Prediction of airframe noise. Technical report, NASA Technical Note TN D-7821.

- [Hayden, 1972] Hayden, R. E. (1972). Noise from interaction of flow with rigid surfaces: A review of current status of prediction techniques. Technical report, NASA Contractor Report CR-2126.
- [Healy, 1974] Healy, G. J. (1974). Measurement and analysis of aircraft far-field aerodynamic noise. Technical report, NASA Contractor Report CR-2377.
- [Herr, 2007] Herr, M. (2007). Design criteria for low-noise trailing edges. *13th AIAA/CEAS Aeroacoustics Conference, AIAA paper 2007-3470*.
- [Hersh, 1983] Hersh, A. S. (1983). Experimental investigation of surface roughness generated flow noise. *8th AIAA Aeroacoustics Conference, AIAA paper 83-0786*.
- [Hersh et al., 1976] Hersh, A. S., Burcham, jr., F. W., Putnam, T. W., and Lasagna, P. L. (1976). Semiempirical airframe noise prediction model and evaluation with flight data. Technical report, Technical Memorandum NASA TM X-56041, NASA Dryden Flight Research Center, Edwards, California.
- [Hinze, 1975] Hinze, J. O. (1975). *Turbulence, Second Edition*. McGraw-Hill, New York.
- [Hosder et al., 2004] Hosder, S., Schetz, J. A., Grossman, B., and Mason, W. H. (2004). Airframe noise modeling appropriate for multidisciplinary design and optimization. *42nd AIAA Aerospace Sciences Meeting and Exhibit, AIAA paper 2004-0698*.
- [Howe, 1978] Howe, M. S. (1978). A review of the theory of trailing edge noise. *Journal of Sound and Vibration*, 61(3):437 – 465.
- [Howe, 1984] Howe, M. S. (1984). On the generation of sound by turbulent boundary layer flow over a rough wall. *Proceedings of the Royal Society of London A*, 395:247 – 263.
- [Howe, 1991a] Howe, M. S. (1991a). Aerodynamic noise of a serrated trailing edge. *Journal of Fluids and Structures*, 5:33 – 45.
- [Howe, 1991b] Howe, M. S. (1991b). Noise produced by a sawtooth trailing edge. *Journal of the Acoustical Society of America*, 90(1):482–487.
- [Howe, 1998] Howe, M. S. (1998). *Acoustics of Fluid Structure Interactions*. Cambridge University Press.
- [Howe, 1999] Howe, M. S. (1999). Trailing edge noise at low Mach numbers. *Journal of Sound and Vibration*, 225:211 – 238.
- [Hutcheson and Brooks, 2004] Hutcheson, F. V. and Brooks, T. F. (2004). Effect of angle of attack and velocity on trailing edge noise. *42nd AIA Aerospace Sciences Meeting, Reno, AIAA paper 2004-1031*.
- [ISO 9053, 1993] ISO 9053 (1993). Acoustics – materials for acoustical applications – determination of airflow resistance. Technical report, International Organization for Standardization.
- [Klewicki et al., 2007] Klewicki, J. C., Saric, W. S., Marusic, I., and Eaton, J. K. (2007). Chapter on *Wall-Bounded Flows* in *Springer Handbook of Experimental Fluid Mechanics*. Springer Science+Business Media, Berlin Heidelberg.

- [Knight and Harris, 1930] Knight, M. and Harris, T. A. (1930). Experimental determination of jet boundary corrections for airfoil tests in four open wind tunnel jets of different shapes. Technical report, NACA, Report No. 361.
- [Kroeger et al., 1971] Kroeger, R. A., Gruschka, H. D., and Helvey, T. C. (1971). Low speed aerodynamics for ultra-quiet flight. Technical Report TR 971-75, AFFDL.
- [Lafarge et al., 1997] Lafarge, D., Lemarinier, P., and Allard, J. F. (1997). Dynamic compressibility of air in porous structures at audible frequencies. *Journal of the Acoustical Society of America*, 102 (4):1995 – 2006.
- [Lasagna et al., 1980] Lasagna, P. L., Mackall, K. G., Burcham, F. W., J., and Putnam, T. W. (1980). Landing approach airframe noise measurements and analysis. Technical report, NASA Technical Paper 1602.
- [Lilley, 1998] Lilley, G. M. (1998). A study of the silent flight of the owl. *4th AIAA/CEAS Aeroacoustics Conference, June 2-4, Toulouse, France, AIAA paper 98-2340*.
- [Lilley, 2001] Lilley, G. M. (2001). The prediction of airframe noise and comparison with experiment. *Journal of Sound and Vibration*, 239:849 – 859.
- [Liu and Dowling, 2007] Liu, Y. and Dowling, A. P. (2007). Assessment of the contribution of surface roughness to airframe noise. *AIAA Journal*, 45 (4):855 – 869.
- [Liu et al., 2008] Liu, Y., Dowling, A. P., and Shin, H.-C. (2008). Measurement and simulation of surface roughness noise using phased microphone arrays. *Journal of Sound and Vibration*, 314:95 – 112.
- [Lockard and Lilley, 2004] Lockard, D. P. and Lilley, G. M. (2004). The airframe noise reduction challenge. Technical report, NASA Technical Memorandum NASA/TM-2004-213013.
- [Lowson, 1968] Lowson, M. V. (1968). Reduction of compressor noise radiation. *The Journal of the Acoustical Society of America*, 43 (1):37 – 50.
- [Lowson, 1992] Lowson, M. V. (1992). Assessment and prediction of wind turbine noise. *Flow Solutions Report*, 92/19:1–59.
- [Lowson, 1993] Lowson, M. V. (1993). A new prediction model for wind turbine noise. In *Renewable Energy, 17 - 19 November 1993*.
- [Mechel, 2008] Mechel, F. (2008). *Formulas of Acoustics, Second Edition*. Springer Science+Business Media, Berlin.
- [Mineck and Hartwich, 1996] Mineck, R. E. and Hartwich, P. M. (1996). Effect of full-chord porosity on aerodynamic characteristics of the NACA 0012 airfoil. Technical report, NASA Technical Paper 3591.
- [Möhlmann, 2011] Möhlmann, O. (2011). <http://www.fashion-base.de/wolle-1a.htm>. online fashion website, 09. February 2011.
- [Moreau et al., 2001] Moreau, S., Iaccarino, G., Roger, M., and Wang, M. (2001). CFD analysis of flow in an open-jet aeroacoustic experiment. *Center for Turbulence Research, Annual Research Briefs*, pages 343 – 351.

- [Moriarty, 2005] Moriarty, P. (2005). *NAFNoise User Guide (NWTC Design Codes*, <http://wind.nrel.gov/DesignCodes/simulators/NAFNoise/>. Last modified 12-April-2006). National Wind Technology Center.
- [Moriarty et al., 2005] Moriarty, P., Guidati, G., and Migliore, P. (2005). Prediction of turbulent inflow and trailing-edge noise for wind turbines. *11th AIAA/CEAS Aeroacoustics Conference, AIAA paper 2005-2881*.
- [Moriarty and Migliore, 2003] Moriarty, P. and Migliore, P. (2003). Semi-empirical aeroacoustic noise prediction code for wind turbines. Technical report, National Renewable Energy Laboratory.
- [Mosher, 1996] Mosher, M. (1996). Phased arrays for aeroacoustic testing: Theoretical development. *2nd AIAA/CEAS Aeroacoustics Conference, AIAA paper 1996-1713*.
- [Mueller, 2002] Mueller, T. J., editor (2002). *Aeroacoustic Measurements*. Springer Science+Business Media, Berlin.
- [Nash, 1966] Nash, J. F. (1966). A note on skin-friction laws for the incompressible turbulent boundary layer. *Ministry of Aviation, Aeronautical Research Council, Current Papers*, 862.
- [Oerlemans, 2004] Oerlemans, S. (2004). Wind tunnel aeroacoustic tests of six airfoils for use on small wind turbines. Technical report, National Renewable Energy Laboratory, NREL/SR-500-35339.
- [Oerlemans et al., 2007] Oerlemans, S., Broersma, L., and Sijtsma, P. (2007). Quantification of airframe noise using microphone arrays in open and closed wind tunnels. *International Journal of Aeroacoustics*, 6 (4):309 – 331.
- [Oerlemans and Migliore, 2004] Oerlemans, S. and Migliore, P. (2004). Aeroacoustic wind tunnel tests of wind turbine airfoils. Technical report, National Aerospace Laboratory NLR-TP-2004-319.
- [Revell et al., 1997] Revell, J. D., Kuntz, H. L., Balena, F., Horne, W. C., Storms, B. L., and Dougherty, R. (1997). Trailing edge flap noise reduction by porous acoustic treatment. *3rd AIAA/CEAS Aeroacoustics Conference, AIAA paper 97-1646-CP*.
- [Romano et al., 2007] Romano, G. P., Ouellette, N. T., Xu, H., Bodenschatz, E., Steinberg, V., Meneveau, C., and Katz, J. (2007). Chapter on *Measurements of Turbulent Flows* in *Springer Handbook of Experimental Fluid Mechanics*. Springer Science+Business Media, Berlin Heidelberg.
- [Sarradj, 2010] Sarradj, E. (2010). A fast signal subspace approach for the determination of absolute levels from phased microphone array measurements. *Journal of Sound and Vibration*, 329:1553 – 1569.
- [Sarradj, 2011] Sarradj, E. (2011). private communication on *The Use of Different Steering Vectors for Three-Dimensional Acoustic Source Mapping*.
- [Sarradj et al., 2009] Sarradj, E., Fritzsche, C., Geyer, T., and Giesler, J. (2009). Acoustic and aerodynamic design and characterization of a small-scale aeroacoustic wind tunnel. *Applied Acoustics*, 70:1073 – 1080.

- [Sarradj et al., 2006] Sarradj, E., Lerch, T., and Hübelt, J. (2006). Input parameters for the prediction of acoustical properties of open porous asphalt. *Acta Acustica United With Acustica*, 92:85 – 96.
- [Scheidegger, 1974] Scheidegger, A. E. (1974). *The Physics of Flow through Porous Media, Third Edition*. University of Toronto Press.
- [Schlichting and Gersten, 2000] Schlichting, H. and Gersten, K., editors (2000). *Boundary Layer Theory*. Springer Science+Business Media, Berlin.
- [Schlinker and Amiet, 1980] Schlinker, R. H. and Amiet, R. K. (1980). Refraction and scattering of sound by a shear layer. Technical report, NASA, Langley Research Center under Contract NAS1-15339.
- [Schlinker and Amiet, 1981] Schlinker, R. H. and Amiet, R. K. (1981). Helicopter rotor trailing edge noise. Technical report, NASA Contractor Report 3470.
- [Schulz-Hausmann, 1985] Schulz-Hausmann, F. K. v. (1985). Wechselwirkung ebener Freistrahlen mit der Umgebung. *Fortschrittberichte VDI*, 7: Strömungstechnik.
- [Schulze et al., 2004] Schulze, C., Sarradj, E., and Zeibig, A. (2004). Characteristics of microphone arrays. In *Proceedings of Inter-Noise 2004, Prague, Czech Republic*.
- [Selig et al., 1989] Selig, M. S., Donovan, J., and Fraser, D. (1989). *Airfoils at Low Speeds*. SoarTech Aero Publications.
- [Shannon and Morris, 2008] Shannon, D. and Morris, S. C. (2008). Trailing edge noise measurements using a large aperture phased array. *Journal of Aeroacoustics*, 7:147 – 176.
- [Sijtsma, 2007] Sijtsma, P. (2007). CLEAN based on spatial source coherence. *13th AIAA/CEAS Aeroacoustics Conference, AIAA paper 2007-3436*.
- [Sijtsma and Stoker, 2004] Sijtsma, P. and Stoker, R. W. (2004). Determination of absolute contributions of aircraft noise components using fly-over array measurements. Technical report, National Aerospace Laboratory NLR, NLR-TP-2004-167.
- [Silverstein and Katzoff, 1937] Silverstein, A. and Katzoff, S. (1937). Experimental investigation of wind-tunnel interference on the downwash behind an airfoil. Technical report, NACA, Report No. 609.
- [Stoica and Moses, 1997] Stoica, P. and Moses, R. (1997). *Introduction to Spectral Analysis*. Prentice-Hall, Upper Saddle River, NJ.
- [Suzuki, 2010] Suzuki, T. (2010). A review of diagnostic studies on jet-noise sources and generation mechanisms of subsonically convecting jets. *Fluid Dynamics Research*, 42 (1):doi: 10.1088/0169-5983/42/1/014001.
- [Theodorsen and Silverstein, 1934] Theodorsen, T. and Silverstein, A. (1934). Experimental verification of the theory of wind-tunnel boundary interference. Technical report, NACA, Report No. 478.

- [Torquato et al., 2000] Torquato, S., Truskett, T., and Debenedetti, P. (2000). Is random close packing of spheres well defined? *Physical Review Letters*, 84:2064 – 2067.
- [Vad et al., 2006] Vad, J., Koszó, G., Gutermuth, M., Kasza, Z., Tábi, T., and Csörgő (2006). Study of the aero-acoustic and aerodynamic effects of soft coating upon airfoil. *JSME International Journal, Series C*, 49 (3):648 – 656.
- [Windisch, 2007] Windisch, T. (2007). Untersuchung der geräuschkindernden Eigenschaften des Gefieders von Eulenvögeln. Master's thesis, Faculty 3 - Mechanical, Electrical and Industrial Engineering, Brandenburg University of Technology Cottbus.
- [Winkler et al., 2009] Winkler, J., Carolus, T., and Moreau, S. (2009). Airfoil trailing-edge blowing: Broadband noise prediction from large-eddy simulation. *15th AIAA/CEAS Aeroacoustics Conference, AIAA paper 2009-3200*.
- [Wynanski et al., 1986] Wynanski, I., Champagne, F., and Marasli, B. (1986). On the large-scale structures in two-dimensional, small-deficit, turbulent wakes. *Journal of Fluid Mechanics*, 168:31 – 71.
- [Zwikker and Kosten, 1949] Zwikker, C. and Kosten, C. W. (1949). *Sound Absorbing Materials*. Elsevier Publishing Company, Inc., New York.

List of Figures

1.1	Basic principle of the noise generation due to a fluid flow interacting with the trailing edge of an airfoil	2
1.2	Block diagram of the noise generation due to a fluid flow interacting with rigid surfaces (figure prepared according to artwork originally given in [Hayden, 1972], Figure 1	3
2.1	Comparison of the spectral shape of turbulent boundary layer - trailing edge noise according to different prediction models	19
3.1	Definition of the air flow resistivity	23
3.2	Photographs of some of the porous materials	24
3.3	Detailed photographs of the surface of two of the porous materials	25
3.4	Comparison of the two airfoil designs	26
3.5	In situ measurement of the specific air flow resistance, measured at two chord positions	28
3.6	Wind tunnel nozzle characteristics: Turbulence intensity and velocity profile for a flow speed of $U_0 \approx 50$ m/s at four different distances from the nozzle	31
3.7	Wind tunnel characteristics: Turbulence intensity and velocity profile for two different flow speeds	32
3.8	A-weighted overall sound pressure level of the aeroacoustic wind tunnel . .	32
3.9	Measurement setup in the aeroacoustic wind tunnel	33
3.10	Definition of the measured lift and drag forces	34
3.11	Setup used for the aerodynamic measurements	35
3.12	Microphone array design	42
3.13	Beam pattern of the 56-microphone array at different frequencies	42
3.14	Comparison of the third-octave band sound maps calculated from all 56 microphones and from the inner 40 microphones to determine the influence of coherence loss	44
3.15	Schematic representation of the two-dimensional sector used for the integration of the trailing edge noise sources	47

3.16	Comparison of sound maps obtained by using different two-dimensional beamforming algorithms for the non-porous reference airfoil	49
3.17	Comparison of sound maps obtained by using different two-dimensional beamforming algorithms for one porous airfoil	50
3.18	Comparison of different two-dimensional beamforming algorithms for three airfoils	51
3.19	Example of a three-dimensional beamforming result: 4 kHz octave band sound map of the non-porous airfoil at zero angle of attack and maximum flow speed (orthogonal beamforming)	53
3.20	Comparison of the power spectral density for all three beamforming algorithms and the weighted sum of the microphone autospectra	54
3.21	Comparison of three-dimensional beamforming algorithms	55
3.22	Sample three-dimensional beamforming results for three airfoils at maximum flow speed, CLEAN-SC	57
3.23	Sample three-dimensional beamforming results for three airfoils at maximum flow speed, orthogonal beamforming	59
3.24	Influence of the vertical extent of the trailing edge sector on third-octave band sound pressure level spectra	61
3.25	Comparison of the influence of different steering vectors for three airfoils	62
3.26	Photograph of the boundary layer probe used for the CTA measurements	64
3.27	Positions for the CTA boundary layer measurements	65
4.1	Normalized lift and drag forces $F_{L,n,0}$ and $F_{D,n,0}$	70
4.2	Measured lift and drag forces F_L and F_D as a function of the flow speed at an geometric angle of attack $\alpha = 0^\circ$	71
4.3	Measured lift and drag forces F_L and F_D as a function of the flow speed at an geometric angle of attack $\alpha = 8^\circ$	72
4.4	Normalized lift and drag forces $\bar{F}_{L,n}$ and $\bar{F}_{D,n}$ as a function of air flow resistivity r of the porous materials	73
4.5	Trailing edge noise third-octave band sound pressure levels, obtained by two-dimensional beamforming, as a function of chord based Strouhal number	75
4.6	Overall sound pressure level of the noise measured at the trailing edge, obtained by two-dimensional beamforming, as a function of the flow speed	76
4.7	Comparison of measured third-octave band sound pressure level spectra for the reference airfoil with NAFNoise prediction	77
4.8	Dependence of the third-octave band sound pressure level spectra of the reference airfoil on the flow speed	79
4.9	Scaling of the trailing edge noise of the non-porous reference airfoil with the 4.5th power of the flow speed	80

4.10	Third-octave band sound pressure levels of the noise measured at the trailing edge of the airfoils as a function of frequency	81
4.11	Third-octave band sound pressure levels of the noise measured at the trailing edge of the airfoils at different flow speeds as a function of frequency	83
4.12	Trailing edge noise reduction of the porous airfoils compared to the non-porous airfoil	84
4.13	Trailing edge noise reduction of the porous airfoils, with the exception of the airfoils made of Arpro and Reapor, compared to the non-porous airfoil	85
4.14	Trailing edge noise third-octave band sound pressure levels as a function of chord based Strouhal number, scaled based on $U_0^{4.5}$	86
4.15	Trailing edge noise third-octave band sound pressure levels as a function of chord based Strouhal number, scaled based on $U_0^{4.5}$ (single plots)	87
4.16	Trailing edge noise third-octave band sound pressure levels as a function of chord based Strouhal number, scaled based on $U_0^{2.5}$ and the measured lift force F_L	89
4.17	Measured boundary layer velocity profiles near the surface of the non-porous reference airfoil	92
4.18	Measured boundary layer velocity profiles near the surface of the airfoil made of Porex	93
4.19	Measured boundary layer velocity profiles near the surface of the airfoil made of Reapor	93
4.20	Measured boundary layer velocity profiles near the surface of the airfoil made of Recemat	94
4.21	Measured boundary layer velocity profiles near the surface of the airfoil made of M-Pore Al 45 ppi	94
4.22	Measured velocity profiles above the trailing edge	95
4.23	Boundary layer thickness of the airfoils	96
4.24	Measured velocity profiles in the wake	97
4.25	Statistic flow parameters boundary layer displacement thickness, boundary layer momentum thickness, boundary layer energy thickness and shape factor	98
4.26	Dependence of the (suction side) boundary layer displacement thickness on the flow speed and the angle of attack	103
4.27	Boundary layer displacement thickness of the airfoils	104
4.28	Turbulence parameters in the wake of the airfoils	106
4.29	Power spectral density of the turbulent velocity fluctuations and third-octave band turbulence spectra of the airfoils	107
4.30	Comparison of measured third-octave band turbulence spectra with normalized turbulence spectra for different flow speeds	110
4.31	Comparison of different normalization approaches	111

4.32	Normalized turbulence spectra of the airfoils, measured at different positions along the chord	113
4.33	Normalized turbulence spectra of the airfoils, measured at different positions along the chord	115
4.34	Third–octave band turbulence spectra measured in the wake of the airfoils	116
5.1	Turbulence spectra measured at different distances above the trailing edge of two airfoils	123
5.2	Mean flow velocity as a function of the viscous permeability of the airfoils .	125
5.3	Gradient of the velocity in the boundary layer above the trailing edge . . .	127
5.4	Comparison of predicted and measured trailing edge noise third–octave band sound pressure levels as a function of chord based Strouhal number for a subset of the airfoils	128
5.5	Influence of the distance of the measurement position from the airfoil surface on the noise prediction	131
5.6	Influence of the distance of the measurement position from the airfoil surface on the mean flow velocity	132
5.7	Influence of the distance of the measurement position from the airfoil surface on the noise prediction	133
5.8	Approximation of the characteristic turbulence spectra and corresponding peak Strouhal numbers	136
5.9	Parameters m_2 and n_2 needed for the modeling of the third–octave band turbulence spectra	138
5.10	Third–octave band turbulence spectra predicted for the porous airfoils . . .	139
5.11	Mean flow velocity, averaged over the velocities measured at suction side and pressure side	140
5.12	Comparison of predicted third–octave band sound pressure levels with measured sound pressure levels of the trailing edge noise of porous airfoils . . .	142
A.1	Turbulence intensity for two flow speeds at four different distances from the nozzle	169
A.2	Wind tunnel nozzle characteristics: Turbulence intensity and velocity profile for a flow speed of $U \approx 20$ m/s at four different distances from the nozzle .	170
C.1	Photograph of the porous airfoils used for the CTA measurements, from upper left to lower right: M–Pore Al 45 ppi, Porex, Reapor, Recemat . . .	173
C.2	Photographs of the setup used for the measurements	174
C.3	Photograph of the setup used for the measurements, including the planar microphone array positioned above the airfoil	174
D.1	Position of the point source S relative to the microphone array	175

D.2	Comparison of 3D beamforming algorithms for a point source	176
E.1	Turbulence spectra measured at three different spanwise positions above the trailing edge of the non-porous airfoil	177
E.2	Normalized turbulence spectra for different flow speeds	178
E.3	Normalized turbulence spectra of the airfoils, measured at different positions along the chord on the suction side	179

List of Tables

3.1	Materials used for the manufacturing of the airfoils	23
3.2	Porous airfoils used for the CTA measurements	63
4.1	Ratio of boundary layer displacement thickness to boundary layer thickness and ratio of trailing edge thickness to boundary layer displacement thickness for the airfoils given in Table 3.2	100
5.1	Coefficients m_2 and n_2 determined for the modeling of the third–octave band turbulence spectra according to Equation (5.6)	137
B.1	Position of the 56 microphones	171

Appendix A

Additional wind tunnel data

In addition to the wind tunnel turbulence data and velocity data given in Figure 3.6 from Section 3.2, further data are given here to show the virtually not turbulent flow of the small aeroacoustic wind tunnel at BTU Cottbus in combination with the circular nozzle with a diameter of 0.2 m.

First, Figure A.1 shows the measured turbulence intensity Tu in a plane parallel to the nozzle exit plane at four distances from the nozzle exit for flow speeds of 50 m/s and 20 m/s.

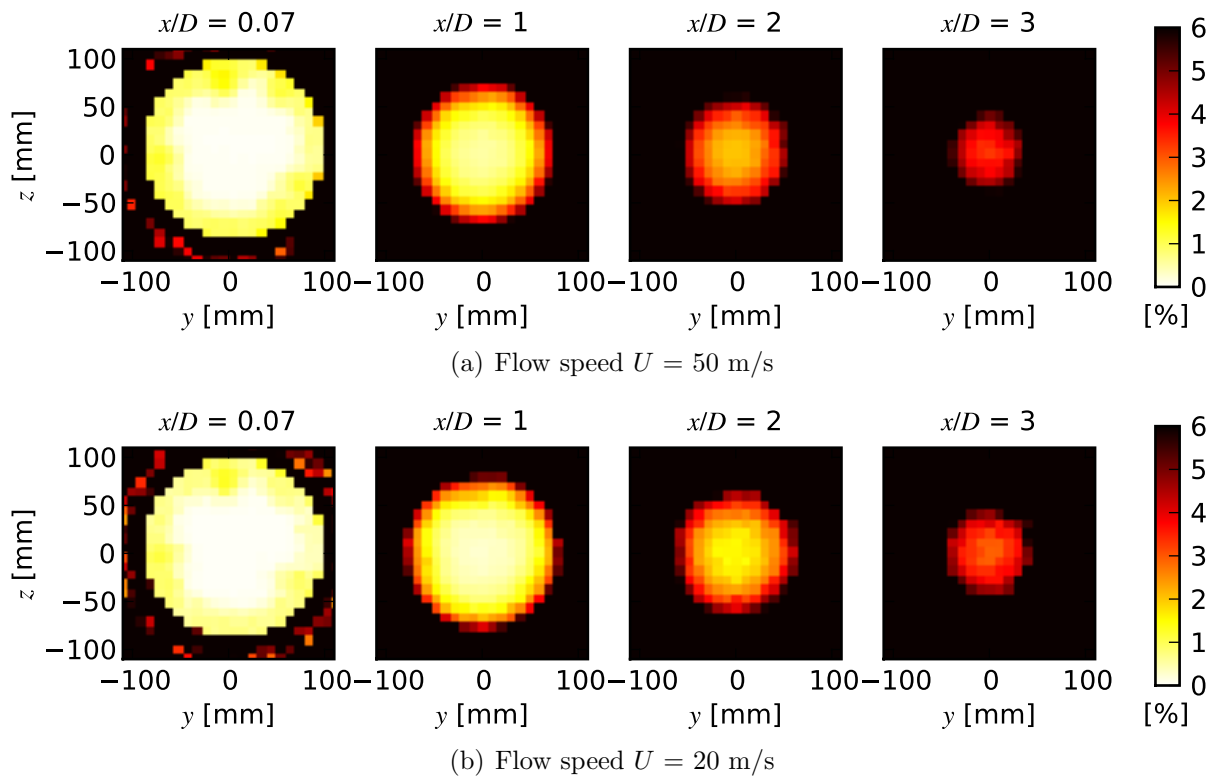
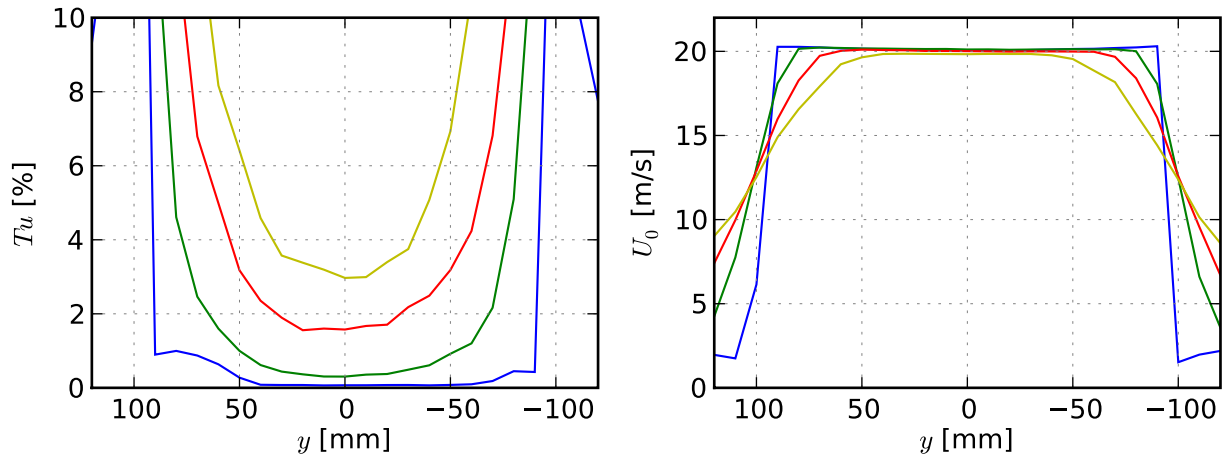


Figure A.1: Turbulence intensity Tu according to Equation 3.15 for two flow speeds at four different distances from the nozzle (diameter $D = 200$ mm)

Second, similar to Figure 3.6, the turbulence intensity Tu as well as the velocity profile at different distances from the nozzle exit can be seen in Figure A.2 for a flow speed of approximately 20 m/s.



(a) Turbulence intensity Tu along a horizontal line at different distances from the nozzle (b) Velocity profile at different distances from the nozzle

Figure A.2: Wind tunnel nozzle characteristics: Turbulence intensity Tu according to Equation 3.15 and velocity profile for a flow speed of $U \approx 20$ m/s at four different distances from the nozzle (diameter $D = 200$ mm): $x/D =$ ■ 0.07, ■ 1, ■ 2, ■ 3

Appendix B

Microphone positions

Table B.1 gives the position of the 56 microphones in the microphone array (all microphones are located in the plane $z = 0$).

Table B.1: Position of the 56 microphones

no	x	y	no	x	y
1	-0.145527	0.633500	29	0.345049	0.550855
2	-0.066774	0.236764	30	0.120201	0.214634
3	-0.376879	0.529587	31	0.107980	0.640968
4	-0.152297	0.193188	32	0.028914	0.244295
5	-0.550855	0.345049	33	-0.029598	0.463341
6	-0.214634	0.120201	34	-0.028790	0.088281
7	-0.640968	0.107980	35	-0.348561	0.306703
8	-0.244295	0.028914	36	-0.082782	0.042067
9	-0.633500	-0.145527	37	-0.463341	-0.029598
10	-0.236764	-0.066774	38	-0.088281	-0.028790
11	-0.529587	-0.376879	39	-0.306703	-0.348561
12	-0.193188	-0.152297	40	-0.042067	-0.082782
13	-0.345049	-0.550855	41	0.029598	-0.463341
14	-0.120201	-0.214634	42	0.028790	-0.088281
15	-0.107980	-0.640968	43	0.348561	-0.306703
16	-0.028914	-0.244295	44	0.082782	-0.042067
17	0.145527	-0.633500	45	0.463341	0.029598
18	0.066774	-0.236764	46	0.088281	0.028790
19	0.376879	-0.529587	47	0.306703	0.348561
20	0.152297	-0.193188	48	0.042067	0.082782
21	0.550855	-0.345049	49	-0.138631	0.241627
22	0.214634	-0.120201	50	-0.268883	0.072829
23	0.640968	-0.107980	51	-0.241627	-0.138631
24	0.244295	-0.028914	52	-0.072829	-0.268883
25	0.633500	0.145527	53	0.138631	-0.241627
26	0.236764	0.066774	54	0.268883	-0.072829
27	0.529587	0.376879	55	0.241627	0.138631
28	0.193188	0.152297	56	0.072829	0.268883

Appendix C

Photographs of the experimental setup

Figure C.1 shows a photograph of the subset of the porous airfoils which was used for the CTA measurements. Figure C.2 and Figure C.3 show photographs of the setup used for the aerodynamic and acoustic measurements described in the present thesis.

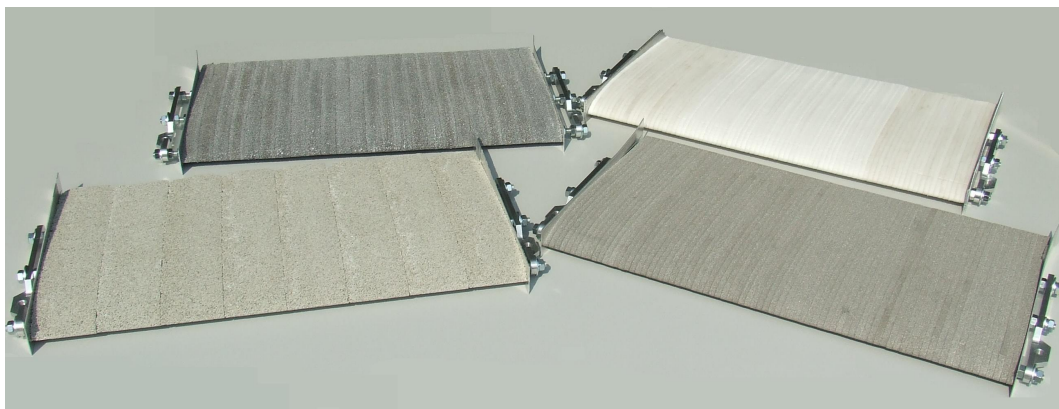


Figure C.1: Photograph of the porous airfoils used for the CTA measurements, from upper left to lower right: M-Pore Al 45 ppi, Porex, Reapor, Recemat

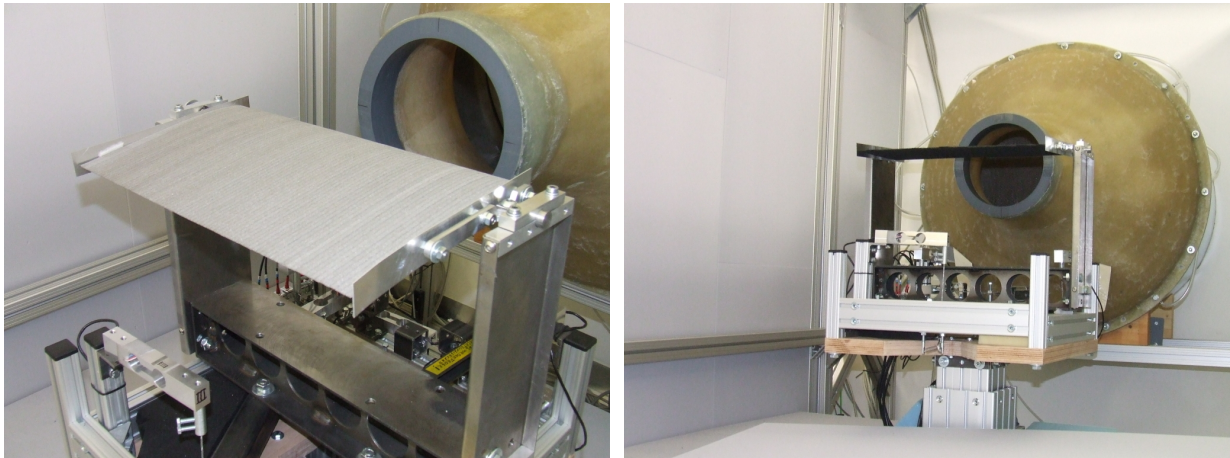


Figure C.2: Photographs of the setup used for the measurements

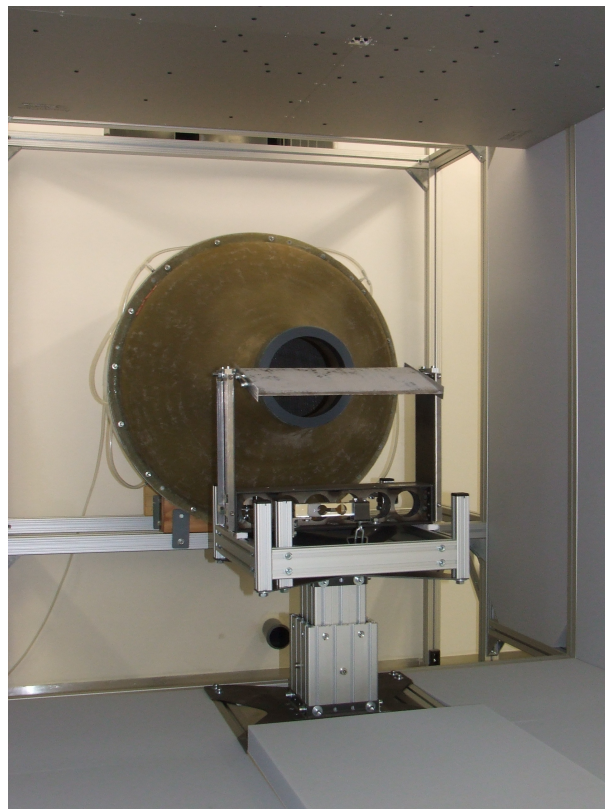


Figure C.3: Photograph of the setup used for the measurements, including the planar microphone array positioned above the airfoil

Appendix D

Comparison of three-dimensional beamforming algorithms for a single point source

In this section the results of different beamforming algorithms regarding the analysis of noise from both a simulated single point source and the measurement of a single loudspeaker will be compared.

The point source for both simulation and measurement was located at $(x, y, z) = (0.05 \text{ m}, -0.05 \text{ m}, 0.78 \text{ m})$ within the cabin that provides a semi-anechoic acoustic environment for frequencies above approximately 500 Hz, with the microphone array positioned above the source and the array center at $(0, 0, 0)$ as shown in Figure D.1.

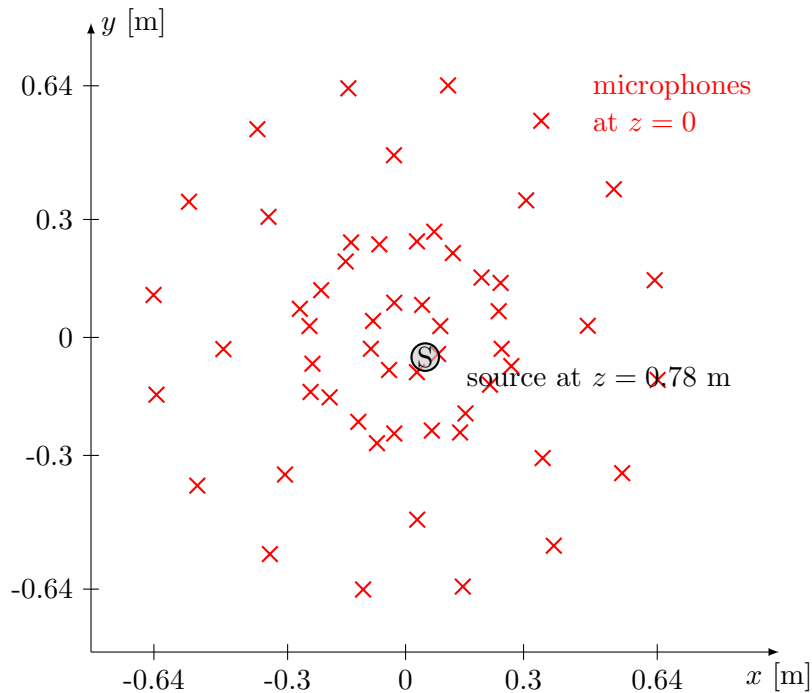


Figure D.1: Position of the point source S relative to the microphone array

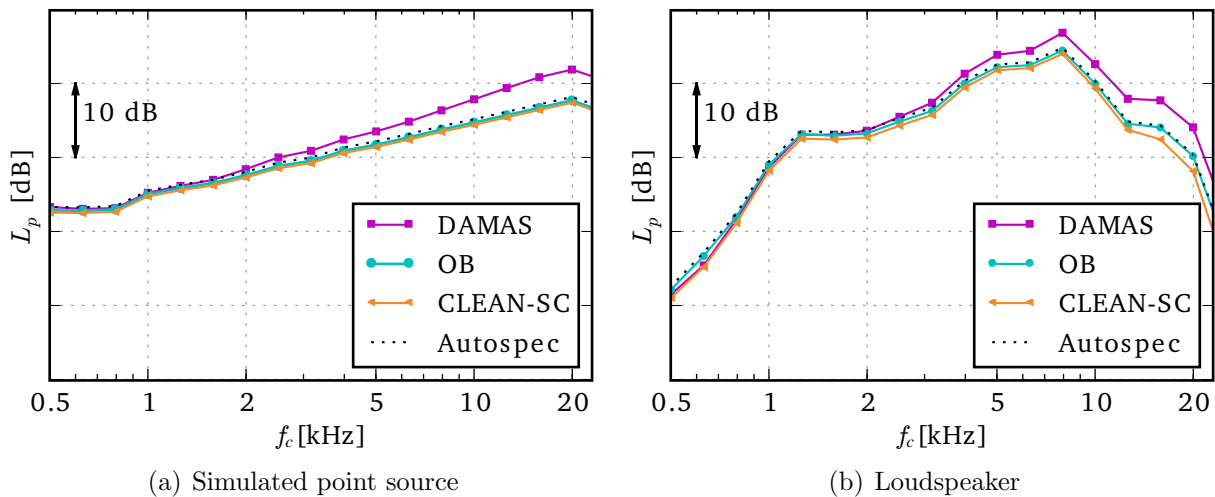


Figure D.2: Comparison of 3D beamforming algorithms for a point source S located at $(x, y, z) = (0.05 \text{ m}, -0.05 \text{ m}, 0.78 \text{ m})$, third-octave band sound pressure level spectra

Three different beamforming algorithms were tested, DAMAS, orthogonal beamforming (OB) and CLEAN-SC. As in the data processing described in Section 3.4.4, the steering vector was applied that was found to deliver the best results regarding the correct determination of the source location [Dougherty, 2002, Suzuki, 2010]. The extent of the grid in x -direction was from -0.2 m to 0.2 m , in lateral (y -) direction from -0.2 m to 0.2 m and in the vertical (z -) direction from 0.58 m to 0.98 m . For the DAMAS beamforming algorithm, the grid increment had a size of 0.02 m due to the large computational effort necessary, while for the CLEAN-SC and the orthogonal beamforming the increment was only 0.01 m . The data processing was identical to that described in Section 3.4.

The simulated point source was driven by white noise signals simulated from a gaussian random process. The single loudspeaker was also driven by a white noise signal, a setup that was already used in [Sarradj et al., 2009].

The results of the integration over the complete source region are shown in Figure D.2(a) for the simulated point source and in Figure D.2(b) for the single loudspeaker setup. Included in each figure is the average of the autospectra of all 56 microphones, weighted with the distance between the source and the individual microphone location.

In general, the comparison of the three beamforming algorithms yields the same results as for the measurements at the airfoils. All three algorithms basically lead to plausible sound pressure levels. But while the spectra obtained by the CLEAN-SC algorithm and the orthogonal beamforming are more or less similar and reflect the averaged microphone autospectra over the complete range of frequencies, the DAMAS algorithm delivers results that are higher than the microphone autospectra at high frequencies. At frequencies approximately above 12.5 kHz , the CLEAN-SC results are slightly below the microphone autospectra for the loudspeaker measurement shown in Figure D.2(b).

Based on this rather simple comparison, and without the investigation of corresponding sound maps, it is therefore concluded that in the present case the orthogonal beamforming algorithm delivers the best results regarding the determination of the correct source strength.

Appendix E

Additional turbulence spectra

E.1 Influence of the spanwise position

Figure E.1 shows the comparison of the turbulence spectra measured at three different positions along the span approximately 1 mm above the trailing edge of the non-porous reference airfoil. The measurement positions are all located within the wind tunnel core jet. The hot-wire measurements were performed in an earlier test campaign in preparation for the measurements described in Section 3.5 and 4.3.

Nevertheless, it can be seen that the influence of the spanwise position on the result of the hot-wire measurements is negligible (maximum difference in the order of 1 dB in case of the third-octave band turbulence spectra, not normalized) when the measurements are performed within the core jet.

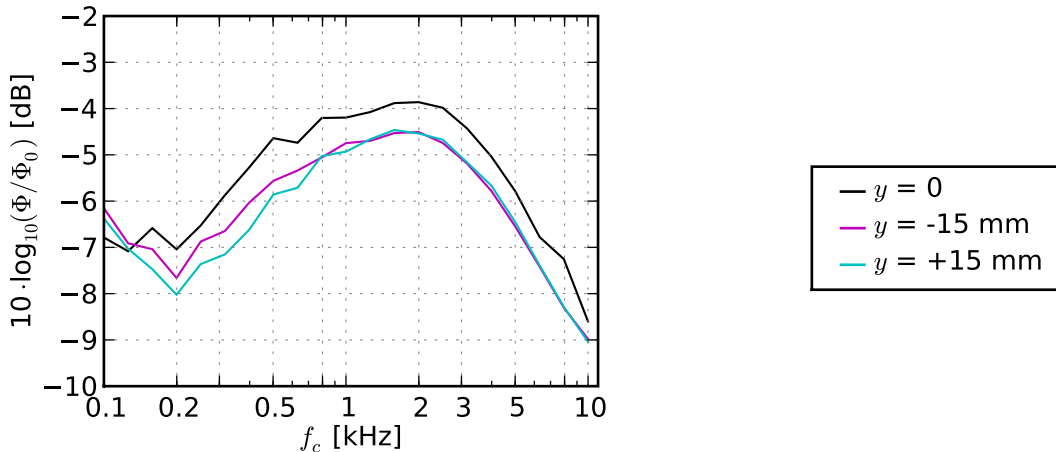
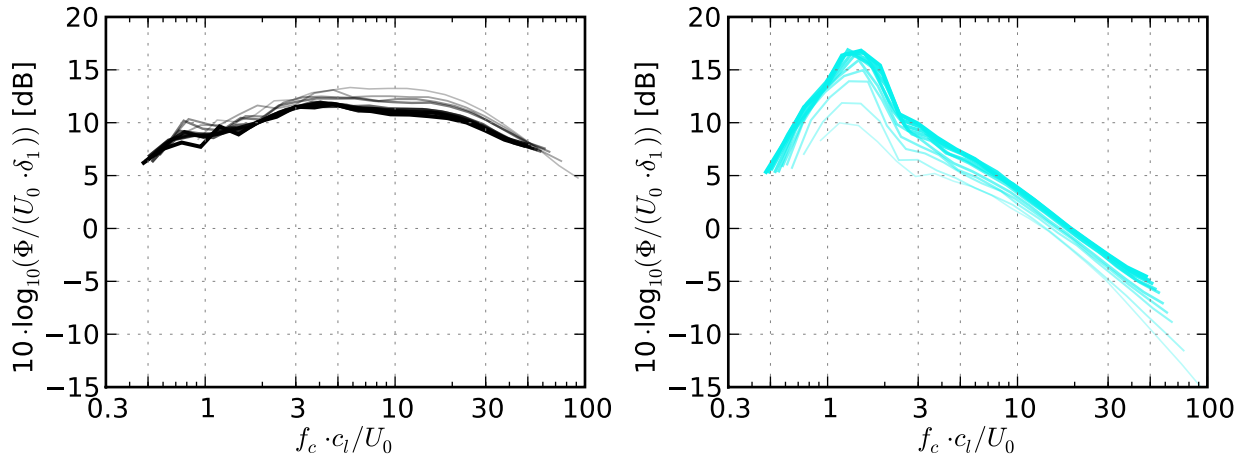


Figure E.1: Turbulence spectra (in third-octave bands) measured at three different spanwise positions above the trailing edge of the non-porous airfoil, $\alpha = 0^\circ$ and $U_0 = 50$ m/s

E.2 Normalization approach

In addition to the normalization approach shown in Figure 4.30, Figure E.2 shows another normalization approach that was tested on the non-porous reference airfoil and the porous airfoil made of Recemat ($r = 8,200 \text{ Pa s/m}^2$). It uses the turbulent boundary layer displacement thickness δ_1 and was also used by Garcia-Sagrado et al. [Garcia-Sagrado et al., 2006]. It is visible that this approach does not lead to a noticeable improvement, since the different curves do not collapse better than when the approach shown in Figure 4.30 is used.



(a) Normalized turbulence spectra of the non-porous reference airfoil ($r = \infty$), from thinnest to thickest line: $U_0 \approx 26, 31, 36, 38, 40, 42, 44, 46, 48, 50 \text{ m/s}$

(b) Normalized turbulence spectra of the airfoil made of Recemat ($r = 8,200 \text{ Pa s/m}^2$), from thinnest to thickest line: $U_0 \approx 26, 31, 36, 38, 40, 42, 44, 46, 48, 50 \text{ m/s}$

Figure E.2: Comparison of turbulence spectra for different flow speeds between $U_0 = 25 \text{ m/s}$ (thinnest, most transparent line) and $U_0 = 50 \text{ m/s}$ (thickest, most opaque line), angle of attack $\alpha = 0^\circ$, normalized using the turbulent boundary layer displacement thickness δ_1 .

E.3 Turbulence spectra at different chord positions

Additional plots of the turbulence spectra measured at different chord positions, similar to those presented in Figure 4.33, but normalized using the mean flow velocity \bar{u} at the according measurement position instead of the flow speed U_0 , are given in Figure E.3. The normalized turbulence spectra $10 \cdot \log_{10}[\Phi / (\bar{u} \cdot c_l)]$ are plotted versus the Strouhal number based on chord length, $f_c \cdot c_l / U_0$.

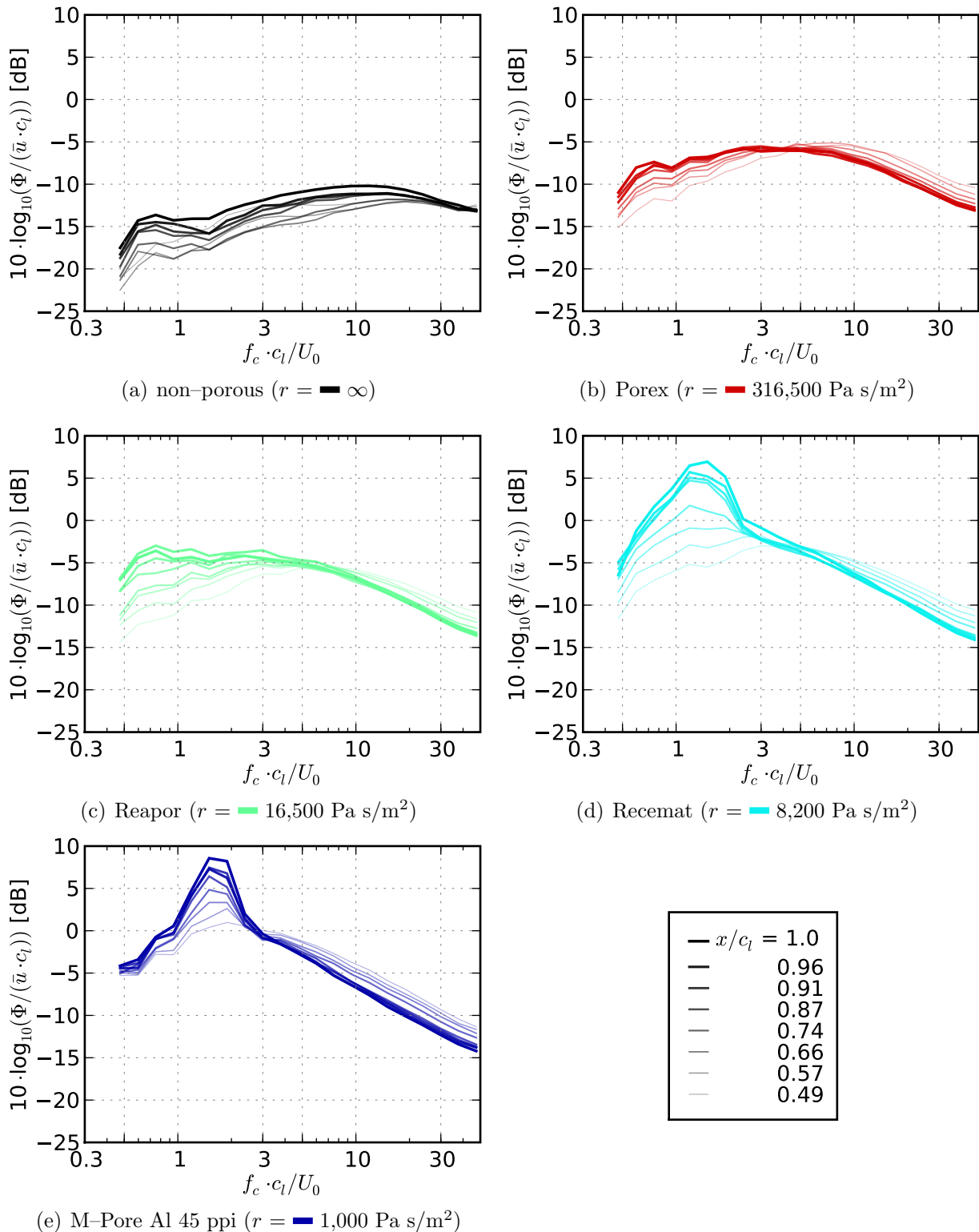


Figure E.3: Normalized turbulence spectra (in third-octave bands) of the airfoils, measured at different positions along the chord on the suction side approximately 1 mm above the surface, $\alpha = 0^\circ$ and $U_0 = 50 \text{ m/s}$ (The line width and the opacity of the solid lines increase with decreasing distance of the measurement position from the airfoil trailing edge with $x/c_l = 0.49, 0.57, 0.66, 0.74, 0.87, 0.91, 0.96$ and $1.$)

